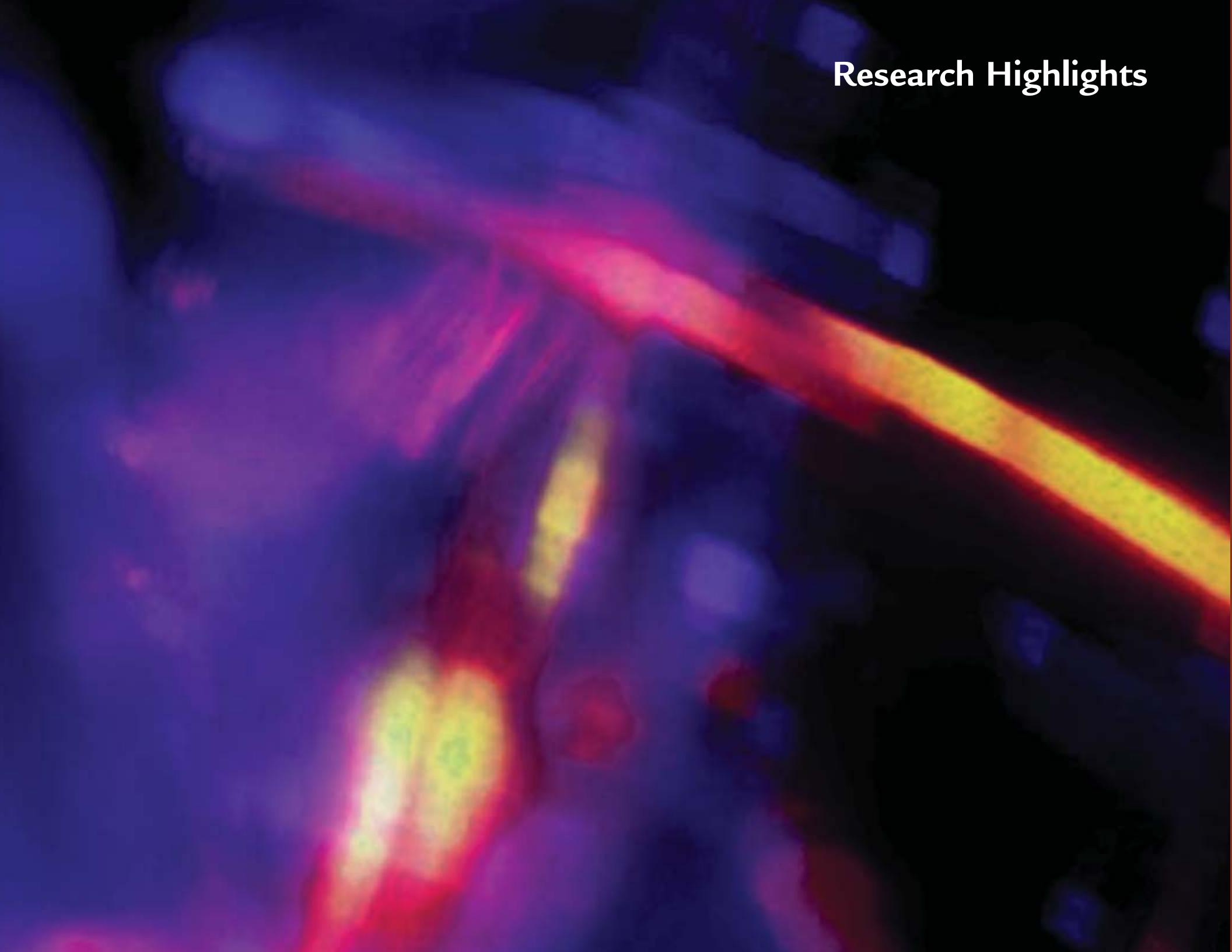# Biosciences

Many of the achievements of science to date have come from a reductionist strategy, in which scientists attempt to decompose the object under study into ever simpler components and to understand those components with ever-increasing quantitative precision. Physics has been particularly successful in this regard. In contrast, much of biology has traditionally been less quantitative and more descriptive in character, both because biological systems are so complex and because some of the key explanatory concepts lie at a more abstract level. Examples of such complex phenomena include coding and processing of genetic information by DNA and information representation, coding, and processing by the nervous system.

Just as the past century is regarded as the century of the physical sciences, the next century will likely become the century of the biological sciences. Physics Division is well positioned to contribute to this biological revolution-in-progress through our emphasis on understanding biological systems using the scientific, technical, and conceptual resources of physics. Recent advances in biophysical measurement and in molecular biology are beginning to allow a detailed physical understanding of biological phenomena that were previously understood only in qualitative terms. The Division is well placed by virtue of its capabilities and research interests to contribute significantly to this important trend in the biosciences.

The Laboratory's neural modeling team. Seated (left to right): Garrett Kenyon (P-21) and James Theiler (NIS-2). Standing: Bryan Travis (EES-6), Janelle Jeffs (P-21), and Kurt Moore (NIS-1).

Synchronization of Spiking Neurons in a Computer Model of the Mammalian Retina

G. T. Kenyon (P-21), J. Theiler (NIS-2), K. R. Moore (NIS-1), B. J. Travis (EES-5), J. Jeffs (P-21), and D. W. Marshak (University of Texas Health Science Center, Houston)

Introduction

In typical man-made imaging devices (*i.e.*, CCDs, video cameras), the output from each pixel changes continuously in proportion to the light intensity at the corresponding location. In the mammalian retina, however, the output neurons, called ganglion cells, do not vary their responses continuously, but rather encode information as sequences of uniform impulses, or spikes. Analysis of spike trains recorded from individual ganglion cells strongly favors the hypothesis that information in the optic nerve is "rate coded." When measuring how a typical mammalian ganglion cell responds to a spot of light presented in its receptive field (the region of the visual space to which that cell is most sensitive), it is usually observed that a different sequence of impulses is generated on each stimulus trial. In general, there exists no precise pattern of interspike intervals that is generated reproducibly from one stimulus presentation to the next. If, however, one estimates the instantaneous firing rate of the cell, which can be done by sorting the spikes generated across many stimulus trials into time bins relative to the onset of the stimulus, a regular—and experimentally reproducible— pattern typically emerges. Thus, electrophysiologists have generally rejected the hypothesis that the mammalian visual system uses a "temporal code," in which the exact sequence of interspike intervals generated by each neuron conveys significant information. Instead, most vision scientists believe, at least at the level of individual neurons, that information is encoded by the instantaneous firing rate. According to the rate-code hypothesis, it is the average number of spikes that arrive within a given time window that is important, while the exact sequence of interspike intervals is ignored. Recent studies that have combined sophisticated analysis using information theory with recordings from individual neurons activated by natural or other complex stimuli have largely reinforced the basic assumptions underlying the rate-code hypothesis.[1] In these studies, most of the information conveyed by individual cells could be accurately modeled by a modified Poisson process, in which spikes are generated randomly with a probability governed by the instantaneous firing rate.

Beyond the Rate-Code

Within the last decade, the dominance of the rate-code hypothesis has been challenged by new experiments in which pairs of visual neurons, both in the retina and in the visual cortex, are monitored simultaneously. These studies have shown that many pairs of visual neurons exhibit a stimulus-selective synchronization.[2,3,4] The stimuli in such experiments typically consist of narrow bars of light projected against a uniform background. Pairs of neurons, which may be separated by many degrees of visual angle, are found to fire synchronously when stimulated by a single, long bar of light, while the same pair of neurons fires asynchronously when stimulated by two separate light bars. Extrapolating these results to the case of more complex images, one can imagine how the different components of an image could be segmented by separately synchronized groups of neurons.

Thus, in the cartoon in Figure 1, neurons responding to the same object, here represented by a banana, fire synchronously, while neurons responding to different objects, represented by an apple and an orange, fire asynchronously. A number of investigators have suggested that this behavior might serve as a mechanism for dynamically binding together elements of the visual scene that are functionally related, thus providing a possible neurobiological underpinning to the principles of perceptual grouping identified by Gestalt psychologists.
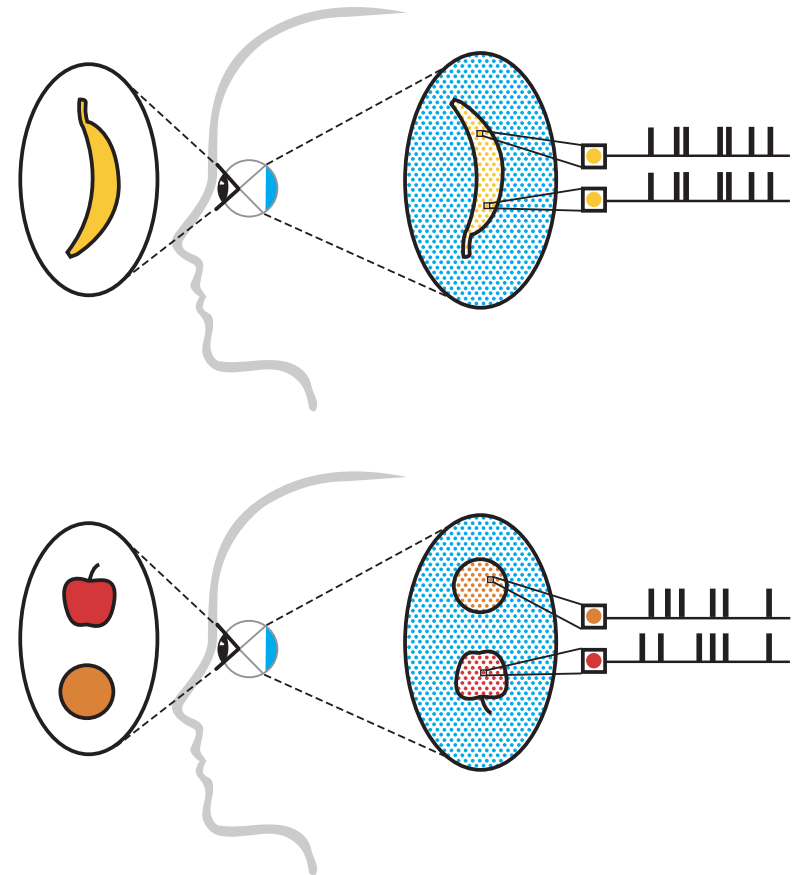

Figure 1. The retina uses synchrony to segment the visual space into objects. Top: Retinal output neurons (ganglion cells) fire synchronously when responding to the same object. Bottom: Ganglion cells fire asynchronously when responding to different objects.

Modeling the Synchronization of Ganglion Cells in the Mammalian Retina

We have constructed a detailed model of the inner mammalian retina (see Figure 2) that reproduces important aspects of the stimulus-selective synchronization between ganglion cells that has been described experimentally. Input to the model retina was conveyed by ON bipolar cells, which were driven by low-pass filtered currents (t = 2 msec) representing synaptic input from cone photoreceptors. The model bipolar cells produced excitatory postsynaptic potentials in both ganglion cells and amacrine cells (inhibitory interneurons) according to a random process. The model ganglion cells were twice as large as the bipolar cells and received inhibitory input from three different amacrine cell types encompassing three different spatial scales:

(1) small amacrine cells that were the same size as the bipolar cells;

(2) large amacrine cells, whose dendritic fields were the same size as the ganglion cells; and

(3) axon-bearing amacrine cells, whose central dendritic fields were the same size as the bipolar cells but whose long axons made synapses out to a distance of nine ganglion cell diameters, excluding a small central region corresponding to the dendritic field.

Of the three amacrine cell types in the model, only the axon-bearing amacrine cells fired spikes. All three amacrine cell types made feedforward synapses onto ganglion cells, feedback synapses onto bipolar cells, as well as synapses among themselves
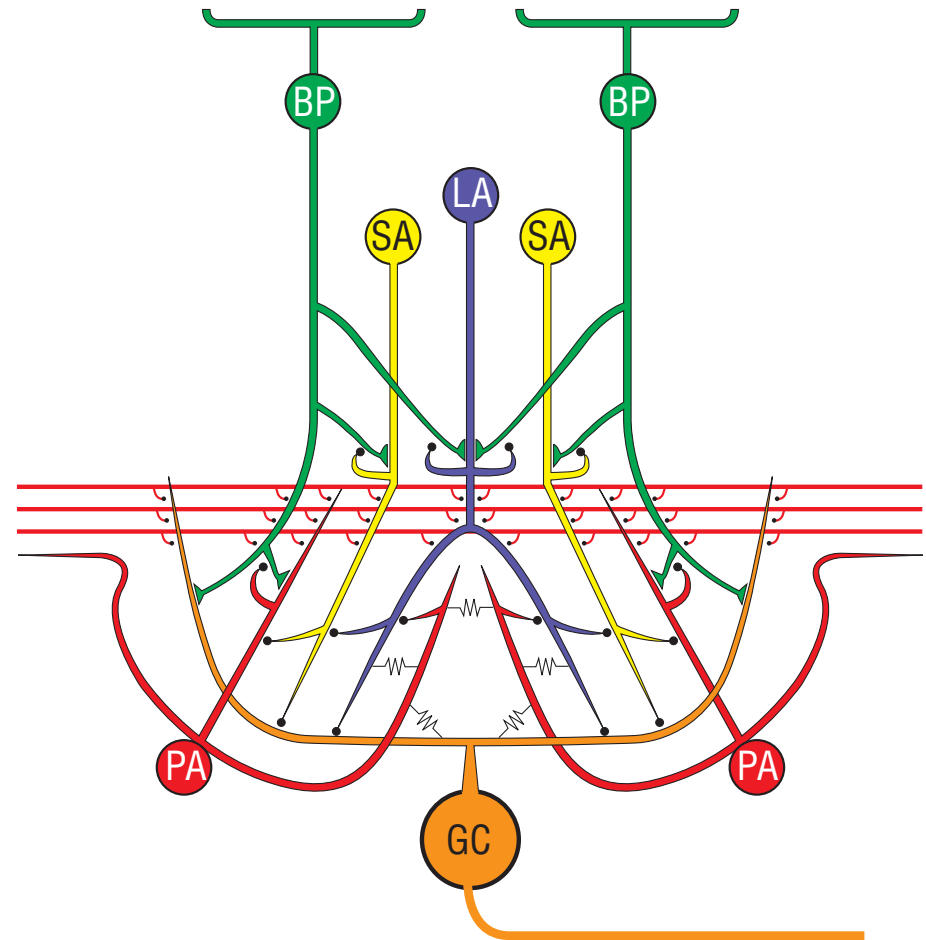

Figure 2. The model retina consisted of a 32 × 32 array of identical local processing units implemented as a torus. Input to each unit was conveyed by a 2 × 2 array of bipolar cells (BPs). The output of each unit was conveyed by the axon of a single ganglion cell (GC). Each local processing unit contained three different inhibitory interneurons, corresponding to small (SA), large (LA), and polyaxonal (PA) amacrine cells (ACs). Filled black circles are inhibitory synapses, triangular contacts excitatory synapses, and resistors gap junctions.

Responses to Small Light Spots

The data in Figure 3 plots the responses of a representative model ganglion cell to simulated light spots of increasing intensity. The illustrations on the left side of Figure 3A show the dimensions of the spot stimulus relative to the size and location of the model ganglion cell's receptive field center. The top trace on the right side of Figure 3A shows the firing activity elicited by a relatively dim spot, while the bottom trace on the right side of Figure 3A shows the firing activity produced by a relatively bright spot. While the bright spot elicits more spikes immediately following the stimulus onset, the precise temporal sequence of spikes appears more-or-less random. Electrophysiological data is therefore typically presented as in Figure 3B, which shows the peri-stimulus time histograms (PSTHs) accumulated over 20 stimulus trials for five different spot intensities. By averaging over multiple stimulus presentations, it is possible to reliably measure the time-dependent changes in firing rate produced by external stimulation.

The intensity series in Figure 3B is very similar to that recorded from ganglion cells in response to analogous stimuli,[5] thus indicating that our model network reproduces important aspects of retinal physiology. As summarized in Figure 3C, the peak firing rate following stimulus onset is strongly correlated with the intensity of the spot stimulus, while the plateau firing rate is only weakly dependent on the spot intensity. This characteristic property of ganglion cells has been termed contrast gain control[6], and in our retinal model, results from nonlinear negative feedback (see Figure 2).
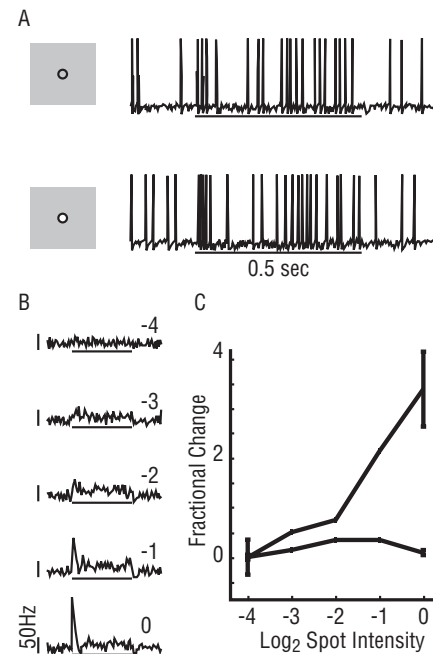

Figure 3. Responses of model ganglion cells to small spots. (A) Ganglion cell output consists of discrete, uniform pulses. A relatively dim spot (top) produces a small increase in the plateau firing rate, while a relatively bright spot (bottom) produces a large transient peak in the firing rate. (B) Peri-stimulus-time-histograms (PSTHs) plotted as a function of increasing spot intensity in $\log_2$ increments. (C) Plot of peak (solid line) and plateau (long-short dashed line) firing rate as a function of spot intensity.

Stimulus-Selective Synchronization between Model Ganglion Cells

Because the exact temporal sequence of spikes is not reproducible from trial to trial, does it then follow that the times of occurrences of individual spikes are of no significance? For many years, this was the attitude of the majority of neuroscientists. In the last decade, however, a rapidly growing body of experimental evidence suggests that the generation of discrete pulse trains provides biological neurons with a natural solution to the problem of dynamic binding and image segmentation.[7]

To investigate whether synchronous firing between the model ganglion cells was stimulus-selective, we examined the cross-correlation histograms (CCHs) between pairs of ganglion cells stimulated by two identical bars that were turned on simultaneously (Figure 4). To ensure that our analysis considered only correlations resulting from synaptic interactions, correlations resulting from stimulus coordination (dashed red traces) were subtracted. The correlations resulting from stimulus coordination were estimated by a shift-predictor, obtained by shifting one of the spike trains making up the

CCH by one or more stimulus trials. The shift-predictor thus preserves correlations resulting from a common modulation of the firing rate produced by the stimulus, but eliminates correlations resulting from synaptic interactions that are not time-locked to the stimulus onset. All CCHs were normalized as a fraction of the expected baseline synchrony, given by the amplitude of the CCH at zero delay in the absence of stimulation. To further reduce the effects of stimulus coordination, only activity during the plateau portion of the response was considered. CCHs were plotted for ganglion cell pairs at opposite ends of the same bar (Figure 4b$_1$, upper bar; Figure 4b$_3$, lower bar), or at the nearest opposing tips of the two separate bars (Figure 4b$_2$). Significant correlations were evident between ganglion cells responding to the same bar but not between ganglion cells responding to different bars (solid black traces). Even though the ganglion cells in each pair were separated by the same distance and were stimulated identically within their receptive field centers, only those pairs that
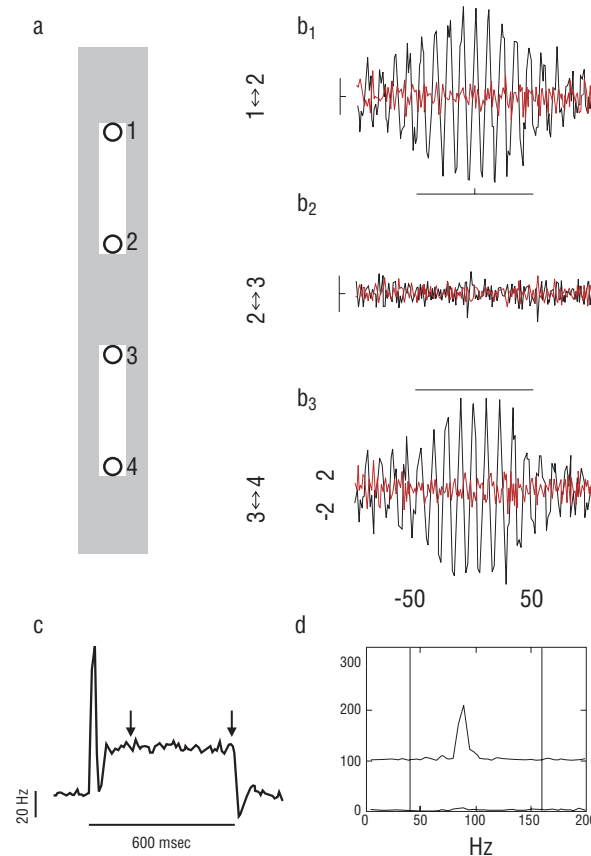

Figure 4. Stimulus-selective synchronization of ganglion cells. (a) Stimulus dimensions relative to the receptive field centers of individual ganglion cells. (b) Cross-correlation histograms (CCHs) computed during the plateau portion of the response for pairs of ganglion cells at opposite ends of the same bar or at opposing tips of separate bars. All ganglion cell pairs were separated by 7 diameters (bin size, 1 msec; scale: 100 msec, 0.5). (b$_1$) pair from upper bar; (b$_2$) pair from separate bars; (b$_3$) pair from lower bar. Correlations were only significant for pairs from the same bar. (c) Combined PSTH of cells 1–4. Arrows indicate plateau portion of response. (d) Power spectra of CCHs between cells stimulated by separate bars (lower trace) or by the same bar (upper trace—offset by 100).

responded to the same bar were strongly correlated. These results suggest that synchronization is able to provide a flexible label that can be used at the earliest stages of visual processing to dynamically bind together groups of elements that are syntactically related. To our knowledge, this is the first model of the vertebrate retina to account for stimulus-selective synchronization.

The CCHs between ganglion-cell pairs stimulated by the same bar show that joint firing probability oscillates as a function of the delay between the two spikes at a frequency of approximately 100 Hz, which falls within the frequency range measured experimentally.[8] There was no evidence of oscillatory activity in the combined PSTH, however (Figure 4c). This is because the 10-msec bin width used to construct the combined PSTH was too large to resolve the high-frequency oscillations evident in the CCHs. Furthermore, synaptically driven correlations only remained phase-locked to the stimulus onset for a short time (~50 msecs) and at longer times tended to average out over multiple stimulus trials. A peak in the power

spectra, given by the Fourier transform of the associated CCH, is only present in the correlations between cells stimulated by the same bar, suggesting that oscillatory activity itself, as well as synchrony, can be used for segmentation (Figure 4d).

The oscillations evident in the CCHs were driven by feedback inhibition from the axon-bearing amacrine cells, as can be understood by examining the synaptic circuitry of the retinal model (Figure 2). In response to a large stimulus, ganglion cells activated neighboring axon-bearing amacrine cells by way of electrical synapses and were then hyperpolarized by the ensuing wave of axon-mediated inhibition. If the stimulus was maintained, the ganglion cells recovered simultaneously, thus setting up the next cycle of the oscillation. Axon-mediated inhibition of the neurons with receptive fields in the gap between the two stimuli furthermore helped to maintain the selectivity of the stimulus-evoked oscillations, since spikes are rapidly attenuated when passively conducted through a chain of electrical synapses.[9]

Modulation of Firing Correlations by Velocity

In addition to being highly sensitive to global properties, such as the "connectedness" between visual regions, the degree of synchrony between the model ganglion cells was also very sensitive to local stimulus properties, such as brightness, size, and velocity. An example of this is illustrated in Figure 5, which examines the correlations produced by bars moving at several different velocities. The correlations produced by slow-moving bars were similar in amplitude and frequency to those measured during the plateau portion of the step response (see Figure 4). For bars swept across the receptive field at high velocity, the change in firing rate became sharply peaked, causing the expected correlations from stimulus coordination to become non-negligible. Even at high velocities, however, the amplitude of the shift predictor was much smaller than the additional correlations resulting from synaptic interactions. The amplitude of these additional correlations increased as a function of velocity,

even after correlations resulting from stimulus coordination were subtracted (Figure 5c). Measured as a fractional change from baseline, the strongest modulation was seen in the average power of the correlation function between 40–160 Hz. In contrast, the average firing rate during the same period of activity (indicated by the short tick marks under the PSTHs), was approximately constant as a function of velocity. These results demonstrate how, under some circumstances, firing correlations between many neurons can respond to changes in stimulus parameters over a greater dynamic range than the firing rates of individual cells.
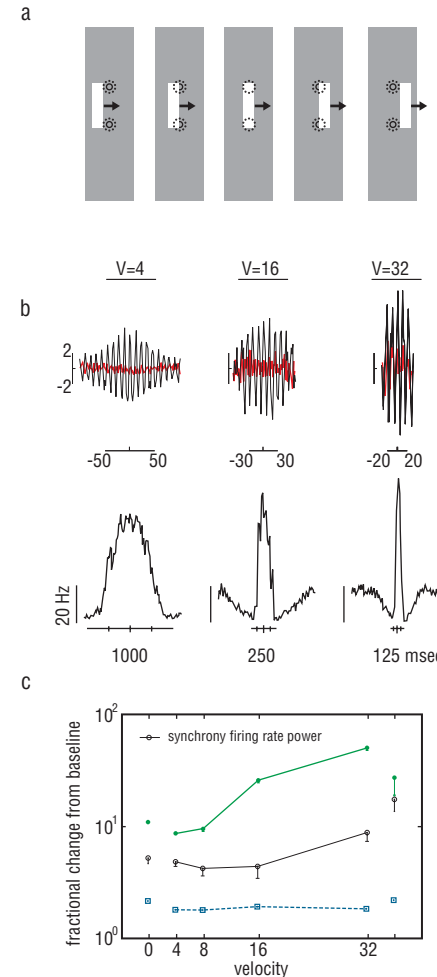

Figure 5. Firing correlations are modulated by velocity. (a) Illustration of stimulus protocol. Second and fourth panels bracket the period during which correlations were measured. (b) Ganglion cell (GC) responses at different velocities, in GC-GC distance/second, indicated at the top of each column. The top row of traces in 5b are CCHs. At high velocity, the correlations (solid black lines) become larger, while the synchrony due to stimulus coordination (solid red lines) remains relatively small. the bottom rowof 5b are combined PSTHs averaged over both recorded cells. Small vertical ticks mark measurement period. (c) The average power between 40–160 Hz (solid green line) is more strongly modulated by stimulus velocity than either the synchrony (solid black line) or the average firing rate (dashed blue line). All quantities measured as a fractional change from baseline.
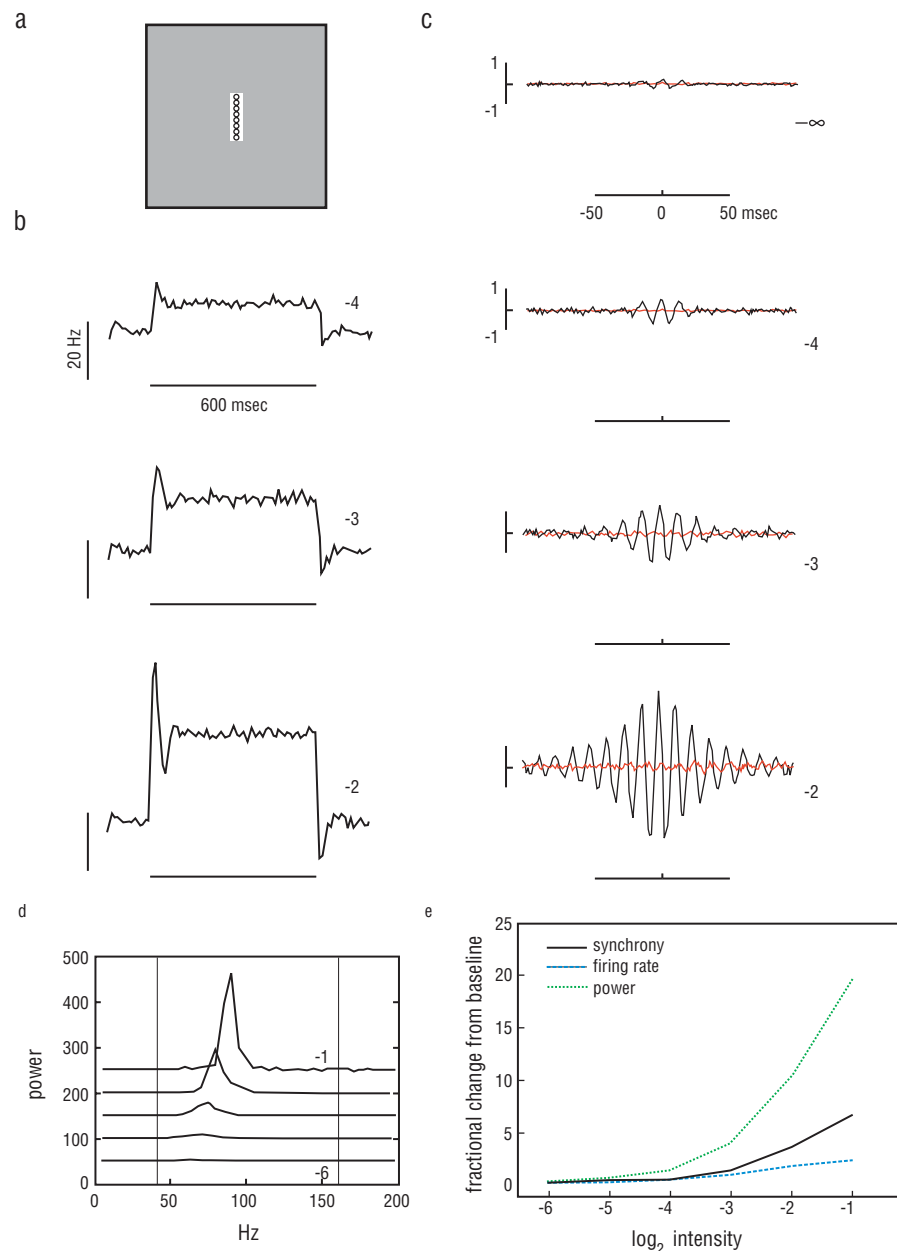
Firing Correlations are Modulated by Stimulus Intensity

Additional studies were conducted to examine how firing correlations could be modulated by the intensity of a stimulus (Figure 6). A line of model ganglion cells was stimulated by a narrow bar, which was presented at a range of intensities. The combined PSTHs, averaged over all stimulated cells, showed that the average firing rate, during both the peak and plateau portions of the response, increased steadily with stimulus intensity. Firing correlations were assessed by combining the individual CCHs of all stimulated cell pairs into a massed CCH measure. The massed CCH also increased in amplitude as the stimulus intensity was raised. This was particularly true of the power spectra of the massed CCH, which developed progressively larger peaks at higher stimulus amplitudes. The location of the peak power shifted slightly towards higher frequencies as the stimulus

intensity was increased, but this did not appear to be a major effect.

It is possible to compare the relative sensitivities of different measures of activity by examining their range of modulation as a function of stimulus intensity. Three measures of activity obtained during the plateau portion of the response were considered; the firing rate, the synchrony, and the average power between 40–160 Hz. Each of these measures was expressed as a fractional change from its respective baseline. With this normalization, the average power was approximately twice as sensitive as the synchrony, which in turn was approximately a factor of 2 more sensitive than the firing rate. These results suggest that significant information regarding the intensity of a stimulus can be encoded in the degree of firing correlations between the activated cells.

Figure 6. Firing correlations are modulated by stimulus intensity. (a) A line of eight ganglion cells was stimulated by a narrow stationary bar. (b) Combined PSTHs, averaged over all eight stimulated cells. As the $\log_2$ stimulus intensity (indicated to right of each plot) increased, firing rates increased correspondingly. (c) Massed CCHs, averaged over all stimulated cell pairs. Firing correlations also increased with stimulus intensity. (d) Power spectra of firing correlations. Increasing stimulus intensity elicited progressively more prominent peaks. Spectra at successive intensities offset vertically for clarity. (e) Sensitivity to stimulus intensity of different measures of activity. The average power in the frequency band 40–160 Hz is modulated over a greater dynamic range than either synchrony or plateau firing rate.

Using Firing Correlations to More Accurately Detect Changes in Stimulus Intensity

Our model suggests that firing correlations between retinal neurons can be modulated over a greater dynamic range than the firing rates of individual cells in response to changes in several important stimulus parameters. This finding led us to ask whether neural circuits could use the information encoded by firing correlations to more accurately resolve such stimulus parameters. To investigate this question, the spiking output of a line of ganglion cells activated by a narrow bar stimulus was fed into an ideal threshold detector (Figure 7). Each stimulus intensity was presented 200 times, and we counted the total number of threshold crossings for a 400-msec epoch during the plateau portion of the response. The average firing rate of the detector was measured at several different stimulus intensities, and the difference in detector output between all possible intensity increments is plotted in Figure 7a. For each point in the plot, the abscissa gives the final stimulus intensity, while the x-intercept of the line passing through that point yields the corresponding baseline stimulus intensity from which the difference in detector output was

calculated. Each difference in detector output was normalized by its standard deviation so that the abscissa value of each point measures the reliability with which the corresponding increment in stimulus intensity could be detected. To assess the extent to which the detector utilized firing correlations between its inputs, the eight stimulated ganglion cells were replaced by independent Poisson generators that, on average, produced the same number of spikes per unit time. Overall, the normalized difference in detector output between all stimulus pairs was 45% greater using correlated input from the retinal model as compared with the Poisson control. The threshold detector illustrates how firing correlations can reliably encode information. The threshold was set to 2.5, meaning that three or more spikes were necessary to produce a detector output on any given time step. For both correlated and Poisson input, the baseline detector firing rate was very low, around 1 Hz. As shown in Figure 7b, increasing the stimulus intensity produced a significantly greater increase in the detector firing rate when the inputs were correlated as compared with the

case in which the inputs were independent. This extra sensitivity was due to the fact that the threshold process is well suited for detecting rare synchronous events,[10, 11] and cortical neurons exhibit supralinear responses to synchronous inputs.[12] By encoding stimulus parameters, such as intensity, as increases in the number of such events, our results suggest that the retina may be able to transmit information more reliably along the optic nerve.
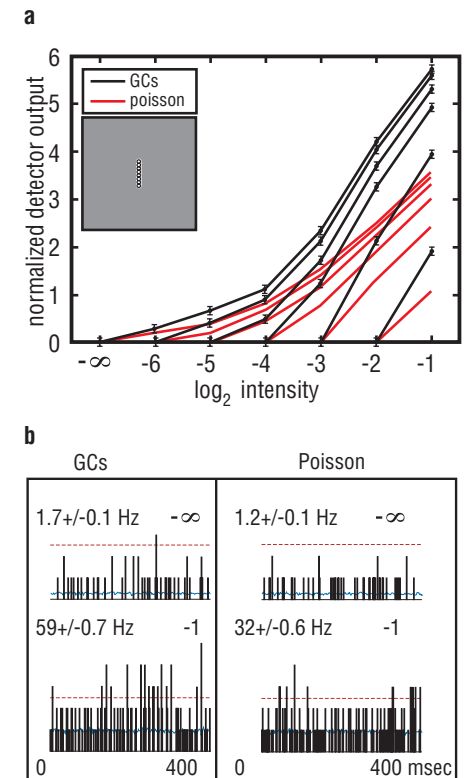

Figure 7. A threshold detector can utilize correlations between ganglion cells to better discriminate differences in stimulus intensity. (a) Incremental change in detector output in response to summed inputs from either model ganglion cells (solid black lines) or from independent Poisson generators (solid red lines). Stimuli were narrow bars of variable intensity (see inset). Each point represents the difference between the firing rate of the detector at the intensity indicated by the abscissa and the detector firing rate at the associated baseline intensity, given by the intersection of the containing line with the x-axis. Each difference was normalized by its standard deviation, thus measuring how well different intensity increments could be distinguished. Normalized detector output was 45% greater, on average, when driven by correlated input. (b) Example of the threshold detection process. Ganglion cell input is shown on the left and equivalent Poisson input on the right. The baseline activity of the detector in the absence of stimulation (top row) is very low. A stimulus with $\log_2$ intensity = -1 (bottom row) produced strong correlations between ganglion cells, resulting in a relatively large number of "rare" synchronous inputs. Dashed red line: detector threshold. Solid blue line: average firing rate per 2-msec bin.

Summary and Outlook

Our retinal model has provided insight into how patterns of retinal connectivity give rise to the high-frequency oscillations that are known to underlie the stimulus-selective synchronization of ganglion cells. We have furthermore used the model to conduct a number of computer experiments that suggest that synchrony between retinal ganglion cells not only reflects global topological properties, such as contiguity, but also encodes other important stimulus parameters, such as the brightness, size, and velocity of individual objects. In some cases, such stimulus properties were encoded more robustly by the degree of firing synchrony than by the firing rates of individual cells. Our results therefore support the contention that the rate-code hypothesis must be modified to incorporate the fundamental role that synchrony plays in how information is represented and processed in the mammalian visual system.

References

1 P. Reinagel and R. C. Reid, "Temporal Coding of Visual Information in the Thalamus," *J Neurosci* 20(14), 5392–400 (2000).

2 A. K. Engel, P. Konig, and W. Singer, "Direct Physiological Evidence for Scene Segmentation by Temporal Coding," *Proc Natl Acad Sci U S A* 88(20), 9136–40 (1991).

3 M. S. Livingstone, "Oscillatory Firing and Interneuronal Correlations in Squirrel Monkey Striate Cortex," *J Neurophysiol* 75(6), 2467–85 (1996).

4 S. Neuenschwander and W. Singer, "Long-Range Synchronization of Oscillatory Light Responses in the Cat Retina and Lateral Geniculate Nucleus," *Nature* 379(6567), 728–32 (1996).

5 O. D. Creutzfeldt, et al., "Sensitivity Distribution and Spatial Summation within Receptive-Field Center of Retinal On-Center Ganglion Cells and Transfer Function of the Retina," *J Neurophysiol* 33(5), 654–71 (1970).

6 R. M. Shapley and J. D. Victor, "The Effect of Contrast on the Transfer Properties of Cat Retinal Ganglion Cells," *Journal of Physiology* 285, 275–98 (1978).

7 W. Singer and C. M. Gray, "Visual feature integration and the temporal correlation hypothesis," *Annual Review of Neuroscience* 18, 555–86 (1995).

8 S. Neuenschwander, M. Castelo-Branco, and W. Singer, "Synchronous Oscillations in the Cat Retina," *Vision Res* 39(15), 2485–97 (1999).

9 G. T. Kenyon and D. W. Marshak, "Gap Junctions with Amacrine Cells Provide a Feedback Pathway for Ganglion Cells within the Retina," *Proc R Soc Lond B Biol Sci* 265(1399), 919–25 (1998).

10 G. T. Kenyon, E. E. Fetz, and R. D. Puff, "Effects of Firing Synchrony on Signal Propagation in Layered Networks," in *Advances in Neural Information Processing Systems 2*, D. S. Touretzky, Ed., (Morgan Kaufmann, San Mateo CA, 1990) pp. 141–148.

11 G. T. Kenyon, R. D. Puff, and E. E. Fetz, "A General Diffusion Model for Analyzing the Efficacy of Synaptic Input to Threshold Neurons," *Biol Cybern* 67(2), 133–41 (1992).

12 J. M. Alonso, W. M. Usrey, and R. C. Reid, "Precisely Correlated Firing in Cells of the Lateral Geniculate Nucleus," *Nature* 383(6603), 815–9 (1996).

Single-Molecule Detection of Specific Nucleic Acid Sequences

A. Castro, L. Bennett, R. Cortes,
K. Lamia, L. Paz, K. Tripp, and B. Shera
(all P-21)

Introduction

The detection of specific nucleic-acid sequences is of fundamental importance in the fields of genetic and medical research, clinical chemistry, and forensic science, among others. The most common method for the identification of specific DNA sequences is the Southern blot. In this procedure, the DNA sample is cleaved with a restriction enzyme, size-separated by gel electrophoresis, and transferred from the gel to a nitrocellulose filter. Detection is then accomplished by adding a hybridization probe. Despite its popularity, Southern blotting suffers from some limitations, mainly because it involves a series of manually intensive procedures that cannot be run unattended and cannot be readily automated; casting gels, applying samples, and running and subsequently staining the gels are all time-consuming tasks that are susceptible to poor quantitative accuracy and poor reproducibility. In most cases, in order to improve sensitivity, a radioisotope must be incorporated into the probe, which brings up a set of safety and environmental concerns.

The development of various techniques for enzymatic amplification of the target sequence before analysis alleviates the sensitivity problem. The polymerase chain reaction (PCR), for example, selectively increases the concentration of the target sequence relative to unrelated sequences, thus enhancing both the specificity and sensitivity of the assay. Amplification methods, however, may introduce ambiguities resulting from contamination, from variability in amplification efficiency and from other mechanisms not fully understood.[1–6]

The need, therefore, exists for economical, automatable methods for the analysis of small amounts of unamplified DNA in the high-throughput analytical laboratory. Recent developments in laser-based detection of fluorescent molecules have made possible the implementation of single-molecule techniques for biochemical analysis. The basis of our approach is to monitor for the presence of a specific nucleic-acid sequence of bacterial, human, plant, or other origin. The nucleic-acid sequence may be a DNA or RNA sequence and may be characteristic of a specific taxonomic group, a specific physiological function, or a specific genetic trait. These techniques have been developed with the following desired properties:

- high sensitivity: detecting a single target-molecule, allowing the analyst to circumvent the use of enzymatic amplification reactions;
- high specificity: detecting a short sequence in the presence of a large genomic background;
- homogeneous assay format: permitting the use of simple reaction protocols, which are amenable to automation; and
- high throughput: obtaining the desired statistical confidence of detection in a short period of time.

Instrumentation for Single-Molecule Detection in Flow Capillaries

The preferred experimental scheme for single-molecule detection of DNA fragments tagged with fluorescent probes for high-throughput analysis is the photon-burst detection with time-gating electronics, because of the high detection throughput and excellent signal-to-noise ratios that are possible.[7–12] The Photon-Burst Detection in Flowing Solutions method consists of pumping a dilute solution of the sample under investigation through a small capillary or flow cell. The concentration of fluorophore (a molecule that fluoresces when excited by light) in this kind of experiment is typically so low that the probability that two molecules would occupy the same volume at a given instant is negligible.

A laser beam is tightly focused through the flow cell. As the molecules travel through the path of the laser beam, they are excited; they subsequently decay by the emission of their characteristic fluorescence radiation (see Figure 1). Flow-rate adjustments limit the residence time of a molecule in the laser beam to the order of a few milliseconds. Because the fluorescence lifetime of most common fluorophores is of

the order of a few nanoseconds, a single molecule undergoes thousands of excitation-emission cycles during its travel through the laser beam, which produces a fluorescence photon burst. This fluorescence is collected at right angles to the excitation beam by high numerical aperture (N.A.) optics. A spatial filter at the image plane rejects out-of-focus scattering of the laser beam. The excitation light from the laser is blocked from

reaching the detector by a bandpass spectral filter with a transmission band that overlaps the molecular fluorescence spectrum. A single-photon avalanche photodiode is usually used as the detector because of its high detection quantum efficiency and fast response time. In spite of the use of spatial and spectral filters, large amounts of incompletely attenuated excitation light, as well as Raman scattering from the solvent, reach the detector. By using a picosecond—or shorter—laser as the excitation

source, it is possible to reject the majority of the background scattering. These two scattering emissions occur only during the duration of the laser pulse, whereas fluorescence occurs up to several nanoseconds after the excitation pulse. Therefore, by setting an electronic time-gate window that includes only delayed photons, one can reject the scattered light and retain the majority of the desired fluorescence signal.[7]

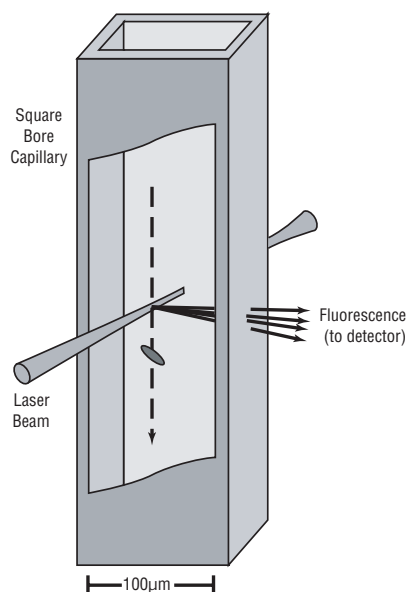Figure 2 shows a schematic representation of our apparatus.

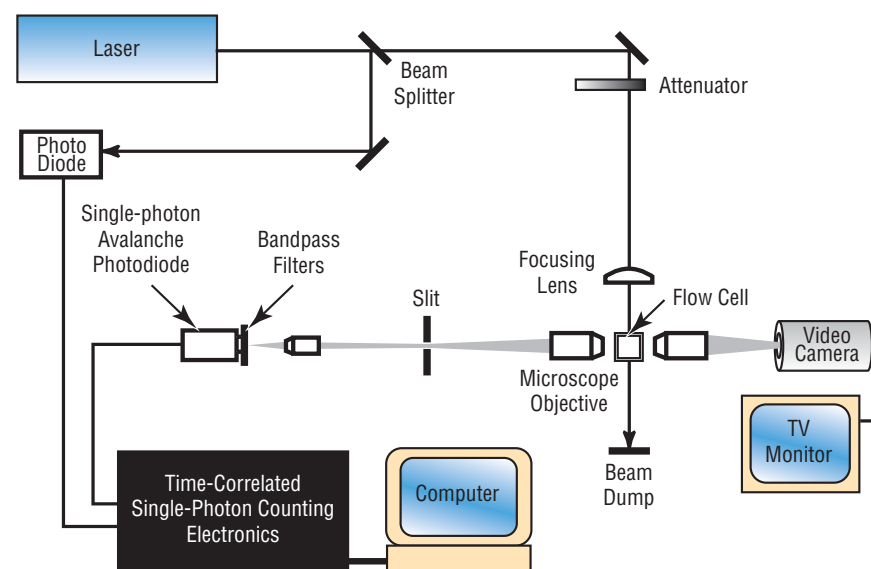**Figure 1. Schematic diagram of the flow cell for single-molecule detection.**

Figure 2. Schematic diagram of the experimental setup for fluorescence photon burst detection of single-molecules in flowing solution.

The excitation source is the frequency-doubled output (532 nm) of a mode-locked Spectra-Physics model 3800 Nd:YAG (neodymium:yttrium-aluminum-garnet) laser that produces 70-ps pulses at 82 MHz repetition rate. The laser output is attenuated to 2–5 mW and focused by a 6× microscope objective into the 0.8 × 0.8 mm ID square cross-section capillary cell to yield a 10-μm spot. A syringe pump is used to pump the sample through the capillary cell at a rate of 200 μL/hr, which translates to an average linear flow velocity of 87 μm/s. As individual molecules move through the laser beam, repeated excitation-emission cycles produce a fluorescence photon burst. The apparatus incorporates two detection channels so that it can detect the photon bursts from two dyes, each with different spectral properties, simultaneously. Fluorescence in each channel is collected by a 40 × 0.85 N.A. microscope objective and spatially filtered by a 0.4 × 0.4 mm square slit, which defines a 10 × 10 μm detection area. Omega (RDF series) 30 nm-bandwidth eight-cavity interference filters then spectrally filter the light. The filter bandpass

on each channel is chosen to achieve sufficient overlap with the emission spectrum of the corresponding dye but negligible overlap with the spectrum of the other dye. EG&G single-photon avalanche photodiodes detect the light. Independent time-correlated single-photon counting electronics under computer control analyze each detector output signal. The detection electronics reject Raman and Rayleigh scattering by using a time-gate window set such that only delayed fluorescence photons are detected. Fluorescence data from each channel is usually collected in 1-ms intervals, for a total running time that ranges from 100 to 1000 s, and saved for later analysis.

Figure 3 shows the experimental results for the detection of single rhodamine 6G molecules in a 5-fM aqueous solution. Large-amplitude bursts that correspond to individual molecules are clearly evident. Molecules that pass through the center of the gaussian laser beam yield as many as 150–200 photons, whereas smaller bursts are caused by molecules that pass through the edges of the beam.
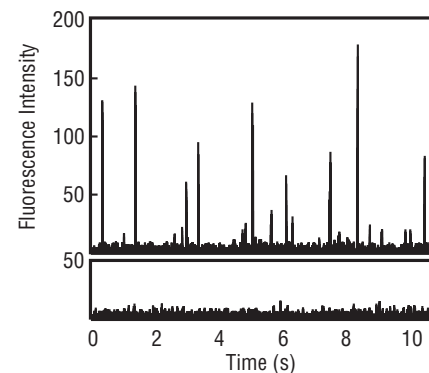

Figure 3. Photon-burst raw data for a 10-fM rhodamine 6G aqueous solution (top) and neat water (bottom). Laser power: 5 mW, flow velocity: 200 μm/s.

Double-Label Assay

The double-label assay detection scheme involves the use of two nucleic-acid probes that are complementary to the DNA target.[13–14] Peptide nucleic acids (PNA) are used instead of DNA probes because PNAs exhibit stronger binding to DNA targets.[15] In PNAs, the entire deoxyribose phosphate backbone has been replaced by a chemically different but structurally homomorphous backbone composed of (2-aminoethyl) glycine units[16–17] (see Figure 4). PNA probes have been found to be very potent DNA mimics, forming Watson-Crick base-paired duplexes with
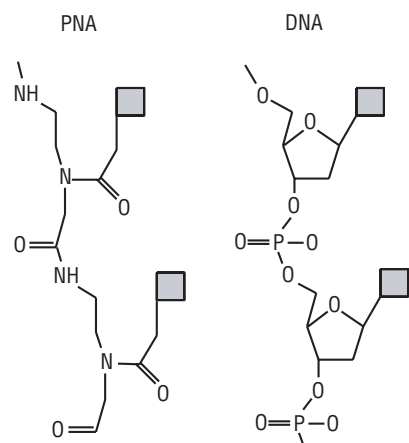
PNA   DNA

Figure 4. Structure of the peptide nucleic acid analog. The phosphate backbone is replaced by a chain of (2-aminoethyl) glycine units.

complementary DNA of high specificity and thermal stability.[18] In our experiments, we hybridized two PNA probes, each labeled with a different fluorescent dye, to the sample. If a target molecule that has both probe binding sites is present, then a complex should form between the target and the two probes. The two-channel single-molecule detector then analyzes the sample. Because the probes are bound to the same DNA target fragment, their signals will appear at the same time. Thus, the simultaneous detection of the two probes signifies the presence of a target molecule (see Figure 5). When no target is present, the probes will emit signals that are not coincident in time. Noncoincident signals will result from unhybridized probes, from targets hybridized to only one probe, or from nonspecifically bound probes. Such background signals are readily distinguished from the coincident signals generated by a target molecule as demonstrated in the following experiments.
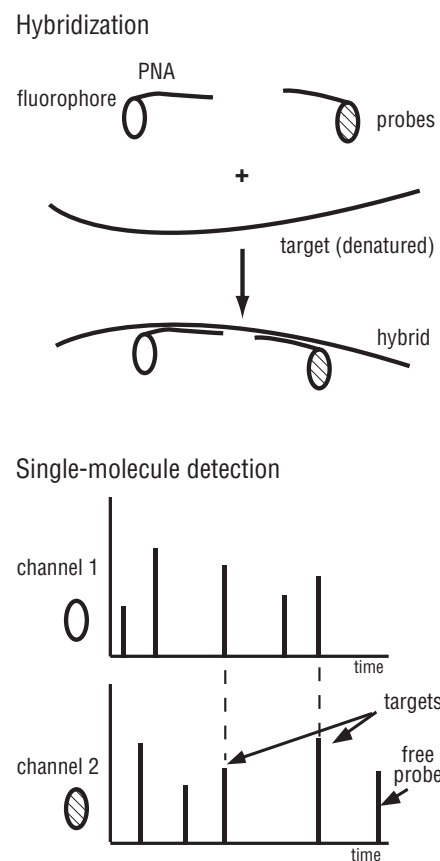
Hybridization

Single-molecule detection

Figure 5. Schematic diagram of the double-label coincidence assay. Simultaneous detection of the two hybridized probes allows the detection of a specific sequence of the target at the single-molecule level of sensitivity.

Detection of lambda DNA in the presence of genomic background
In this case, we used two PNA probes labeled with different fluorescent dyes, rhodamine 6G and Bodipy Texas Red, to identify the lambda DNA target sequence. These probes have sequences that are complementary to target sequences at positions 48406 and 48425 respectively. Single molecules of the probe-target complex are expected to be identified by the coincident detection of both dyes, while unbound probes or single probes bound to randomly occurring complementary sequences should appear as independent signals.[19] We prepared the sample by mixing lambda and salmon DNA in a genomic ratio of 1:1. The salmon DNA provides a background of unrelated sequences to test specificity for the lambda target. The hybridized sample was loaded into the system at a final concentration of 5 fM. Figure 6 shows the raw data obtained (top and middle traces). It is apparent that some signals occurred in only one of the channels (independent signals), while others occurred simultaneously in both channels (coincident signals). Cross-

correlation analysis yields a large peak at zero lag time (see Figure 6, bottom trace). A control experiment, described in the next paragraph, shows that the coincident signals above background are due to the binding of two probe molecules to one complementary target sequence, and not to nonspecific probe-DNA complexes or from PNA probe
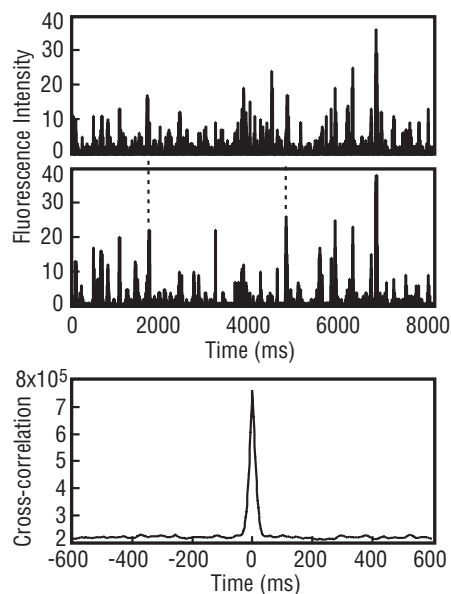

Figure 6. Single-molecule fluorescence photon bursts for intact lambda DNA hybridization mixture samples. Top: rhodamine channel raw data. Middle: Bodipy Texas Red channel raw data. Two representative coincident bursts are indicated by dashed lines. Bottom: cross-correlation analysis.

complexes unrelated to the presence of DNA.

To see whether the coincident signals of Figure 6 indicate the presence of specific probe-target complexes, we repeated the experiment under identical conditions, except that the lambda target was cut between the two probe binding sites before mixing with the salmon DNA and hybridizing to the probe. Probes should still bind to target sequences as before, but coincident signals should be eliminated because the binding sites would now be on independent target fragments. On the other hand, if the coincident signals were due to nonspecific complexes, cleavage of the target DNA should have no effect on the occurrence of coincident signals. Photon bursts were recorded and analyzed as before (see Figure 7). Cross-correlation analysis revealed no coincident events, which shows that the coincident signals seen with intact lambda DNA are due to specific probe-target complexes. We conclude that coincidence detection of two probes provides the specificity required to identify single-copy target sequences in complex samples.
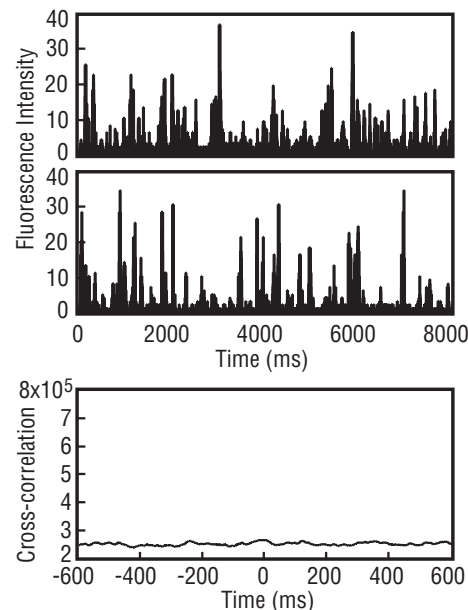

Figure 7. Control experiment for the analysis of lambda DNA in Figure 6. Top: rhodamine channel raw data. Middle: Bodipy Texas Red channel raw data. Bottom: cross-correlation analysis. No coincident signals were found when the target was cleaved between the two probe binding sites.
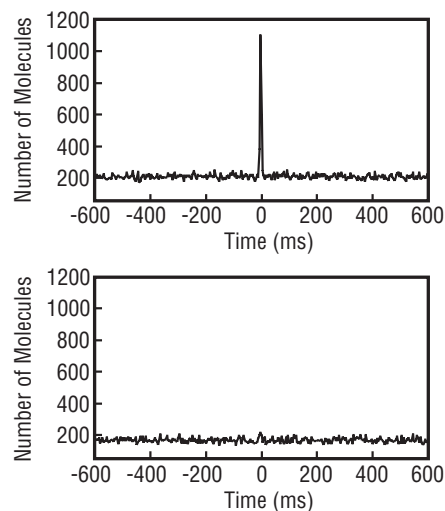
Detection of a single-copy gene in a transformed maize plant

We obtained the experimental results of Figures 6 and 7 with a synthetic sample comprising a mixture of lambda and salmon DNA. To confirm these results with natural samples, we prepared DNA from a homozygous-transformed maize plant containing one copy of a BT (*Bacillus thuringiensis* toxin) transgene per haploid maize genome (3×10^9 bp). The two probes used in this case (15-mers) hybridize at two positions 620 nucleotides apart in the sequence of the BT gene.[20] Instead of using cleaved DNA for a negative control as in the lambda experiments, here the control is an isogenic plant that lacks the BT gene. Photon bursts were recorded as before. We observed coincident signals only with the BT-positive sample (see Figure 8, top trace) and not with the negative control (Figure 8, bottom trace). This example illustrates that coincidence single-molecule detection can identify a single-copy transgene integrated in a chromosome of a complex genome.

Figure 8. Detection of a single-copy BT transgene in a maize genomic sample. Cross-correlation for the BT-positive (top) and BT-negative (bottom) samples.

Detection of a specific sequence of a pathogen

We have also demonstrated the use of this technique for the detection of *Bacillus anthracis* DNA in solution. *B. anthracis* is a gram-positive endospore-forming bacterium capable of producing fatal infections in both livestock and humans.[21] Virulent strains of *B. anthracis* are encapsulated and cause death in humans and animals by producing various toxins.[22,23] The detection of a specific sequence of *B. anthracis* in the presence of excess amounts of unrelated DNA from salmon sperm, and in the presence of large amounts of genomic DNA from a related bacillus (*B. globigii*), have been accomplished, as described below.

The *B. anthracis* DNA content consists of a 5.7-Mb genome, the 184-kb pXO1 virulent plasmid, and the 95-kb pXO2 capsule plasmid. Our target samples consisted of a 1:1 mixture of the genomic and pXO2 plasmid components at a concentration of either 5 fM or 0.5 fM. In one series of experiments, we added salmon sperm DNA to the target sample at increasingly larger ratios (Table 1), in order to simulate the large amounts of unrelated background DNA usually found in environmental samples. In another case, we added a 100:1 genomic excess of *B. globigii* to a 5-fM *B. anthracis* sample in order to test the sensitivity and specificity of the technique for detecting the pathogen in the presence of another—closely related—bacillus. In all cases, the DNA target samples were denatured by heating at 95°C and then cooled to room temperature. We used two fluorescently labeled, 12-base PNA probes, one tagged with rhodamine 6G (Rho) and the other with Bodipy Texas Red (BTR). These probes have sequences that are complementary to a short region of the capB gene of the pXO2 plasmid, corresponding to nucleotides 475 to 486 and 1082 to 1093, respectively (H-Rho-O-CTGGTACATCTG-CONH$_2$ and H-BTR-O-TGATCCCTCATC-CONH$_2$). The PNA probes were added to the samples at a final concentration of 2 pM and allowed to hybridize to the target for 30 minutes. Immediately afterwards, the samples were loaded into the instrument and single-molecule data was collected as described above.

Table 1. Sample Concentrations Used for the Detection of *B. anthracis* DNA in the Presence of Salmon Sperm DNA

	Expt 1	Expt 2	Expt 3	Expt 4
B. anthracis concentration (fM)	5	5	0.5	0
B. anthracis w/v (pg/ mL)	5	5	0.5	0
Salmon sperm (ng/mL)	0	100	100	100
Mass ratio	—	2×10^4	2×10^5	—
Number of fragments ratio*	—	4×10^4	4×10^5	—

*   for an average sheared salmon sperm DNA fragment size of 700 base pairs.

Detection of B. anthracis DNA in the presence of salmon sperm DNA

Table 1 summarizes the various experiments and controls performed in this case. Experiment 1 (see Figure 9a) corresponds to the detection of *B. anthracis* alone at a concentration of 5 fM. The large cross-correlation peak in Figure 9a is an indication of the relative amount of *B. anthracis* DNA present in the sample. Experiments 2 and 3 (see Figures 9b and 9c) correspond to the detection of *B. anthracis* DNA in the presence of large amounts of salmon-sperm background DNA. Experiment 4 (see Figure 9d) was a control where no *B. anthracis* was added and only background DNA was present. No target signal was detected in this case (see Figure 9d).

Detection of B. anthracis DNA in the presence of B. globigii DNA

In this case, we added the complete genome of *B. globigii* to a 5-fM sample of *B. anthracis* DNA at a genomic ratio of 100:1. Figure 10 shows the cross-correlation results

(top trace in the graph). The large peak indicates the presence of the target. A control experiment was run under identical conditions, except that *B. anthracis* DNA was not added to the sample (see

Figure 10, bottom trace in the graph). No cross-correlation peak was observed in this case, indicating that *B. globigii* does not contribute to the signal.

Figure 10. Detection of *Bacillus anthracis* in the presence of *Bacillus globigii*. Top: 5-fM *B. anthracis* DNA and 100× *B. globigii* genomic excess. Bottom: *B. globigii* alone.
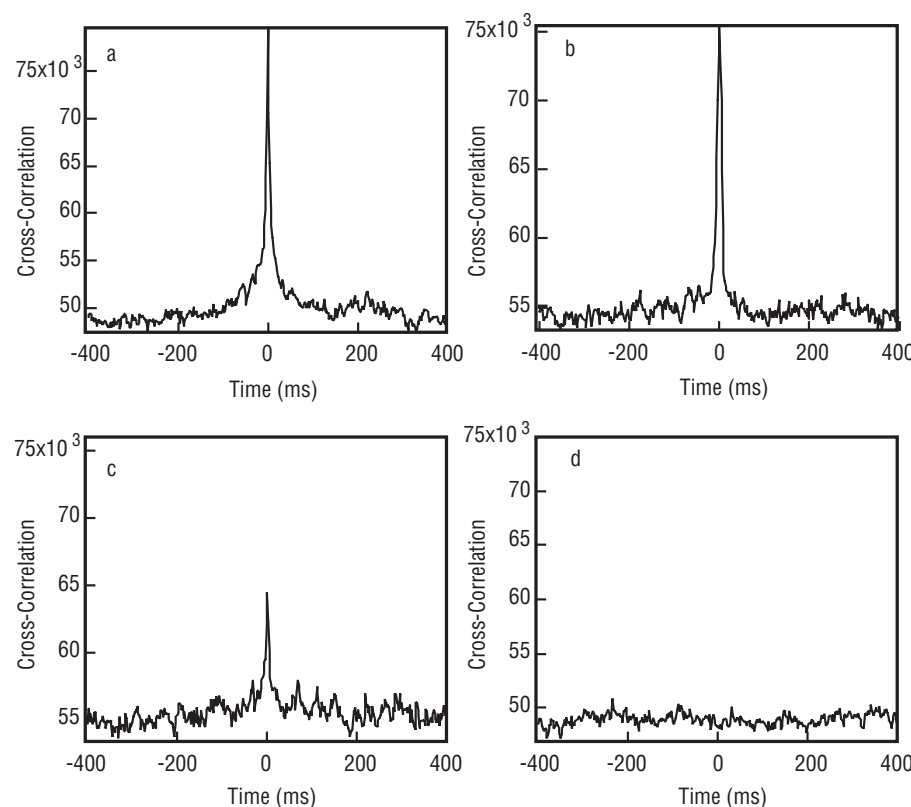

Figure 9. Cross-correlation results for the detection of *Bacillus anthracis* DNA. (a) 5 fM *B. anthracis* alone. (b) 5-fM *B. anthracis* DNA in the presence of 2×10^4 -times excess (by weight) salmon sperm DNA. (c) 0.5-fM *Bacillus anthracis* DNA in the presence of 2×10^5 -times excess (by weight) salmon sperm DNA. (d) Control: Salmon sperm DNA alone.
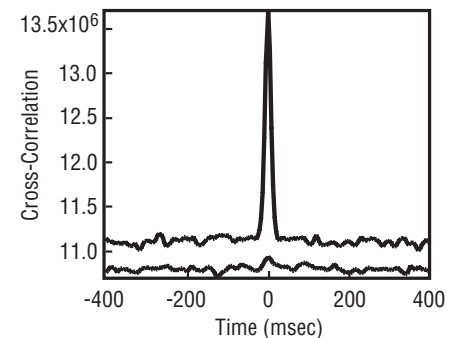
PNA Clamp Probes

This method enables the detection of specific nucleic-acid sequences in double-stranded DNA. The detection scheme involves the use of a specially designed homopyrimidine PNA clamp probe that binds to a complementary sequence in a double-stranded DNA target. Homopyrimidine-PNA oligomers form triplex structures with complementary homopurinic sequences and have been found to recognize double-stranded DNA targets by a mechanism that involves displacement of the pyrimidine DNA strand.[24,25] A PNA clamp probe binds to the complementary DNA target strand by forming a very stable local triplex in which one PNA arm is bound by Watson-Crick base-pairing and the other arm is bound by Hoogsten base-pairing to the central purinic strand[26] (see Figure 11). The noncomplementary DNA strand is displaced into a loop structure.[27,28] In addition to the PNA clamp probes, we added an intercalating dye to the sample, which provides a signature for the passage of each fragment through the detection volume. Simultaneous detection of the intercalator fluorescence signal and the labeled probe signifies the presence of the

Double-stranded DNA
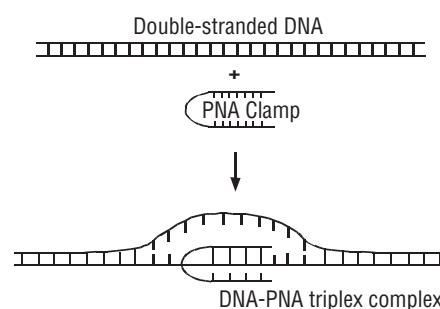
+

PNA Clamp

DNA-PNA triplex complex

Figure 11. Schematic representation of a PNA-DNA triplex structure. One PNA arm is bound by Watson-Crick base-pairing to the target DNA sequence, and the other PNA arm is bound by Hoogsteen base-pairing to the central purinic strand. The noncomplementary DNA strand is displaced into a free loop structure.

target molecule. When no target is present, the free probe will emit a signal that is not coincident in time with that of the free intercalator. Therefore, the analysis of genomic samples without the need for a denaturing step becomes possible.

An important property of intercalator dyes is that they bind stoichiometrically to the double-stranded DNA target (*i.e.*, the number of intercalator molecules is proportional to the size of the target).[29] Therefore, after delivering homogeneous excitation to the sample volume, measuring the intensity of the detected photon

burst that originates from a target that contains the intercalator allows the determination of the length of the DNA target. The simultaneous use of a sequence-specific probe and an intercalator dye will allow the determination of both the quantity and molecular weight of specific target DNA molecules in complex samples. An additional advantage of this technique arises from the fact that only one probe is used, and, therefore, the hybridization kinetics are faster than the two-probe methods.

Our preliminary experiments have shown the detection of a specific DNA sequence in double-stranded lambda DNA. We hybridized a PNA clamp probe labeled with rhodamine to base position 23892 of lambda DNA. The intercalator dye used was TOTO-3, which has an absorption peak at 642 nm and an emission peak at 660 nm. We used a helium-neon laser, which emits at 633 nm, as the excitation source. Figure 12 shows the experimental results. The top trace shows the raw data for the rhodamine channel, whereas the middle trace shows the raw data for the TOTO-3 channel. A cross-

correlation between these two data sets (bottom trace) reveals a peak at zero time that is indicative of the simultaneous detection of the clamp probe and the intercalator dye on the same DNA fragment.
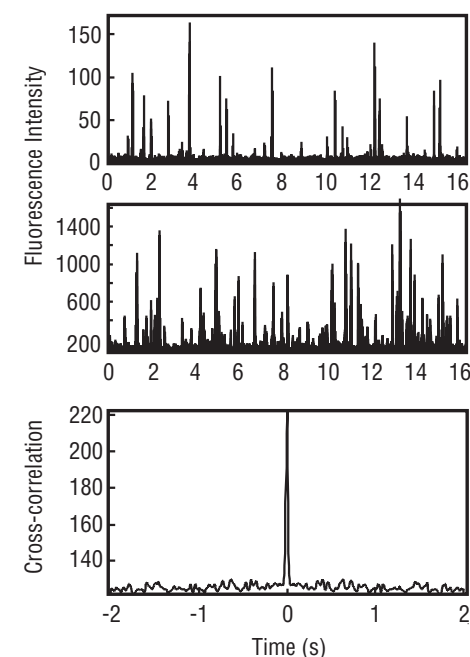

Figure 12. Detection of a specific sequence of double-stranded lambda DNA by the PNA clamp probe method. Top: rhodamine-labeled clamp probe channel. Middle: TOTO-3-stained lambda DNA channel. Bottom: cross-correlation analysis.

Polymerase-Extended Fluorescence Reporters

This method consists of synthesizing a highly fluorescent nucleic-acid reporter molecule, using a sequence of the target as a template. Detection of this highly fluorescent target in our single-molecule detection apparatus signifies the presence of the target being sought. We used a short oligonucleotide primer that is complementary to the target to synthesize the reporter molecule and added suitable polymerase and free nucleotides to the sample. One of these oligonucleotides is—at least partially—labeled with a fluorophore. If the target is present in the sample, the primer binds to it, and the polymerase will incorporate the labeled and unlabeled nucleotides reconstructing the target's complementary sequence (see Figure 13). If the labeled nucleotide concentration is kept below that of the unlabeled nucleotides, most of it will be incorporated into the reporter DNA molecule. Nonetheless, some free labeled nucleotide will remain in the reaction mixture, but fluorescence from the reporter molecule will be much stronger than that of the free nucleotide background over the detection time. Detection of the
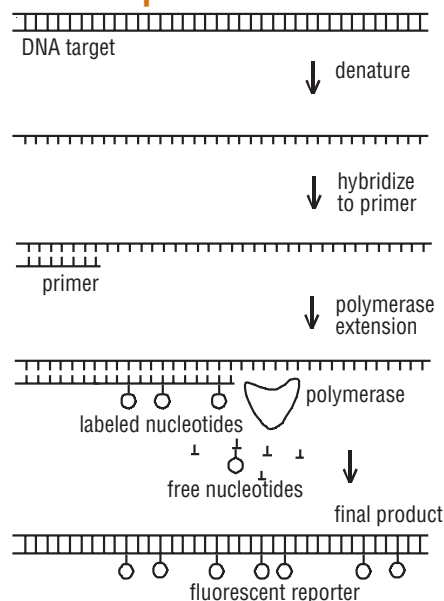

Figure 13. Schematic representation of the sequence-specific synthesis of a fluorescent reporter.

reporter signifies the presence of the target being sought. The fluorescent signal from the reporter molecule is expected to be much larger than that of the background originating from free labeled nucleotides because the reaction is allowed to proceed until the reporter molecule is hundreds or thousands of bases long.

This method has been demonstrated for the detection of

pUC19 DNA, (a 2686 base-pair plasmid). Before all experimental procedures, we digested pUC19 DNA with the restriction endonuclease Bgl I, which yields two fragments, 1568 bp and 1118 bp in length, and added a 24-mer primer that anneals to nucleotides 352–375 of pUC19, along with Taq polymerase and a mixture of dATP, dGTP, dCTP, and partially labeled dUTP. As a control, we ran identical experiments, except that pUC19 DNA was substituted with lambda DNA. We used a single-channel, single-molecule detection apparatus as described above to detect fluorescence from the reporter molecule. Figure 14 shows the results for the detection of a specific sequence of the 1568-bp pUC19 fragment at the single-molecule level of sensitivity (top trace). The lambda DNA control yielded negative results (bottom trace).

A possible enhancement to this technique is to simultaneously perform "single-molecule electro-phoresis" on the sample.[13] In this method, the electrophoretic mobil-ity of fluorescently labeled mol-ecules (free labeled nucleotides and
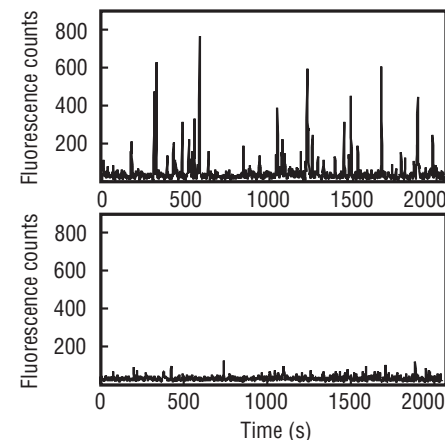
Figure 14. Detection of a specific DNA sequence by the fluorescent reporter method. Top: Raw data for the detection of the 1568-bp pUC19 fragment. Bottom: Raw data for the lambda DNA control.

reporter molecules in this case) can be determined with single-molecule sensitivity. Because single nucle-otides exhibit an electrophoretic mobility vastly different to that of nucleic acid targets, interference from free nucleotides is further eliminated. This modification to the method also allows simulta-neous determination of the size of the target.

Conclusions and Outlook

The methods described here promise to combine the advantages of flow-based analytical systems (system automation, speed, reproducibility) with the unsurpassed sensitivity of single-molecule detection. The sensitivity of these methods allows for the direct detection of specific genes without the need for using amplification methods such as PCR and exhibits advantages over current methodologies in terms of sensitivity, specificity, and speed. Also, the high sensitivity of the method means that sample size and reagent use are minimal, which should result in significant cost savings relative to existing analytical methods. Ultimately, assay reliability and low operating costs, combined with high sensitivity, may be the primary advantages of using single-molecule detection methods in the analytical laboratory.

We anticipate that the nonradioactive approaches for the ultrasensitive detection of specific sequences described here will find applications in a wide variety of fields, such as gene identification, gene mapping, medical diagnostics, and biotechnology. When the size of the target is also determined, it will be possible to determine both the quantity and molecular weight of specific target DNA molecules in complex samples, without the need for DNA amplification. The simplicity of the assay chemistry (probe hybridization in solution phase under DNA-denaturing conditions) promises reliability. The high level of target specificity demonstrated in the present experiments suggests that single-molecule detection coupled with single-molecule electrophoresis could be used successfully for many applications in analytical genetics. The inheritance of genes and chromosome segments could be tracked using DNA markers such as restriction fragment length polymorphisms (RFLPs) or tandem repeats. Single-nucleotide differences could be detected by probe hybridization as has been shown for PNA probes.[30] Finally, specific mRNA transcripts could be counted and sized.

References

[1] A. K. Bej, M. H. Mahbubani, R. M. Atlas, *Crit. Rev. Biochem. Biophys.* 26, 301–334 (1991).

[2] J. Peccoud, C. Jacob, *Biophys. J.* 71, 101–108 (1996).

[3] J. Reiss, M. Krawczak, M. Schloesser, *et al.*, *Nucleic Acids Res.* 18, 973–978 (1990).

[4] T. Schmidt, S. Hummel, B. Herrmann, *Naturwissenschaften* 82, 423–431 (1995).

[5] J. Taranger, B. Trollfors, L. Lind, *et al.*, *Pediatr. Infect. Dis. J.* 13, 936–937 (1994).

[6] W. W. Wilke, L. D. Sutton, R. N. Jones, *Clin. Chem.* 41, 622–623 (1995).

[7] E. B. Shera, N. K. Seitzinger, L. M. Davis, *et al.*, *Chem. Phys. Lett.* 174, 553–557 (1990).

[8] S. A. Soper, L. M. Davis, E. B. Shera, *J. Opt. Soc. Am. B* 9, 1761–1769 (1992).

[9] A. Castro, F. R. Fairfield, E. B. Shera, *Anal. Chem.* 65, 849–852 (1993).

[10] S. A. Soper, Q. L. Mattingly, P. Vegunta, *Anal. Chem.* 65, 740–747 (1993).

[11] A. Castro, E. B. Shera, *Anal. Chem.* 67, 3181–3186 (1995).

[12] A. Castro, E. B. Shera, *Appl. Opt.* 34, 3218–3222 (1995).

[13] A. Castro, J. K. G. Williams, *Anal. Chem.* 69, 3915–3920 (1997).

[14] A. Castro, R. T. Okinaka, *Analyst* 125, 9–11 (2000).

[15] H. Orum, P. Nielsen, M. Jorgensen, *et al.*, *Biotechniques* 19, 472–480 (1995).

[16] M. Egholm, O. Buchardt, P. E. Nielsen, *et al.*, *J. Am. Chem. Soc.* 114, 1895–1897 (1992).

[17] L. Christensen, R. Fitzpatrick, B. Gildea, *et al.*, *J. Peptide Sci.* 3, 175–183 (1995).

[18] M. Egholm, O. Buchardt, L. Christensen, *et al.*, *Nature* 365, 566–568 (1993).

[19] J. W. Chen, A. S. Cohen, B. L. Karger, *J. Chromat.* 559, 295–305 (1991).

[20] C. L. Armstrong, G. B. Parker, J. C. Pershing, *et al.*, *Crop Sci.* 35, 550–557 (1995).

[21] D. M. Poretz, in *Principles and Applications of Infectious Disease*, ed. G. L. Mandell, (Wiley, New York, 1979).

[22] S. H. Leppla, *Proc. Natl. Acad. Sci. USA*, 79, 3162 (1982).

[23] J. L. Stanley, K. Sargeant and H. Smith, *J. Gen. Microbiol.* 22, 206 (1960).

[24] P. E. Nielsen, M. Egholm, R. H. Berg, *et al.*, *Science* 254, 1497–1500 (1991).

[25] D. Y. Cherny, B. P. Belotserkovskii, M. D. Frank-Kamenetskii, *et al.*, *Proc. Natl. Acad. Sci. U.S.A.* 90, 1667–1670 (1993).

[26] L. Betts, J. Josey, J. Veal, *et al.*, *Science* 270, 1838–1841 (1995).

[27] P. E. Nielsen, M. Egholm, R. H. Berg, *et al.*, *AntiCancer Drug Design* 8, 53–63 (1993).

[28] P. E. Nielsen, M. Egholm, O. Buchardt, *J. Mol. Recognit.* 7, 165–170 (1994).

[29] H. S. Rye, S. Yue, D. E. Wemmer, *et al.*, *Nucleic Acids Res.* 20, 2803–2812 (1992).

[30] C. Carlsson, M. Jonsson, B. Norden, *et al.*, *Nature* 380, 6571 (1996).

Fusion Research

The Department of Energy supports the study of fusion—the process by which energy is generated when light nuclei combine—to advance plasma science, to enhance the nation's defense program, and to attempt to harness fusion as a commercially viable energy source. Fusion research has long been a part of Physics Division's efforts. The goal of these efforts, controlled thermonuclear ignition in a laboratory setting, is one of the grand scientific challenges of the 21st century.

Fusion is one of only a few long-term energy supply options. It offers the possibility of an economically and environmentally attractive system for producing central-station electric power, beginning in the middle of the century. Fusion-energy research also provides important near-term scientific and technological benefits to society. Fusion is attractive as an energy source because of the virtually inexhaustible supply of fuel, the promise of minimal adverse environmental impact, and its inherent safety. The experimental results of the last decade indicate that fusion can be an energy source, and the challenge now is to optimize the science to make it practical and affordable.

The FRX-L team of technical staff members, technicians, engineers, and students has been designing and building the experiment. A substantial student population from many institutions increases during summertime. As the experiment comes on line, everyone is also involved with taking and interpreting data. The current group is standing in the FRX-L laboratory, next to the large high-voltage transmission line (right) that leads from the main capacitor bank (right rear). They are

(from left to right) Glen Wurden, Tom Intrator, Ed Mignardot, Kathy Barela, Daniel Begay, Bernie Martinez, Laure Vermare, Matthew Fisher, Kit Werley, Martin Taccetti, Bill Waganaar, Bill Fienup, Phil Assmus, Matthew Langner, Phil Sanchez, and Chris Grabowski
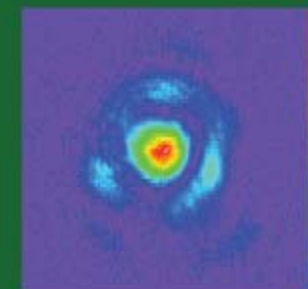
Inertial-Confinement Fusion

The magnetic fusion energy effort was significantly redirected in the mid-1990s so as to broaden the program from an exclusive focus on achievement of fusion energy in tokamaks to include an expanded exploration of scientific foundations and of other confinement approaches. Physics Division has been a significant partner in investigating these new approaches. Inertial confinement fusion (ICF) is a method of controlled fusion in which the rapid implosion of a fuel pellet, produced by laser, electron, or ion beams, raises the temperature and density of the core to levels at which nuclear fusion can take place. The National Ignition Facility (NIF) under construction at Lawrence Livermore National Laboratory is designed to further these efforts. Two of the research highlights in this section detail preliminary experiments designed to refine the design of NIF and optimize experimental efforts once it becomes operational. If NIF successfully achieves the scientific goal of igniting a fusion reaction in a small mass of fusion fuel, sometime around 2005, then the most important technological hurdle to economical inertial fusion power-plant design will have been passed. The remaining work leading to an economically viable plant can then occur over a few decades, with annual research and development investments smaller than those that the United States currently provides for fossil- and renewable-energy research.

Magnetized Target Fusion

Magnetized target fusion (MTF) is a relatively new concept in fusion-energy research. The basic concept is to use a collapsing magnetic field to implode a metal liner that both confines and compressionally heats a plasma to fusion-relevant conditions. The initial plasma used to power the MTF process will be of a relatively low energy density when compared with other fusion approaches. The high-energy potion of the apparatus is the machine that contains the bank of capacitors that generates the compressional magnetic field. The fast moving metal wall, driven by pulsed-power liner technology, has been developed for many years and is fairly mature. The Laboratory recently opened Atlas, a 23-MJ facility—one of the most powerful in the world. This means that once this fusion regime has been developed, fusion power plants could be developed for expenditures of a few hundred million dollars instead of well over a billion dollars for each facility. This will not only have the effect of making the power generated by such a plant cheaper, it will also allow more power plants to be built and in countries with a more diverse cross section of economic strata.

Double Shell Implosions in the Inertial-Confinement Fusion Program

R. G. Watt (P-22)
T. Archuleta, C. W. Barnes,
S. C. Evans, J. Jimerson, T. J. Murphy,
T. Sedillo, and P. Walsh (P-24)
W. S. Varnum (X-1),
N. D. Delamater, D. C. Wilson (X-2)
R. D. Day, P. Gobby, V. Gomez,
D. Hatch, R. Manzanares, J. Elliot,
N. Elliot, and G. Rivera, (MST-7)
J. D. Colvin, R. E. Turner,
P. Amendt (LLNL)

Introduction

The National Ignition Facility (NIF),[1] a large laser presently under construction at the Lawrence Livermore National Laboratory, is designed to produce 1.8 MJ of 0.35-μm light in a 500-TW, temporally shaped, laser pulse for defense applications and inertial-confinement fusion (ICF) ignition. The possibility of capsule ignition and gain at NIF, given the laser energy and power available, is far from a certainty and requires further laboratory experimentation and theoretical simulation to remove as many uncertainties as possible to reduce the risk of failure. Fusion ignition and gain require that the laser-driven implosion create a fuel region of sufficient size, density, and temperature that the fusion burn wave becomes self-sustaining. This requires deposition of the charged fusion products created by the burn within the high-density core to continue to heat the core despite competing energy-loss mechanisms.

Current Target Design

Such a self-sustained fusion burn is easiest to obtain using a deuterium-tritium (DT) fuel mixture. For DT fuel, the requirements for a self-sustained burn are that the ion temperature be of order 20 keV and that the density be high enough that the DT-reaction-produced alpha particles deposit their energy inside the fuel rather than escaping the fuel region. A density-radius product of a few g/cm² satisfies this local-deposition requirement. At NIF, rather than producing these conditions in a uniform volume (which would require a laser energy on the order of 100 MJ), the mainline capsule design employs a concept known as "hot-spot" ignition. In this concept, a small fraction of the fuel mass is ignited in a central hot spot, and then a thermonuclear burn wave propagates outward into the surrounding, lower-temperature, compressed fuel to produce a significant fusion yield.[1]

The production of such a central hot spot, with sufficient fuel at sufficient temperature to ignite and burn a reasonable fraction of the available fuel is believed to require cryogenic targets. A solid DT ice layer of order 100 microns thick held inside a thin CH or beryllium shell is required in order to contain enough fuel to ignite and at the same time not break under the extreme pressure that would be present for such a fuel load, if the target were at room temperature. This requires a cryogenic target-manipulation system, which implies a very complex engineering effort. Additionally, the inner surface of the DT ice layer must remain very uniform so that Rayleigh-Taylor instabilities, seeded by any inner surface nonuniformity, do not grow to a large enough amplitude during the final deacceleration phase of the implosion to cause the target to break up and the burn to be disrupted. Both of these requirements constitute significant unknowns relative to successful ignition using the cryogenic-point design target as currently envisioned.

A Double-Shell Target

If a target could be designed that could operate at room temperature with an adequate fuel load to ignite, it would provide a valuable alternative to the cryogenic-point design. If such a target were also able to operate with a simple square temporal power history out of the laser, rather than the severely shaped laser power pulse required for the cryogenic-point design target, that would be a significant additional advantage. A set of double-shell target designs that have been under investigation for the past several years by Los Alamos National Laboratory constitutes such a target. The physics goal of the double-shell implosion campaign, beginning at the NOVA laser at Lawrence Livermore National Laboratory several years ago and currently in progress at the Omega laser at the University of Rochester, Laboratory for Laser Energetics, has been to assess the viability of a potential noncryogenic implosion target for ignition applications at NIF. This design uses a room temperature, thin, gold inner capsule capable of holding enough gas at room temperature to ignite when driven in a staged manner by the collision of an outer shell onto the gold

inner capsule. The gold wall is strong enough to support the extreme pressure needed for the required gas load without recourse to cryogenics. The penalty paid for the strong inner gold capsule is the need to compress it with a massive outer layer directly accelerated by the radiation field in the hohlraum. This is inherently a somewhat less efficient drive technique than a single-shell implosion because of the very massive set of shells involved. Figure 1 shows a double-shell design for a NIF ignition target designed for operation at a convergence ratio (CR) of 32. (This ICF target "pie" diagram should be interpreted as a section of a spherical object, indicating the various layers in that object by the horizontal lines in the drawing.) A significant further advantage to this design is that, rather than a 1:10 ratio of early foot to peak laser power, as is required for the cryogenic point design, a simple 6-ns, 300-TW, square power pulse is adequate for ignition. Such a pulse is much easier to produce and much less expensive in terms of additional active laser components than the required 1:10 NIF cryogenic-point design shaped pulse.

The key to laboratory studies of both single-shell cryogenic targets and double-shell, room-temperature targets, in an effort to determine whether they will ignite at NIF, is to get the numerical simulations to agree with experimental data. In particular, if the data can be understood in the context of simple one-dimensional (1-D) simulations, then the confidence with which one can plan ignition experiments at NIF, with 100 times more energy than current laser experiments, finally becomes sufficient to pursue particular designs. This is the stumbling block for all present-day experiments; such simple figures of merit as the total neutron yield from a 1-D calculation, when compared with the actual experimental yield, have been off by orders of magnitude at the high CRs needed to get to ignition at NIF. The task of the experimental program that is looking at double-shell implosions is to bring theory and experiment into agreement, preferably with as few modifications of the simulations away from simple 1-D behavior as possible.
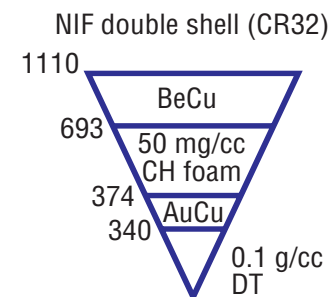

Figure 1. NIF CR 32 double-shell ignition design. This target requires a 300-TW, 6-ns square laser drive for ignition. The radial surface dimensions are in μm.

Double-Shell Target Experimental Work

The history of double-shell ICF targets is quite long. The earliest double-shell targets were fired at the Gekko XII laser in 1983, with an infrared (IR) drive and very tiny capsules, with a resultant measured yield well under 1% of that calculated by the simulation codes in use at the time. The concept fell from favor after that and lay dormant until several years ago, when a new attempt to use the double-shell target concept was started at NOVA by Los Alamos National Laboratory. As in 1983, the NOVA targets again produced poor results, with a yield compared with clean (YOC) in the 0.5%–2.5% range for a burn-averaged CR of approximately 32. Because this CR is the same as the double-shell design for NIF, this result was not very encouraging. Because the
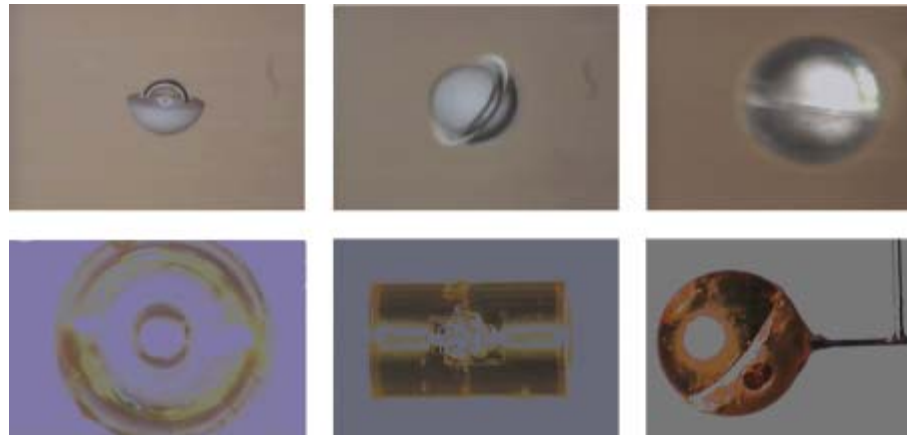
implosions were done in a cylindrical hohlraum on a laser with relatively poor energy and power balance, the belief at that time was that the thermal radiation environment uniformity was too poor to correctly drive the target, which resulted in poor performance. With this assumed degradation mechanism, better drive symmetry was assumed to be needed for successful implosions. Consequently, the concept was taken to the Omega laser at Rochester for further tests, using the tetrahedral hohlraum geometry, which was expected to produce a much better thermal drive symmetry than was the case in the NOVA cylindrical hohlraum. Examples of the various assembly stages and views of a cylindrical

(NIF or NOVA style) hohlraum and the equivalent spherical (tetrahedral) hohlraum are shown in Figure 2. (The spherical hohlraum is called a tetrahedral hohlraum because the laser entrance holes are located at the four points of a tetrahedron on the surface of the sphere.)

The initial tetrahedral hohlraum double-shell implosions produced nearly identical results to the earlier NOVA data, suggesting that the thermal radiation environment was perhaps not the main culprit in the failure of these implosions. An examination of the radiation drive in the tetrahedral hohlraum indicated that about 7% of the radiation power was actually in the gold

M-band in the 2–2.5 keV range. This component can be much more nonuniform than the thermal component, because of localization of the M-band source at the laser spot location, in contrast to the essentially uniform thermal radiation that comes from all locations on the inside gold wall. Because the M-band is more penetrating than the thermal component and can therefore more easily affect the inner layers of the target, we felt that the nonuniform M-band might be the culprit in double-shell implosion degradation. Consequently, we generated a new double-shell design that would be less susceptible to the M-band asymmetry. The intent of the new design was to eliminate the majority of the material present in the inner capsule that strongly absorbs the M-band (the glass in the thick-wall microballoon) and also to modify the outer surface of the inner capsule to be less unstable to the growth of instabilities driven by any nonuniformity. To accomplish this, we designed a capsule that removed 80% of the glass volume from the inner capsule and re-placed that mass with a CH layer. In so doing, the outer surface of the remaining glass was tamped by an

Figure 2. Images of the various stages of the assembly of the many shells in the capsule for a double-shell target, and examples of the cylindrical (NIF or NOVA style) and spherical (tetrahedral) style hohlraums used in this study. The first three images show the inner capsule surrounded successively by the foam and then the outer ablator shells. The fourth image shows the end view of a cylindrical hohlraum with such a capsule installed in it, and the fifth and sixth image are exterior views of a cylindrical and spherical (tetrahedral) hohlraum, respectively.

a

Type A thick ablator
imaging capsule

275
199

129
106

3-μm wall GMB
+ 19-μm GDP

b

Type B thin ablator
imaging capsule

275
237

129
106

3-μm wallGMB
+ 19-μm GDP

c

Type C pure CH
imaging capsule

275
199

129
106

23 μm wall single
shell CH, with
PVA gas barrier

Figure 3. Three "imaging" double-shell target designs were used in the November 2000 double-shell campaign. The original-concept "imaging" target was used in both the normal ablator and in a thinned ablator variant, and a new "pure CH" "imaging" design that had the same thickness for the inner capsule, but of pure CH without the glass, provided another variation on the theme.

overcoating of CH, thus reducing its instability growth relative to that of a bare glass surface. The new unstable interface in the target, the outer surface of the inner capsule (now CH, which has a lower density than the original glass) was also less susceptible to the growth of instabilities than the original glass/ foam interface had been. This target also had the advantage that for the first time x-rays from the hot core could penetrate to the outside, and it allowed an image of the imploded core, similar in nature to the x-ray images usually taken for single-shell implosions, to be taken for this "imaging" double-shell design. Thus, the target allowed an image of the core that would both reveal any asymmetry in the imploded core directly and reduce the response of the inner capsule to any existing M-band asymmetry. The preliminary results from these targets were striking—a YOC of 40% and 60% on two shots taken in March 1999 at a CR of 32, compared with all previous work on double shells, which had a YOC <2.5%. These results were significantly better than seen in any previous CR 32 single- or double-shell implosions in the ICF pro-
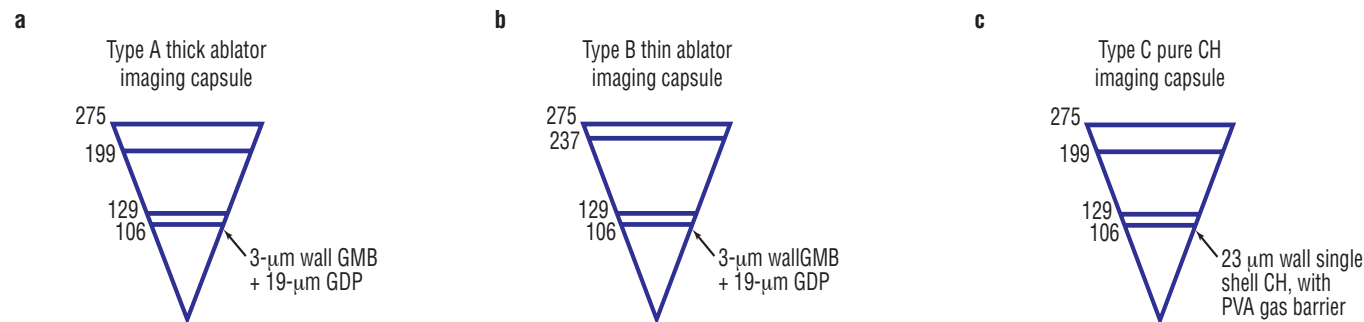
gram, in which typical YOC values had historically been less than 10%, regardless of the target type.

These two preliminary shots led to a full follow-up series of tetrahe- dral-hohlraum double-shell implo- sions. This follow-up series used the new design capsule at several fill pressures and consequently several different CRs. Along with the new design, this series also used the "standard" double shell. The historically poor-performing "standard" target was included in the campaign as a standard against which to measure the other de- signs. This series was shot in October 1999, and once again the new CH over thin-walled glass inner capsule double-shell design yielded a YOC in the 30%–70% range— verifying the earlier preliminary results, as well as this time extend- ing those results to other higher

and lower CRs.[2] As expected, the "standard" capsule again produced a poor YOC. With this confirmation that an "imaging" double-shell capsule could operate at a high YOC at a CR now well beyond that required for the NIF double-shell design, it became mandatory to determine whether the capsules would work well in a NIF-style cylindrical hohlraum. A campaign of shots was done in November 2000 to determine whether the consistently good results with the "imaging" capsule in the tetrahe- dral hohlraum would translate to cylinders.

The three November 2000 "imag- ing" double-shell variants are shown in Figure 3. Figures 3a and 3b were the original-concept thin- wall glass plus plastic over-coated "imaging" capsules, in both the original version, with its 76 micron

ablator, and in a thinned-ablator (38 micron) version, which calcula- tionally produced a much higher yield and allowed better diagnostics of the neutron production. (Experi- mentally, type B's yield went up significantly, allowing a measure- ment of the secondary DT neutrons for the first time.) Figure 3c was another new-design "pure CH" imaging capsule, which removed the remaining glass from the central capsule. We placed a constraint on the target-fabrication team in MST-7 that we would not accept any targets with visible external imperfections. Detailed examination of the targets showed them to be essentially visually perfect.

Results

This final campaign using indirectly driven double-shell targets in ICF was designed primarily to determine whether the favorable performance seen in the "imaging" double shells in tetrahedral hohlraums would translate to NIF-style cylindrical hohlraums. The plot of YOC vs CR for the deuterium-filled capsules of all "imaging" variants for all shots, both tetrahedral and NIF style, shown in Figure 4, indicates that the performance in either type of hohlraum is comparable. In all cases, the performance of the "imaging" CH-over-glass double-shell design approaches that of a clean 1-D simulation.

Additionally, although the results have more spread than desired, the new pure-CH capsules also worked well in the NIF-style hohlraum. This suggests that preheat decompression caused by x-ray absorption in the remaining glass part of the "imaging" capsule and its resulting effect on the implosion dynamics, which are somewhat different for the pure-CH and the CH-over-glass "imaging" capsules, while it probably plays a role, is not mandatory for good performance. (It may be that the very reproducible results at a given CR for the CH-over-glass

"imaging" capsules, as opposed to the somewhat larger data spread seen for the pure-CH capsules, is connected to this). Static x-ray images of the imploded cores of all the new-design "imaging" capsules in November 2000 indicated an essentially round time-integrated implosion, consistent with the good performance of these capsules. Figure 5 shows an 80-ps frame from an implosion of the "imaging" capsule shot in October 1999.

Finally, for the first time in this experimental campaign, a successful set of density-radius measurements was returned. As mentioned in the introduction, in order to reach ignition, it is critical to have a long enough path at high density to absorb the alpha particles from the DT reaction before they escape the core. As in the case of the yield figure of merit, it is necessary to show that the simulations are producing density-radius product values close to that measured in order to have confidence in the calculational tools. The density-radius product values calculated for this set of shots ranged from 6 to 9 as did the measured values, which

suggests that the simulations are getting this correct, and nothing about the real implosion is radically different from 1-D behavior, the same conclusion arrived at from the measured yield.

□ NOVA 1ns single shell, cyl.
◇ NOVA 1.4 ns single shell, cyl.
+ Omega 1ns tetrahedral single shell
○ Imaging 1ns double shell, tets
● Pure CH imaging 1ns double shell, cyl.
○ Imaging 1ns double shell (DD only), cyl.
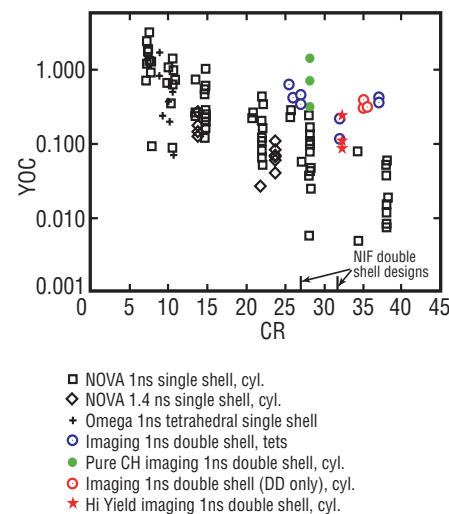★ Hi Yield imaging 1ns double shell, cyl.

Figure 4. YOC vs CR for all Omega imaging and pure-CH DT shots to date, in tetrahedral and NIF-style hohlraums. The data for NIF-style hohlraums is shown in shades of red, while the tetrahedral results are in shades of blue. The DT-filled capsules used in November are not shown because of remaining uncertainties in the gas fill. In the legend, cyl is a cylindrical hohlraum, tet is a tetrahedral.
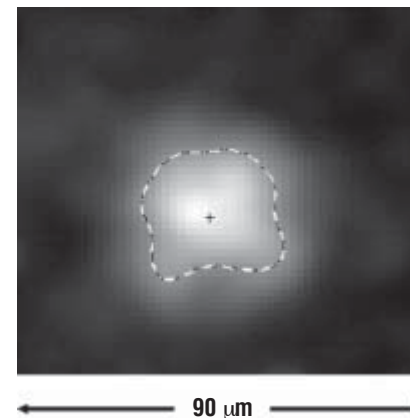

Figure 5. An 80-ps-duration x-ray image of an imploded core at minimum radius for a CH-over-glass "imaging" capsule.

Conclusions

The type of hohlraum used for an indirect-drive, double-shell implosion, given high-quality targets and an "imaging"-type capsule design, seems to be unimportant. The behavior of "imaging" double shells, regardless of whether they contain glass or not in their inner capsule, seems to significantly exceed the performance of comparably sized single-shell capsules. Both the pure-CH and the CH-over-glass "imaging" capsules approach clean 1-D performance at calculated CRs well beyond that required for an ignition double-shell design to work at the original NIF energy level. The agreement between the measured and calculated density-radius product values indicates that use of the calculated CR in the comparison with prior YOC data is a valid one. This means that the double-shell concept remains a viable alternative to cryogenic single-shell ignition target designs for NIF.

References/For Further Reading

[1] S. W. Haan, S. M. Pollaine, J. D. Lindl, *et. al.*, *Physics of Plasmas* 2(6), 2480 (1995).

[2] W. S. Varnum, N. D. Delamater, S. C. Evans, P. L. Gobby, J. E. Moore, J. M. Wallace, R. G. Watt (LANL), J. D. Colvin, R. Turner (LLNL), V. Glebov, J. Soures, C. Stoeckl (UR/LLE), *Physical Review Letters* 84, 5153 (2000).

Laser-Plasma Interactions in a Single Hot Spot

D. S. Montgomery, J. A. Cobble, J. C. Fernández, and R. P. Johnson (P-24); H. A. Rose (T-13); R. Focia (Massachusetts Institute of Technology); and N. LeGalloudec (University of Nevada, Reno)

Introduction

Understanding the growth and saturation of laser-driven parametric instabilities such as stimulated Raman scattering (SRS—the scattering of light as it passes through a plasma; the light undergoes a change in frequency due to a change in the vibrational frequency of the scattering plasma waves), stimulated Brillouin scattering (SBS—light scattering by sound waves in the plasma), and self-focusing is important for the success of laser fusion. These instabilities can occur throughout the underdense (transparent) plasma in targets designed to achieve ignition, such as those for the proposed National Ignition Facility (NIF)[1], and may also constrain experimental designs for weapons physics and high-energy-density physics experiments planned on NIF. One major reason researchers are concerned with laser-plasma instabilities (LPI) is that they can significantly reduce the amount of laser energy absorbed by the target. Other deleterious effects can be produced by these instabilities such as target preheat due to fast electrons generated by SRS and degradation of the implosion symmetry caused by flow-induced beam steering,

beam spraying, and crossed-beam energy transfer. Quantitative prediction of the onset and saturation of these instabilities under given laser and plasma conditions is the goal of research in this field, and will lead ultimately to their control.

Both SBS and SRS are three-wave processes which involve the resonant decay of the incident laser wave into a scattered light wave and a plasma wave. The instabilities must satisfy the frequency and wave-vector matching conditions

$$\omega_0 = \omega_s + \omega_{es}$$
$$\vec{k}_0 = \vec{k}_s + \vec{k}_{es} \qquad (1)$$

where ω, $\vec{k}$ are the frequency and the vector wavenumber of the waves, and the subscripts 0, s, and es refer to the incident, scattered, and electrostatic plasma waves. For SBS, the plasma wave is a low-frequency ion acoustic wave (IAW), whose dispersion is approximately

$\omega_{es} \cong c_s k_{es} + \vec{v} \cdot \vec{k}_{es}$, where c_s is the sound speed and v is the local flow velocity. The plasma wave

involved in the SRS process is a high-frequency electron-plasma wave (EPW), with a frequency given approximately by the Bohm-Gross dispersion

$$\omega_{es}^2 \cong \omega_p^2 + 3k_{es}^2 v_{th}^2 \text{ ,}$$

where $\omega_p = \sqrt{4\pi n_e e^2 / m_e}$ is the electron plasma frequency which depends on the electron plasma density n_e, and v_{th} is the electron thermal speed.

A major complication in understanding these instabilities is that the plasma waves created by these processes can interact with other waves in the plasma, can interact with each other, and can interact with the particles or bulk plasma to modify the background laser and plasma conditions. However, much progress has occurred in recent years in qualitative understanding of the onset, saturation, and interplay between these instabilities. This may be attributed in part to the use of beam-smoothing techniques such as random phase plates (RPP), which smooth the large-scale spatial structure often found in high-power lasers. The focal-plane intensity distribution created

in vacuum by a RPP consists of an ensemble of fine-scale hot spots or speckles with well-defined statistical properties. An example of a RPP-smoothed laser beam is shown in Figure 1a. The characteristic size of each speckle (hot spot) is related to the diffraction limit of the focusing optic (*i.e.* the width and length are $d_{sp} \sim f \lambda_0$ and $L_{sp} \sim 7 f^2 \lambda_0$ respectively, where f is the ratio of focal length to beam diameter, and λ_0 is the laser wavelength). Recent work has demonstrated the importance of the laser hot-spot distribution in determining the onset behavior for SBS and SRS.[2,3]

Experimental History

In the absence of a quantitative predictive capability for laser-plasma instabilities, experiments have traditionally been performed in the largest possible laser-plasma volume using the largest available lasers in order to attempt to extrapolate the results to the even larger plasma volumes expected for NIF experiments. The plasmas produced in these scaling experiments are often quite complex and dynamic,[4,5] and may not mimic all aspects of NIF plasmas. Additionally, the instabilities can be *interdependent* in a laser beam with an ensemble of hot spots, and issues such as seeding and coupling of instabilities between hot spots arise and complicate our understanding of these processes. Further, because there is a distribution of laser intensities, SRS, SBS, or self-focusing can all occur to some extent throughout the laser-plasma volume, depending on the local intensities. All of these factors contribute to our lack of confidence in extrapolating the results of these scaling experiments to NIF. We must take a more fundamental approach to laser-plasma instabilities in order to develop a quantitative predictive capability for large plasmas.

The laser-plasma volume for ignition-scale plasmas is too large to be modeled from first principles using either current or planned advanced computing resources due to the relatively small spatial and time scales over which the instabilities occur. The smallest fundamental volume where the instabilities occur in a realistic laser beam is within a single laser hot-spot volume. The intensity pattern from an idealized single hot spot is well defined compared to the wide range of intensities present in the ensemble of hot spots in a realistic laser beam. Present computational resources are capable of performing first-principles calculations of LPI at the single-hot-spot volume. Therefore, experimental and computational studies of the coupling and saturation of instabilities in a single laser hot spot is a key first step to quantitative understanding of these processes in realistic ignition-scale laser plasmas.

This approach utilizes the detailed measurements from single-hot-spot LPI experiments to develop and benchmark *ab initio* models. The models would then be used to reduce the detailed microscopic processes to a simpler physical model (reduced or mesoscale model). Because most processes arising from the instabilities are localized within the hot-spot volume, the reduced model would serve as a sort of equation-of-state for the instabilities, averaging over the detailed microscopic processes. The reduced models could then be incorporated into the large hydrodynamic codes used to design NIF targets, and benchmarked against experiments with large laser-plasma volumes.

a.

1000μm

Figure 1a. Plot of the intensity pattern at best focus for a laser smoothed by using a random phase plate (RPP). The focal pattern is typical for large-scale laser experiments and those planned for NIF. The intensity pattern consists of thousands of individual hot spots or speckles.

b.

Figure 1b. Plot of the measured intensity pattern at best focus for the single-hot-spot laser used in these experiments. Its size is similar to one of the hot spots found in the ensemble of hot spots in a RPP beam.

c.

Figure 1c. Plot of the measured intensity profile at focus for the single-hot-spot laser, compared to the theoretical curve for an ideal laser beam. The laser-beam intensity pattern is very similar to that of an ideal beam.
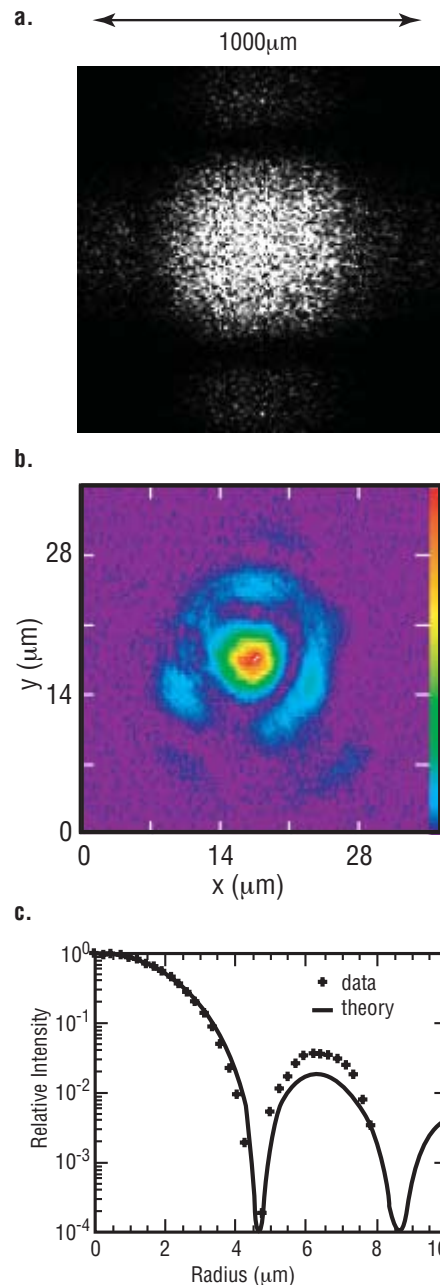
Laser and Plasma Conditions

The laser and plasma conditions for single-hot-spot experiments must be well characterized in order to compare the data directly to numerical models. The experiments were performed at the TRIDENT laser facility.[6] One of the three 527-nm laser beams was used to create and heat a 1-mm size plasma, which is large compared to a single-hot-spot volume. The single-hot-spot (diffraction limited) laser was produced by configuring a second, lower-energy laser to generate minimal wavefront distortion so that a nearly ideal diffraction-limited beam is produced. Lateral shearing interferometry was used to measure the relative wavefront quality of the 527-nm beam. Fringe analysis shows that the root-mean-square wavefront distortion is ~0.3 λ_o over 90% of the aperture, and the wavefront is fairly reproducible for each experiment.

The single-hot-spot laser is focused using a high-quality lens with a beam diameter to focal length ratio of either f/4.5 or f/7. The focal plane intensity distribution of the single hot spot was measured *in situ* using a high-quality 40× microscope objective and a charge-

coupled device (CCD) camera. Figure 1b shows an image of the interaction laser at best focus, and an azimuthally averaged radial profile is also shown in Figure 1c. The data show a nearly classic Airy pattern for a circular aperture. Superposed is the theoretical radial profile for diffraction from a plane wave incident on a circular aperture at f/7, and is in excellent agreement with the measured results. The focal spot deviates somewhat from the perfect diffraction limit in that there is more energy beyond the first Airy minima.

The interaction laser has a full width at half maximum (FWHM) of 3.8 ± 0.15 μm for f/7 focusing, and produces a peak intensity of 1.0×10^{16} W/cm^2 for a nominal energy of 0.8 J (max), in a 200-ps FWHM Gaussian pulse. The peak intensity is ~1/2 the peak intensity for a perfect diffraction-limited focus. The laser power output is kept roughly constant to maintain beam quality, and the peak intensity can be adjusted over the relevant range of intensities (10^{14}–10^{16} W/cm^2) using polished, calibrated neutral density filters.

The plasma was characterized using collective Thomson scattering from the heater beam by measuring spatial profiles of thermal levels of EPWs or IAWs using gated-imaging spectroscopy. The instrument collects the Thomson scattered light and spatially resolves the spectrum along the direction of plasma expansion. Profiles of the electron temperature (T_e), ion temperature (T_i), and flow velocity (v_z) along the direction of plasma expansion are obtained from measurements of the Thomson IAW spectra. The electron-density (n_e) spatial profile is obtained from measurements of the Thomson EPW spectra. A sample IAW spectrum is shown in Figure 2, and the measured plasma profiles are plotted in Figure 3 for a typical experiment. These measurements, together with the laser measurements, provide the initial conditions for comparing our data with the theoretical models.
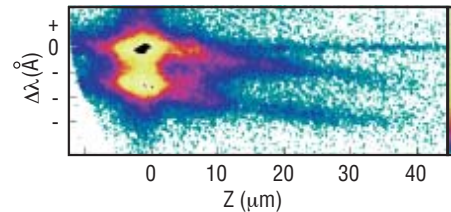
Figure 2. Time-resolved snapshot of imaging Thomson scattering spectra from thermal levels of ion acoustic waves. The waves are resolved as a function of distance from the target surface. The separation between the two peaks provides a measure of the electron temperature, and the spectral shift provides a measure of the flow velocity. Details of the spectral shape provide a measure of the ion temperature.
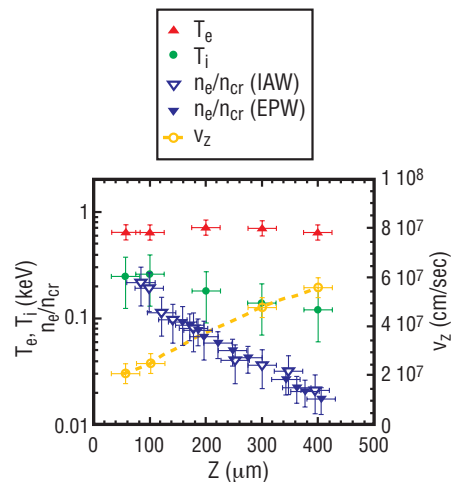
Figure 3. Typical measured profiles of the electron temperature, ion temperature, electron density, and flow velocity plotted versus distance from target. These data are all obtained from the imaging Thomson scattering spectra.

Flow-Induced Beam Steering

Supersonic plasma flow past a laser beam resonantly drives ion acoustic waves and scatters the laser power in the flow direction; this results in deflection of the laser beam. This instability is a branch of the forward SBS instability and can deflect the laser by several degrees. This is an important effect for inertial-confinement fusion (ICF) target designs because near-sonic transverse flows can exist in regions of high laser intensity and may affect capsule implosion symmetry.

Measurements of the laser beam angular distribution are made after it has propagated through the plasma. Figures 4a and 4b show plots of the transmitted-beam angular distribution at two different intensities for a plasma with Mach ≈ 2 supersonic flow. The beam is deflected in the downstream flow direction and shows an interesting bow-like structure. Other instabilities such as SRS and SBS were negligible for these experiments at sufficiently low laser intensities. Therefore, the beam-deflection results can be directly compared to models that contain only the beam-steering and self-focusing physics over this range of intensities.
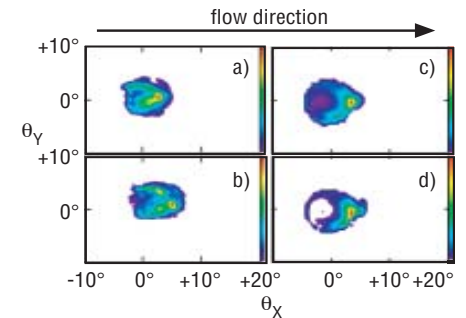
Figure 4. Transmitted beam angular distribution showing the effects of flow-induced beam steering from experiments with laser intensity of (a) 1.1×10^{15} W/cm² and (b) 2.7×10^{15} W/cm². Note the bow-like curvature toward the direction of flow. Three-dimensional (3-D) direct numerical simulations of these experiments are shown for a laser intensity of (c) 7.5×10^{14} W/cm² and (d) 1.5×10^{15} W/cm².

The experiment was compared to a three-dimensional (3-D) hydrodynamic model that solves a wave equation for the forward propagating light waves but neglects SRS and SBS backscattering. Figures 4c and 4d show plots of the transmitted-beam angular distribution from the 3-D model, using the initial conditions obtained in the experiment, and are remarkably similar to the experimental results. In order to be more quantitative, profiles taken parallel and perpendicular to the flow direction from the measurements and simulation results are shown in Figures 5a and 5b. The comparison is quite good in the parallel direction, but the simulation underestimates the amount of scattering in the perpendicular direction. Figure 6 shows a plot of the deflection angle in the flow direction from the experiment and model for a range of laser intensities. This represents the first successful quantitative comparison between a direct numerical simulation and a LPI experiment.[7] The good quantitative agreement is encouraging for the soundness in developing quantitative modeling using the single-hot-spot approach.
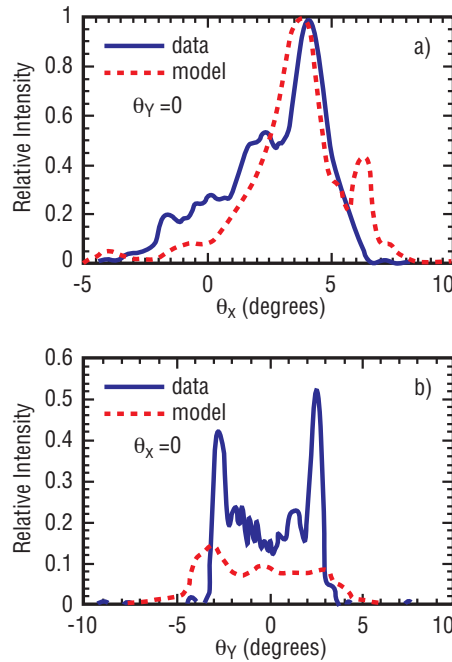

Figure 5. Comparison of transmitted beam angular distribution (see Figure 4b) for an experiment with peak laser intensity of 2.7×10^{15} W/cm^2. Three-dimensional direct numerical simulations were performed for these experimental conditions. Profiles of the measured and simulated transmitted beam distribution are shown (a) parallel to the flow direction and (b) perpendicular to the flow direction. Quantitative comparison between the measured and simulated profiles allow us to benchmark and refine our modeling.
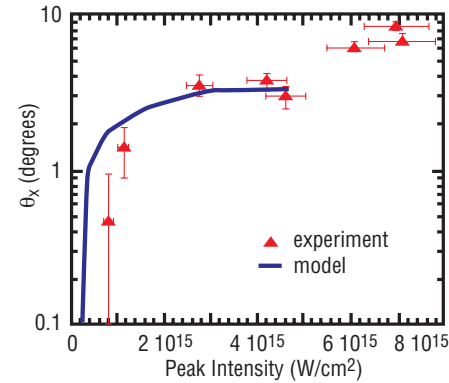

Figure 6. Plot of deflected beam centroid versus peak laser intensity for the experiments (triangles) and the 3-D model (solid line). The experimental results are in good agreement with the 3-D modeling and represent the first-ever quantitative comparison between a laser-plasma instability experiment and modeling.

Stimulated Raman Scattering Growth

We studied SRS backscatter in these plasmas at low enough densities such that the electron plasma wave involved in SRS growth should be strongly damped according to classical theory. Figure 7 shows a typical plot of the time-resolved SRS spectra from a low-density experiment. According to Equation 1 (see page 82), the laser wave frequency is the sum of the scattered light frequency and the EPW frequency for the SRS process. Therefore, the EPW frequency, which depends on the electron density, is easily calculated from the scattered light spectrum. The relatively narrow SRS spectrum is indicative of the expected density uniformity over the hot-spot volume. Figure 8 shows a plot of the SRS reflectivity as a function of laser intensity. SRS grows rapidly up to intensities ~2×10^{15} W/cm^2, at which point the SRS reflectivity saturates and grows very little with laser intensity.
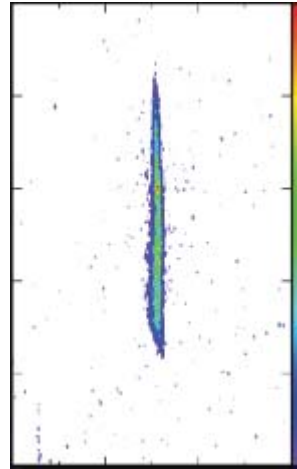
Figure 7. Time-resolved SRS spectrum from a typical single-hot-spot experiment in the so-called "strongly damped" regime. The SRS typically lasts for the duration of the laser pulse (~200 ps). The narrow spectral width (~2 nm) indicates that the SRS instability occurs in a plasma with a fairly uniform density.

We can estimate the expected SRS reflectivity with a simple comparison to classical analytic theory. The theoretical SRS reflectivity depends exponentially on a gain factor, $R_{SRS} \sim e^G$, where

the gain factor $G \propto I \cdot L_{sp}/\nu_{EPW}$, I is the single-hot-spot peak intensity, L_{sp} is the single-hot-spot speckle length, and ν_{EPW} is the electron plasma wave damping that depends on the electron density and temperature. Assuming a static value for L_{sp}, and calculating ν_{EPW} based on the measured plasma conditions, one can easily estimate the SRS reflectivity versus intensity from classical linear theory. The classical theory estimate of SRS reflectivity is also shown in Figure 7 and predicts that large SRS levels should not be observed at ~2×10^{15} W/cm^2, where rapid SRS growth is observed in the experiment.
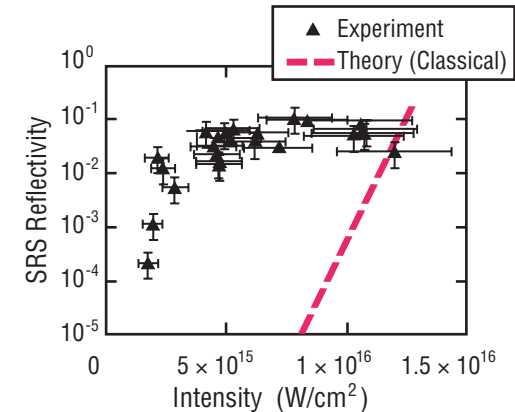
Figure 8. SRS reflectivity versus peak laser intensity. The experimental data (triangles) show that the SRS instability strongly turns on at an intensity of ~ 2×10^{15} W/cm^2 and quickly saturates at the several percent level for higher intensities. Classical SRS theory (dashed line) fails to predict the observed SRS onset at low intensities. These data serve to guide future theoretical research for SRS.

Because other processes such as self-focusing and beam-steering physics may also be present in the experiment, a better comparison is to incorporate the classical SRS theory in the 3-D hydrodynamic code used to model the beam-steering experiments and calculate the SRS reflectivity with these other dynamic processes included. The self-focusing and beam-steering processes might change the laser conditions in the plasma compared to the vacuum laser conditions and increase the level of SRS. This type of approach is believed to be valid and has been used in the past to estimate SRS reflectivity.[8]

The modeling was performed using the measured laser and plasma initial conditions and assumed a peak intensity of 2×10^{15} W/cm^2. The model indicated that self-focusing and beam-steering physics were negligible for these laser and plasma conditions so that the laser intensity and speckle length assumed in the analytic estimate were correct. The calculated transmitted beam distribution was quantitatively similar to the measured transmitted beam and showed little beam-steering effects, which indicates that the code is

correctly modeling the self-focusing and beam-steering physics. However, the 3-D model predicts negligible SRS levels at this laser intensity comparable to the simple estimates obtained from analytic theory. Because the laser intensity and speckle length are not modified by self-focusing or beam-steering physics, one can infer that the damping rate is much lower than that obtained by classical theory.

Previous large-scale experiments indicated large levels of SRS for plasma conditions where SRS was expected to be strongly damped,[5,9] but these experiments could not be fully compared with 3-D models including the effects of SRS, self-focusing, and other relevant physics. The advantage of the

single-hot-spot experiment is that these comparisons can be made and indicate SRS levels much larger than classical theory predicts. These results have stimulated much recent theoretical work in wave-particle (kinetic) processes which could result in EPW damping rates much lower than classical theory values.[10,11,12] Although the SRS experiments cannot be currently modeled, they are indicating areas where the classical theory is inadequate and serve to guide future theoretical research areas.

Summary and Outlook

Single-hot-spot experiments are a fundamental approach to a quantitative understanding of laser plasma instabilities and represent a paradigm shift in this research field. The experiments are performed using laser and plasma conditions that are well characterized so that the initial conditions are well known. Flow-induced beam steering is measured and compared to 3-D direct numerical simulations. Good quantitative agreement is obtained between the experimental results and the *ab initio* model and is the first quantitative comparison between a laser-plasma instability experiment and simulation. Finally, SRS experiments were performed in a regime where the instability should be strongly damped and the SRS reflectivity was found to be large. Comparison was made to simple analytic theories and 3-D models using classical SRS theory. The classical models predict SRS significantly lower than the experimental results. These results are an example where the single-hot-spot experiments serve to guide new theoretical research.

References/Further Reading

1   J. Lindl, "Development of the Indirect-Drive Approach to Inertial Confinement Fusion and the Target Physics Basis for Ignition and Gain," *Physics of Plasmas* 2, 3933–4024 (1995).

2   H. A. Rose, D. F. Dubois, "Laser Hot Spots and the Breakdown of Linear Instability Theory with Application to Stimulated Brillouin Scattering," *Physical Review Letters* 72, 2883–2886 (1994).

3   R. G. Watt, J. Cobble, D. F. Dubois, *et al*. "Dependence of Stimulated Brillouin Scattering on Focusing Optic F Number in Long Scale-Length Plasmas," *Physics of Plasmas* 3, 1091–1095 (1996).

4   D. S. Montgomery, B. B. Afeyan, J. A. Cobble, *et al.,* "Evidence of Plasma Fluctuations and Their Effect on the Growth of Stimulated Brillouin and Stimulated Raman Scattering in Laser Plasmas," *Physics of Plasmas* 5, 1973–1980 (1998).

5   J. C. Fernández, J. A. Cobble, D. S. Montgomery, *et al.,* "Observed Insensitivity of Stimulated Raman Scattering on Electron Density," *Physics of Plasmas* 7, 3743–3750 (2000).

6   N. K. Moncur, R. P. Johnson, R. G. Watt, *et al.*, "Trident: A Versatile High-Power ND-Glass Laser Facility for Inertial Confinement Fusion Experiments," *Applied Optics* 34, 4274–4283 (1995).

7   D. S. Montgomery, R. P. Johnson, H. A. Rose, *et al.,* "Flow-Induced Beam Steering in a Single Laser Hot Spot," *Physical Review Letters* 84, 678–681 (2000).

8   R. L. Berger, C. H. Still, E. A. Williams, *et al.*, "On the Dominant and Subdominant Behavior of Stimulated Raman and Brillouin Scattering Driven by Nonuniform Laser Beams," *Physics of Plasmas* 5, 4337–4356 (1998).

9   D. S. Montgomery, J. D. Moody, H. A. Baldis, *et al.,* "Effects of Laser Beam Smoothing on Stimulated Raman Scattering in Exploding Foil Plasmas," *Physics of Plasmas* 3, 1728–1736 (1996).

10   B. B. Afeyan, A. E. Chou, J. P. Matte, *et al.,* "Kinetic Theory of Electron-Plasma and Ion-Acoustic Waves in Nonuniformly Heated Laser Plasmas," *Physical Review Letters* 80, 2322–2325 (1998).

11   H. X. Vu, D. F. Dubois, B. Bezzerides ,"Transient Enhancement and Detuning of Laser-Driven Parametric Instabilities by Particle Trapping," *Physical Review Letters* 86, 4306–4309 (2001).

12   H. A. Rose, D. A. Russell, in preparation (2001).

Magnetized Target Fusion

T. P. Intrator, G. A. Wurden,
J. M. Taccetti, R. J. Maqueda,
K. Schoenberg, F. J. Wysocki,
D. W. Begay, G. Sandoval,
W. J. Waganaar, P. Sanchez, K. Barela,
E. M. Tejero, K. J. Scott, and J. Lamb
(P-24); R. E. Siemon (STB); D. Clark,
P. Turchi, R. Newton, P. Rodriguez,
K. Forman, and L. Tabaka (P-22);
M. Tuszewski (NIS-2); R. Kirkpatrick
(NIS-9); I. Lindemuth and
R. Faehl (X-1); and C. Grabowski,
E. Ruden, J. Degnan, S. Coffey,
M. Frese, D. Gale, T. Cavazos, and
W. Sommars (AFRL Albuquerque)

Introduction

A new project called Magnetized Target Fusion (MTF), which involves Los Alamos National Laboratory (the Laboratory) in Los Alamos, New Mexico, and the Air Force Research Laboratory (AFRL) at Kirtland Air Force Base in Albuquerque, New Mexico, is aimed at a qualitatively different approach to fusion energy. Unlike conventional tokamak and laser fusion approaches, MTF has the potential of creating fusion energy in an inexpensive apparatus. In recent years the focus of effort for fusion researchers, especially in the United States, has shifted from scientific feasibility to economic practicality. If successful, the cost savings implied by the MTF approach would allow fusion to be developed on a much faster time scale than conventional fusion.[1,2]

The MTF approach to fusion preheats and injects fusion fuel into a volume the size of a beer can as shown in the figure. Then the "beer can" (AKA aluminum cylinder) is rapidly compressed by magnetic forces that ensue from drawing a giant electrical current pulse axially along the wall of the cylinder. The compressed, high-density plasma fuel then burns in a few microseconds. The fast moving

Linear implosion system
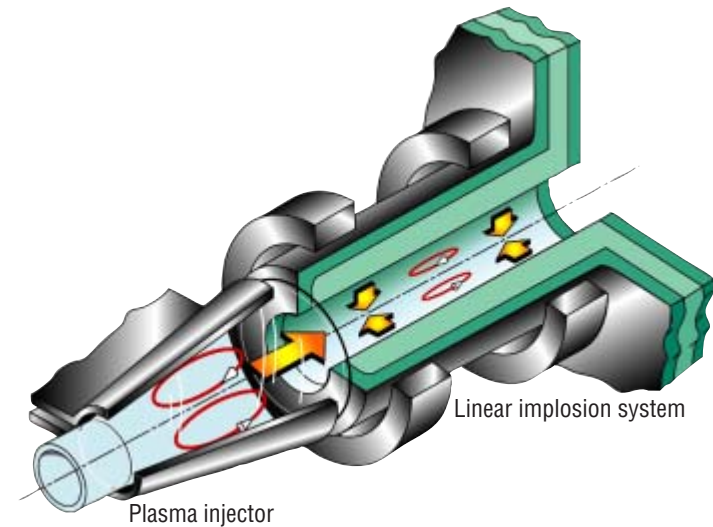
Plasma injector

metal wall, driven by pulsed-power liner technology, has been developed for other purposes by defense programs and is a specialty of New Mexico laboratories. The left side of Figure 1 shows the plasma injector, and the right side shows the liner compressor region, which implodes under millions of atmospheres of pressure. The process is analogous to that of a diesel engine, which compresses fuel to conditions where it burns more readily. The essential advantage of MTF is its potential to be tested for scientific feasibility and even developed to the stage of prototype power generation using an apparatus that costs orders of magnitude less than either conventional magnetic- or inertial-fusion approaches.

Figure 1. MTF will require us to create the initial plasma configuration, inject it axially into a flux-conserving shell, and finally compress the plasma to fusion-relevant density and temperature.

Context of MTF in Magnetic Fusion Energy Research

To explore this truly different fusion concept, we are taking advantage of the past 20 years of compact toroid (CT) research in the Magnetic Fusion Energy program (MFE). The CT plasma chosen for the target is a high-density field-reversed configuration (FRC)[3] similar to the early reversed-field theta pinch work carried out at the Naval Research Laboratory on PHAROS[4], at Julich on JULIETTA[5], and at Garching[6]. Similar to earlier work at the Laboratory, we will translate the FRC (see review paper)[7] into a compression region but then compress it using well-established liner technology developed in recent years by Department of Energy and Department of Defense program research. As sketched in Figure 2 there are "O" points that correspond to the nulls (B = 0) in magnetic field.

The crosses and dots also show the centroid of a doughnut or toroidally shaped circulating electrical current, which exits the figure on the top (dots) and re-enters the figure on the bottom (crosses). Surrounding the toroidal plasma current distribution are closed magnetic surfaces indicated by the arrows. These magnetic field
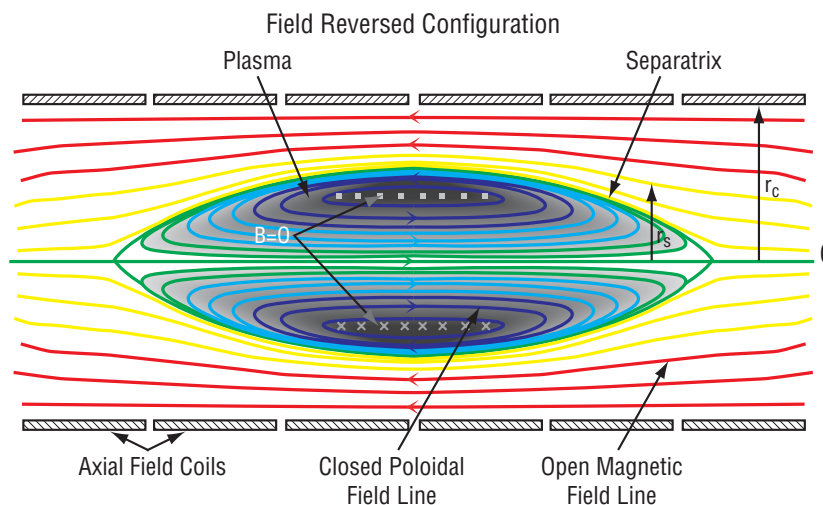

Figure 2. FRC equilibrium geometry, showing the closed magnetic surfaces that constitute a toroidally shaped magnetic equilibrium which is in force balance with the external magnetic field (red lines pointing to the left).

lines circulate poloidally according to the right-hand rule, counter clockwise about the dots and clockwise about the crosses. Note that the field lines are reversed on the inside compared to the outside, which is why we name this plasma equilibrium a FRC. Charged particles have difficulty diffusing across the magnetic-field lines and surfaces. Hence these closed toroidal magnetic surfaces of the FRC should provide enough thermal-energy confinement during compression inside a metal liner flux conserver to allow compressional work and heating of the plasma to fusion-relevant conditions. There is also an "X" point at the left- and

right-hand sides of the football shape where the external magnetic field points in the opposite direction to the internal magnetic field on axis. This also corresponds to a null in magnetic field and accounts for some of the particle and energy losses in a FRC. Fusion energy will be generated in a microsecond pulse during which pressure (plasma and magnetic) is magnetically and inertially confined by the imploding liner wall. At the Laboratory, magnetic fields of this magnitude (200 Tesla) have already been confined in an explosively compressed shell[8] that was designed to test some of the MTF

assumptions. Small-size and high-density fusion by MFE standards could achieve significant performance ($nt_E > 10^{13}$ s-cm^{-3}, T~5 keV) in just a few years at modest cost using available pulsed-power facilities, including the SHIVA Star capacitor bank driver at the Air Force Research Laboratory at Kirtland Air Force Base.

The density regime and time scale of MTF is intermediate between MFE and inertial confinement fusion (ICF). Three technical considerations explain why the regime is important. First, fusion reactivity scales as density squared; MTF density can be increased by many orders of magnitude over conventional MFE. Second, all characteristic plasma scale-lengths

decrease with density. Hence, system size is naturally reduced at a high density. Third, magnetic insulation greatly reduces the power and precision required to compressionally heat plasma to fusion-relevant conditions compared with ICF and brings the pulsed-power requirements within reach of existing facilities.[2]

Table 1 shows parameters of the FRC target plasma at the formation stage and the predicted final fusion relevant conditions for this FRC after compression by the MTF liner.

The initial density of 10^{17} cm^{-3} is large compared to present-day FRC experiments but consistent with experiments of thirty years ago[4,5,6] that we will describe in more detail in a later section on the history of FRC research. The initial temperature of 250 eV or approximately 3 million degrees Celsius must be large enough so

that radiation from partially ionized impurity atoms (Bremsstrahlung) will not dominate the power balance. The formation 5-Tesla magnetic field is large and will provide us a large latitude in choosing the internal magnetic reversed "bias" magnetic field (in the vicinity of 10% of the 5-Tesla formation field). The field energy from the bias magnetic field is dissipated into particle energy that would be observed as a plasma temperature for whatever particle density we choose for the formation FRC. During compression of this plasma inside the MTF liner, work is done on the plasma and its energy, and magnetic field consequently increases to the parameters noted on the right-hand column of Table 1. It can be shown that the magnetic flux (product of axial magnetic field times the circular area) is conserved during this

process. Because the area gets vanishingly small at the end of the compression, the magnetic field grows enormously. This 500-Tesla magnetic field confines the hot charged particles to small gyro orbit radii and thus magnetically insulates the hot plasma. The dwell time of the converging shell at maximum compression is a fraction of a microsecond and occurs when the inward implosion forces are balanced by the internal plasma pressure pushing radially outwards. We expect the lifetime of the FRC to be at least this long in this final compressed state.

Any fusion-power reactor design that follows from this path is obviously pulsed, and pulsed concepts have fallen out of favor compared with steady-state reactor designs. "Low" density, "long" pulse tokamaks operate at densities of n ~10^{14} cm^{-3}, but the large 2–10-billion-dollar price tag for proof-of-ignition devices such as the International Thermonuclear Experimental Reactor (ITER) compels us to consider other options. Some people argue that we need a technology breakthrough for the MFE tokamak approach. Another very different possibility is

ICF at very high density and pressure. The cost for this approach evidently exceeds $2 billion for the National Ignition Facility (NIF).

On the other hand, it may turn out that the engineering problems of pulsed-power-plant concepts are easier to solve than the steady-state ones.[2] We are engaging in a high-risk, high-payoff investigation of MTF as one of the concepts alternate to the tokamak fusion power-plant designs that presently dominate the MFE world view. MTF has intermediate density n_{MTF} ~10^{20} cm^{-3} which is approximately one million times the MFE tokamak scenario and approximately one million times less dense than the ICF paradigm n_{MTF} ~ 10^6 n_{MFE}, $\approx 10^{-6}$ n_{ICF} at a temperature near 10 keV. This has the consequence that megabar pressures are accessible, at the price of an intrinsically pulsed scenario. The liner imparts energy via integrated $\int PdV$ work that heats fuel by compressing it inside an imploding "pusher" wall. A magnetic field embedded in the fuel thermally insulates it from the pusher.

Table 1. FRC target plasma pre- and post-compression parameters.

FRC Parameters	FRC Parameters at Formation	FRC Parameters after Flux Compression (100×)
Density	$0.5-1 \times 10^{17}$ cm^{-3}	$\approx 10^{19}$ cm^{-3}
Temperature Te ≈ Ti	250 eV	10 keV
Magnetic Field	5 Tesla	500 Tesla
Lifetime	15–20 μsec	200 nsec

Recent Experimental Results

In April 1999, a joint Laboratory/ Air Force collaboration demonstrated MTF-relevant liner technology. We used the SHIVA-Star capacitor bank facility at the AFRL in Albuquerque to generate 11 Mega-Ampere current pulses into a cylindrical flux-conserving shell. These successful results gave credibility to a joint Laboratory/ AFRL proposal to carry out proof-of-principle experiments creating a MTF-relevant FRC. Experimental results of this successful first step confirm a shell exceeding the requisite characteristics to compress a FRC suitable for MTF. These requirements include high compression ratio and symmetry for a 3:1 aspect ratio thin liner. X-ray photographs (see Figure 3) show excellent uniformity for three snapshots of the shell radius as it radially converges to the axis. The top radiograph was taken before the compression started and shows the outer shell at radius of 4.89 cm and the inner diagnostic stalk at a radius of 0.317 cm. The second radiograph shows the compression approximately half way converged.

Note the final radiograph, which shows a very small gap between the central probe stalk with our various

t = 0 μsec

t = 20.0 μs

t = 23.5 μs

gap ≈ 1.1 mm
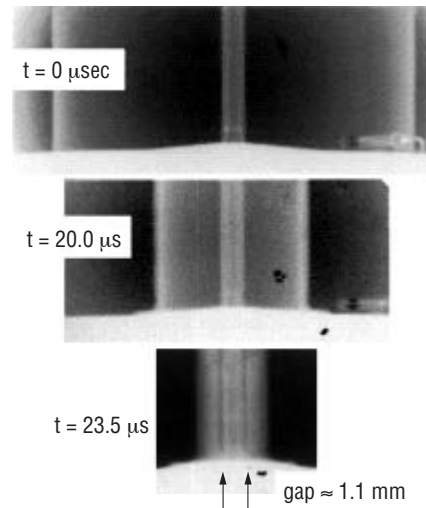
magnetic field diagnostics inside and the interior of the flux-conserving cylindrical shell. The bottom radiograph corresponds to a final compression ratio of 11.5:1 in radius, and compression to the probe stalk radius would correspond to a compression ratio of greater than 15:1.

We created a small magnetic field for this experiment that was trapped inside the converging flux conserver as the compression proceeded. Independent experimental measurements of the time-dependent internal magnetic field were extracted from magnetic

Figure 3. Side-on radiographs near the lower glide plane of initial liner and at three times t = 0.0, 20.0, and 23.5 μsec during the implosion. The 0.64-cm stationary probe jacket which contains magnetic and optical probes is visible on axis.

coil detectors and optical Faraday rotation measurements of magnetic field. The axial magnetic flux was defined as the product of the axial magnetic field and the area inside the conducting boundary (the aluminum cylindrical shell in our case). It can be shown that the flux is conserved, so that a measurement of the internal magnetic field history is equivalent to measuring the time evolution of the interior cylinder radius and its speed. Time histories of these data are shown in Figure 4, where the singular behavior as the radius
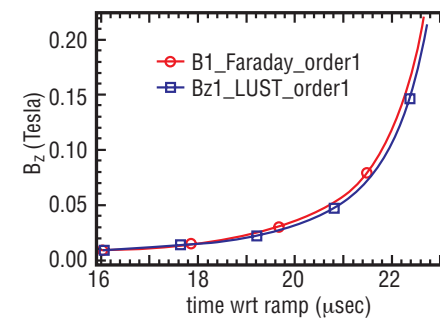

Figure 4. Faraday Bz data at the midplane compared with the adjacent Bdot probe data.

converges to zero is evident. These data are consistent with each other.

We take advantage of the flux-conservation argument to infer the radius r(t) as shown in Figure 5. Fiber-optic impact detectors (FIDs) were also embedded in the central probe stalk on axis. They show the symmetry and arrival time of the implosion. The radial symmetry appears to be better than 1% (i.e., ±300 μm out of an initial liner radius of 4.89 cm). All of the data are displayed in Figure 5, where good agreement is evident between data from several Bz probe locations, the radius inferred from the radiographs, the FID impact data and a model invoking the actual capacitor bank circuit with no free parameters.
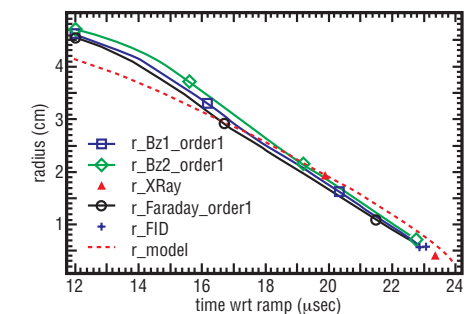

Figure 5. Time history of the inferred shell radius near the midplane. Data from Bdot, Faraday, FID, and radiographs are overlaid and quite consistent with each other.

Field Reversed Configuration Research has a Long History at the Laboratory

Our immediate goal for this year is to demonstrate, in the laboratory, a suitable FRC target plasma for MTF. The FRC is a type of "theta pinch" which consists of azimuthal image currents in the core plasma that are induced by opposite azimuthal currents in the exterior magnetic coil. A large magnetic field encircles this plasma image current to form toroidal- (doughnut) shaped closed magnetic field surfaces, as shown in Figure 2. It turns out the similar high-density FRC's were created in the early days of magnetic fusion research in the late 1960s. Scientists were not yet aware that such a reversed magnetic equilibrium could exist, but rather that such a reversed field "frozen" into the plasma increased the number of neutrons counted. The quest for fusion-relevant plasmas and increased neutron fluxes had the consequence that we know these MTF-relevant theta pinches were created, but not much detailed data was ever published. Over the next few decades, the typical FRC density decreased by a factor of 100 as researchers attempted to increase the lifetime of their plasma equilibria. The MTF concept is intrinsically pulsed and only requires a short equilibrium lifetime of 15–25 μsec for the target plasma we plan to inject into the compression region. This duration is well within reach of the published FRC theta pinch data.[4,5,6] Our experimental program takes advantage of many years of FRC research experience at the Laboratory. We will improve our understanding of high-density FRC's that were a hot topic 30 years ago, as we create them in the laboratory.

Field Reversed Configuration Target Plasma is Coming Online Soon

After somewhat more than one year of preparation, the first in a series of FRC experiments is coming on line at the Laboratory with considerable logistical help from the AFRL. The 15-person experimental team comprises fractions of 4 Technical Staff Member scientists from the Laboratory and AFRL, 5 technicians, and approximately 6 students. We have fabricated all the necessary hardware and are integrating the entire experiment. This requires several sets of capacitor banks, pulsed-power switching systems, safety interlocks, and suitable diagnostics of plasma properties. Figure 6 shows the pre-ionization capacitor bank on the bottom and the COLT theta pinch 0.25-megajoule capacitor bank on the left.

We expect the first plasma in mid-February 2001 for an experiment to explore strategies that could pre-ionize the plasma. The high-density FRC theta pinch experiment is expected to be operational in late June 2001. Plasma chararcteriz-

ation will be our focus in FY02. We plan to perform the first integrated FRC plasma/liner implosion experiments at the AFRL in Albuquerque beginning in FY03. The near-term goals for FRC MTF Project are

1. to have a working FRC experiment in the laboratory, with safety documentation, pre-ionization, bias, theta pinch, and cusp banks operational (no translation);

2. to have a full complement of diagnostics on the FRC in the quartz tube (this includes measurements of density, temperature, magnetic fields, and impurities); and

3. to explore the operating space for finding an optimum FRC target plasma (including how it behaves when translated into a "fake" aluminum liner).

The question is: just how close to an $\sim 10^{17}$ cm^{-3}, 100–300 eV, 15–25 μsec lifetime FRC plasma do we come?

Figure 6. Standing in front of the FRX-L main capacitor bank and behind the main header current feed assembly, are (from left to right, all Laboratory personnel unless otherwise indicated) Glen Wurden, Bill Waganaar, Daniel Begay, Matt Langner, Kit Werley, Ed Mignardot, Bill Fienup, Kathy Barela, Chris Grabowski (AFRL), Tom Intrator (Principal Investigator), Ricky Maqueda, Philip Sanchez, Bernie Martinez (AFRL).

Conclusion

MTF is beginning to be recognized as a dark-horse candidate approach to fusion energy. The MTF vision is easy to recognize, and we believe it is one of the few things in today's fusion program that actually produces excitement (…. that it just might work and is so cheap, that we ought to just go "do it").

MTF has goals which are simple to explain to both the general public as well as potential postdocs and staff. There is some relation to pulsed power technologies originally developed for defense programs at the Laboratory. This is why we can leverage our local Laboratory expertise and hardware into an extremely cost-effective experiment. However, all of our work is in the open literature.

For the actual embodiment of the MTF concept into a fusion power reactor, one needs to solve the engineering challenges of an intrinsically pulsed reactor scenario. A steady-state scheme is preferred by most power-company engineers. But as we noted already, it may turn out that the engineering problems of pulsed fusion power-plant concepts are easier to solve than the steady-state ones.[2] We are engaging in a high-risk, high-payoff investigation of MTF as one of the concepts alternate to the tokamak-fusion power-plant designs that presently dominate the MFE worldview. Interestingly, the most common reaction when we present MTF is not that it can't work or is on too unrealistic of a time-schedule, "but how can it be a reactor?"

The MTF high-density FRC experiment is the first step in a long-range program that could have a smaller budget and shorter time scale than the mainstream fusion energy options. The energy crisis is real and present, and current events such as global warming and electrical energy deregulation in California only serve to underscore this point. We feel that in the long run, our children will need to pay a high price if we do not address alternative basic energy-producing technologies today. Many of us still harbor the idealistic dream of producing and studying a viable fusion-energy source before we retire.

Contact Information

For further information, contact the Los Alamos Fusion Energy Program Manager, Richard E. Siemon, or visit the fusion energy web page: http://fusionenergy.lanl.gov.

References/Further Reading

[1] I. R. Lindemuth, *et al.*, "Target Plasma Formation for Magnetic Compression/Magnetized Target Fusion," *Physical Review Letters* 75, 1953–1956 (1995).

[2] R. E. Siemon, I. R. Lindemuth, K. F. Schoenberg, "Why Magnetized Target Fusion Offers A Low-Cost Development Path for Fusion Energy," *Comments on Plasma Physics and Controlled Fusion* 18, 363 (1999).

[3] D. C. Barnes, "Scaling Relations for High Gain, Magnetized Target Fusion Systems," *Comments on Plasma Physics and Controlled Fusion* 18, 71–84 (1997).

[4] E. A. McLean, A. D. Anderson, H. R. Griem, "Measurement of Plasma Density and Particle Losses in a Large Theta Pinch," *Proceedings of the APS Topical Conference on Pulsed High Density Plasmas*, (19–22 Sep 1967 Los Alamos Scientific Laboratory), A5-1:A5-5, LA-3770 (1967).

[5] A. Kaleck, L. Konen, P. Noll, *et al.*, "Limitation of the Confinement of Plasma in a Linear Theta Pinch with Trapped Reverse Magnetic Field," Plasma Physics and Controlled Nuclear Fusion Research, CN-24/K4, Novosibirsk (IAEA, Vienna, 1968) pp. 581–593.

[6] A. Eberhagen, W. Grossman, "Theta Pinch Experiments with Trapped Antiparallel Magnetic Fields," *Zeitschrift fur Physik* 248, 130–149 (1971).

[7] M. Tuszewski, "Review Paper: Field Reversed Configurations," *Nuclear Fusion*, 28(11), 2033–2092 (1988).

[8] W. T. Armstrong, J. A. Morgan, "Liner Compression of Magnetically Confined FRC Plasmas," *Proceedings of the 4th Intl. Conf. on Megagauss Magnetic Field Generation and Related Topics* (Santa Fe, 1986), (Plenum Press, New York, 1987), pp. 683–690.

[9] T. P. Intrator, *et al.*, "Experimental Measurements of a Converging Flux Suitable for Compressing a Field Reversed Configuration for Magnetized Target Fusion," to appear in *Nuclear Fusion*, (2002).

Nuclear and Particle Physics

Nuclear physics research seeks to understand the fundamental forces and particles of nature as manifested in nuclear matter. Work is typically carried out at large national accelerator facilities, but important cutting-edge research is also performed in house or at local facilities. The Department of Energy supports the bulk of the nuclear-physics effort at Los Alamos, with Laboratory-Directed Research and Development and some National Science Foundation funds providing support for important aspects of the overall program.

Los Alamos plays an important role in many of the national research thrust areas within nuclear physics. This includes major technical contributions and scientific leadership roles at the Relativistic Heavy Ion Collider (RHIC) at Brookhaven National Laboratory, neutrino physics at Fermi National Laboratory (FNAL), the Sudbury Neutrino Observatory (SNO), as well as the Los Alamos Neutron Science Center (LANSCE) facility and the Milagro observatory at Los Alamos.
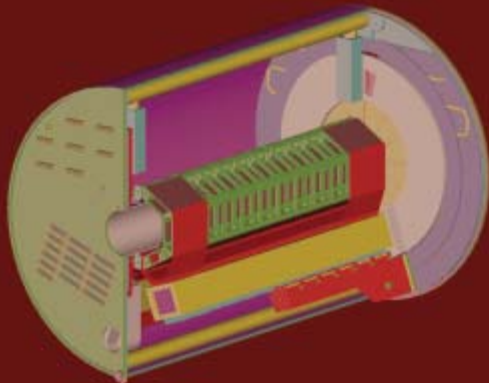
The major elements of the Los Alamos Physics Division experimental program include (1) major construction activities at RHIC leading to a research program in proton-proton, proton-nucleus, and nucleus-nucleus physics at high energies; (2) a new neutron physics program at the LANSCE using cold and ultra-cold neutrons for fundamental symmetry studies; and (3) neutrino physics both at FNAL on the Mini-BooNE experiment and SNO. Smaller, but important, efforts include precision symmetry measurements with trapped atoms and high-energy gamma astronomy with the Milagro detector at Los Alamos.

A major new initiative at Los Alamos has been in pulsed cold and ultra-cold neutrons (UCNs) at LANSCE. We have achieved the most intense pulsed cold and UCN neutron sources in the world. Our current effort is to complete construction of the $n + p \rightarrow d + \gamma$ and UCN "A"

The P-25 subset of the MEGA experimental team (from left to right): Gary Hogan, Jim Amann, Martin Cooper, Richard Mischke, and Melynda Brooks. To their right is an end cap of the large superconducting magnet that was the heart of the experiment.

experiments. The pulsed cold neutron effort makes use of Flight Path 12 at the Lujan Center and will be the only pulsed cold neutron beam in the world devoted to nuclear physics. The first experiment using the beam line will be the $n + p \rightarrow d + \gamma$ experiment, run by a large international collaboration. Possible future experiments on FP12 include neutron beta decay measurements, spin precession in liquid helium and liquid hydrogen, and the electric dipole moment (EDM) of the neutron. Our R&D work on UCNs has allowed us to proceed with construction of a low power (3-kW beam) first-generation UCN source at LANSCE. An international collaboration plans to use this source in an accurate measurement of the beta asymmetry in neutron beta decay. The physics that we can study will probe the structure of the hadronic weak interaction, provide the

most stringent test of the unitarity of the CKM matrix, probe the structure of the semi-leptonic weak interaction, and probe the size and origin of time-reversal-violating forces in strangeness-conserving processes. Further UCN source development will take place to advance a new National UCN User Facility.

The nuclear physics program has also made important contributions to more applied fields, such as the national security mission of the Laboratory. Recent examples have been the invention of proton radiography as the premier technology for an Advanced Hydrotest Facility for the national Stockpile Stewardship Program in NNSA and neutron resonance spectroscopy as a diagnostic for shock and materials physics.

High-Energy Gamma-Astronomy with Milagro

T. J. Haines, C. M. Hoffman,
F. Samuelson, and G. Sinnis (P-23);
G. Gisler (NIS-2); R. S. Delay,
S. Hugenberger, I. Leonor, A. Shoup, and
G. B. Yodh (University of California,
Irvine); B. Shen, O. T. Tumer, K. Wang,
and M. Wascko (University of California,
Riverside); W. Benbow, D. G. Coyne,
D. E. Dorfan, L. A. Kelley,
J. F. McCullough, M. F. Morales,
M. Schneider, S. Westerhoff, and
D. A. Williams (University of California,
Santa Cruz); R. W. Ellsworth (George
Mason University); D. Berley,
E. Blaufuss, J. Bussons-Gordo,
M.-L. Chen, J. A. Goodman, E. Hays,
D. Noyes, A. J. Smith, and
G. W. Sullivan (University of Maryland);
A. Falcone, M. McConnell, R. S. Miller,
and J. Ryan (University of New Hamp-
shire); L. Fleysher, R. Fleysher,
A. I. Mincer, and P. Nemethy (New York
University); and R. Atkins, B. L. Dingus,
and J. E. McEnery (University of
Wisconsin)

Introduction

High-energy gamma-ray astronomy probes nonthermal, energetic acceleration processes in the Universe. The list of known gamma-ray sources includes active galaxies, supernova remnants, and gamma-ray bursters (GRBs). Gamma rays are also produced when high-energy cosmic rays interact with matter in the Galaxy. Other potential sources include more exotic objects such as evaporating primordial black holes, topological defects, and dark-matter particle annihilation and decay.

Cosmic gamma rays up to 10–100 GeV can be directly detected with satellite-based detectors, such as EGRET[1] (now defunct) and GLAST[2] (currently under construction). EGRET observed a number of point gamma-ray sources as well as the diffuse emission of gamma rays from the galactic plane. Approximately 170 of the EGRET sources have not been identified with known astronomical objects, and so warrant further study. GLAST, presently scheduled for a launch in 2005, will extend and improve these measurements.

At higher energies, the gamma-ray flux from even the brightest source is too low to be measured with the relatively small detectors that can be placed in satellites; thus Earth-based techniques are used. High-energy gamma rays interact high in the Earth's atmosphere producing a cascade of particles called an extensive air shower (EAS). Ground-based gamma-ray telescopes detect the products of an EAS that survive to ground level, either the Cerenkov light produced in the atmosphere by the shower particles (atmospheric Čerenkov telescopes [ACTs]) or the shower particles (predominantly electrons, positrons, and gamma rays) that reach ground level (extensive air shower arrays [EAS arrays]).

After many years of perfecting the technique, ACTs have been successfully employed to detect very-high-energy gamma rays (VHE, ≈400 GeV–10 TeV) from several sources including three plerions (a system like the Crab, in which a young pulsar powers a compact nebula via synchrotron emission and inverse Compton scattering), at least three active galaxies, and one supernova remnant. These observations have greatly expanded our understanding of the acceleration mechanisms at work in these objects. EAS arrays, including the CYGNUS array in Los Alamos (now dismantled), use widely spaced scintillation counters to search for gamma-ray sources above ≈40 TeV. No convincing evidence for gamma-ray emission from any source has been obtained with EAS arrays in this energy region.

While ACTs have excellent angular resolution and sensitivity, they can only be used on clear, dark nights and can only view one source at a time (and only during that part of the year when that source is in the night sky). Thus they are not well suited to perform an all-sky survey, to monitor a known source for episodic emission, or to search for the emission of gamma rays from a source at an unknown direction and/or time (such as from a GRB).
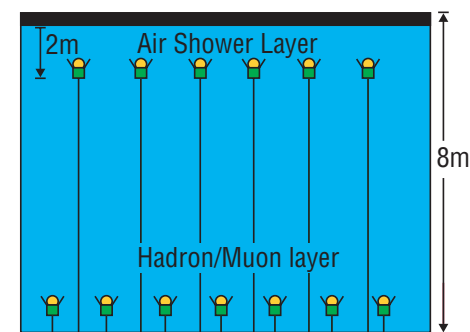

Figure 1. A schematic diagram of Milagro showing the two layers of photomultiplier tubes (PMTs) deployed in the water.

By contrast, an EAS array can operate 24 hours per day, regardless of weather, and can observe the entire overhead sky. The trick is to build an EAS array with a significantly lower energy threshold to overlap the energy regime studied with ACTs, where gamma-ray sources are known to exist.

The energy threshold of an EAS array is determined by the fraction of the shower particles reaching the ground that are detected and by the altitude of the detector (more shower particles survive at high altitudes so the energy threshold is lower). Milagro achieves a low energy threshold by employing photomultiplier tubes (PMTs) installed in a large, high-altitude, covered pond of water. The charged shower particles emit Čerenkov radiation when they traverse the water, which is detected by the PMTs: gamma rays in the shower convert in the water to electron-positron pairs, which in turn emit Čerenkov radiation and are detected. Figure 1 shows a schematic diagram of Milagro. Milagro is the first continuously operating, large-solid-angle detector sensitive to cosmic gamma rays below 1 TeV.

Milagro Project Summary

Milagro has been built in an existing man-made 5,000,000-gallon pond of water at Fenton Hill, ≈35 miles west of Los Alamos. Fenton Hill, at an altitude of 2650 meters above sea level (an atmospheric depth of 750 g/cm^2), is a technical area (TA-57) of Los Alamos National Laboratory (the Laboratory) leased from the US Forest Service for the purpose of performing fundamental geothermal research. When the geothermal project ended, the Milagro collaboration was able to take over the pond for gamma-ray astronomy. Figure 2 shows an aerial view of the Milagro pond. To construct Milagro, the collaboration spent several years on a number of tasks, including:

- emptying and cleaning the pond;
- installing a new polypropylene liner in and cover over the pond;
- constructing a utility building to house a water recirculation and purification system and fans to inflate the cover (to allow the installation of the detector elements in the pond);
- setting up an electronics trailer;
- installing electric power and communications (a T1 line);
- testing the PMTs;
- building electronics and a data-

acquisition system; and
- installing the PMTs and cabling in the pond and connecting them to the electronics.

In 1996 a prototype detector called Milagrito[3], consisting of 225 8" PMTs tethered to a grid of sand-filled PVC pipe on the bottom of the pond, was installed. The pond was filled with water to a level 1 m above the PMTs, and in February 1997 data collection began. Milagrito gathered data until May 1998, at which time it was dismantled to allow the full Milagro detector to be installed. In addition to obtaining some notable results (see below), the experience with Milagrito led to

some important changes in the detector design including the implementation of conical "baffles" on each PMT, which are reflecting on top to increase the effective area of the PMT and black on the bottom to absorb stray light.

The construction of the central Milagro detector, which has 723 PMTs in two layers and 8 m of water, was completed in late 1998, followed by a series of engineering runs. The bottom layer is used to reject showers initiated by background charged cosmic-rays. Data-taking began in late 1999 and the collaboration is now embarking upon an ambitious program of

Figure 2. An aerial view of the Milagro pond. In this photograph, the cover is inflated to allow construction activities inside the pond. The buildings beyond the pond house the water recirculation and purification system, the electronics, and the data analysis computers.

data collection and physics analysis.

A small team of Laboratory scientists has played a leading role in all aspects of the Milagro project from its inception, including design, construction, operation, and physics research. An array of 150 "outrigger" detectors, each an 8'-diameter tank of water with a PMT, is now being deployed in the 10 acres that surround the pond; the outriggers will greatly improve the sensitivity of Milagro to gamma-ray sources.
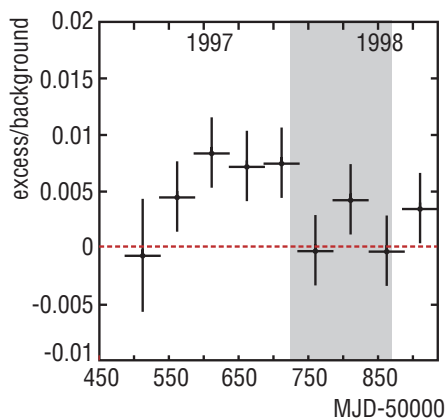

Figure 3. The fractional event excess observed with Milagro for 50-day periods from Markarian 501 as a function of time. The shaded area indicates the period for which the source is in the daytime sky and is not observable with air Čerenkov telescopes.

Milagro Detector Results

Milagro is the first gamma-ray detector that can continuously monitor the entire overhead sky at energies as low as a few hundred GeV. Milagro is the ideal instrument to study the transient and variable sources (such as GRBs and active galactic nuclei) of VHE gamma rays in the universe and to discover new gamma-ray sources. Results from Milagrito include:

- The detection of TeV emission from Markarian501, an active galaxy[4]. Markarian501 was in an active flaring state in 1997. Milagrito was the only detector to study Markarian501 in winter 1997–98 when it is in the daytime sky (Figure 3). It appears that the flare ended in late 1997.
- The apparent detection of TeV emission from a gamma-ray burst (GRB 970417a)[5]. If this result is confirmed, it is the highest energy emission ever observed from a GRB, and would place severe constraints on models of the mechanism responsible for GRBs. The distribution of the observed events on the sky are shown in Figure 4. The probability that this observation is a fluctuation of the background is quite small (1.5×10^{-3}).

- The observation of a solar ground-level event[6]. Figure 5 shows the detection of the November 6, 1997 ground-level solar event by the neutron monitor at Climax, Colorado together with the scaler and trigger rates from Milagrito. A preliminary analysis indicates that Milagrito detected particles in excess of 10 GeV.

While Milagro only recently began taking data and data-analysis algorithms are still being developed, an early analysis of the first eight months of data from indicates that emission from the Crab has been observed and that the lower PMT layer is effective at rejecting background events.
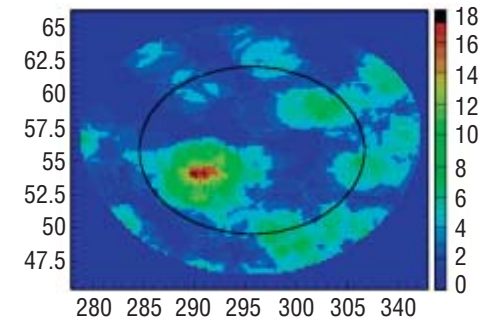

Figure 4: The number of events observed by Milagro in 1.6°-radius bins in the vicinity of GRB 970417a for the 7.9 s of the burst. The plot encompasses the location and its error as determined by BATSE. The best location determined by Milagrito is centered at R.A. = 289.9°, δ = 54.0°, and has 18 observed events, with an expected background of 3.46 events.

Figure 5: The observed rate from the Climax neutron monitor for the ground-level event of Nov. 6, 1997, together with the total scaler rate and trigger rate from Milagrito.
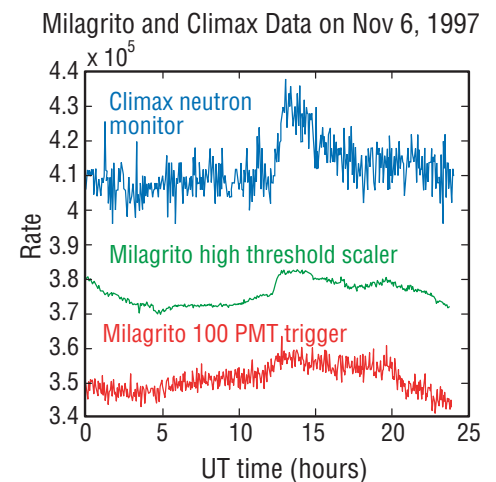
Importance/Significance of Results

The early results from Milagrito and Milagro have demonstrated that the water-Čerenkov technique works well and that continuous sensitive TeV observations of the sky are possible. While the sensitivity of Milagrito was much poorer than what is being achieved with Milagro, the year-round study of emission from Markarian 501 demonstrates the power of the technique. The observations of GRB970417a and the November 6, 1997 solar flare both represent the highest-energy emission detected from these phenomena and have generated considerable interest within the astrophysics community. The observation of TeV photons from the Crab with Milagro verifies the expected sensitivity of the telescope including the background-rejection capability. The sensitivity of Milagro is being further enhanced by the outrigger detectors, now being installed.

The Milagro collaboration is gratified that years of hard work are now beginning to show results. This new instrument, now shown to work well, should provide many new insights into the high-energy universe.

References

[1] C. E. Fichtel and J. L. Tromba, *Gamma-Ray Astrophysics*, NASA Reference Publication 1386 (1997).

[2] P. Michelson *et. al.*, *GLAST Large Area Telescope*, NASA Proposal AO99-OSS-03, (1999).

[3] R. Atkins *et al.*, "Milagrito, a TeV Air-Shower Array," *Nucl. Instru. & Meth. In Phys. Research* A449, 478 (2000).

[4] R. Atkins *et al.,* "TeV Observations of Markarian 501 with the Milagrito Water Čerenkov Detector," *Astrophysical Journal* 525, L25 (1999).

[5] R. Atkins, *et al.*, "Evidence for TeV Emission from GRB970417a," *Astrophysical Journal* 533, L119 (2000).

[6] A. Falcone, *et al.*, "Detection of the 6 November, 1987 Ground-Level Event by Milagrito," *Proceedings of ACE2000: Acceleration and Transport of Energetic Particles Observed in the Heliosphere*, AIP Conference Proceedings 528, 189 (2000).

For Further Reading

C. M. Hoffman, C. Sinnis, P. Fleury and M. Punch, "Gamma-Ray Astronomy at High Energies," *Reviews of Modern Physics* 71, 897 (1999).

R. A. Ong, "Very High-Energy Gamma-Ray Astronomy," *Physics Reports* 305, 94, (1998).

L. Rowan and R. Coontz, "Bursts, Rays and Jets," *Science* 291, 65 (2001).

T. C. Weekes, "Particle Astrophysics with High Energy Photons," *Physics Scripta* T85, 195 (2000).

Figure 6. A typical event in Milagro. The upper panel shows fits to the shower plane from the timing of the PMTs (to give the incoming direction): the upper line is for the shower layer and the lower two lines are for the muon layer, whose PMTs are on two different elevations. The bottom panel shows the pulse heights from the shower-layer PMTs (green) and muon-layer PMTs (blue). The location of the shower core is evident in both layers.
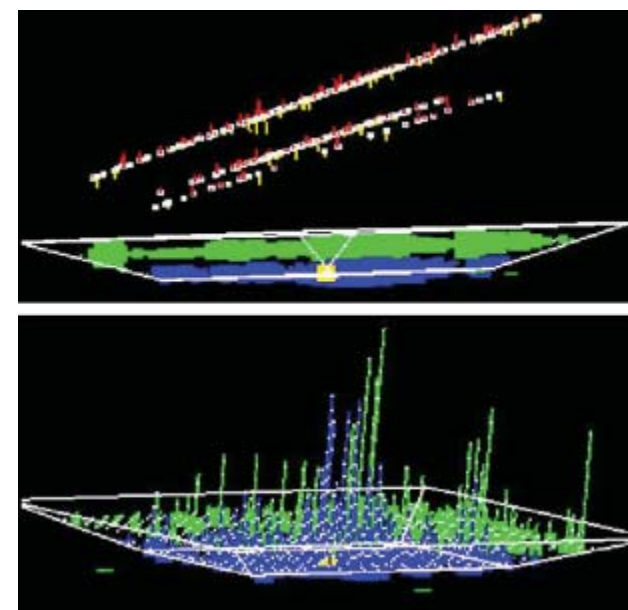
Measuring the Weak Nuclear Force between Protons and Neutrons

J. D. Bowman, G. S. Mitchell, S. I. Penttila, and W. S. Wilburn (P-23); G. L. Greene (LANSCE-DO); C. S. Blessinger, G. Hansen, H. Nann, D. R. Rich, and W. M. Snow (Indiana University); R. D. Carlini (Thomas Jefferson National Accelerator Facility); T. E. Chupp, K. P. Coulter, R. C. Welsh, and J. Zerger (University of Michigan); M. S. Dewey, T. R. Gentile, T. B. Smith, and F. E. Wietfeldt (National Institute of Standards and Technology); T. Case and S. J. Freedman (University of California, Berkeley); S. Ishimoto, Y. Masuda, and K. Morimoto (KEK National Laboratory, Japan); G. L. Jones (Hamilton College); M. B. Leuschner and V. R. Pomeroy (University of New Hampshire); and S. A. Page and W. D. Ramsay (University of Manitoba and TRIUMF)

Introduction

A team of scientists from Physics Division, the University of Indiana, UC Berkeley, the Joint Institute for Nuclear Research-Dubna, the University of Michigan, the University of New Hampshire, the KEK National Laboratory-Japan, and the National Institute of Standards and Technology is developing an experiment to answer long-standing questions concerning the weak interaction of nucleons. This experiment will be done at the LANSCE spallation neutron source using cold polarized neutrons. The pulsed cold-neutron beam line is being constructed now and data collection is scheduled to begin in summer 2003. In this report, we describe the physics goals of the experiment and technical progress on the apparatus to do the experiment. We have recently completed tests of a one-tenth-scale prototype of the apparatus and validated the performance of the design using a pulsed cold-neutron beam.

Nucleons are bound together to form nuclei by the strong interaction. Both nucleons and nuclei decay through the much more feeble weak interaction. For example, a neutron decays into a proton, an electron, and an electron anti-neutrino. The existence of weak decays of nucleons implies that pairs of nucleons interact weakly as well as strongly. The strong interaction is invariant under the parity transformation, reflection in a mirror. The signature of the weak interaction is parity-violation. This signature will be used to experimentally isolate the small effects from the weak interaction in the presence of the much stronger (10 million times) strong interaction. Examples of phenomena that result from the small parity-violating weak force between nucleons are the existence of static anapole moments in the ground states of nuclei such as cesium-133, circular polarization of photons from transitions between states of unpolarized nuclei, parity-odd correlations from photons emitted from polarized nuclei, and large parity-violating longitudinal asymmetries of the total cross sections for compound-nuclear resonances. Although scores of parity-violating asymmetries have been observed in nuclei, a quantitative description of these measurements has yet to be developed. The goal of this experiment is to unambiguously determine the most important coupling constant in the potential that describes the weak force between nucleons. The modern theory of weak and strong interactions is known as the standard model. The weak interaction of nucleons involves the basic constituents of the standard model and is shown diagrammatically in Figure 1.
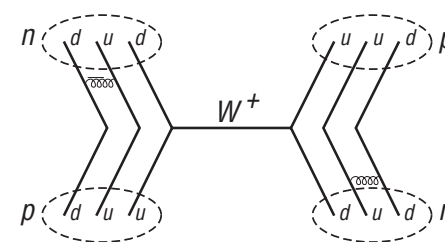

Figure 1. Two nucleons exchange a vector boson.

Each of the two nucleons is made up of three quarks. Two quarks bound in different nucleons interact weakly through the exchange of a vector bosons, the W^+, W^-, and Z^0. The weak couplings of quarks have been well determined through experiments in nuclear and high-energy physics. Because of the properties of the strong interaction, the above picture must be modified. The strong interaction between nucleons is mediated by the exchange of mesons, each consisting of a pair of quarks. The light pi (π) meson produces a long-range attractive force and the heavier rho (ρ) and omega (ω) mesons produce a repulsive short-range force. The short-range repulsive strong interaction between nucleons prevents pairs of nucleons from getting closer than one Fermi (Fm), 10^{-13} cm. The vector boson exchanged between quarks is very heavy, 100 GeV, and at the momentum transfers characteristic of the interactions of pairs of nucleons in nuclei, is highly virtual. The range of the vector bosons is approximately 10^{-2} Fm, much shorter than the distance between nucleons. How then can the nucleons interact weakly? The same mesons that mediate the strong interaction also

can mediate the weak interaction and bridge the distance between nucleons. The strong and weak interactions between nucleons are illustrated in Figure 2.

The light, 0.14 GeV, π meson is much less virtual than the heavier vector bosons, and provides for a range of the weak interaction between nucleons the same as the strong interaction, ~1 Fermi. This
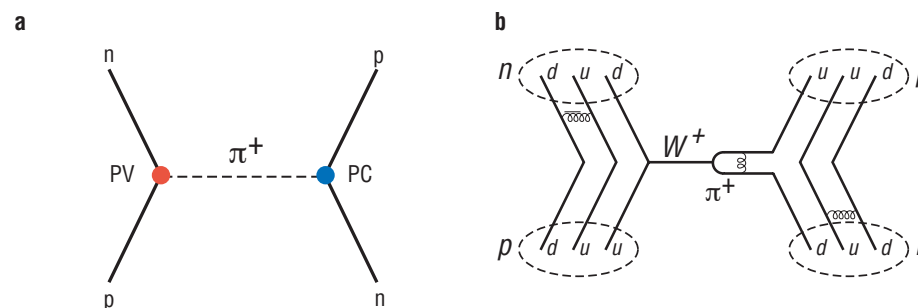

Figure 2. (a) Two nucleons exchange a π meson. (b) One nucleon emits a π meson strongly, the π turns into a W, and the W scatters from a quark in the other nucleon.

picture of the weak interaction of nucleons is known as the meson-exchange model, and is characterized by a number of nucleon-nucleon-meson couplings. The most important of these is the long-range π-nucleon-nucleon weak coupling.

Not So Clear a Picture

The picture painted above does result in some difficulties of interpretation. First, the quarks that interact in Figure 2b are not free, but are bound in nucleons. The couplings between quarks and vector mesons are appropriate for free quarks. The strong interaction between quarks is carried by gluon exchange, shown as curly line in Figure 2b. The exchange of gluons between quarks modifies the weak couplings between quarks and vector bosons, and the weak couplings between nucleons are different than those of free quarks. In principle, these modifications can be calculated in the standard model, which describes the strong as well as the weak interactions of quarks. However, at present the strong interaction can be treated only at very large momentum transfer in a framework known as perturbative quantum chromodynamics (QCD). In order to describe phenomena involving weak interactions of nucleons, the weak couplings shown in Figure 2b must be determined experimentally.

The second difficulty arises because nuclei are many-body systems and the many-body problem can not be solved in general. In order to determine the meson-nucleon-nucleon couplings, it is necessary to know the wave functions that describe the initial and final states for the process being observed. The weak interaction between the nucleons can be treated as a perturbation between the states that result from solving the many-body strong-interaction problems. Experimental observables can be expressed as matrix elements of the operators describing the meson-nucleon-nucleon interaction and weak meson-nucleon-nucleon couplings. Because the many-body strong-interaction can not be solved in general, attempts to interpret the results of experiments have depended on model wave functions. The observation of a parity-violating asymmetry in the two-body neutron-proton system does not suffer from this difficulty because the two-body strong interaction problem can be solved exactly.

Our Experiment

In the experiment, a polarized cold neutron beam is stopped in a liquid-hydrogen target. The neutrons capture on the protons to form deuterium (D) nuclei with the emission of a 2.2 MeV photon. If parity is conserved, the direction of emission of the photon is isotropic with respect to the neutron polarization, s. The connection between parity violation and isotropy is shown in Figure 3. Under mirror reflection, the vector, k, that describes the photon direction does not change. However the pseudo vector, s, that describes the neutron spin direction or handedness does

change. When reflected in the mirror the direction of rotation, shown by the rotating arrow, changes handedness, much as a person's left and right hands are interchanged in his mirror image.

The experiment isolates the isovector weak pion-nucleon-nucleon coupling, $H_{\pi,1}$. The (somewhat simplified but correct) reasoning is as follows. The transition between the initial scattering state and the deuteron ground state has a magnetic-dipole or character. If the deuteron wave function has a parity impurity, an electric-dipole transition can occur between the

initial scattering state and the odd-parity component of the deuteron. The transition operator has an isovector character. The scattering state and deuteron ground state both have isospin 0, and can not be connected by the isovector transition operator. The weak interaction between nucleons has isoscalar, isovector, and isotensor parts. The isovector transition operator connects only isovector admixtures to the isoscalar deuteron scattering state. The weak interaction between nucleons has isovector contributions from the π, ρ, and ω mesons. The π is lighter than the ρ and ω mesons and the interaction it carries has a longer range than the others. The deuteron is very weakly bound and the two nucleons are far apart. Only the long-range π component of the weak nucleon-nucleon interaction makes a significant contribution to the transition amplitude.
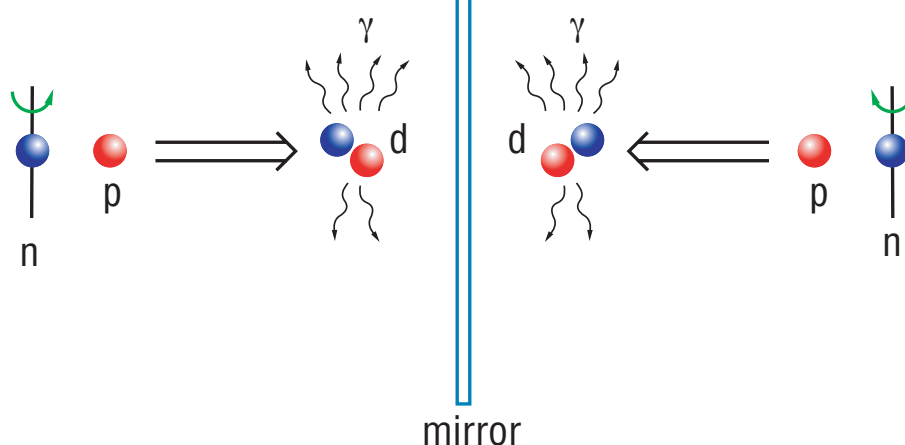

Figure 3. Mirror images of photon emission.

The apparatus, shown schematically in Figure 4, consists of a cold-neutron source, followed by a neutron polarizer, and a liquid para-hydrogen target, surrounded by an array of gamma-ray detectors. Neutrons from the spallation source are moderated by a liquid-hydrogen moderator. The source is pulsed, thus allowing measurement of neutron energy through time-of-flight techniques. The neutron guide transports the neutrons from the moderator through the biologi-

cal shield with high efficiency. The neutrons are then polarized in the vertical direction by transmission through polarized helium-3 gas. The neutron spin direction can be subsequently reversed by the radio-frequency resonance spin flipper. The use of this type of a spin flipper is only possible at a pulsed neutron source. The use of this spin flipper reduces the systematic error associ-

ated with spin-dependent deflection of the neutron beam due to the interaction of the neutron magnetic moment with magnetic field gradients. The neutrons are captured in the target, which consists of liquid para-hydrogen. This state of hydrogen is required because neutrons depolarize quickly in ortho-hydrogen, while those with energies below 15 MeV

retain their polarization in para-hydrogen. Gamma rays emitted in the capture process are detected in the cesium-iodine(thallium) detectors surrounding the target. The light of scintillation for these detectors is converted to an electrical current by vacuum photo diodes and amplified by low-noise preamplifiers. The parity-violating asymmetry causes an up-down asymmetry in the angular distribution of the gamma-rays for vertical neutron spin. When the neutron spin is reversed, the up-down gamma-ray asymmetry reverses.
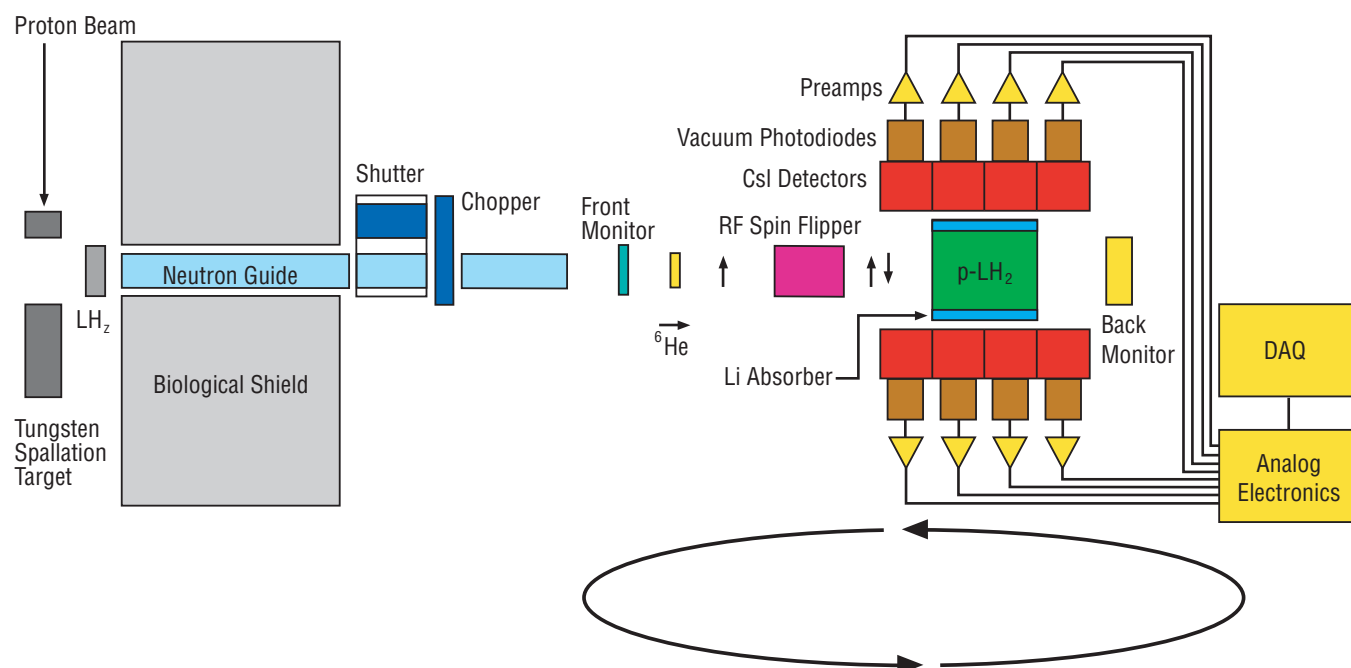

Figure 4. A schematic of our experimental apparatus.

Experimental Results

In 2000, we conducted a test run using a one-tenth-scale prototype of the experiment at an existing cold neutron beam line at LANSCE. The test include a polarized helium-3 neutron polarizer, the radio-frequency neutron spin flipper that will be used in the final experiment, four of the 48 cesium-iodine gamma-ray detectors that will be used in the final experiment, and ionization chamber beam monitors. Instead of a liquid hydrogen target, we used nuclear targets that have known parity-violating asymmetries.

Review committees had identified the helium-3 polarizer and the radio frequency neutron spin flipper as the most challenging technological problems in the experiment. The neutron polarization produced by the polarized helium-3 cell was in quantitative agreement with the expected performance although the size of the test cell was smaller than required for the final experiment. Since the test run was completed, our collaborators have successfully produced a 12-cm-diameter polarized helium-3 cell and demonstrated 50% helium-3 polarization. We expect further improvements in cell performance, but the 12-cm-diameter cell is adequate to do the experiment. The radio frequency spin flipper had a measured efficiency for reversing the neutron spin of 97%. This efficiency corresponds very well with our design calculations.

We performed a careful measurement of the cold neutron flux from the liquid hydrogen moderator. We found that the measured flux was 10% higher than the predictions of the Monte Carlo simulation used by the designers of the neutron source. Thus, we expect that the neutron flux in the beam line we are building will be adequate for the experiment. In most nuclear-physics experiments radiation produces pulses in detectors that is counted by digital electronics. The error, Δn, in the number of detected radiation quanta, n, is given by Poisson statistics $\Delta n = \sqrt{n}$. The cesium-iodine gamma-ray detectors operate by converting gamma radiation into light that is converted to a current signal by vacuum photodiodes. The small current is amplified by low-noise preamplifiers and linear amplifiers and recorded by transient digitizers. We have taken this approach because the rates at which gamma quanta are detected, $\sim 10^{10}$ Hz, is too great to be counted by digital electronics. We measured the response of the cesium-iodine detectors and photodiodes, number of photo electrons/gamma quantum, to be 1000 photo electrons/gamma quantum. This yield is two times larger than the design goal of the experiment and should allow us to attain the counting statistics limit. In order to test our ability to attain the counting statistics limit we measured the parity-violating asymmetries produced by a number of nuclear targets, lanthanum-139, chlorine-35, and cadmium. The measured asymmetries agreed well with the previous measurements. The observed statistical errors corresponded to our expectations. When we scale the observed errors to the neutron beam intensity, neutron polarization, and detector solid angle of the final experiment, we obtain the design statistical error. On the basis of the test-run results, we are confident that the experiment will run as designed and provide a valid and statistically significant measurement on the parity-violating asymmetry in the $n + p \rightarrow d + \gamma$ reaction and a determination of the weak isovector pion-nucleon coupling.

Beta Decay of Rubidium-82 in a Magnetic TOP-Trap

A. Hime, S. J. Brice, A. Goldschmidt, and R. Guckert (P-23) and S. G. Crane, J. J. Kitten, D. J. Vieira, and X. Zhao (CST-11)

Introduction

Of the four fundamental forces in nature (electromagnetic, strong, weak, and gravity) the weak interaction is unique in that it violates parity, or space-reflection symmetry. More than four decades have passed since the first suggestion by Lee and Yang that parity could be violated in weak interactions[1] and the subsequent discovery in the beta decay of polarized cobalt-60 nuclei.[2] Today, maximal violation of parity symmetry is accommodated in the standard model describing a purely vector-axial vector (V-A) helicity structure for the weak interaction. This structure was developed largely upon the empirical observations of nuclear beta decay during the latter half of the past century.[3,4] Despite the phenomenological success of the standard model, the fundamental origin of parity violation is unknown and modern pursuits in nuclear beta decay continue to serve as a probe of the origin of symmetry and symmetry-breaking in the weak interaction.[4]

Parity violation is manifest in nuclear beta decay as an asymmetry in the angular distribution of beta particles emitted relative to the spin orientation of the parent nucleus (see Figure 1). In pure Gamov-Teller (GT) transitions, wherein the nucleus undergoes a change in angular momentum by one unit ($\Delta J = 1$), the electrons are emitted preferentially in a direction opposite to the spin of the parent nucleus. Furthermore, because both the electron and the antineutrino that emerge from the decay must each carry away one-half unit of angular momentum (intrinsic spin) it follows that the electron must carry off its spin angular momentum aligned anti-parallel to its direction of motion. In other words, the weak interaction is *left-handed* (see Figure 2). An electron-nuclear spin asymmetry can be defined,

$$\chi(E,\Theta) = AP\beta(E)\cos\Theta ,$$

where　E　= the electron energy,
　　　$\beta(E)$　= its velocity relative to light,
　　　Θ　= the angle between the electron momentum vector and the nuclear spin orientation,
　　　P　= the polarization of the parent nucleus, and
　　　A　= the observable of interest (the correlation coefficient) which is nonzero when parity symmetry is violated
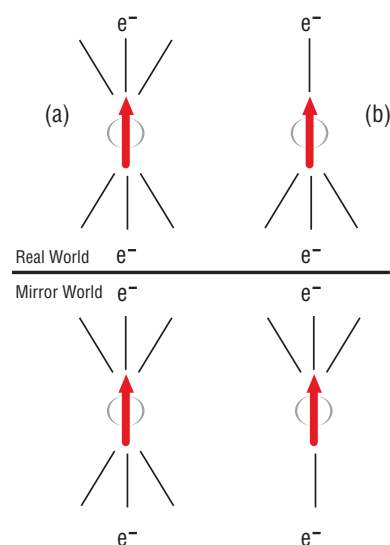

Figure 1: (a) If parity (or space-reflection symmetry) were preserved in nuclear beta decay, no asymmetry would be detected in the distribution of electrons relative to the spin-orientation of the parent nucleus. In this scenario, the real world and mirror world would be indistinguishable. (b) Due to parity violation, electrons observed in nature exhibit an asymmetry in their angular correlation with the nuclear spin direction. In the experiment of Wu *et al.*[2], this asymmetry was first observed in the beta decay of cobalt-60 that was cooled to a low temperature and spin-aligned in a magnetic field.

(a) Four states of a spin -1/2 partical
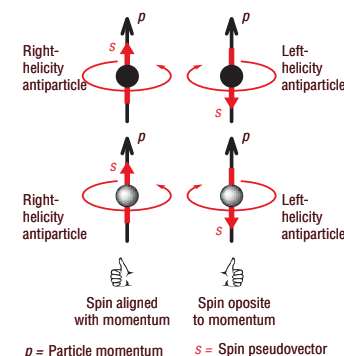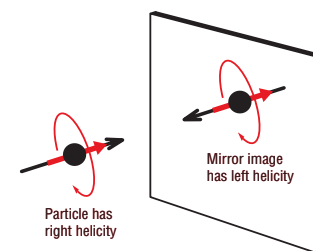
(b) Mirror Reflection of a Right Helicity Particle

Figure 2. The four states of a lepton. The helicity of a particle relates its intrinsic spin to its direction of motion. (a) Leptons such as the electron and neutrino emitted in nuclear beta decay are spin-1/2 particles and, because spin is quantized, they have four independent states. A particle is said to have right-handed helicity if its spin and momentum point in the same direction and left-handed helicity if these two vectors point in opposite directions. (b) The mirror image of a right-handed particle is a left-handed particle and *visa versa*. A pseudovector such as spin (angular momentum) does not change direction under spatial inversion whereas a regular vector such as momentum does. The weak interaction is said to be left-handed in that it appears to couple only to left-handed particles and right-handed anti-particles. Consequently, the weak interaction violates parity (or space-reflection) symmetry.

Experimental History

The value of the correlation coefficient is uniquely defined within the framework of the standard model and precision measurements are aimed to search for new physics that is thought to be manifest in the presence of interactions beyond the standard model. The pure GT transitions still offer the most direct route to study parity violation in nuclear beta decay because they proceed solely through the axial-vector coupling responsible for parity violation. To date, the most precise measure of the electron-nuclear spin correlation coefficient (A) comes from a modern experiment that used polarized cobalt-60 nuclei.[5] In that experiment the angular dependence of the asymmetry was verified, and a value of A = -1.01 ± 0.02 was deduced for the correlation coefficient, in agreement with expectations for a pure GT, electron emitter with $\Delta J = 1$. Due to difficulties in reducing systematic error associated with absolute polarization and electron scattering effects in a solid sample, it appears unlikely that precision can be significantly improved using conventional technology. The advent of optical and magnetic traps for neutral atoms provides a new technology to harness a point-like,

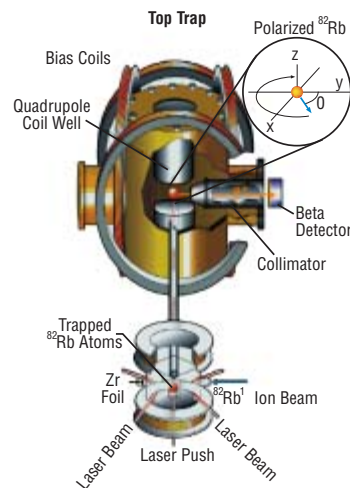essentially massless source with a potentially high degree of polarization.

Figure 3. Schematic diagram of the apparatus used to trap, transfer, and retrap rubidium-82 atoms. After implanting radioactive rubidium-82 ions into a zirconium catcher foil, neutral rubidium-82 atoms are released into MOT-I, where they are trapped and confined to a small cloud at the center of a glass cell. The atoms are then transferred to the experimental chamber of MOT-II through a hexapole guide tube using an optical push-beam. After retrapping in MOT-II, the TOP-trap is rapidly switched on where the direction of the magnetic bias field that aligns the nuclear spin rotates uniformly in a plane. This rotating beacon of spin-polarized rubidium-82 nuclei is used to measure the parity-violating correlation by detecting the positron energy in a plastic scintillator and recording a snap-shot of the nuclear-spin orientation from knowledge of the magnetic-field configuration.

Our New Approach

Our research aims specifically at exploiting magnetically trapped rubidium-82 in a new generation of fundamental-symmetry experiments. Rubidium-82, a pure and allowed GT beta decay nucleus, has the appropriate atomic structure and lifetime (75 seconds) to be exploited in a magneto-optical trap (MOT). We previously reported a world record by trapping several million radioactive rubidium-82 atoms in a MOT.[6,7] Since that time, we have successfully mounted a prototype experiment aimed to measure the positron-nuclear spin correlation coefficient from polarized rubidium-82 atoms confined to a time-orbiting-potential (TOP) trap.[8] Rubidium-82 follows from the electron capture of the longer lived parent, strontium-82, which is produced at the Isotope Production Facility at the Los Alamos Neutron Science Center (LANSCE). Strontium-82 is placed in the hot-ion source of a mass separator, which selectively ionizes, separates, and implants rubidium-82 ions into a zirconium foil located inside our primary trapping cell. Subsequent heating

of the implantation foil releases neutral rubidium-82 atoms into this cell where they are cooled and trapped in a MOT (see Figure 3). The atoms are then transferred to a second, high-vacuum chamber using a short pulse of laser light. The atoms are retrapped in a second MOT and prepared for loading into the TOP trap. Once retrapped, the atoms are further cooled and optically pumped into the fully stretched atomic ground state, ensuring that the nuclear spin is aligned with the local magnetic field. The TOP trap confines the atom in a quadrupole field gradient to which a rotating bias field is added. The rotation frequency (830 Hz) is small relative to the Larmor precession frequency, consequently the nuclear spin vector adiabatically follows the bias magnetic field vector. The TOP trap thus serves to provide a rotating beacon of spin-polarized rubidium-82 nuclei to study the parity violating angular correlation of positrons ensuing from the beta decay process. Positrons are detected in a plastic scintillator after they pass through a thin stainless-steel window that separates the detector from the high-vacuum chamber.

Experimental Results

Prototype experiments were performed to address a number of experimental details in measuring the positron-spin correlation coefficient. The fruits of these efforts have been submitted for publication[9] and are highlighted in Figure 4. In Figure 4a we show the angular distribution obtained after binning one of our data samples according to the reconstructed angle between the positron momentum vector and the spin-direction of the decaying nucleus. The data are well described by a cosΘ distribution with a preponderance of positrons emitted in the same direction as the nuclear spin, which is expected for rubidium-82 positron decay. The data distinctly demonstrate the successful confinement of a rotating, nuclear-polarized sample of rubidium-82 atoms in a TOP trap and marks the first observation of parity-violation in nuclear beta decay using atom-trapping technology. By integrating the data over the observed emission angle we obtained an unpolarized sample and the differential energy spectrum for positrons. This spectrum is shown in Figure 4b, where comparison to detailed Monte Carlo simulations indicates that the rubidium-82 spectrum is consistent with a pure and allowed GT decay and that our understanding of the positron detection optics in our experiment is well understood.

Future Directions

Detailed analysis of these proof-of-principle experiments indicated several improvements necessary before we can realize a precision measurement of the correlation coefficient of interest. In the absence of background, the amplitude of the angular correlation is directly proportional to the product AP. Hence it follows that, in order to extract the correlation coefficient (A), one requires independent knowledge of the absolute polarization (P). We have not, as yet, instrumented the appropriate hardware to measure the polarization but plans are now in place to perform such measurements using high-resolution charge-coupled device (CCD) camera images of the atom cloud. This, in conjunction with a mapping of the magnetic-field distribution over the trap region, then allows one to determine the global polarization of the atom cloud.

The amplitude of the angular correlation shown in Figure 4a is smaller than expected because the absolute polarization of the atom cloud is less than optimal and also from background associated with atoms that are ejected from the trap. A number of mechanisms are responsible for atoms to be lost from the trap. These wayward atoms make their way to the walls of the vacuum chamber where they subsequently decay from an unpolarized state, producing an uncorrelated background that falsely masquerades as a signal with less-than-maximal parity violation. We can circumvent this background through optimization of the trapping procedure and through the design of a positron telescope capable of discriminating positrons that are emitted from the trap region.
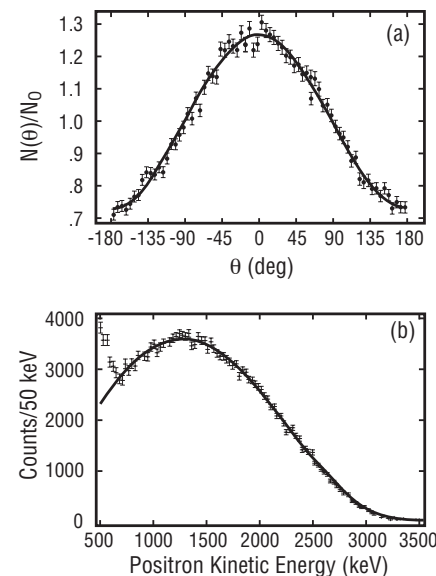
Figure 4. Rubidium-82 beta-decay data accumulated over a period of six hours. (a) The angular distribution obtained after binning the events as a function of positron-nuclear spin angle and integrated over positron kinetic energy above a threshold of 800 keV. The solid curve results from a cosine fit to the distribution, the nonzero amplitude resulting from parity-violation and indicating the successful confinement and polarization of rubidium-82 atoms in the TOP trap. (b) The differential positron kinetic energy spectrum obtained after integrating out the angular degree of freedom. The solid curve results from detailed Monte Carlo simulations that account for the full decay scheme for rubidium-82 decay and the details of the positron detection optics. The spectrum departs from a pure positron signal at low energy due to Compton scattering of 776 keV gamma rays from the 2$^+$ state of the krypton-82 daughter nucleus.

Summary & Outlook

In summary, we have successfully demonstrated the feasibility to exploit a TOP trap to explore fundamental symmetries such as parity violation in a new generation of beta decay experiments. We have a golden opportunity at Los Alamos to play an active and lead role in the next generation of fundamental symmetry experiments that exploit trapped radioactive atoms. The combination of nuclear chemistry, atomic-, nuclear-, and particle-physics capabilities inherent in this collaboration makes the possibility of precision and world-class experiments unique, and it is unlikely that such an experiment will take place elsewhere in the foreseeable future. The success of future experiments hinges on our ability to optimize and measure the polarization of the atom cloud and the design and construction of an efficient positron telescope capable of reducing background to an acceptable level. The necessary upgrades and improvements to our experiment will now be the focus of our attention. We hope also that successful measurements with polarized rubidium-82 will pave the way to a whole new class of experiments, including the possibility to exploit trapped lithium-8 atoms ... but that is another story!

References/Further Reading

[1] T. D. Lee and C. N. Yang, "Question of Parity Conservation in Weak Interactions," *Physical Review* 104, 254 (1956).

[2] C. S. Wu, E. Ambler, R. W. Hayward, *et al.*, "Experimental Test of Parity Conservation in Beta Decay," *Physical Review* 105, 1413 (1957).

[3] R. E. Marshak, Riazuddin, and C. P. Ryan, *Theory of Weak Interactions in Particle Physics, Monographs and Texts in Physics and Astronomy*, V24, R. E. Marshak, Ed. (Wiley, New York, 1969).

[4] J. Deustch and P. Quin, *Symmetry Tests in Semileptonic Weak Interactions, Precision Tests of the Standard Electroweak Model*, Advanced Series on Directions in High Energy Physics, V14, P. Langacker, Ed. (World Scientific, NJ, 1995).

[5] L. M. Chirovsky, W. P. Lee, A. M. Sabbas, *et al.*, "Directional Distributions of Beta-Rays Emitted from Polarized ^{60}Co Nuclei," *Physics Letters B* 94, 127 (1980).

[6] R. Guckert, X. Zhao, S. G. Crane, *et al.*, "Magneto-Optical Trapping of Radioactive ^{82}Rb Atoms," *Physical Review A* 58, R1637 (1998).

[7] A. Hime, S. J. Brice, A. Goldschmidt, *et al.*, "Fundamental Symemtries with Magnetically Trapped ^{82}Rb," in "Physics Division Progress Report, January 1, 1997–December 31, 1998," C. K. Crosby, Ed., Los Alamos National Laboratory report LA-13606-PR (May, 1999), pp. 102–105.

[8] W. Petrich, M. H. Anderson, J. R. Ensher, *et al.*, "A Stable, Tightly Confining Magnetic Trap for Evaporative Cooling of Neutral Atoms," *Physical Review Letters* 74, 3352 (1995).

[9] S. G. Crane, S. J. Brice, A. Goldschmidt, *et al.*, "Parity Violation Observed in the Beta Decay of Magnetically Trapped ^{82}Rb Atoms," *Physical Review Letters* 86, 2967 (2001).

Neutron Resonance Spectroscopy:
The Application of Neutron Physics to Shock and Material Physics

V. W. Yuan, J. D. Bowman, and
G. L. Morgan (P-23); R. L. Rabie,
D. J. Funk, and D. Graff (DX-2);
R. M. Boat and L. M. Hull (DX-3); and
C. E. Ragan (X-5)

Introduction

Neutron resonance spectroscopy (NRS) has developed a technique that uses Doppler-broadened neutron resonances to take fast snapshots of internal temperatures in dynamically loaded samples. The use of neutron resonances to measure temperatures in static samples was first pioneered at the Los Alamos Neutron Science Center (LANSCE) by British experimenters in the mid 1980s. The experimenters were working in conjunction with the Rolls-Royce company which was interested in measuring the internal temperature of turbine blades. Many of the detectors and experimental techniques for NRS were first developed in nuclear-physics symmetry experiments performed at Los Alamos in the late 1980s and early 1990s. The time scale for the NRS measurements is very fast: one microsecond (μs) or faster.

Examples of dynamically loaded systems studied by NRS are a metal through which a shockwave has just passed, high explosives behind the burn front after they have been detonated, or an explosively driven metal sheet jet (a jet of molten metal extruded past the neutron beam in the form of a flat sheet). The NRS temperature measurements are important because they provide temperature data that has previously been unavailable and which can lead to a better understanding of the equation-of-state for the dynamical systems under study. They also provide important tests of critical modeling calculations. In contrast to other techniques which seek to measure surface temperatures, NRS measures internal, volume temperatures.

What is a Neutron Resonance?

When a neutron that possesses an energy between 1 and 100 eV passes through a sample of atomic weight "A", at certain resonant energies the neutron can be captured by a nucleus of the sample to form an excited state in the "compound nucleus" of atomic weight "A+1". A detector placed downstream of the sample counts the neutrons that successfully pass through it. The instrument detects scintillation light from the interaction of the neutrons with lithium-6 within the detector and tags arriving neutrons by their energies; it does so by measuring the time of flight it takes for the neutrons to reach the detector.

In counting the number of neutrons versus energy, there will be absences or "resonant dips" (see Figure 1) in the observed spectra at the energies that the compound nuclei were formed. The depths of the resonances and their energies are unique to the materials the neutrons pass through. Different isotopes of the same material possess different resonances. NRS can take advantage of this uniqueness to localize temperature measurements in space by inserting a dopant that resides only in the region of interest. The shapes of these resonances depend on both intrinsic resonance properties and on the Doppler broadening produced by the motion of atoms in the target sample. By measuring the amount of broadening produced, NRS determines the temperature of the sample.
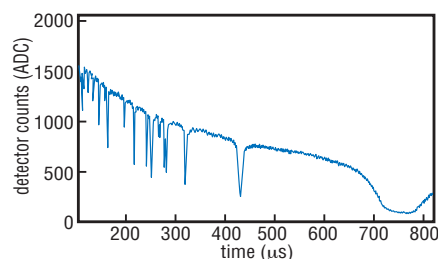

Figure 1. Transmission spectrum demonstrating resonance dips for neutrons passing through a silver sample. The dips occur at times (energies) at which neutrons are removed from the incident beam by neutron capture.

LANSCE Accelerator Provides Intense Source of Neutrons

To obtain the necessary statistics for accurate NRS temperature measurements, one requires a copious source of epithermal (1–100 eV) neutrons, and at Los Alamos, LANSCE generates the neutron source by the impinging its proton beam upon a spallation target. The linear accelerator at LANSCE accelerates protons to an energy of 800 MeV. The protons are then loaded into a circular storage ring (PSR) where they are accumulated and then released as a short, intense pulse which contains 30 trillion protons. The intense pulse of protons is directed at a uranium spallation target and, upon striking the target, produces many high-energy neutrons. These high-energy neutrons are then allowed to bounce around in a polyethylene moderator where they slow down to epithermal energies and then emerge into the NRS secondary beam line. By utilizing a specially designed uranium/ polyethylene target and moderator combination, we achieve neutron flux levels an order of magnitude larger than is presently available at the main LANSCE production target.

Time Scale for Temperature Determinations

We typically place our experimental sample in the secondary beam line at a distance of 1 m from the neutron-producing target. The shorter we make this distance, the faster the temperature snapshot we can take of the dynamic state of interest. We select a specific resonance of a chosen energy to use for the NRS measurement. The time resolution of the NRS measurement is determined by the transit time of the neutrons of the chosen resonance to traverse the sample. According to the formula:

$$\Delta t \propto \frac{L \Delta E}{E^{3/2}} \; , \qquad (1)$$

this transit time is directly proportional to the distance (L) from neutron source to sample. For the 21.1-eV resonance in tungsten-182 located 1 m from the neutron source, Figure 2 shows that the observed resonance width is 170 ns.
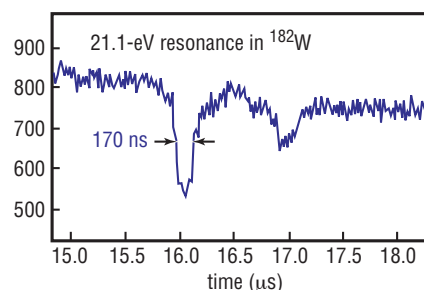

Figure 2. NRS data showing the time width of the 21.1-eV resonance in tungsten-182 for a sample located 1 m away from the source of neutrons.
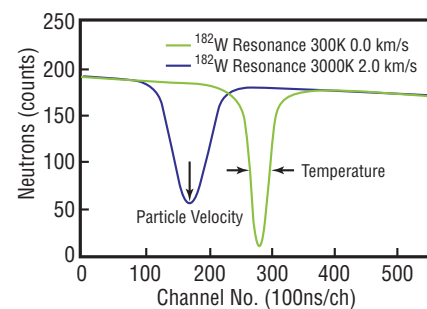

Figure 3. Expected change in the resonance line shape and position as a result of an elevation in temperature of the sample from room temperature to 3000 K and motion of the sample from being at rest to acquiring a velocity of 2 km/s.

Temperature Contribution to Resonance Line Shape

For sample temperatures above the Debye temperature (see Box 1), the resonance is broadened as a result of a motion of the target atoms which can be described by Maxwell-Boltzmann theory. The resulting resonance line shape is the convolution of the intrinsic Lorentzian line shape with an energy-dependent Gaussian $(\delta_{rms} \approx \sqrt{2EkT/A})$ from the Doppler contribution. If we transform a sample to a dynamic state of elevated temperature and put it into motion as well, then the result will be both a broadening and a shift in the centroid of the probing resonance. Figure 3 illustrates this expected behavior.
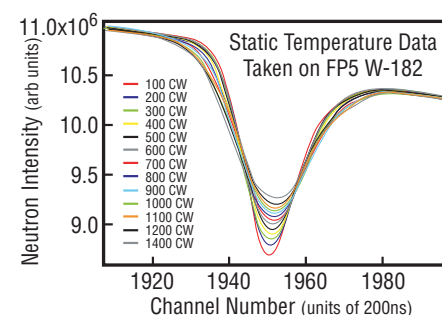

Figure 4. Measured variations in line shape for a tungsten-182 sample heated to different temperatures in a controlled oven.

Is the temperature broadening observable? The curves shown in Figure 4 are actual measured NRS data for a tungsten sample heated to the indicated temperatures in an oven. One can easily see the progressive change in line shape as the sample temperature is increased.

In the NRS experiment, the qualitative determination of the resonance broadening is complicated by the presence of other, nontemperature-dependent factors that also affect the resonance line shape. Most prominent are the effects due to moderation of the neutrons and due to phosphorescence in the

detector. The first effect occurs because the high-energy neutrons produced in the spallation source do not always slow down to a final epithermal energy in a fixed amount of time. Rather, because of the statistical process involved, the neutrons exhibit a distribution of slow-down (moderation) times. The end result is that neutrons of the same energy emerge from the moderator over a range of time, and this spread causes a smearing of the resonance.

Phosphorescence also plays a big part in the resonance line shape. When a neutron interacts with the detector, a rapid burst of light is given off. A property of the detector's scintillation medium is to continue emitting light (phosphorescence) for a long time after the initial burst. The accumulated effect of phosphorescence is to create a false background signal under the resonances that changes their observed depth. Figure 5 compares a resonance spectrum with and without the presence of phosphorescence. The data were taken with two different detector systems, one subject to phosphorescence and one where

phosphorescence was absent. Unfortunately, the one without phosphorescence cannot count rapidly enough to be used in NRS dynamic measurements. We removed the unwanted phosphorescence contribution from the data computationally.
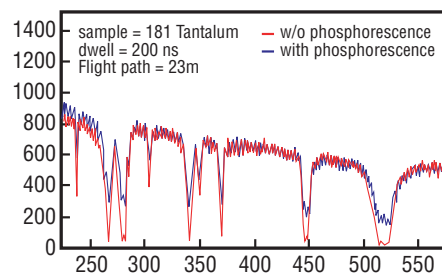

Figure 5. Comparison of resonance spectra from tantalum-181 with (blue curve) and without (red curve) the presence of phosphorescence.

A NRS Experiment: The Silver Sheet Jet

The dynamically formed silver sheet jet is one of the first systems in which NRS was used to measure temperatures. The sheet jet is formed by launching two metal liners that collide with each other to form an extruded sheet. The sheet jet passes at right angles across the neutron beam. The isotope silver-109 possesses a resonance at a neutron energy of 30.4 eV. We adjusted NRS timing so that the neutrons of this resonance passed through the sheet jet at the time of full jet formation— thus allowing broadening in the resonance to give a measure of internal jet temperature. As a reference against which to compare the dynamic experiment, we made a NRS measurement on a static silver sample of known thickness (1 mm) at a known temperature (room temperature).

Figure 6 shows the comparison between the static and dynamic resonance spectra. The plot of the sheet jet's 30.4-eV resonance in the dynamic shot is less deep because the thickness of the sheet jet is smaller than 1 mm. If one removes the influence caused by the difference in thickness between the

two experiments from the line shapes, then the resonance for the silver-sheet-jet experiment is also broader than the resonance in the static experiment. A fit to the data indicates an internal sheet-jet temperature of 875 K. When we performed temperature measurements on jets formed from liners with different initial profiles, we measured varying temperatures in the range of 815–1050 K. In an attempt to better understand the observed variations in
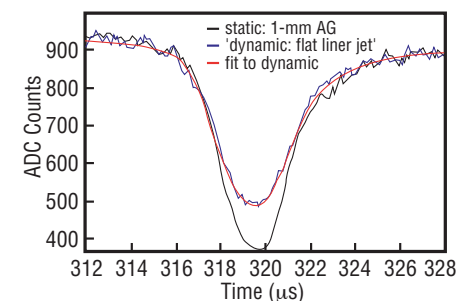

Figure 6. Comparison of 30.4-eV resonance in silver-109 for silver sheet jet (blue curve) to resonance line shape for static 1-mm sample at room temperature. Red curve shows fit to dynamic data which indicates a temperature of 875 K for a jet without variations in thickness.

temperature for the different sheet jets, we enlisted the help of the proton radiography (P-RAD) team at LANSCE. By firing the same sheet-jet shots at the P-RAD facility, we obtained proton radiographs of the sheet jet during different stages of its formation. Figure 7 shows a sequence of radiographs taken with 2 µs between radiographs. The unexpected presence of thickness variations (ripples) within the sheet jet is clearly apparent. An analysis of the data that takes the ripples into account results in a temperature that is approximately 100 K smaller than what was given by our original analysis.

Figure 7. Sequence of P-RAD radiographs that depict the evolution of the silver sheet jet. The interval between images is approximately 2 µs.

Temperature Behind the Passage of a Shock Wave in Molybdenum

An important area of research for shock-wave physics is determining the temperature behind the passage of a shockwave in a metal. Before now, no technique has been able to measure this important thermodynamic quantity for a shocked metal. We have performed NRS experiments to attempt this measurement. Figure 8 shows the set up for the NRS experiment. An aluminum flyer plate is explosively launched towards a block of molybdenum metal. The final velocity of the flyer plate (3.6 mm/µs) is great enough to initiate a shock wave in the molybdenum. At a distance between 1 mm and 2 mm into the molybdenum block, we doped a 1-mm-thick layer of the molybdenum with 1.7% tungsten-182. At 21.1 eV, the tungsten-182 possesses a resonance that can be used to measure the temperature in the doped layer immediately following the passage of the shock wave. A multipoint array of 61 detonators propels the aluminum flyer plate in a way that best maintains the flatness of the flyer plate. Approximately 0.33 µs after the flyer impacts the molybdenum, the shock wave has passed through the doped layer.

For it to be significant, the temperature measurement must be done in the short time window after the passage of the shock wave—but before the shock has had a chance to reach a boundary in the sample and to send back a release wave that alters the shocked state. NRS verifies that the measurement is made at the correct time by employing a separate laser diagnostic to observe when the shock breaks out of the back end of the molybdenum target. Figure 9 compares the 21.1-eV tungsten resonance after passage of the shock with the same resonance taken in the unshocked state. We are presently analyzing this data to extract a temperature.
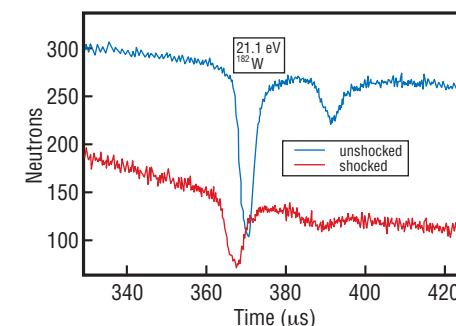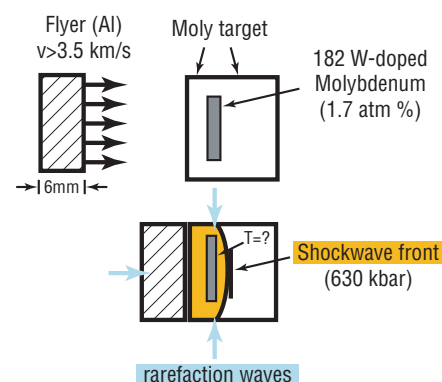
Figure 9. Resonance line shape for 21.1-eV resonance in tungsten-182 recorded before (blue curve) and immediately after (red curve) the passage of a shock wave.

Figure 8. Cartoon showing concept for the "Temperature Behind the Passage of a Shock" experiment. An aluminum flyer impacts a molybdenum target. Inside the molybdenum target is a region doped with tungsten-182. The challenge is to measure the temperature after the shock has passed through the doped region but before rarefaction waves come in from the boundaries.

Future NRS Applications

In addition to these temperature measurements, NRS has carried out scoping measurements for future experiments that will measure the temperatures at frictional interfaces in detonating high explosives. Imagine two materials which possess dissimilar sound speeds in contact with each other, as shown in Figure 10. If a shock wave is propagated (from left to right), then the different shock speeds in the two materials will cause the shock wave in one material to outrun the shock wave in the other. Further along the length of the sample there will be a region where the top material will be shocked while the bottom material will be unshocked at the same moment in time. The difference in particle velocities of the two materials will cause one to slide relative to the other; a question of interest to scientists is: what is the friction between the two surfaces? One way to get information about the friction is to measure the temperature at the interfacial surface between the two materials. We plan to isolate the interfacial surface in the region of interest by carefully placing a dopant with the resonance to be studied only in that region.
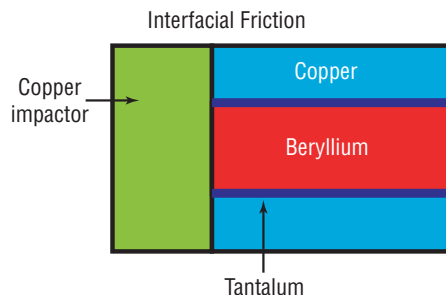

Figure 10. Cartoon showing the concept for an experiment to study interfacial friction between copper and beryllium after a copper impactor generates a shock wave in both materials. A thin tantalum layer at the interface isolates the temperature measurement to that region.

Figure 11. Improvement in knowledge of parameter space for high explosive equation-of-state that would result from a NRS temperature measurement with several hundred degrees of uncertainty.

The temperature behind the detonation wave in detonating high explosive is another case where little or no data presently exists. We plan to use NRS to measure high explosive samples doped with tungsten oxide to study the resonance broadening in the tungsten after the detonation of the high explosive has begun. Figure 11 compares the large region of uncertainty in equation-of-state space that now exists with a much more restricted region that would exist after a successful NRS measurement.

What appear to be pockets of undetonated high explosives or "dead zones" have been observed in radiographs of detonating explosives that "turn a corner." Figure 12 shows the locations of these pockets relative to the path of the detonation wave. The signature for the undetonated explosive is a difference in density from the burned regions of high explosive. But how can one confirm that these regions are truly undetonated explosive? One method is through the use of NRS. We have begun NRS scoping measurements for a set of experiments that will attempt to measure the temperature in

these "dead zones" at different times in the evolution of the detonation process.

Finally, on a beamline at the Manual Lujan Center neutron production target, we have begun a series of static measurements that utilize NRS to provide important information about the individual alloy content of uranium-niobium alloys. By measuring the depth of niobium resonances in alloy samples, we are able to quantitatively determine the average niobium content in the section of alloy through which the neutrons pass. Unlike in NRS

Figure 12. Schematic drawing of neutron beam used to measure temperature in a suspected "dead zone."
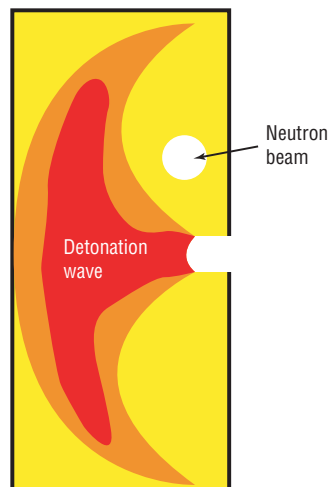
dynamic measurements, we perform NRS static measurements on a sample that is not changing on short time scales. Hence, the measurement uses many repetitive neutron pulses for accumulated statistics. As a reference to calibrate the measurement of a sample of unknown composition, we have made measurements on a range of alloy "sandwiches" put together from layers of prepared known amounts. The resonance curves shown in Figure 13 show the data from an alloy sample of unknown composition juxtaposed against a set of reference curves.
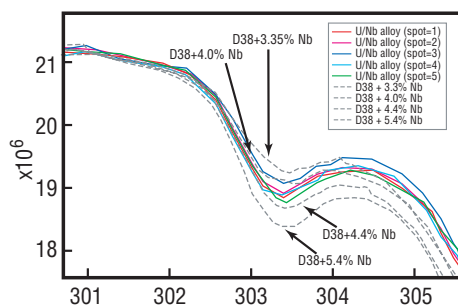

Figure 13. Change of depth of 193-eV resonance in niobium for different niobium content. Dashed lines represent reference data taken with fixed niobium content varying between 3.3 and 4.4 wt%. The colored squares represent data taken with a test U-Nb alloy sample of content to be determined.

Summary

NRS offers the possibility to determine temperatures on very fast time scales in systems where, previously, temperature information has been unavailable. Numerous applications important to shock physics and materials physics have either been performed or are being planned. We have successfully measured the temperature in a sheet metal jet, and variations that we detected in the measured temperatures have led to the discovery of thickness ripples in the jet. Work that would model the temperatures is currently ongoing in another division of Los Alamos National Laboratory. NRS has obtained successfully timed data in an experiment to measure the internal temperature of a metal immediately following the passage of a shockwave. No previous experiment has yet to measure this thermodynamic quantity important to understanding the equation of state for shocked metals. Future NRS experiments are planned to understand the physics of shock-induced friction and the equation of state of high explosives after they have been detonated.

Further Reading

B. E. Crawford, J. D. Bowman, P. P. J. Delheij, *et al*., "Neutron Resonance Spectroscopy of [106]Pd and [108]Pd from 20 to 2,000 eV," *Physical Review C* 58, 729 (1998).

D. J. Funk, B. W. Asay, J. L. Mace, *et al*., "Dynamic Measurement of Temperature using Neutron Resonance Spectroscopy (NRS)," Shock Compression of Condensed Matter (Amherst, July 1997).

L. Y. Lowie, J. D. Bowman, B. E. Crawford, *et al*., "Neutron Resonance Spectroscopy of [107]Ag and [109]Ag," *Physical Review C* 56, 90 (1997).

New Limit for the Lepton-Family-Number Nonconserving Decay μ⁺→ e⁺γ

M. D. Cooper [Spokesman],
M. L. Brooks, G. W. Hart, G. E. Hogan,
M. A. Kroupa, L. J. Marek, and
R. E. Mischke, (P-25); S. C. Wright
(Chicago); P. S. Cooper (Fermilab);
Y. K. Chen, M. Dzemidzic, A. Empl,
E. V. Hungerford III, K. A. Lan,
B. W. Mayes II, and W. H. von Witsch
(Houston); J. E. Knott, K. M. Stantz,
and J. J. Szymanski (Indiana);
C. C. H. Jui and E. B. Hughes
(Stanford); C. A. Gagliardi,
R. E. Tribble, X. L. Tu, and
L. A. Van Ausdeln (Texas A&M);
D. D. Koetke, R. Manweiler, and
T. D. S. Stanislaus (Valparaiso);
K. O. H. Ziock (Virginia); and
L. E. Piilonen (VPI)

Introduction

It is generally believed that the standard model that describes the electroweak force is a low-energy approximation to a more fundamental theory. Yet there is no clear experimental evidence either to guide its extension to additional physical processes or to predict the model parameters. One of these model assumptions is lepton family-number conservation, which has been empirically verified to high precision but is not a consequence of a known theory. Lepton family-number conservation is the idea, based on experimental observation, that the property of being an electron or a muon must be maintained even when particles transform through reactions; neutrino oscillations would be the first evidence that this principle is not absolute. Indeed many theoretical extensions to the standard model allow lepton-family-number violation within a range that can be tested by experiment.[1]

The predictions of the rate for a given family-number nonconserving process vary among these extensions, and the most sensitive process depends on the model. Many possibilities have been explored, and highly-precise experimental limits exist for a wide variety of processes. Of these, the rare muon decays have some of the lowest branching-ratio (BR) limits because muons can be copiously produced and have relatively long lifetimes. A BR is the fraction of a decay into a particular channel compared to all possible decays, and in the case of the muon, there is only one major mode, a muon decaying into an electron and two neutrinos $[\mu^+ \rightarrow e^+\nu_e\nu_\mu]$; this mode is referred to as normal muon decay. The rare process, $\mu^+ \rightarrow e^+\gamma$, is the classic example of a reaction that would be allowed except for muon and electron number conservation; there are no neutrinos to carry the family characteristic. The previous limit[2] is BR($\mu^+ \rightarrow e^+\gamma$) $< 4.9 \times 10^{-11}$. This decay is particularly sensitive to the standard model extension that involves supersymmetric particles.[3]

We report here a new limit for the BR of the decay $\mu^+ \rightarrow e^+\gamma$ from the analysis of data taken by the MEGA experiment at the Los Alamos Meson Physics Facility, LAMPF (renamed LANSCE). The dominant source of background in high-rate $\mu^+ \rightarrow e^+\gamma$ experiments is random coincidences between high-energy positrons from the primary decay process, $\mu^+ \rightarrow e^+\nu_e\nu_\mu$, and high-energy photons from internal bremsstrahlung (IB), $\mu^+ \rightarrow e^+\gamma\nu_e\nu_\mu$. IB is normal muon decay modified by the emission of a photon by one of the charged particles. MEGA isolates the $\mu^+ \rightarrow e^+\gamma$ process from the background by identifying the signature of the process: a 52.8-MeV photon and a 52.8-MeV positron that are aligned back to back, in time coincidence, and arise from a common origin. These kinematic constraints arise from the conservation of momentum and energy for a particle at rest decaying into two others.

Therefore, quality position, timing, and energy information are crucial. In comparison to the detector used to set the previous limit[2], the MEGA detector sacrifices larger acceptance and efficiency for better resolution, background rejection, and rate capability. It has been described in several papers[3,4] and will be discussed only briefly below.

Experiment

Muons for the experiment are provided by a surface muon beam at the stopped-muon channel at LAMPF. Protons from the accelerator produce pions, and if these pions stop very close to the surface of the production target, they will decay to muons that can be transported and focused into a beam by a magnetic channel. The muons, which are nearly 100% polarized, are brought to rest in a 76 μm Mylar foil, centered in the 1.5-T magnetic field of a superconducting solenoid; see Figure 1. The angle between the muon beam and the normal to the target plane is 82.8° so that the stopping power in the beam direction is increased, while the thickness of material presented to the decay positrons is minimized. A sloped target plane also extends the stopping distribution along the beam, enhancing the sensitivity of the apparatus to the measurement of the decay position, which is the intersection of the outgoing photon and positron trajectories with the target foil.

The positron and photon detectors are placed in the 1.8-m diameter and 2-m axial-length bore of the solenoid. Decay positrons from stopped muons are analyzed by a set of high-rate, cylindrical multiwire-proportional chambers (MWPC) that surround the target. A MWPC is a detector that measures the position of a particle that passes through it; ours have positively charged anode wires and grounded cathode foils. The set consists of seven MWPCs arranged symmetrically outside of a larger MWPC, coaxial with the central axis of the beam. These MWPCs have a thickness of 3×10^{-4} radiation lengths (an amount of matter that will induce with high probability the radiation of a photon by a charged particle), which minimize energy loss while maintaining high acceptance and efficiency under the stopping rates of the experiment.[3] The azimuthal location of a passing charged particle is determined by anode wire readout. The position of an event in the axial direction is obtained from the signal induced on stereo strips scribed on the inner and outer cathode foils of the MWPCs. The positrons come to rest at either end of the

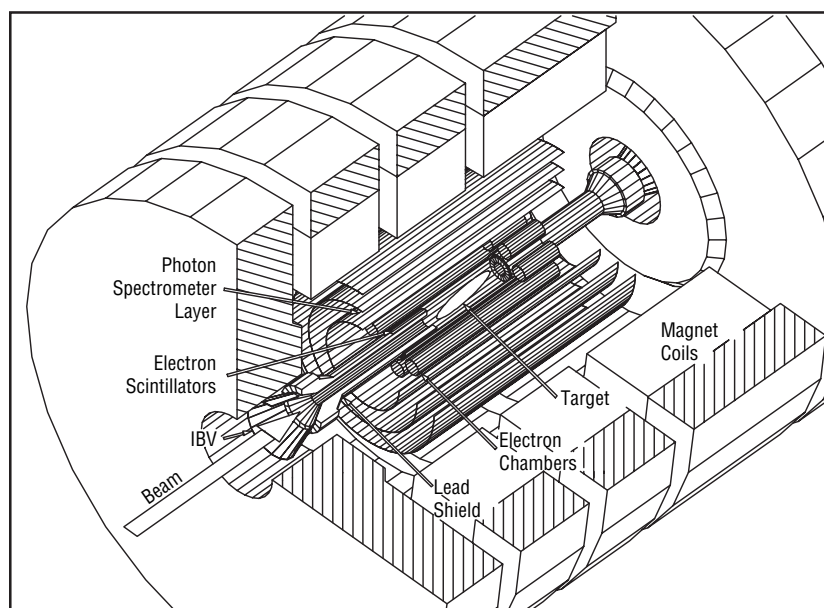**Figure 1. A simplified cutaway view of the MEGA apparatus. The detector is mounted inside a superconducting solenoid with a 1.5-T field. The muons enter along magnetic field and stop in the target. Positrons from muon decays are detected in the eight cylindrical wire chambers and the cylindrical arrays of scintillators surrounding the beam pipes. The three large cylinders are pair spectrometers for photon detection.**

spectrometer in thick, high-Z material after passing through a barrel of 87 scintillators used for measuring the time of passage of the positrons. Scintillators detect the passage of a charged particle by emitting visible light in proportion to the energy deposited in them. Outside these MWPCs, photons are detected in one of three coaxial, cylindrical pair spectrometers.[4] A pair spectrometer is a device that measures the kinematic properties of the electron and positron pair that may be produced when a photon interacts with matter. Each pair spectrometer consists of a scintillation barrel, two 250-μm Pb conversion foils that sandwich a MWPC, and three layers of drift chambers (similar to a MWPC), with the innermost having a delay-line readout to determine the axial position of a hit. The delay line determines the axial position by comparing the propagation time of the signal to each end. In this case, the line is highly folded to make the velocity of propagation slow, thus improving the precision of the position.

The hardware trigger indicates the occurrence of an interesting event; it consists of two stages of specially-constructed high-speed logic circuits, and is fed signals from each of the three photon spectrometers.[5] By using pattern recognition programmed on the basis of Monte Carlo (MC) simulations, the trigger requires an electron-positron pair that can be potentially reconstructed as arising from a photon of at least 37 MeV. Because the instantaneous muon stopping rate in this experiment is 250 MHz, with a macroscopic duty cycle of 6%–7%, the positron chambers and scintillators have too many hits at any given time to be part of the trigger. Signals are digitized in FASTBUS (an electronics module that meets proscribed circuit standards) with 6% dead time at the instantaneous trigger rate of 18 kHz. Between each macropulse (120 Hz) of the accelerator, the data are read into one of eight networked workstations, where an on-line algorithm reduces the data rate for storage on magnetic tape to roughly 60 Hz.

Each event is characterized by five kinematic parameters: photon energy (E_γ), positron energy (E_e), relative time between the positron and photon ($t_{e\gamma}$) at the muon decay point, opening angle ($\theta_{e\gamma}$), and photon traceback angle ($\Delta\theta_z$). These properties, in conjunction with the detector response, determine the likelihood that a signal is detected. The determination of the detector acceptance (the fraction of all decays observed by the detector) and response functions (the distribution of measured values for particle properties of a fixed value) relies on a MC simulation to extrapolate from experimental input to the kinematic region of the $\mu^+ \rightarrow e^+\gamma$ signal. To verify the MC calculation, a number of auxiliary measurements are performed. The two most important are the $\pi_{stopped}p \rightarrow \pi^0 n \rightarrow \gamma\gamma n$ process and the prompt $e\text{-}\gamma$ coincidence signal from the IB decay.

Figure 2. The E_γ spectrum from photons converting in the outer layer of lead. The data points are produced by stopping pions in CH_2 via the reaction $\pi_{stopped}p \rightarrow \pi^0 n \rightarrow \gamma\gamma n$, scaled from 54.9 to 52.8 MeV. The curve is the response function generated from the MC and used in the analysis of the $\mu^+ \rightarrow e^+\gamma$ data.

Pion capture at rest on hydrogen produces photons with energies between 54.9 and 83.0 MeV, and such events have been collected using a loose-coincidence trigger. Under the condition that the two photons have a minimum opening angle of 173.5°, these photons are restricted to have energies close to 54.9 and 83.0 MeV respectively and a spread much smaller than the detector response. Figure 2 shows the experimental line shape for the 54.9 MeV photon for conversions in the outer Pb foils of the three pair spectrometers, scaled to 52.8 MeV. The curve is the response function generated from the MC that is used in the analysis of the $\mu^+ \rightarrow e^+\gamma$ data. The central energy and width of the distribution are well reproduced.
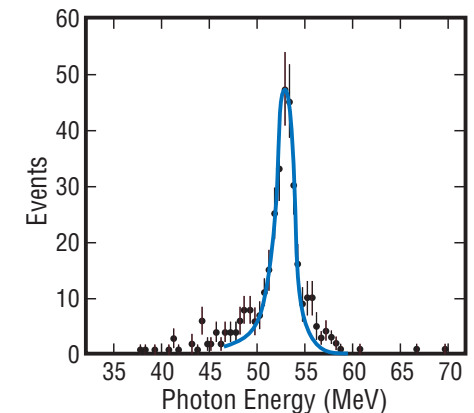
We attribute differences in the low-energy tail to charge exchange of in-flight pions from carbon in the CH_2 target and discrepancies in the high-energy tail to contributions from other opening angles due to special difficulties in conversion-point identification for the 83.0-MeV photon. The measured and simulated line shapes agree better for conversions in inner Pb foils, which have worse resolution. The energy resolutions are 3.3% and 5.7% full width at half maximum (FWHM) at 52.8 MeV for conversions in the outer and the inner Pb layers, respectively. The π^0 decays also provide the time response between the two photons, which is reasonably characterized by a Gaussian with a $\sigma = 0.57$ ns for each photon.
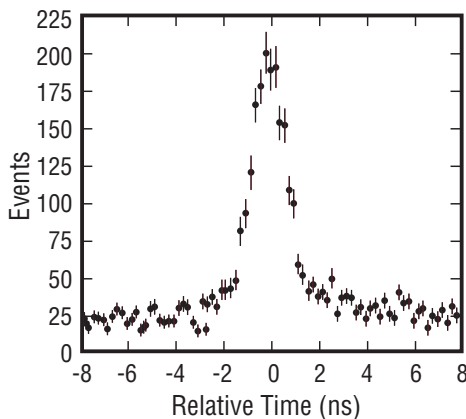
Observation of the IB process demonstrates that the apparatus can detect coincident e-γ events. At nominal beam intensity, this process is completely engulfed by random coincidences. Figure 3 shows the spectrum for $t_{e\gamma}$, with the beam intensity reduced by a factor of 60, the magnetic field lowered by 25%, and the $\mu^+ \rightarrow e^+\gamma$ on-line filter suppressed. The peak shown is for all energies of the detected decay products. The area of the peak is very sensitive to the exact acceptances of the detector at its thresholds and can be calculated by MC simulation to better than a factor of two. If the data and the simulation are restricted to $E_\gamma > 46$ MeV, $E_e > 40$ MeV, and $\theta_{e\gamma} > 120°$, the BR is reproduced within 20%. The uncertainties of

the IB normalization do not affect the precision of the $\mu^+ \rightarrow e^+\gamma$ acceptance because the IB prefers to occur near the energy-cut boundaries while the $\mu^+ \rightarrow e^+\gamma$ process occurs well above these cuts. The shape of the peak can be characterized by a Gaussian with a $\sigma = 0.77$ ns. The dominant contributor is the photon timing, as measured in the stopping-pion experiment, which must be scaled down from about 70 to 40 MeV for the comparison. At 52.8 MeV, the MC simulation indicates the photon-positron resolution is $\sigma = 0.68$ ns.

In the IB and $\mu^+ \rightarrow e^+\gamma$ processes, the origin of the photon is defined to be the intersection of the positron with the target. The photon traceback angle, $\Delta\theta_z$, specifies the difference between the polar angles of the photon as determined from the line connecting the decay point to the photon-conversion point and from the reconstructed $e^+ - e^-$ pair. The resolution of $\Delta\theta_z$ is dominated by multiple scattering of the pair in the Pb converters. The observed response for inner and outer conversion layers for the IB process is in excellent agreement with the

MC simulation. The traceback resolutions appropriate for the $\mu^+ \rightarrow e^+\gamma$ analysis are $\sigma = 0.067$ and 0.116 rad for conversions in the outer and the inner Pb layers, respectively.

The resolution of E_e is determined by the slope of the high-energy cut-off edge in the spectrum of the decay, $\mu^+ \rightarrow e^+\nu_e\nu_\mu$. It depends on the "topology" of the track, which is determined by the number of loops these particles make in the magnetic field between the target and scintillator and the number of chambers they traverse. The E_e spectrum is shown in Figure 4 for one of three topology groups. The
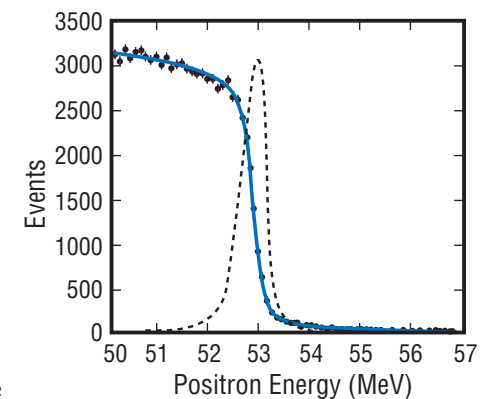

Figure 4. The E_e spectrum from $\mu^+ \rightarrow e^+\nu_e\nu_\mu$ extracted from full rate data for the middle topology group. The solid curve is the fit used to extract the line shape (dashed curve).

Figure 3. Values for $t_{e\gamma}$ from the process $\mu^+ \rightarrow e^+\nu_e\nu_\mu$ under the conditions of reduced rate and magnetic field.

MC line shape is characterized near the centroid by a Gaussian and in the tails by different powers of the deviation from the central energy. To extract the response function from the data, this line shape is convoluted with the spectrum from normal muon decay, modified by detector acceptance and unphysical "ghost" tracks. Ghost tracks are a high-rate phenomenon and are reconstructions made from the fragments of several physical tracks. They are the source of events well above the kinematic limit for the positron energy. The solid curve in Figure 4 is the fit, and the dashed curve is the corresponding line shape. The central Gaussians of the three topology groups have $\sigma = 0.21$, 0.23, and 0.36 MeV.

There is no way to measure the response function for $\theta_{e\gamma}$. The MC simulation is relied upon to produce this distribution and gives the FWHM for $\cos(\theta_{e\gamma})$ as 1.21×10^{-4} at 180°. Given helical tracks, knowing the location of the target is critical to obtaining the correct absolute value of $\theta_{e\gamma}$, and the mechanical survey provides the most accurate measurement for the analysis.

Analysis

The data for this experiment have been taken in three calendar years, 1993–95. The full data set is based on 1.2×10^{14} muon stops collected over 8×10^6 s of live time and results in 4.5×10^8 events on magnetic tape. These events are passed through a set of computer programs that reconstruct as many as the pattern-recognition algorithms can interpret. The programs include physical effects such as mean energy loss in matter and nonuniformities in the magnetic field. The size of the data sample is reduced by cutting out events of poor quality or whose kinematic properties are far from those of a $\mu^+ \rightarrow e^+\gamma$ event. Events are required to satisfy separate χ_ν^2 (quality) cuts on the positron and photon fits and loose cuts on the signal kinematics ($E_e > 50$ MeV, $E_\gamma > 46$ MeV, $t_{e\gamma} < 4$ ns, $\cos(\theta_{e\gamma}) < -0.9962$, and $\Delta\theta_z < 0.5$ rad). Events in which the positron momentum vector at the decay point appears to lie within 5° of the plane of the target are discarded. After roughly one year of computing on a farm of UNIX workstations, the data set has been reduced to 3971 events that are fully reconstructed and of continuing interest. This sample is large enough to allow a study of the background. To remove incorrectly reconstructed events, the images of the photon showers in the pair spectrometers are manually scanned. The efficiency for keeping real photons is monitored by mixing about 500 52.8-MeV MC events into the sample in a nonidentifiable way and finding that 91% of the MC events pass, whereas only 73% of the data events are selected. Most of the excess data events that are rejected consist of two overlapping low-energy photon showers that have been reconstructed by the analysis program as a single high-energy shower.

The acceptance of the apparatus— which includes geometrical, trigger, and pattern-recognition constraints—is obtained by simulating 1.2×10^7 unpolarized $\mu^+ \rightarrow e^+\gamma$ decays and finding that 5.2×10^4 events survive processing by the same codes used for the data analysis. Thus the probability that a $\mu^+ \rightarrow e^+\gamma$ decay would be detected is 4.3×10^{-3}. This value is reduced by 9% for the inefficiency of manual scanning. The acceptance is further reduced by 20% to account for inadequacies in the MC simulation that overestimate the acceptance. The shortcomings primarily involve cross talk amongst channels of electronics and are estimated by comparing the images of many data and MC events to contribute only 4% to the overall uncertainty in the acceptance. The total number of muon stops is determined by calibrating the rates in the positron scintillators to a known muon flux. After correcting for dead time, the single event sensitivity for the experiment is $2.3 \pm 0.2 \times 10^{-12} = 1/N_\mu$, where N_μ is the number of useful stopped muons.

Results

The determination of the number of $\mu^+ \rightarrow e^+\gamma$ events in the sample is evaluated using the likelihood method described in the analysis of previous experiments.[6] This likelihood analysis is analogous to a least-squares fit of data that contain two signals and a background but depends upon the properties of five independent variables. The analysis is carried out by evaluating the kinematic properties of each event and estimating the probability that that event is either $\mu^+ \rightarrow e^+\gamma$, IB, or background. The analysis uses the response function of the detector to each possibility. The total number of events is fixed at 3971. The number of $e^+\gamma$ events, $N_{e\gamma}$, and the number of IB events, N_{IB}, are treated as independent variables.

The likelihood function evaluates the statistical separation between signal, IB, and background; it is maximal at the preferred values of the independent variables. To observe the impact of quality constraints in the pattern recognition, they have been relaxed to produce a sample three times larger. One event emerges with a large signal probability and is significantly separated from the distribution. However, this event has a large positron χ_ν^2, indicative of a ghost track. The adopted constraints produce a sample with considerably less background. The result presented below is stable against changes in the constraints; e.g., the higher value of $N_{e\gamma}$ is compensated by a corresponding increase in acceptance. The contours of constant likelihood are shown in Figure 5. The peak of the likelihood function is at $N_{e\gamma} = 0$ and $N_{IB} = 30 \pm 8 \pm 15$. The systematic error assigned to N_{IB} is due to the uncertainty in the shape of the background time spectrum after the events are filtered by the on-line program. The expected number of IB events is $36 \pm 3 \pm 10$, where the systematic error is due to finite resolution effects across the cut boundaries.

The 90% confidence limit is the value for $N_{e\gamma}$ where 90% of the area of the likelihood curve lies below $N_{e\gamma}$ and N_{IB} is maximal. This value is $N_{e\gamma} < 5.1$. Therefore, the limit on the BR($\mu^+ \rightarrow e^+\gamma$) is 5.1/ N_μ = 1.2×10^{-11} with 90% confidence. In comparison to the previous experimental limit[2], this result represents a factor of 4.1 improvement. The previous experiment would have had 100 background events at the same BR instead of the 2 found here. The background level of 2 events is the mean value of a Poisson statistical distribution and may be made up of the probability tails of many events. This improvement further constrains attempts to build extensions to the standard model.[1] Grand-unified supersymmetric extensions to the standard model have many parameters, and this new limit on $\mu^+ \rightarrow e^+\gamma$ increases the appropriate masses by 40%.
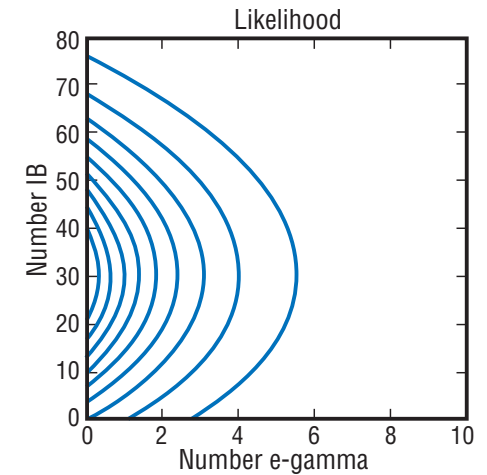

Figure 5. The contours of constant likelihood for the processes $\mu^+ \rightarrow e^+\gamma$ and $\mu^+ \rightarrow e^+\nu_e\nu_\mu$. The best estimate for the number of events in the final sample of each type is given by the coordinates where the likelihood function is a maximum.

References

[1] R. Barbieri, L. Hall, and A. Strumia, "Violations of Lepton Flavour and CP in Supersymmetric Unified Theories," *Nuclear Physics B*, 455, 219–251 (1995);

N. Arkani-Hamed, H-C. Cheng, and L. Hall, "Flavor Mixing Signals for Realistic Supersymmetric Unification," *Physical Review D*, 53, 413–436 (1996);

T. Kosmas, G. Leontaris and J. Vergados, *Progress in Particle and Nuclear Physics*, 33, 397 (1994) and included references.

[2] R. Bolton, *et. al.*, "Search for Rare Muon Decays with the Crystal Box Detector," *Physical Review D*, 38, 2077–2101 (1988).

[3] M. D. Cooper, *et. al.*, "Construction and Performance of MEGA's Low-Mass, High-Rate Cylindrical MWPCs," *Nuclear Instruments and Methods in Physics Research A*, 417, 24–49 (1998).

[4] M. Barakat, *et. al.*, *Nuclear Instruments and Methods in Physics Research A*, 349, 118 (1994).

[5] Y. Chen, *et. al.*, *Nuclear Instruments and Methods in Physics Research A*, 372, 195 (1996).

[6] W. W. Kinnison, *et. al.*, "Search for $\mu^+ \to e^+ \gamma$," *Physical Review D*, 25, 2846–2868 (1982).

The PHENIX Detector Program at RHIC

V. Armijo, J. Boissevain, M. Brooks, D. Clark, A. G. Hansen, G. Hart, D. Lee, M. Leitch, M. Liu, J. Lopez, L. Marek, P. McGaughey, R. Mischke, B. Montoya, J. Moss, M. Simpson, W. Sondheim, J. P. Sullivan, R. Towell, and H. van Hecke (P-25); J. B. Archuleta, J. R. Archuleta, M. Cafferty, M. Echave, S. Robinson, and G. Smith (NIS-4); C. Britton, V. Cianciolo, M. Emery, N. Ericson, R. Lind, T. Moore, F. Obenshain, F. Plasil, K. Read, P. Stankus, A. Wintenberg, and G. Young (Oak Ridge National Laboratory); R. Savino (Brookhaven National Laboratory); A. Baker, W. Bland, A. Brown, D. Isenhower, C. Kuberg, J. Qualls, M. Sadler, and M. Shaw (Abilene Christian University); R. K. Choudhury, B. V. Dinesh, S. S. Kapoor, and A. Mohanty (BARC); M-S. Chung, B. Hong, W. Y. Jang, M. J. Kweon, and K. S. Sim (Korea University); H. Enyo and K. Imai (Kyoto University); D. Brown, A. Hoover, G. Kyle, V. Papavassiliou, S. Pate, and C. Velissaris (New Mexico State University); T. Ichihara, M. Ishihara, K. Kurita, Y. Mao, J. Murata, N. Saito, H. Sato, T-A. Shibata, M. Sugioka, and A. Taketani (RIKEN); T. Shiina (University of Alabama, Huntsville); J. Chang (University of California, Riverside); B. Bassalleck, N. Bruner, D. Fields, S. Klinksiek, B. Lewis, and T. Thomas (University of New Mexico); J. Newby, K. Pope, and S. Sorensen (University of Tennessee); C. Maguire (Vanderbilt University); and J.-H. Kang, D. Kim, and S. S. Ryu (Yonsei University)

Introduction

The relativistic heavy-ion collider (RHIC), located at Brookhaven National Laboratory (BNL), began operation in June 2000, with the collisions of co-rotating beams of high-energy gold ions at a center-of-mass energy of 140 GeV · A GeV. The principal goal of RHIC is to create extraordinarily hot and dense matter in the laboratory—matter such as is believed to have existed fleetingly in the first second following the big-bang beginning of the universe.

The sequence of pictures shown in Figure 1 visualizes this goal schematically. At the top, highly relativistic gold ions, shown as Lorentz-contracted disks, head towards each other and collide to form a new state of matter, shown in yellow. This matter is so hot and dense that the fundamental constituents of the protons and neutrons of the atomic nuclei— quarks and gluons—are free to roam over a volume the size of a gold nucleus. This hypothetical state of matter is termed the quark-gluon plasma (QGP).

Demonstration of its creation in the laboratory and determination of its physical characteristics are the raison d'être of RHIC.

A second, very compelling program for which the RHIC collider is uniquely suited is the study of the spin structure of the nucleon. Thanks to technical developments made during the past 15 years, it is now possible to accelerate polarized protons in synchrotrons and maintain their polarization in storage rings. Thus with a modest investment in spin-manipulating equipment, RHIC will, for the first time, be able to produce collisions between polarized protons in the multi-hundred GeV range.

The spin structure of the nucleon, one of the least understood aspects of nucleon structure, has been extensively investigated with high-energy electron- and muon-proton collisions for the past ten years.

However, many features of spin structure are intrinsically inaccessible with electromagnetic probes. The contribution to the spin the nucleon from gluons, the mediators of the strong interaction, is such a feature. Thus polarized-proton collisions will open significant new terrain in the examination of the structure of the nucleon at small-distance scales.
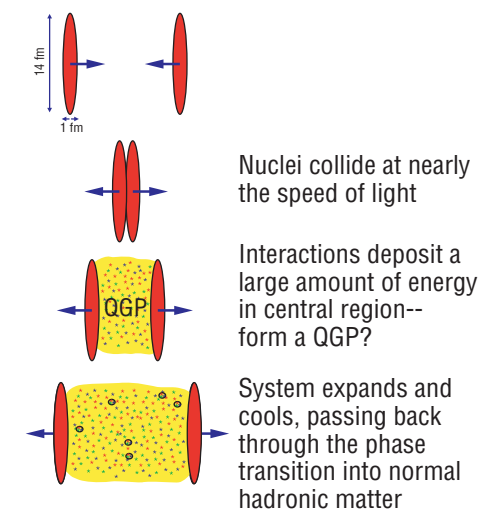
Figure 1. Schematic evolution of a high-energy nucleus-nucleus collision. Starting at the top, we see two Lorentz-contracted nuclei move toward each other, collide, and the separation of the residual fragments in the bottom frame. The yellow region remaining is the hypothetical quark-gluon plasma.

Nuclei collide at nearly the speed of light

Interactions deposit a large amount of energy in central region-- form a QGP?

System expands and cools, passing back through the phase transition into normal hadronic matter

Los Alamos National Laboratory's Role

The Physics Division's nuclear-physics program at Los Alamos National Laboratory (LANL) has been at the forefront of experimental work at high-energy accelerators since the mid 1980s. This included major involvement in the first high-energy heavy-ion collisions at CERN's (European Center for Nuclear Research) superproton synchrotron, and a few years later, the series of proton-nucleus experiments at Fermilab that led to the 1998 American Physical Society Bonner Prize in Nuclear Physics. These off-site efforts were clearly identified as LANL-led experiments. Much of the detector hardware, including electronic and data handling systems was designed and built at Los Alamos. LANL also hosted the subsequent analysis and interpretation of the data as well as the writing of the scientific papers.

Physics Division played a central role in the RHIC program, beginning in the early 1990s when collaborations were being formed to create the very large and technically complex devices required to diagnose ultra-relativistic heavy-ion collisions. In the years 1991–93, we helped form the collaboration and the physics program of the PHENIX detector (Pioneering High Energy Nuclear Interaction eXperiment), one of two large multipurpose collider detectors at RHIC. As with past off-site programs, LANL leadership is evident within the collaboration. We are the lead institution of two of the most technically challenging subsystems within he PHENIX detector, the muon spectrometer—largest of all the PHENIX detectors and the multiplicity and vertex detector (MVD), physically the smallest detector, but itself composed of some 35,000 channels of electronic readout.

In the mid 1990s, Physics Division initiated collaboration with physicists from the RIKEN Institute in Japan. This collaboration led to a significant investment of Japanese funding in the PHENIX detector (the south muon arm) and in the specialized magnets required to permit the acceleration and storage of polarized protons in RHIC. Thanks to this investment, the RHIC spin program became a reality. The construction of both the muon tracking system and the MVD required extensive interaction between Physics Division physicists

and professional engineers during the conceptual design stages. Much of the engineering expertise was found in Los Alamos; within LANL in Engineering Sciences and Applications (ESA) Division, Nonproliferation and International Security (NIS) Division, and at HYTEC, a LANL spin-off company. Production of actual components involved Space Instrumentation and System Engineering Group (NIS-4), Subatomic Physics Group (P-25) personnel working at facilities both at LANL and BNL, and an array of outside institutions including the University of New Mexico (UNM); New Mexico State University (NMSU); the University of California, Riverside; and the Bahbba Atomic Energy Institute of India, as well as numerous firms in the private sector.

Muon Tracking System Project

The muon tracking system consists of three planes of segmented-cathode multiwire proportional chambers, a technology developed in the Los Alamos Meson Physics Facility (LAMPF) program. Readout is accomplished by accurate determination of the image charge on cathode strips—hence the name cathode-strip chamber (CSC). Space points are determined by the three planes of CSCs that fix the radius of curvature of the tracks of charged particles moving through the magnetic field of the two PHENIX muon magnets. This measurement then leads to an accurate determination of the momentum of the particle. Figure 2 illustrates this concept, showing an elevation view that emphasizes the two-muon arms for the PHENIX detector with a simulated nucleus-nucleus collision.

We had to overcome a number of technical challenges to realize the goals of this project. First, the PHENIX muon magnets are very large, but with limited space available to contain the precision readout of electronic signals. The CSCs are divided into octants. The octants of the Station 3 chambers

(largest planes at the extreme left and right in Figure 2) are about two meters tall, the largest CSCs ever built. Second, the middle CSCs (Station 2) are required tobe lightweight in order to minimize the degradation of the energy of charged particles whose momentum is measured by the tracker. To achieve this, the cathodes are formed from etched metalized Mylar foils, a technology pioneered at Los Alamos. The cathodes of Stations 1 and 3 are routed copper foils laminated to foam-composite boards.

The electronic readout of the CSCs is a particularly challenging task. In order to minimize electronic noise, the first stage of amplification must be very close to the chambers. This imposed severe electrical and mechanical constraints on the tracker, which is entirely contained within the two muon magnets. Nevertheless, by clever engineering design, some 20,000 channels of cathode readout were successfully constructed into each of the two muon-arm trackers.

The total project cost of the tracker is approximately $12 M; $7.3 M
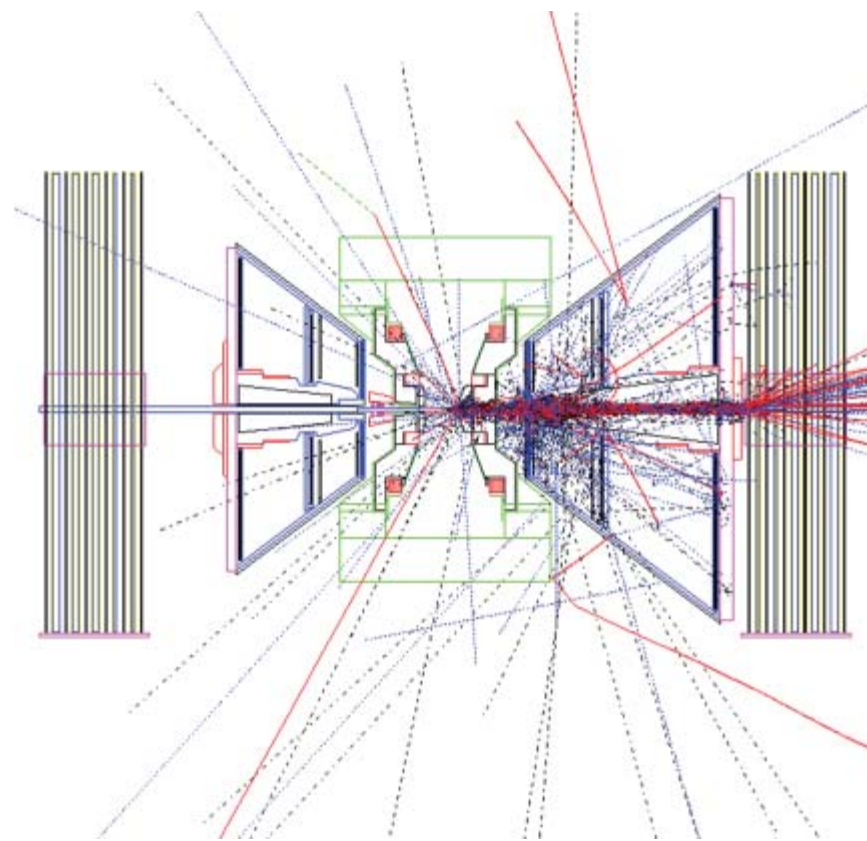
Figure 2. Elevation view of the PHENIX muon arms superimposed with particle tracks from a simulated 100 GeV · A nucleus-nucleus collision. The muon tracker consists of three planes of CSCs that are located inside the two muon-arm magnets (trapezoidal elements on the left and right sides of the picture). To set the scale, the vertical structures to the left and right of the picture are 11-meter-tall plates of the muon identifier.

has come through the LANL financial system. The bulk of the remaining funding has been associated with the LANL-run facility at BNL. The construction project was successfully completed for the PHENIX south arm in

January 2001. The tracking system for the north arm (for which funding arrived at a later date) is currently under construction at assembly factories at LANL, UNM, NMSU, and BNL. It will be installed and commissioned during 2002.

Physics with the PHENIX South Muon Arm during 2001

The completion of the south muon arm is an enormous success for LANL, achieved in the face of significant technical, financial, and temporal obstacles. It has been commissioned and will be ready for physics during the next running period of RHIC, currently scheduled to start in June 2001. Figure 3 shows the south arm in its staging area in early January 2001.

With collisions of gold ions at 200 A · GeV, RHIC presents a capability to create hot dense hadronic matter in the laboratory, which has never before been achieved. Thus, is it difficult to speculate what measurements to be made in the next few months will turn out to be most exciting. With its unique capability to detect muons, the PHENIX detector is in an enviable position among the four RHIC detectors.

A much-anticipated signal for the formation of the QGP is the suppression of the J/ψ resonance. This meson, composed of a charmed and anticharmed quark, is created readily in high-energy collisions. In a QGP however, very general arguments lead to the conclusion the J/ψ would be unstable, dissociating quickly into other particles.

Thus one of the most robust signatures of the successful formation of the QGP is the absence of the J/ψ most clearly seen through its distinctive decay in to a pair of oppositely charged muons. Although the absence of a signal seems to be an odd way to infer the presence of a new form of matter, experimental benchmarks exist that can be used to quantify the suppression of the J/ψ in central collisions of heavy ions. The most immediate is the production in peripheral collisions, where QGP formation is unlikely. Additionally one may examine collisions of lighter ions or of protons where QGP effects are either much reduced or absent altogether. Unlike many of the proposed signatures of the formation of the QGP, the J/ψ signal is quite robust, requiring little correction for nonphysics backgrounds.

The spin-structure program is also scheduled to begin operation during the last eight weeks of the RHIC 2001 running period. This will feature collisions of 200 GeV (in the center of mass) longitudinally-polarized protons. The south muon arm will be poised to make significant new measurements of polarization observables during this period. Because the luminosity (a measure of the intensity of collisions) will be comparatively low, there will be a premium on recording the rate of processes that have a large cross section. One such process that is likely to produce new information for the spin structure of the proton is open heavy-flavor production (open heavy flavor refers to hadrons that contain either a charm or bottom quark and one or two light quarks). Open heavy-flavor production should be observable through production of single muons with a large component of momentum perpendicular to the beam direction. According to detailed simulations of this process, the south muon arm should be capable of making a significant measurement of the contribution of gluon spin to the total spin of the proton within the next two years.

Figure 3. The south muon arm of the PHENIX detector, shown in the staging area of the PHENIX detector hall.

The Multiplicity and Vertex Detector

The multiplicity and vertex detector (MVD) is a vital part of nearly every physics measurement made by the PHENIX detector. As its name suggests, its purpose is twofold:

1. to identify the point at which the colliding particles actually hit each other (collisions may actually occur anywhere in a region about a meter in length along the beam axis) and
2. to measure the multiplicity and distribution of charged-particle tracks from the collision.

The latter is a key measurement in the determination of the centrality of the collision. For example, gold ions that collide nearly head on produce as many as 7,000–10,000 charged particles, but collisions that are more peripheral in nature produce substantially fewer.

The MVD (Figure 4) consists of a large number of silicon detectors, microstrip detectors along the beam axis, and pad detectors at the two ends. There will be approximately 35,000 readout channels when it is fully instrumented in 2002. The MVD would be a simple detector to build if it were not for a very serious constraint that renders the project

an exercise in state-of-the-art mechanical and electrical engineering. Because it is the first detector to intercept particles from the collision, and because other critical detector systems must determine charged-particle and photon energies at larger radii, the MVD must be nearly massless. Thus the detectors and their support system represent less than 1.5% of a radiation length of material along a particle's trajectory. The readout electronics are highly miniaturized in order to fit into small regions of the detection area that do not have active measurement elements.

Four years ago a large Class 10 clean tent facility was constructed and instrumented in SM-218 near the Physics Building in technical area (TA)-3 at LANL. All MVD prototyping and construction activities were carried out at this facility. One of the key elements of the MVD electronic readout system is a state-of-the-art device called a multichip module (MCM). The MCM packs the function of some 12 application-specific integrated circuits (ASIC) into a wafer of silicon about 2 cm square. Manufactured by Lockheed-Martin,
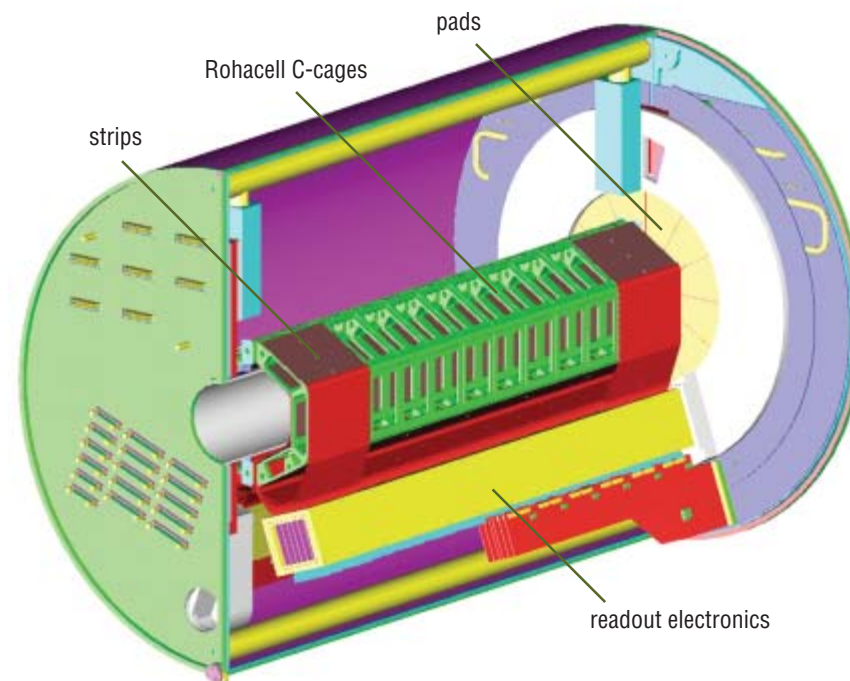

Figure 4. Schematic view of the MVD. The green-hatched area at the center represents Rohacell foam C-cages (two opposing C-cages surround the beam axis) that hold the silicon-strip detectors, some of which are shown in maroon. At the two ends of the MVD are silicon pad detectors (yellow area at the right). The readout electronics are shown schematically as a yellow bar along the bottom of the MVD.

the MCMs, when constructed correctly, achieve an incredible miniaturization of electronic components. Unfortunately, the manufacturing process has achieved a success rate of only ~40%. This has resulted in a significant cost growth of the MVD system and a consequent delay in

its final implementation into the PHENIX detector. During the 2000 RHIC running period, a scaled-down version of the MVD, comprising about 25% of the total system was successfully installed and operated. We expect that the remaining 75% will be installed in PHENIX for the 2001 running period.

Physics with the Multiplicity and Vertex Detector

The MVD's determinations of vertex and collision centrality are critical features of nearly every measurement of the PHENIX detector. However, in two areas the MVD alone can provide important data. In central collisions of heavy ions, a measurement of the multiplicity leads via a well-established relation (called the Bjorken formula) to a determination of the energy density achieved in the collision. This measurement can be made, in principle, from a single central collision. In addition, the MVD on its own can be used to search for fluctuations in the pattern of charged-particle production, predicted to occur in some theories of the phase transitions that may occur in high-energy heavy-ion collisions.
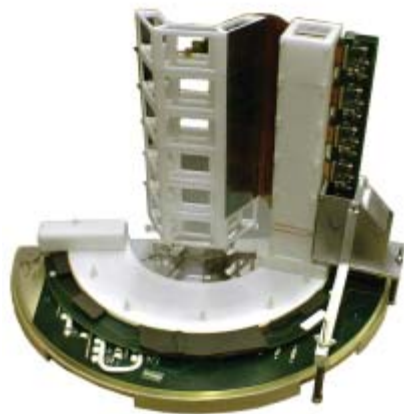

Figure 5. Multiplicity and vertex detector during assembly at Brookhaven in June 2000. One of two Rohacell C-cage assemblies is shown in the vertical position (horizontal in Figure 4) with some of the strip detectors and kapton cables attached.

Summary and Outlook

The RHIC era opens a qualitatively new chapter in accelerator-based physics. Never before has the capability existed to examine the results of ultrahigh-energy collisions of the heaviest elements (Previous results from the CERN SPS fixed-target program were obtained at center-of-mass energies an order of magnitude lower.) Similarly, RHIC offers for the first time, the capability of examining detailed structures of the nucleon that depend on the spin orientation of its fundamental constituents—quarks and gluons. For these reasons the next few years promise much exciting new physics with the new instruments conceived and built by LANL personnel.

Further Reading

Y. Akiba, R. Begay, J. Burward-Hoy, *et al*., "Ring Imaging Cerenkov Detector of PHENIX Experiment at RHIC," *Nuclear Instruments and Methods in Physics Research A* 433, 143–148 (1999).

K. Ikematsu, Y. Iwata, K. Kaimi, *et al*., "A Start-Timing Detector for the Collider Experiment PHENIX at RHIC-BNL," *Nuclear Instruments and Methods in Physics Research A* 411, 238–248 (1998).

M. Mukerjee, "A Little Big Bang," *Scientific American*, March 1999, pp. 60–66.

R. P. Pisani, T. K. Hemmick, H. Chung, *et al*., "Successful Test of a Prototype Hadron Blind Detector," *Nuclear Instruments and Methods in Physics Research A* 400, 243–254 (1997).

A New Ultra-Cold Neutron Source for Fundamental Physics Measurements at LANSCE

*A. Saunders, J. Boissevain, G. Hogan,
L. Marek, and C. L. Morris (P-25);
J. Anaya, T. Bowles, R. Hill, K. Kirch,
S. Lamoreaux, R. Mortensen,
A. Pichlmaier, and W. Teasdale (P-23);
S. Seestrom (P-DO); S. Hoedl and
C. Y. Liu (Princeton University);
A. R. Young (North Carolina State
University); B. Filippone, T. M. Ito,
J. Martin, B. Tipton, and J. Yuan
(California Institute of Technology);
P. Geltenbort (Institut Laue-Langevin,
Grenoble, France); M. Hino and
T. Kawai (University of Kyoto, Japan);
and A. Serebrov (Petersburg Institute for
Nuclear Physics, St. Petersburg, Russia)*

Introduction

Ultra-cold neutrons (UCNs) are neutrons of sufficiently low energy that they cannot penetrate the potential barrier formed by a variety of materials. They have a variety of characteristics that make them uniquely suitable for high-precision measurements of the properties of the decay of the neutron, which are intimately tied to fundamental physics. For example, the neutron decays, with a lifetime of about 890 s, into a proton, an electron, and a neutrino. There is an angular correlation between the direction of the spin of the decaying neutron and the angle of emission of the electron. Measurement of this correlation, called A, when combined with knowledge of the neutron lifetime, determines the values of the vector and axial vector weak coupling coefficients. We have proposed a new experiment to measure the A correlation using UCNs produced at a new source to be built at the Los Alamos Neutron Science Center (LANSCE).

Properties of Ultra-Cold Neutrons

Because UCNs lack the energy to penetrate the surface of a material, they undergo total external reflection at all angles. The probability that a UCN will be absorbed on each bounce has been measured to be very small: less than one in ten thousand. Therefore, UCNs can be stored in a bottle for long periods of time, greater than 100 s. Also, they can be guided through pipes with sharp bends. Together, these facts allow an experiment using UCNs to be shielded from the source of the neutrons both by physical shielding (because one can transport the UCNs around the shield material) and by time (because one can store the UCNs in a bottle until the background caused by the production process has died away). Also, UCNs have sufficiently low energy that they can be 100% polarized by passing them through a magnetic field of about 7 Tesla. UCNs with spins coaligned with the field pass through it, but those with spins aligned in the opposite direction are turned back by a potential higher than their kinetic energy. Therefore, 100% polarized UCNs can be available to an experiment that measures correlations to the spin of the neutron. Previous measurements of the A correlation have been dominated by the systematic errors caused by high backgrounds and incomplete polarization of the neutrons; both of these effects are almost eliminated by using UCNs for the measurement. These two factors will allow our experiment to achieve unprecedentedly low systematic errors for an A correlation measurement, and also systematic errors that are independent of those affecting the previous measurements conducted using cold neutrons or at reactors. The dominant systematic uncertainties for our experiment will be caused by depolarization of the UCNs by interactions with the walls of their decay volume and by interactions with the magnetic fields in the decay volume.

In order to run our experiment, however, we need to build a new source to supply it with UCNs. No existing source in the world can supply enough UCNs with low enough background rates for the experiment to work. In principle, UCNs could be produced in cold neutron sources by thermal processes. Energetic neutrons from a reactor or spallation source would be moderated by a material,

such as liquid hydrogen, at a temperature of about 20 K. The resulting temperature distribution of the neutrons, called the Maxwell-Boltzmann distribution, has long tails that reach to high and low energies, even down to the energy region of UCNs. But the number of UCNs produced by this method would be relatively small because the UCN energy region is orders of magnitude lower than the moderator temperature, and the number of UCNs produced would be suppressed accordingly.

Therefore, in order to produce UCNs in quantity, it is necessary to somehow enhance their production. This is possible using the super-thermal UCN production process. If the dominant interaction between the neutrons and the medium through which they pass is by single-phonon absorption or creation, then UCN production will be (possibly greatly) enhanced. A cold neutron can downscatter to produce a UCN by creating a phonon and giving up the corresponding energy. The probability of this happening is proportional to the density of states available for the phonon to be created in. Similarly, a UCN can upscatter by absorbing a single

phonon and receiving its energy and turn into a cold neutron. But if the temperature of the moderator is much less than the temperature of the cold neutrons, relatively few phonons will be available for the UCN to achieve upscatter by absorption. So, the upscattering process is suppressed in such a material, which results in greatly enhanced UCN production over thermal rates. Candidate materials are rare, though. In addition to the single-phonon interaction forming a link between cold-neutron and UCN energies, the nuclear absorption in the material must be very small; otherwise, the UCN will likely be absorbed before it can escape from the medium in which it was created. Only two materials satisfy the requirements: superfluid helium and solid deuterium.

Figure 1. A concept drawing of the prototype UCN SD$_2$ source. The 800-MeV proton beam from the LANSCE accelerator strikes the tungsten target, producing about 18 neutrons for every incident proton. These neutrons are reduced to cold-neutron temperatures (~40 K) by scattering in polyethylene moderators at 4 K and 77 K. They downscatter into the UCN regime as they interact with the solid deuterium.
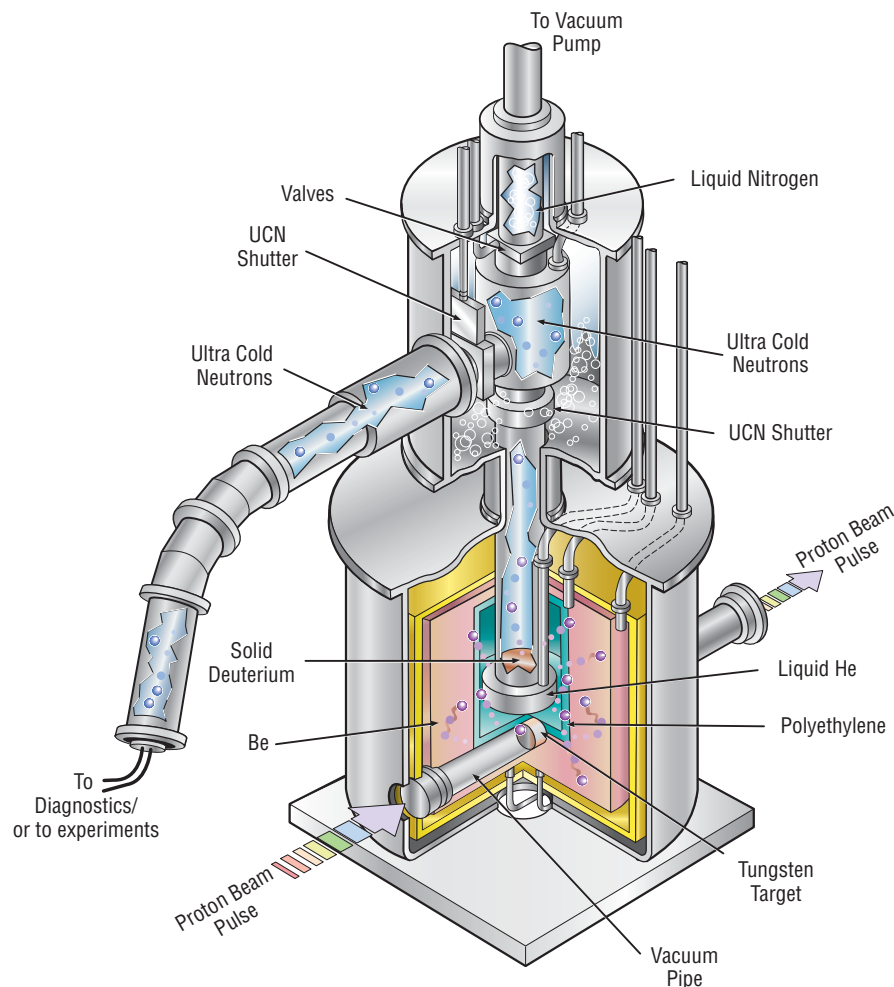
Our Approach to Enhanced Ultra-Cold Neutron Production

For the past several years, our collaboration has been working to design and build a UCN source based on enhanced production in solid deuterium. In our source, the 800 MeV proton beam at LANSCE hits a tungsten spallation target (see Figure 1). Each incident proton produces about 18 energetic neutrons in the spallation target. These neutrons are reflected by and contained in a box made of beryllium metal. Layers of polyethylene at liquid-nitrogen temperature (77 K) and liquid helium temperature (5 K) moderate the neutrons to a temperature of about 40 K. Inside the polyethylene moderators is a stainless steel pipe coated with a thin layer of nickel-58. The pipe, in turn, contains a block of solid deuterium at a temperature of about 5 K. The cold (40 K) neutrons can pass right through the stainless-steel-and-nickel wall of the pipe, but when they encounter the solid deuterium, some of them are downscattered to produce UCNs. These UCNs are now trapped in the pipe, or guide tube, because nickel-58 has a high enough potential to hold UCNs. So the UCNs, if they escape the deuterium without being absorbed

or upscattered again, bounce off the interior walls of the guide tube and are conducted to a bottle, detector, or experiment away from the source. For our test setup, shown in Figure 1, we had a bottle formed of a length of guide tube with valves at both ends atop the source and a detector at the bottom of a vertical stretch of tube off to the side of the detector.

Problems in Producing Ultra-Cold Neutrons

We have tested and improved our prototype UCN source from 1998 to 2000. In the early tests, in 1998–1999, the source produced far fewer UCNs than predicted. Much of our subsequent work has focused on identifying and eliminating this unexpected suppression. The first version of the source had a cold aluminum window above the solid deuterium block, which was designed to confine the deuterium to the cold region of the guide tube. Unfortunately, it also confined the UCNs to that region. Aluminum would normally be almost transparent to UCNs, because both its potential and absorption are low, but the window in our source was opaque. Because the window

was cold (about 20 K), any impurities in the deuterium gas used to fill the cell froze out on the surface of the window. These impurities, such as water, oxygen, and nitrogen, have high enough potentials and absorptions for neutrons that no UCNs could get through them.

After eliminating the window from the system, so that the UCNs had an unobstructed path from the deuterium to a storage bottle or detector, we still observed unexpectedly low UCN production from the source. It was clear that the UCNs were failing to escape from the solid deuterium block. After a UCN is created in the deuterium, by being downscattered from a cold neutron, it starts to travel through the deuterium. As it passes through the solid deuterium, it can get upscattered again by reacting with a phonon in the deuterium crystal, or it can get absorbed on either a deuterium nucleus or a hydrogen nucleus which has contaminated the deuterium. Because the cross section for each of the processes is proportional to the inverse of the velocity of the UCN, the probability of each interaction occurring and removing the UCN can be

characterized by a lifetime that it is independent of UCN velocity. The lifetimes caused by each process then add like resistances to form the total lifetime for a UCN in solid deuterium. That is, if there are three limiting processes, with lifetimes designated τ_1–τ_3, then the total lifetime, τ_T, would be

$$\frac{1}{\tau_T} = \frac{1}{\tau_1} + \frac{1}{\tau_2} + \frac{1}{\tau_3}. \qquad (1)$$

The lifetime caused by nuclear absorption on deuterium (~150 ms) is unavoidable. All deuterium has some contamination of hydrogen atoms, but the lifetime caused by nuclear absorption on hydrogen can be extended by reducing the hydrogen contamination. If the hydrogen contamination is reduced to 0.2%, then the lifetime for nuclear absorption on hydrogen is also about 150 ms. Finally, the lifetime for phonon absorption from the deuterium crystal is dependent on the temperature of the deuterium, because the population of phonons increases with higher temperature. For a deuterium temperature of 5 K, the lifetime for phonon

absorption is also 150 ms. If you add these three lifetimes as resistances (using Equation 1), the total lifetime is 50 ms. Because a UCN moves at a speed of about 0.5 cm/ms, and the thickness of the solid deuterium was about 10 cm, we expected the UCN to escape from the solid in about 20 ms. As 20 ms is less than the predicted lifetime of 50 ms, we expected a substantial fraction of the UCNs would escape. But we detected dramatically fewer UCNs than we expected. We realized that we needed to directly measure the UCN lifetime in the deuterium in order to check the predicted lifetime of 50 ms.

The lifetime of the UCNs in the solid deuterium can be measured by not allowing the UCNs to travel directly along the guide tube from the deuterium to the detector, but instead of trapping them in the section of tube with the deuterium for varying lengths of time after production, then counting how many survive. UCNs trapped in the section of guide with the deuterium can be lost in three ways: first, they can be lost by interacting with the walls of the guide or with the valve trapping them with the deuterium.

Second, they can be lost by interacting with the deuterium. Finally, they decay with a lifetime of about 890 s. We could disregard this last source of loss because the other two sources have much shorter lifetimes and dominated the loss. Thus, the sum (as resistances) of the wall losses and the deuterium losses formed a total lifetime of the system. We directly measured this total lifetime by counting the reduction in detected UCNs as a function of the amount of time they were trapped within the deuterium (see Figure 2). Because the lifetime caused by wall losses in the guide could be predicted both analytically and by using Monte Carlo techniques, we could then extract the lifetime of the UCNs in the deuterium.
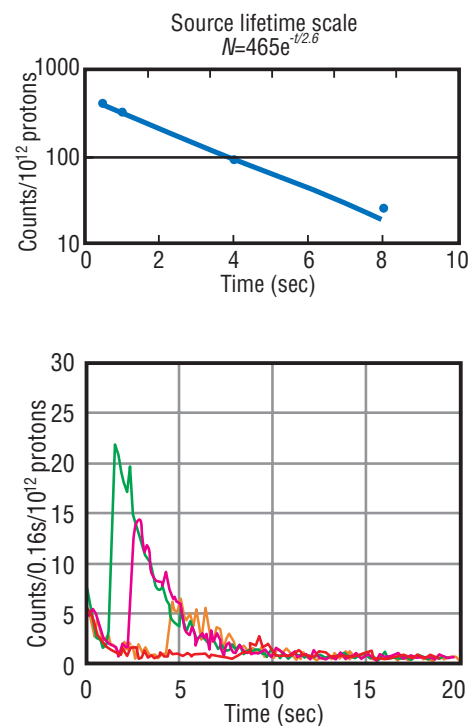
Figure 2. SD$_2$ Lifetime Measurements. The UCNs were trapped in a 5 L bottle that also contained the solid deuterium moderator. The exit valve was opened after different times. The detected UCNs are shown in the bottom plot for different opening times. The decrease in detected UCNs for later opening times (shown in the top plot) corresponds to the lifetime of UCNs in the system, which is 2.6 s in the example shown. By correcting for other sources of UCN loss, the lifetime of UCNs in the solid deuterium could be extracted. In the example shown, the lifetime in the SD$_2$ was about 30 ms.

Our Solution

The result was surprising: the lifetime was only a few milliseconds—not the 50 ms that we had predicted. Another source of loss of UCNs must exist in the deuterium in addition to the three listed above. The deuterium molecule, like the hydrogen molecule, has different spin states. In hydrogen, the spins of the two protons in the molecule can either be aligned (total spin = 1) or opposite to each other (total spin = 0). The first state is called ortho-hydrogen, and the second is called para-hydrogen. In deuterium, the situation is slightly more complicated, because deuterium has a spin of 1, as opposed to hydrogen, which has a spin of 1/2. The total spin of the two spin-1 deuterons in a deuterium molecule can be either 0, 1 or 2. The two states with even total spins are called ortho-deuterium and the state with odd total spin is called para-deuterium. Ortho-deuterium is the ground state (the state with the lowest possible energy); para-deuterium has an energy about 7 meV higher than ortho-deuterium. Because 7 meV is much greater than the typical UCN energy of 100 neV, if a UCN were to cause

the transition from para- to ortho-deuterium to occur and receive some of the released energy, it would definitely be upscattered and no longer be a UCN. At room-temperature equilibrium, 33% of deuterium is in the para- state, so there are plenty of para-deuterium molecules available to give up their 7 meV of energy to passing UCNs.

Members of our collaboration made the first calculation of the upscattering probability for UCNs on para-deuterium and found that the cross section is large enough that the room temperature abundance of para-deuterium was sufficient to explain the very short lifetimes we had observed. But they found that if the fraction of para-deuterium could be reduced to about 2%, the lifetime caused by this new upscattering process would be about 150 ms, comparable to the lifetimes caused by the other sources of UCN loss. The total lifetime for a UCN in the deuterium would then be predicted to be about 38 ms. Because we needed to increase the lifetime of the UCNs in the solid deuterium in order to increase the number of UCNs produced by the source, we built a converter to change the para-deuterium to ortho-deuterium

before it was introduced into the guide tube. The converter consisted of a cell full of a material, ferrous hydroxide, which has both a magnetic moment and a large surface area. By exposing the deuterium to this material, held at a temperature of about 20 K by the cold head of a cryo-pump, we can reduce the fraction of para-deuterium to below 2%.

Experimental Results

When we measured the lifetime of the UCNs in the deuterium using the converted deuterium, we saw the expected value. Furthermore, the lifetime depended on the para-deuterium fraction and the temperature of the solid deuterium in the predicted way. Finally, the number of detected UCNs was greatly enhanced relative to our earlier measurements and was close to our Monte Carlo predictions of UCN production. This higher UCN production encouraged us to test our prototype source at proton currents comparable to those to be used for a full-scale production UCN source. The result of the test was the highest density of UCNs stored in a bottle in the world so far (see Figure 3). The linearity of the number of detected neutrons with incident proton charge was also encouraging because it indicates that the full-scale source would not be limited by beam heating or other effects of higher proton currents.
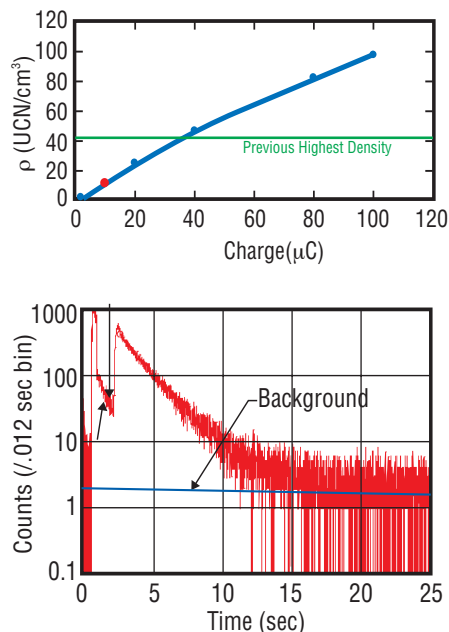
Figure 3. World Record UCN Density. On June 29, 2000, we tested the prototype UCN source with beam intensities similar to those we would use for the full-scale source. The result was the highest density ever achieved of UCNs stored in a bottle, a factor of 2.5 greater than the world's previous highest density. The top plot shows the density achieved as a function of incident proton charge. The bottom plot shows the time structure of the detected UCNs, after the start of the proton pulse at time zero. The UCNs were stored for 1/2 second, from t = 2.0 to t = 2.5 s. About 30,000 UCNs were detected in the run shown, which corresponded to an incident charge of 100 microCoulombs of protons and a UCN density of 100 UCN/cc.

Summary and Outlook

We are therefore proceeding to design and build a full-scale UCN source to be installed at LANSCE. Our predictions are that steady state UCN densities of about 300 stored UCN/cm³ will be achieved, as opposed to the 10 UCN/cm³ we stored in our test run and the 41 UCN/cm³ that had previously been achieved by a production source. A density of 300 UCN/cm³ will allow us to make measurements with previously unattainable precision of neutron decay asymmetries, and hence of the weak coupling constants. The first experiment, by making precise measurements of the weak coupling constants, will push the limits of our understanding of the fundamental forces of nature, and possibly even prove that the standard model, which describes the fundamental particles, is incomplete. The design and initial stages of construction of the full-scale source and first experiment are now in progress. Possible upgrades to the first source are now being studied, as well: UCN densities of up to several thousand per cubic centimeter might be possible with an upgraded source. Such a source could supply UCNs
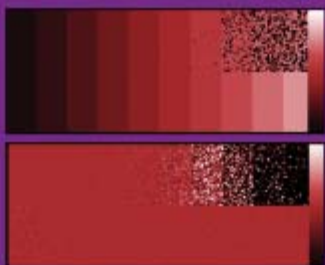
to a user facility, supporting multiple experiments running at the same time. These experiments could simultaneously make the world's best measurements of the neutron lifetime, electric dipole moment, and decay constants, for example. The first source and experiment, while making the best measurement so far of the A decay constant and testing the standard model, will also prove the feasibility of such a source and user facility, which could be completed and on line within ten years. The development of the UCN source at LANSCE achieved a density of 100 UCN/cm³ (2.5 times the previous world record) in its first two years of work; in the next year, the full-scale source will achieve another factor of three increase in density, to 300 UCN/cm³; and we hope that our work over the next several years will raise the best density by up to another factor of a 30, to several thousand UCN/cm³. A new era of precision UCN-based measurements is starting, and Physics Division and Los Alamos are in the lead!

For Further Reading

R. Golub, D. Richardson, and S. Lamoreaux, *Ultra-Cold Neutrons*, (Adam Hilger, Bristol, 1991).

C. Y. Liu, A. R. Young, and S. K. Lamoreaux. "Ultracold Neutron Upscattering Rates in a Molecular Deuterium Crystal," *Physical Review B* 62, 2000. p. 3581.

Hydrodynamic and Shock Physics

Physics Division research into hydrodynamics and shock physics supports the core missions of the Laboratory. With the cessation of underground nuclear testing and the reliance science-based stockpile stewardship (SBSS) to maintain the certification of the nuclear-weapons stockpile, this area of research becomes even more important. Physics Division acts as a primary research organization and provides support to other such organizations with the development of important diagnostic instruments and tools.

In the past, Physics Division has been a major collaborator in the underground testing program at the Nevada Test Site (NTS). We harbor the data archive from that testing program. We are working to update this archive to modern database standards and glean new physical principles and performance data from the archive by reanalyzing it with modern computational tools. This data can then be used to validate new tools and instruments that are a part of the SBSS program. It is through this chain of validation that we can assure confidence in our aging nuclear stockpile.

The Division uses or contributes to such facilities as the linear accelerator at the Los Alamos Neutron Science Center (LANSCE), the Dual-Axis Radiographic Hydrotest (DARHT) facility, the Trident laser facility, and the Atlas pulsed-power facility. Recently the Division has pioneered the invention of neutron resonance spectroscopy at LANSCE as a diagnostic for shock and materials physics. These facilities and smaller experimental tools such as gas guns provide the high-energy experimental regimes to allow investigation into the fundamental properties of materials under high hydrodynamic or shock stresses.
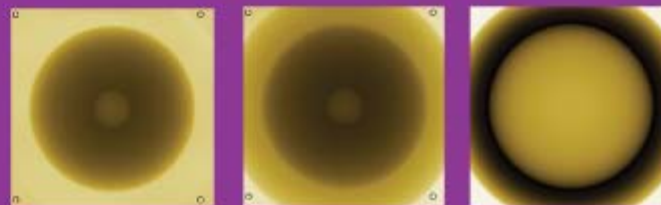
Spall Strength and Shock Release Kinetics Following the Alpha-Epsilon Phase Transition in Iron

L. R. Veeser (P-22) and R. S. Hixson, J. E. Vorthman, and D. B. Hayes (DX-1)

Introduction

Spall, the dynamic fracture of a material, can occur when the tensile stresses from colliding rarefaction waves [*] exceed the strength of the material. By passing rarefactions through a sufficiently thick sample, they can be made to rise relatively slowly to allow detection of dynamic features of the spall. We are using techniques, many of which were developed over several decades by shock-wave experts at Los Alamos and elsewhere, to study spall in iron. Iron is known to experience an alpha-to-epsilon [bcc to hcp, body-centered cubic to hexagonal close packed] phase transition, which has a significant density change, when shocked to pressures above about 13 GPa (130 kbar). This phase change was studied extensively by Barker and Hollenbach[1] and others. We are interested in spall of the material after it transforms from alpha to epsilon phase and reverts to alpha. Studies of recovered targets of similarly spalled iron indicate increased shock hardening relative to targets shocked to below the transition.[2] We also studied the kinetics of shock release from the epsilon state for the case where spall is suppressed by placing an impedance-matched window adjacent to the target.

Measurements

Spallation

The experiments were performed using a 50-mm-diameter light gas gun, one of several research guns owned and used by Group DX-1. The gun accelerates a flyer plate a few millimeters thick and 50 mm in diameter to speeds of up to about 800 m/s, and the flyer impacts inelastically onto a target. In this work the target and usually the flyer are iron. Strong, planar shock waves are produced at the flyer-target interface and propagate

Flyer   Target

VISAR senses spall

VISAR senses shock arrival

Impact

Rarefaction fan

Time

Position

both forward into the target and backward into the flyer plate. These shock waves reflect at the distal surfaces of both the flyer and target and travel as rarefactions back into the flyer and target. Rarefactions are pressure-reducing waves. Each of the rarefactions reduces the pressure from its peak to near zero pressure. When they collide, large tensions are produced. It is the interactions of these rarefactions that are of interest here. By suitable design of the experiment we arrange for them to collide in the target, and where they meet the tension can spall it. Figure 1 shows (upper) a schematic of a flyer and spalled target and (lower) a graph (time vs position) of the shock fronts and rarefactions. While a shock front typically
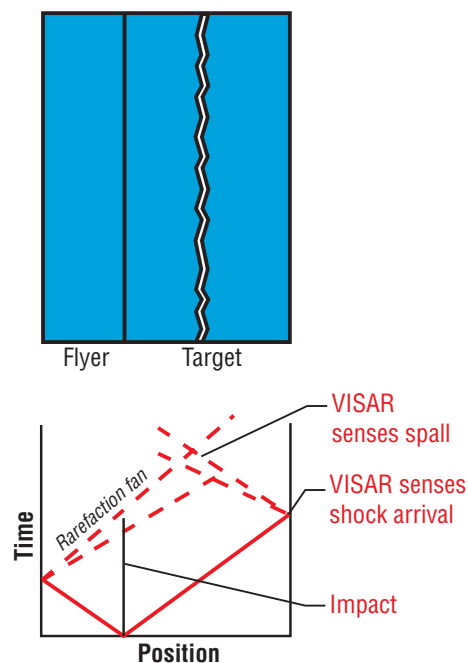
Figure 1. Upper: Schematic of a flyer in contact with a spalled target. Lower: Time vs shock positions (solid lines) and rarefaction positions (dashed lines). In this representation steeper curves imply slower waves. Spall can occur where the rarefactions collide when the tensile stresses exceed the material strength. In iron a phase change occurs, and the "shocks" are really three structures: elastic wave, plastic wave, and the phase-changing wave. The release waves have similarly complex structures.

[*] A pressure wave induced by the reduction in density following a shock wave; it travels in the opposite direction of the shock wave.

steepens as it travels through a target, a rarefaction usually spreads out with distance traveled and is better described as a rarefaction "fan."

The free surface of the target, the surface opposite the one shocked by the gun projectile (the right boundary in Figure 1), is set into motion by the shock roughly a microsecond after impact, and it is simultaneously further accelerated by the reflection of the shock back into the target, the rarefaction. Because of the acceleration, the free-surface velocity immediately after shock release is approximately twice the particle velocity, the velocity initially given the material by the passage of the shock. (This acceleration is analogous to the doubling of an electrical pulse in reflecting from an unterminated

end of a cable.) The rarefactions, one from the release at the front surface and one from the rear surface, eventually collide near the middle of the target, and the tension is sufficient to cause the material to spall.

Figure 2 shows a schematic of the experimental set-up. It illustrates the configuration for shock-release measurements, described later. For spall there was no sapphire window in back of the iron target. The flyer, held in an aluminum or magnesium "sabot" to keep it from tilting, is accelerated in a 50-mm-diameter, single-stage, light-gas gun. A foam cushion between the flyer and the sabot allows the large rarefactions needed for these experiments to form upon shock reflection at the trailing surface of the flyer. Between six and ten electrical shorting pins, placed in a 44-mm-diameter circle around the 38-mm-diameter target, measure the flyer velocity and tilt. Flyer velocities were measured with an accuracy of < 0.2%. Tilt was small, typically between 1 and 2 mrad.
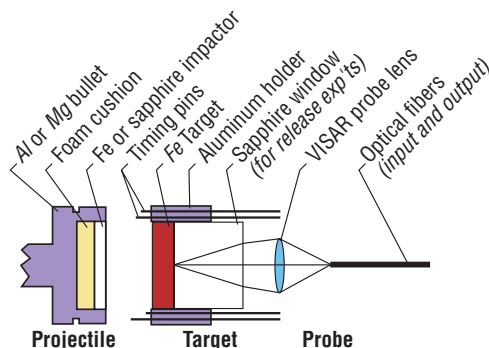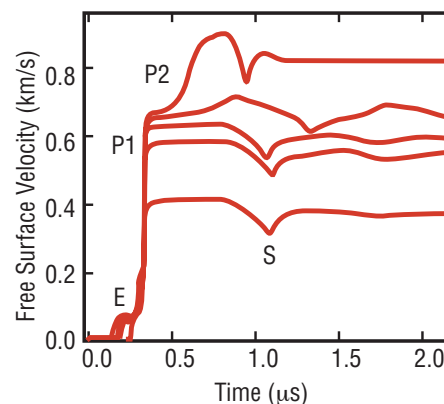

Figure 2. Schematic of a shock-release experiment. For spall the set-up is similar but does not have the sapphire window in back of the iron target.

The principal diagnostic is a VISAR (Velocity Interferometer System for Any Reflector)[3] measurement of the velocity of the free surface for spall or of the target-window interface for shock release. Argon-ion-laser light of wavelength 514.5 nm is brought in on an optical fiber and focused onto the target free surface. This surface is prepared by roughening it slightly to make the reflections somewhat diffuse so that the signal will not be lost if the reflecting surface tilts slightly during the experiment. The reflected light is focused into a second fiber leading back to the recording room. There the fiber-optic signal is split and sent to a pair of VISARs. By using two VISARs with different sensitivities, we can determine whether any interference fringes are lost during

Figure 3. VISAR signals for iron showing the velocity of the free surface as a function of time. Zero time was adjusted for each experiment so that the P1 waves would all arrive at the same time. In these five experiments the iron is shocked to peak pressures of (top to bottom) 16.5, 14.5, 11.0, 10.1, and 7.0 GPa. The shock wave separates into two or three distinct waves while progressing through the target, and the VISAR detects them when they arrive at the free surface and accelerate it. The first wave to appear is an elastic wave (E); it is very dependent on the microstructure of the target and therefore varies greatly from shot to shot, as various target types were investigated. Next is a plastic wave (P1), which takes the target up to a pressure no higher than that at which the alpha-to-epsilon phase transformation begins (13.0 GPa). The third wave (P2) occurs only when the shock is sufficient to cause the phase transformation; it takes the target to the final, partially-phase-transformed, state. Because the phase transformation occurs gradually, P2 rises slowly as the material transforms. Around 0.7 to 0.8 μs the leading edge of the rarefaction from the flyer arrives at the free surface, and it begins to slow. The bottom of the dip (S) indicates that the material has fractured. The depth of this dip is an indication of the spall strength. (Otherwise the free surface would have continued to slow to near zero velocity.) After spall the release of the tension allows a gap to open; the interior spalled surfaces separate and the momentum trapped in the spall scab causes ringing.

the fast-rising shock front. In these experiments typically one or two fringes are missed, and unless the proper number are added to the raw signals at shock-arrival time, the two signals will not agree. Four of the five spall tests were conducted in symmetric-impact geometry, with an iron flyer and an iron target. However to increase the pressure attainable with this gun, we used a z-cut sapphire flyer for the highest-pressure spall shot. Sapphire's large elastic modulus allows us to produce higher pressures in the iron target than using symmetric impacts at the same velocity. Both geometries were designed so that spall would occur roughly midway through the target. VISAR measurements of the free-surface velocity in five experiments are shown in Figure 3. The large dips, which occur between 0.8 and 1.3 μs in the VISAR traces, indicate the spall as shown schematically in Figure 1. The three lowest curves were for pressures below the 13-GPa phase transition. They all show a spall signal arriving at the free surface about 1 μs after the shock. The second curve from the top is for a shock at 14.5 GPa. Here the beginning of a transition to epsilon phase in the iron is

evident, but before the transition is completed the rarefaction from the flyer reduces the pressure, reverses the transition, and spalls the target. When the rarefaction from the target arrives the target spalls. These four shots had 2-mm-thick iron flyers and 4-mm-thick iron targets. The top curve was for an experiment using a 3-mm-thick sapphire flyer and a 2.2-mm-thick iron target; because this target was thinner than the others, and because the wave speed in sapphire is very fast, the spall was earlier. It is apparent from the four symmetric-impact experiments that the presence of the phase transformation above 13 GPa delays the spall considerably, suggesting an alteration in the kinetics of the damage evolution leading to spallation above and below the alpha-to-epsilon phase transition. Simulations with the hydrodynamics code[4] WONDY indicate spall strengths of around 2.4 GPa below the transition and 3.5 GPa when the material is cycled through the phase transition and back.

Reverse phase change

To observe the reverse transformation, we conducted experiments with a thick sapphire window instead of a free surface. Laser light from the VISAR penetrated the window to view the iron. We used a 3-mm-thick, z-cut sapphire flyer, a 1-mm-thick iron target, and a 15-mm-thick, z-cut sapphire window glued to the back of the target. The sapphire's impedance (sound speed times density) is nearly that of iron, minimizing reflections at the interfaces and allowing us to observe the arrival of the rarefaction from the trailing edge of the flyer almost as it existed in the iron; i.e., the shock and release pass into the sapphire largely unaffected by the window. The thin iron target guaranteed that the rarefaction from the back of the sapphire flyer did not overtake the iron shock until it had passed into the window, allowing us to observe the slowing of the target-window interface when the rarefaction arrived there. No spall occurs because one of the rarefactions has been suppressed by the presence of the window, and a single rarefaction in the iron target
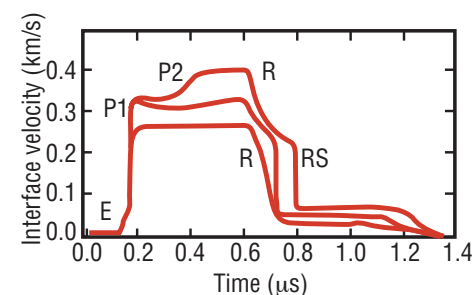

Figure 4. VISAR signals for iron, in contact with a sapphire window, showing the velocity of the target-window interface as a function of time. Zero time is arbitrary. In these three experiments the iron is shocked to pressures of (top to bottom) 16.3, 13.8, and 10.3 GPa. The shock wave separates into two or three distinct waves while progressing through the target, and the VISAR detects them when they arrive at the interface and accelerate it. The first wave to appear is an elastic wave (E). Next is a plastic wave (P1), which takes the target up in pressure no higher than that at which the alpha-to-epsilon phase transformation begins (13.0 GPa). The third wave (P2), which occurs only if the shock is sufficient to cause the phase transformation, then takes the target to the final, phase transformed, state. Because the phase transformation occurs gradually, P2 rises slowly as the material transforms. Later the leading edge of the rarefaction (R) from the flyer arrives, and the surface begins to slow. For the lowest pressure this release continues until the interface has slowed to near zero velocity. For the higher pressures the reverse phase transformation begins below 10 GPa, and it proceeds very quickly, producing a rarefaction shock (RS).

does not produce significant tensile stress. The window limited the maximum pressure in the iron to around 16 GPa; above this pressure the sapphire becomes opaque. Figure 4 shows the VISAR data for three shock-release measurements at pressures of 16.3, 13.8, and 10.3 GPa. Again, as for spall, the shock separates into an elastic wave, a P1 plastic wave, and at the higher pressures a P2 plastic wave. For the middle pressure, which is just barely above the transition, almost no P2 wave exists because the iron has just begun transforming to epsilon phase when the rarefaction arrives at the window. For the lowest curve, the 10.3 GPa shot, the rarefaction arrives at 0.6 µs and takes the interface velocity nearly to zero in about 100 ns. For the two upper curves the rarefaction again appears at 0.6 µs, but when the velocity has dropped to about 200 m/s a rarefaction shock forms. This shock indicates the reverse transformation, from epsilon phase back to alpha-phase iron. The density of iron in its epsilon phase is about 6% larger than in alpha phase. Upon reverse phase transformation, the density drops and the sound speed increases. The result is

a sudden steepening of the rarefaction front, a rarefaction shock. (Zel'dovich and Raizer give a good description of rarefaction shocks in Reference 5.) The slope of the rarefaction shock is steeper than can be resolved by the VISAR, implying that the reverse transition occurs in less than 1 or 2 ns, much faster than the forward transition rate. In contrast, the release in the 10.3-GPa experiment never forms a shock, indicating that there was no transformation to the epsilon phase.

Calculations

To simulate the shock experiments, we used a one-dimensional, Lagrangian, finite-difference wave propagation code[4], WONDY, using a nonequilibrium-mixture model developed for iron by Andrews.[6,7] The model assumes that for mixed phases of material, constituent phases locally share the same pressure and temperature but are not otherwise necessarily in equilibrium. Others have used this assumption extensively since the mid-1960s for modeling the dynamics of nonequilibrium phases. Experimental studies on numerous materials have shown that the phase-change rate is not constant but that the first part of the transformation proceeds rapidly to a metastable state and that the subsequent transformation proceeds either slowly or not at all.[1,8] Iron displays such behavior, having a fast (tens of nanoseconds) but measurable initial rate to a metastable state with essentially no subsequent transformation until conditions are changed by various impinging waves. The metastable state is best modeled by adding a

term to the Gibbs potential of the high-pressure phase.[9] The modified potential is

$$G_2' = G_2 - C \log(1-X_2) \qquad (1)$$

where G_2' and G_2 are the Gibbs potentials for the high-pressure phase in the metastable and in the equilibrium condition, respectively; X_2 is the mass fraction of the high-pressure phase; and C is a constant determined by matching the calculations to the measurements. We used $C = 1.15 \times 10^8$ [erg/g]. This modification to the Gibbs potential has the effect of causing our calculated phase transformation to halt when the metastable state is reached. We described the kinetics of the phase change by a simple phenomenological model in which the rate of transformation is proportional to $G_1 - G_2'$, where G_1 is the Gibbs potential for alpha-phase iron. The proportionality constant was chosen to match the transformation rates in the experiments. It is likely that strength effects during phase transformations are quite complex. However, our constitutive behavior was modeled as elastic, perfectly plastic.

Figure 5 shows a comparison of the measurements with the WONDY simulations for both a spall and a shock-release measurement. The elastic wave, the small precursor to the main shock rise, is a sensitive indicator of the material purity. We measured targets of varying purity to see what effects there would be on the spall and release signals, but differences were minimal despite large differences in the elastic-wave appearance. We did not develop a detailed model of the elastic waves. The calculated rarefactions have wiggles in them from the reflections

of the elastic precursors, while in the data the rarefactions have smoothed out. Calculations of the shape and timing of the spall dip agree well when we used proportionality constants which fit the P2 rise times[1] and the P1 decays.[10] For the release measurements, we have generally good agreement, but the timing of the calculated rarefaction arrival and the rarefaction shock onset do not quite exactly match the measurements. Small changes to some of the parameters will be needed. We intend to obtain more shock-release data at pressures above the transformation to better define these parameters.

Summary

We have seen that the alpha-to-epsilon phase transformation in iron increases the spall strength by about 50%. This result is consistent with measurements of increased hardness of similarly shocked samples.[2] Our simulations of the phase transformation to alpha phase show that the transformation requires a few tens of nanoseconds, in agreement with previous results.[1] In our data we found that the reverse transformation, in contrast, proceeds in < 2 ns.

About the Team

Robert S. Hixson has been involved in dynamic material properties research for the last 25 years. Rob has co-authored dozens of publications in the area of shock compression of condensed matter, with some work in static high pressure physics as well as the physics of expanded liquid metal states. Rob is currently team leader of the shock physics team within group DX-1 of the Dynamic Experiments Division. The gas gun used for this experiment is one of several operated by his team. Like Hixson, John Vorthman, has been using gas guns for over 25 years. In addition to research on various metals he has used shock waves to study the dynamics of high explosives. John also spent several years working on explosive-pulsed-power devices. Dennis Hayes has a long-standing interest and research record in shock waves and phase transformations. He presently works part time at Los Alamos (DX-1), Sandia National Laboratories, and Washington State University. All three of the authors above earned Ph.D. degrees from Washington State University.
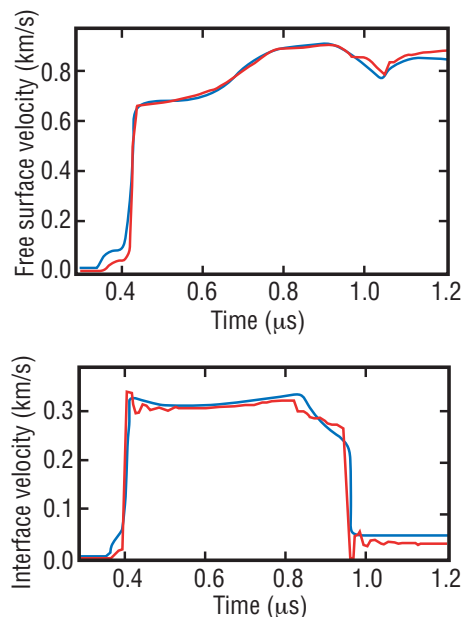

Figure 5. Comparisons of measured velocity data (blue curves) with the WONDY simulations (red curves) for iron that has transformed to the epsilon phase. The upper graph is for spall at 16.5 GPa and the lower graph is for a shock-release experiment at 13.8 GPa.

Lynn Veeser has worked on a wide variety of basic and applied physics problems in nuclear, plasma, pulsed-power, and shock-wave physics at Los Alamos for the past 33 years and has roughly 100 publications in those areas. He is the deputy group leader of Hydrodynamics and X-Ray Physics group (P-22). His Ph.D. is from the University of Wisconsin.

Acknowledgments

References

1   L. M. Barker, R. E. Hollenbach, *J. Appl. Physics* 45, 4872–4887 (1974).

2   G. T. Gray, D. B. Hayes, R. S. Hixson, *J. de Physique IV* 10, 755–760 (2000).

3   L. M. Barker, R. E. Hollenbach, *J. Appl. Physics* 43, 4669–4675 (1972).

4   M. E. Kipp, R. J. Lawrence, Sandia National Laboratories report SAND81-0930 (1982).

5   Ya. B. Zel'dovich, Yu. P. Raizer, *Physics of Shock Waves and High-Temperature Phenomena*, (Academic Press, New York, 1967) pp. 757–762.

6   D. J. Andrews, *J. Phys. Chem. Solids* 34, 825–840 (1973).

7   D. J. Andrews, *J. Comp. Phys.* 7, 310–326 (1971).

8   D. B. Hayes, *J. Appl. Phys.* 46, 3438–3443 (1975).

9   J. C. Boettger, D. C. Wallace, "Metastability and Dynamics of the Shock-Induced Phase Transition in Iron," *Phys. Rev. B* 55, 2840-2849 (1997).

10   R. S. Hixson, J. E. Vorthman, private communication (1999).

The Reaction-History Archive

*K. Croasdell, L. Zongker,
R. Collinsworth, R. Kelly, J. Lamkin,
D. Thayer, C. Young, and D. Bartram
(P-22); J. Kneidel, G. Simon, R. Boyd,
and M. Rogers (Bechtel Corp); and
E. Hodson and H. Kruse (retired)*

Introduction

The last Physics Division Progress Report on the archiving of data from nuclear tests began with the following statements, which are still true:

Los Alamos National Laboratory (LANL) has been traditionally responsible for the certification of our nuclear stockpile. With the cessation of nuclear testing, this task has become much more difficult. The charge of Science Based Stockpile Stewardship (SBSS) requires the certification of how the weapons perform as they age without the benefit of actual testing. Valid and realistic computational models of the performance of nuclear devices are required before any confidence can be gained in calculating the effects of aging on weapons.

Over the last few decades, during testing, the approach to nuclear-weapons design was largely empirical. Nuclear testing at the Nevada Test Site (NTS) allowed for the refinement and efficiency of nuclear devices, the performance of which is very complex. Codes and physical models were not adequate for calculating device performance from first principles. Nuclear testing established empirical parameters for interpolative calculations. Much diagnostic data obtained were not incorporated into the physical modeling because of the inadequacies of the computational tools. Presently, more powerful computers and more sophisticated models are available, but the codes must be compared to the experiment before they can be used to calculate effects of aging or design modifications of the nuclear stockpile as mandated by SBSS.

This Progress Report research highlight will discuss the definition and analysis of the reaction-history diagnostic and how it is used as a tool in SBSS. Because of the ban on actually testing a device, the next best proof that a needed change in a stockpile system will not affect yield is to calculate the weapon's effects and match the NTS test data before the change then calculate the weapon's effects after the change and see if it still matches the past NTS test data. If it does not match the data, then further study is needed to determine the effect of the change on the yield and whether the yield is changed enough to invalidate the stockpiled weapon. Without an actual testing program, certification of a weapon system after a change may be difficult.

Figure 1. This chart depicts the number and frequency of nuclear tests carried out by Los Alamos National Laboratory (LANL), Lawrence Livermore National Laboratory (LLNL), the Department of Defense (DoD), the Defense Nuclear Agency (DNA), and the United Kingdom (UK—actually their Atomic Weapons Establishment [AWE]) from post World War II until the cessation of testing in 1992.

Why is the Archiving Program Important?

Nuclear testing was halted in September of 1992. In the absence of nuclear testing, Presidential Directive 15 states that national laboratories will have the responsibility to maintain the ability to perform nuclear tests when needed. However the directive does not detail the type of experiments and diagnostics that may be required for the resumption of testing. An indefinite testing moratorium under the Comprehensive Test Ban Treaty will inevitably lead to the loss of the capability of promptly fielding diagnostic experiments. As the hardware ages, we will be required to reconstitute experiments from the ground up. In order to meet the presidential mandated 2–3 year time period for fielding prompt diagnostics, the following areas have to be evaluated for solutions.

· The knowledge base is disappearing.
· The shelf life of appropriate hardware is depleting in a stagnant inventory.
· The ability to understand, maintain, and operate appropriate software is dependent on contemporary computer systems.

· How will 1992 recording methods keep pace with new technologies? Only part of this required recording system can be exercised on contemporary stockpile physics experiments.
· As weapon designers develop and enhance their ability to calculate weapon performance, new diagnostic data requirements will be more stringent.
· What are the requirements for a new set of scientists and engineers to develop their own recording tools in a timely and cost effective manner?
· Can a system be developed that meets the accuracy and precision requirements needed by the weapon designers?

The United States has detonated more than 1000 nuclear bombs during its testing history. Reanalyzing and re-evaluating the data that has been produced by this testing program can find solutions for the majority of the listed issues. Using the data to transfer knowledge and placing the data in an electronic form that can be used by the weapon designer are key benefits to the current "archiving" program.

Definition

"Reaction history" and "alpha" are terms that are often used interchangeably, but alpha is actually a part of the reaction history. The reaction history is the entire measurement of a device history including not only the alpha but also the time relationships between the different stages of the device, for example high explosive detonation, neutron initiation, and, for a two-stage device, the peak flux times for the Primary and Secondary (see Figure 1, on the previous page, for a graph of the number and frequency of nuclear tests which constitute the reaction history archive). Neutron-source levels and gamma-flux levels are also a part of the reaction-history analysis. The "alpha" is the time derivative of the logarithmic flux calculated from the device's Primary or Secondary signal. It is a measurement of the neutron multiplication rate for each of these outputs.

In a supercritical nuclear assembly the neutron population increases exponentially with time:

$$n(t) = n_0\, e^{\alpha t}\,. \qquad (1)$$

Or if α is not constant, as is the case in an explosive assembly,

$$n(t) = n_0\, e^{\int \alpha(t)\, dt}\,. \qquad (2)$$

The quantity α characterizes the degree of criticality of the assembly. The fission neutron multiplication produces gamma rays. The primary method for recording this reaction is by observing the leakage gamma radiation (flux), which may rise through 20 or more orders of magnitude. From Equation 2, α is the derivative of the natural logarithm of the gamma-flux output from the device. The neutron population is directly proportional to the surface gamma output of the device. This is important because the neutron multiplication can be determined by measuring the gamma output, thus avoiding the energy time-of-flight smear of the neutron output.

The Reaction-History Experiment

High Explosive Transit Time (HETT) is the interval between the time of the initiation of the high explosive and the time of an inflection on the alpha curve. For reaction history, this basic experimental time between the voltage breakout of the electrical X-unit that initiates the detonators on the device and the Primary alpha curve, usually alpha boost is an essential initial condition for the weapon designer. Before 1977 the HETT was measured using four oscilloscopes. After 1977, only one digitizer unit, called a biomation unit, was necessary to measure this time. About 1982, the time interval meter (TIM) was introduced to timing technology and was used to record the HETT. (A TIM is like a stopwatch that gets its start from the X-unit and multiple stops from voltage levels on various detectors, which record the current for the related alpha function. The accuracy using the TIM is a magnitude better than the ±30 ns from oscilloscopes).

The Zipper is a pulsed 14 MeV neutron source used to initiate the fission reaction chain in nuclear devices. The Zipper is triggered at a prescribed time after the high

Figure 2. An array of oscilloscopes are needed to record the dynamic range of the device output.

explosive initiation to ensure the initiation of the fission reaction chain. The quantity of neutrons being output by the Zipper is another important "initial condition" experimental result needed by the designer. In the 1960s and the early 1970s, the Zipper output was reported in R/s. After that date it was reported in $N/cm^2/\mu s$. When we reanalyze one of the "older" past events, we recalculate the R/s output level to $N/cm^2/\mu s$ and place the Zipper function in electronic output (x,y

pairs) for use by the weapon designer. (Occasionally, the designers would request the center time of the Zippers, which is extracted from the same timing system that is used to determine HETT.)

The part of the reaction-history experiment that measures the criticality, thus the overall nuclear performance of a device is the alpha curve. The dynamic range of the device output requires the use of a series of electrical instruments

to measure the total output of the device. If a perfect recording system could be designed, the measurement result would be a continuous function as previously defined by Equation 2. The inability to precisely calibrate all the recording-system components both in time and amplitude produces a result that is not continuous in gamma flux. However the derivative of the natural logarithm (ln) of the flux is continuous and is used to precisely relate the piecewise recording of the curve by the detector, oscilloscopes and their related electrical components.

The diagnostic measurement of the HETT and Zipper output plus the reconstruction of the device's gamma-flux output and its related alpha function requires the expertise of a multitalented technical team. The effort actually begins with the weapon-design physicist(s) communicating with the diagnostic physicist(s) about the purpose of the test. The communication will include the expected experimental time relationships and the general shape of the output function(s). Experimentalists record the gamma-output signals of the

Primary and Secondary stages in a similar fashion, so the diagnostic challenges, which include proper selection of recording components, calibrations, and analysis techniques, are much the same for each function. Briefly describing the recording of the Primary part of the experiment is sufficient for demonstrating the complexity of the entire reaction-history experiment, which also includes the length of the time intervals between each stage's activation.

The gamma signal from the Primary covers such a large range that no one single recording device can record the entire function. Detectors that convert the gamma flux to an electrical signal are engineered to detect the output signal at various sensitivity levels. Typical detectors used for the experiment are a suite of very sensitive photomultipliers, less sensitive photodiodes, and the least sensitive Compton diodes. All of these detectors are sensitivity-calibrated using the radiation sources in the diagnostic community, such as the cobalt source in Las Vegas Nevada and the Linac accelerator in Santa Barbara, California. Bandwidth
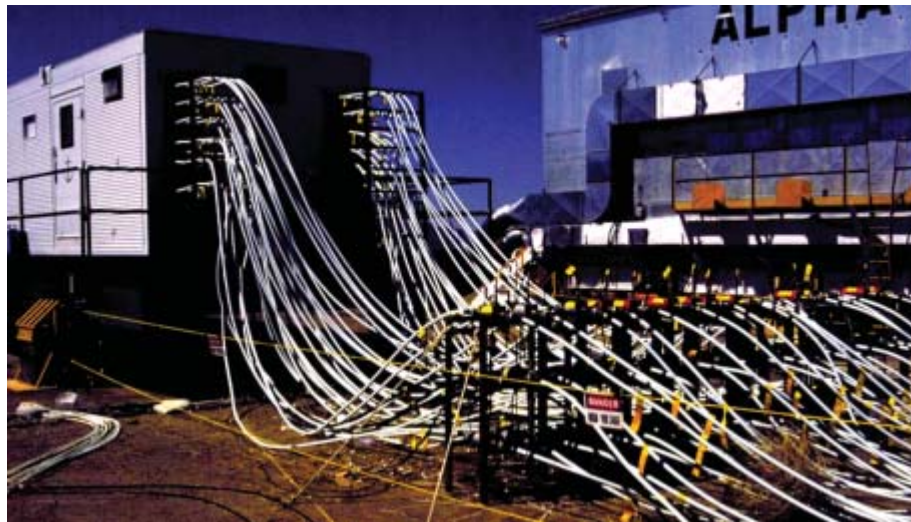

Figure 3. Many cables are needed to record the range of the signal in a reaction-history experiment.

determination is also a part of the calibration of a detector. A continuous alpha curve can be constructed only if the bandwidths of the detector array are nearly equal for all of the detector recording systems. Knowledge of the detector sensitivity is the first step used by the diagnostic physicist to place detectors in the correct amplitude position to record all of the gamma-flux signal. The coverage is adjusted using distance from the device (slant range), collimator attenuation effects and slab attenuation (lead, iron, aluminum, etc.) in the

downhole rack line of the site pipe. Shielding is an important technique that eliminates cross talk between the arrays of detector recording systems. Knowledge of the effects of this "detector geometry" has to be known to determine the optimal recording of the entire gamma-flux output. The amplitude calibration of the recording system is used in the analysis of the output signal.

Because calibration uncertainties of as much as a factor of two can exist between detectors, to correctly time one detector to another, experimentalists measured transit

times from the device through the detector. This is part of a "common timing" scheme that also includes transit time through the coaxial cables to the recording station.

The measured signal paths in the recording station carry the device output to an array of oscilloscopes. Multiple oscilloscopes of various sensitivities have to be used to cover the dynamic range of a single detector. No one oscilloscope will cover the entire range of any detector. So, just as in the case of the detector array, the diagnostic physicist has to determine an optimal array of oscilloscopes to cover the sensitivity range of each detector. For some experiments, over 100 oscilloscopes were used. Using the knowledge of the basic voltage sensitivity of each oscilloscope, and applying electrical splitters, attenuators, terminators, etc., achieves the optimal amplitude coverage. All of these oscilloscopes have to be calibrated; first to determine their correct placement in the total coverage of the detector signal, and then to analyze the output signal from the device after the device has been tested.

The time-base selection and calibration for each of the oscilloscopes is another challenging part of the diagnostic set up and analysis of the curve. The Rossi display is used to record the gamma flux, which in turn is used to calculate the related alpha curve. The Rossi technique for recording a signal is basically a sine wave from an oscillator mixed with a linear signal. The frequency is related in time as: period = 1/frequency. The period is one cycle on the sine wave. This makes the time base inherently a part of the recorded signal and provides the accuracy needed to calculate the time derivative of the ln of the flux, which is alpha. In regards to satisfying sampling theory, the selected frequency of the sine wave is dependent on the speed of the signal that the oscilloscope will be recording. For this reason it is critical that the diagnostic physicist know the general shape of the output signal from the device. On the same level as signal-path bandwidth matching, selection of the optimal Rossi oscillator frequency is necessary for the efficient recording of the output signal throughout the various changes in the shape inherent in the

output signal. The effect of inadequate sampling of the output is just as destructive to the accurate determination of the output of the device as is inadequate bandwidth or the mixing of bandwidths from detector to detector or oscilloscope to oscilloscope. In the latter days of testing, technology was advancing enough to allow serious consideration for recording the curve with high-speed digitizers and optical recording systems. The unique challenges related to the diagnostic set up of these types of systems will not be discussed in this document. The oscilloscopes that recorded the Primary gamma-flux output are reconstructed in time and amplitude with continuity confirmed by using the calculated alpha and/or the time differences of the signal paths from detector to detector.

At the time of many of the actual NTS tests, secondary-weapon designers occasionally requested that only the time between the two stage's activation be recorded because the computing hardware and software did not exist to provide the ability to calculate the device output and match it to the recorded data. The time between Primary-stage and Secondary-stage

activation is measured using a variety of diagnostic timing methods. Some of these timing systems are very complicated and careful calibration was absolutely necessary. Requests for only the time between stages are very rare during the reanalysis of the archived data because the weapon designer now has computing tools available to intelligently use all of the data from a test. This brings to light a couple of benefits of the archiving program: to extract new information and/or re-evaluate the interpretation of previously reported data. A recent reanalysis of a 1970s NTS test provided all of the data from a secondary signal and played a significant role in the certification of one of our principal weapon systems.

It was sometimes important to measure accurate gamma-flux amplitudes for each of the device's stages. The major component to accuracy is the precise calibration of the effect of rack geometry on the gamma signal. The "absolute" gamma measurement was only a diagnostic goal in the last five years or so of testing. During one of the last tests, careful attention to downhole effects on the detector

signals resulted in a flux curve with level shift errors of ±10%. As stated earlier, a factor of two or three between detectors was common or at least not unusual.

Finally, there cannot be enough emphasis on the fact that the fielding and analysis of a nuclear test required the expertise of several individuals working together. For example there were teams of people covering areas that supported detector calibration and installation, cables and compensators, recording station set up, preshot analysis, standards and calibration, photo, post-shot analysis and many other tasks too numerous to mention. It was very important to document all activities accurately. Because this documentation of these activities was done, the reanalysis of past NTS events is possible.

Alpha Analysis Tools

The basic tools for reaction-history analysis include the computing hardware and software plus the experience of the analyst(s). The ability to archive/store data electronically was not a convenient option until 1979 because of the lack of computing tools and large memory units. So, the reanalysis of events fired before 1979 starts as if the event were just executed. That is, we start by reading the oscilloscope traces, then use the event calibration documentation to run the data through contemporary software. We re-evaluate events fired after 1979 using the files that have been archived on the VAX computer. All data, reanalyzed and/or re-evaluated, is placed on the XWARP database (X-Division Archiving and Retrieval Project) for use by the weapon designers.

Before the routine use of electronic computers, the alpha data was analyzed using a slide rule and/or calculator. The resulting points were plotted on graph paper. In the mid 1960s, electronic computers were introduced, and over the years the analysis team had access to bigger and faster computers as

technology advanced. The first alpha-analysis software was written in 1964. This "batch"-operated code remained the basic tool until an interactive version was written in 1979. The 1979 version was written for the DEC operating system, and, although the hardware was updated and enhanced from a DEC PDP/1170 computer with 32K of memory to the MicroVAX 4000, the software remained unchanged through the end of testing in 1992. Because of the limited number of experienced personnel and the high level of effort needed for fielding experiments, moving to each new VAX machine required that production codes be able to be moved straight across to the new system thus avoiding a large software-conversion task. In 1998, six years after the last NTS event was fired, the software was still basically the same as it was in 1979. In 1998 it was clear that a new code was needed; one based on contemporary computing tools because the vendor was no longer supporting the VAX/VMS operating system.

The basic requirements of a new code were the ability to continue to process reaction-history data from past events, maintain the historical precision of the analysis process, and have the ability to operate independent of any hardware platform. Contemporary software was written and is able to meet these requirements now being utilized to reanalyze past NTS events. It is important to understand that the collection of

new data from NTS is not very probable, so the 50-year-old treasure (31 years of underground tests [UGTs]) must be preserved, and in addition, the "capability of reanalyzing" event data is part of that treasure. The code conversion also preserves the ability to support any "new" testing program that may be a part of the future of nuclear-weapon stewardship.

Figure 4. Readying a rail for insertion down hole.

The Analysis of Alpha

The basic methods for analyzing reaction-history data have not changed since the first nuclear test. The philosophy is still the same, but the process has improved as technology has advanced over the years. Constructing a continuous alpha curve requires many steps starting with digitizing the film trace recorded by each oscilloscope, through amplitude fitting and baseline correcting within a detector, common timing between detectors, and general editing. When the final curve is constructed, other steps complete the analysis of the curve, such as a polynomial fit, deconvolution, a continuous-flux curve, timing between the two stages, and analysis of the front-end data, which includes the neutron-initiation analysis and high-explosive detonator analysis.

To determine continuous alpha, the function used for device performance, a primary curve may need the relationship in time and amplitude of up to 10 detectors covered by 60–120 oscilloscopes to record the large dynamic range produced by the device. During the analysis of the reaction history, the recording system for each

oscilloscope has to be taken into account, that is, the downhole geometry, cable lengths, and recording-station configuration. A further complication is the need for higher bandwidths to reduce data distortion as alpha increases. Some early NTS data (1965–1980) may have been recorded using up to four different bandwidths, which encourages less distortion for the faster regions of the curve—but makes it nearly impossible to construct a continuous curve. Data recorded at different bandwidths cannot be composited as one curve without precise timing between systems or by numerically applying a deconvolution process. Even then, data precision is compromised.

Obtaining a continuous alpha curve is one goal of our analysis. Of equal importance to the weapon designer is the distortion effect of bandwidth on the entire set of experimental data because the data produced by the theoretical calculation has to be folded with the response of the experimental-data recording system to legitimately match the calculation to the experimental data. The

required precision of this match is presently a collaborative study between P, X, C, and DX Divisions. The results of the study promise to have a significant impact on the accelerated strategic computing initiative (ASCI). The ASCI program is fundamentally a method of testing weapons on supercomputers—hopefully satisfying the requirements of an actual testing program.

The recording system includes the detector, the coaxial cable system, and the various signal paths in the recording station. Over the years the system response was measured very carefully by inserting a step function into the system and recording the distortion of the output step function. This measured response is always given to the designer as part of the complete set of data for an event that is placed on XWARP.

Using the contemporary software that went into production in late 1999, many examples related to the speed and efficiency of the new software plus the large memory of the PC show the improvement in the analysis process. It is important

to realize that through all the software changes the precision of the curve has remained constant over all the years of the UGT data interpretation. This precision has been verified over and over again during the reanalysis of past events during the past eight years.

Presently, the designers have become very aware of the cache of data on the XWARP database and have been asking for detailed interpretation as they learn what is available to them for each set of reaction-history data. In examining the database, they find system information starting from the device and ending at the recording oscilloscope. This includes all the downhole parameters and the system response needed to fold with their calculation. Several ASCII-format files provide the final gamma-flux, alpha, and neutron-source curves. Also included in the database are scanned analysis reports for all the UGTs executed by LANL. Some Lawrence Livermore National Laboratory (LLNL) data is also on XWARP. It is hoped that Aldermasten Weapons Establishment (AWE-United Kingdom) test data will soon be on the database.

Results of the Archiving Program

Reaction history, which has been the basic measurement of device performance on virtually all nuclear tests, is only one of many experiments that are being archived for use by future scientists. Using reaction history as an example, a list of benefits from the archiving program are as follows.

· The knowledge base is being transferred. New physicists and analysts are being integrated into the program. An important feature is our effort to focus on communication between the experimentalist and the weapon designer.

· P-22 is placing the reanalyzed reaction-history data in a well-organized electronic database for convenient access by the nuclear-weapons community. Electronic archiving is more permanent and useful than hard copy archiving.

· Computer software is being transferred and/or developed for contemporary computing requirements. It is important that this area be continually updated because of the rapid changes that occur in computer technology.

· Reanalyzing a set of data requires the understanding of the recording system. This understanding can be applied to any new hardware that may have to be fielded again—whether it is in its original form or in a similar reconstituted system based on modern technology.

· Reanalyzing the data has, in many cases, led to a better understanding of the data and has motivated the investigation of new areas of study which enhances the value of the data. An important fact to remember is it is very unlikely that the U.S. will collect new nuclear test data for some time to come.

· A suite of contemporary experiments can be done, and the knowledge gained from past NTS data is a precursor to deciding which of these experiments have the most benefit to the certification of the stockpile and the understanding of the weapon codes being used by the weapon designers.

State of the Reaction-History Archive

The reanalysis of archived reaction-history data from NTS has been funded since 1993. The annual funding has grown from $100,000 in FY93 to $1,523,000 in FY01. The FY01 amount covers all or part of six regular full-time employees (FTEs) in P-22. In addition, this budget also funds five subcontractors. Additional help for the archiving program (about two FTEs) is obtained from our Bechtel contractor.

P-22 has data in its hard copy archive for all of LANL's 408 UGTs. Of these 408 tests, the vast majority are either directly related to the current stockpile or have significant physics value to the nuclear-weapons program. By the end of FY01, all tests directly related to the stockpile will be in electronic format and stored on the XWARP database for use by the weapon designers. Up to five years of effort will be needed to complete processing of the other events.

P-22 has expended a significant effort to train and mentor individuals to continue our communication with the designers in X-Division after some of our key personnel retire in FY01. This is particularly important with regard to the communication with the recently formed Campaign committees. Additional help, primarily with basic reanalysis problems, is being recruited from the P-22 subcontractor, Bechtel Corp. Bechtel has been particularly helpful with the required software conversion from the VAX/VMS system to the Windows NT computing platform. The last major production code will be completed in FY01.

All data and software from the VAX computer are being transferred to PC servers and the VAX will be decommissioned. The principle production codes are on the server and in production. Other significant production codes that deal with recording-system design and evaluation, calculation of downhole effects, and the convolution effect on data by recording systems are in various levels of software conversion.

Increasingly, the weapon designers are requiring detailed interpretation of the available reaction-history data. This includes verifying the accuracy and completeness of stored data and in many cases comparing the data from one test to another. As the ASCI project develops over the next few years, an intense interest in the advanced diagnostics archived by P-22 promises to develop. Presently, these advanced diagnostics, such as various radiation-flow experiments, spectrometry, and other energy measurements are archived in hard copy form and accounted for in a P-22 database.

Summary and Outlook

Project Description

The P-22 archiving project emphasis is on the conversion of reaction-history data from NTS events to an electronic format that is readily available to the weapon's community and can be understood by the weapon designer. The data are used to enhance the understanding of the performance of a weapon system and are used in the development of weapon design codes. The comparison of the data to theoretical calculations is a primary exercise used in SBSS to certify the current stockpile's safety and reliability.

In addition to reaction-history data analysis, P-22 owns and has in part analyzed data from advanced diagnostic experiments including electromagnetic pulse (EMP). The archiving of fielding issues surrounding the EMP experiment plus the interpretation of the data is presently key information for the Threat Reduction Program. Writing diagnostic procedure handbooks, analysis reports, and the conversion of production codes to a contemporary platform are an integral part of the P-22 archiving program. Finally, mentoring to preserve the knowledge gained from 50 years of nuclear-weapon testing is a requirement of the P-22 archiving program.

Collaboration and Coordination

The P-22 archiving program closely collaborates with the weapon designers to insure the availability of data on a priority basis. Much effort is expended to insure that the designers fully understand the interpretation of the data available to them. With regard to the actual analysis task, Bechtel, a Laboratory contractor, is called upon to perform initial analysis of reaction-history data, which includes in part, film reading, recording system calibration input, and data compositing.

A study of the quality of the alpha function is presently in progress, using expertise from TSA-1 and DX-3 as well as P-22. The Laboratory is mentoring interested individuals that will potentially replace current archiving team members who are nearing retirement. Finally P-22 is an important partner in the LANL NWAP (Nuclear Weapon Archiving Project).

Issues, Constraints, and Assumptions

The most important issue in the P-22 archiving program is "aging team members and no definite replacements". The Bechtel contractor has added a new FTE to the effort and training by P-22 personnel is in progress. Two TSMs in P-22 have shown some interest in the archiving program and have volunteered to begin a training plan. The lack of personnel contributes to our inability to keep past skills alive—a real readiness issue. The recent LANL hiring freeze has been a very real roadblock to the future health of the P-22 archiving program. On a positive note, there is some indication that the program will have sound funding for the foreseeable future.

Further Reading

Written materials related to reaction history can be found in the P-22 vault. Many of the papers are unclassified. Contact Kent Croasdell [(505) 667-2483, crosdell@lanl.gov] for further information or a copy of an unclassified report.

Unclassified Reports

E. Bennett, "Fifty Years of Reaction History," Los Alamos National Laboratory report LA-UR-92-2667 (August 1992).

E. K. Hodson, "Predictable Unfolding in the Time Domain," Los Alamos Scientific Laboratory report LA-03830 (December 1967).

E. K. Hodson, D. R. Thayer, C. Franklin, "Adaptive Gaussian Filtering and Local Frequency Estimates using Local Curvature Analysis," Los Alamos National Laboratort report LA-UR-80-0481 (February 1980).

Classified Reports

E. K. Hodson and K. C. Croasdell, "Recording Reaction History with Digital Systems (U)," Los Alamos National Laboratory report LA-CP-93-0302 (November 1993).

Proton Radiography

*D. A. Clark, C. J. Espinoza, J. J. Gomez,
G. E. Hogan, F. E. Merrill, B. Montoya,
C. L. Morris, M. M. Murray, and
A. Saunders (P-25); K. R. Alrick,
N. T. Gray, M. Y. Hockaday, N. S. King,
K. B. Morley, P. D. Pazuchanics, and
M. D. Wilke (P-23); D. J. Clark (P-22);
J. B. McClelland (P-DO);
A. R. Mathews and J. S. Sarracino (X-4);
J. Favorite, A. B. Kaye, and
J. D. Zumbro (X-5); K. L. Buescher,
D. J. Cagliostro, J. E. Pearson,
G. L. Sandine, and K. R. Vixie (X-8);
W. J. Deninger, E. N. Ferm, and
K. H. Mueller (DX-3);
C. T. Mottershead (LANSCE-1);
E. Ables, M. B. Aufderheide,
P. D. Barnes, Jr., E. P. Hartouni,
H.-S. Park, R. A. Soltz, A. S. von
Wittenau, and D. M. Wright (LLNL);
S. D. Gardner, N. S. Khalsa,
R. P. Liljestrand, D. V. Morgan,
R. T. Thompson, T. W. Tunnell, and
A. Whiteson (BN LA); R. Prigl and
J. Scaduto (BNL CAD); G. A. Greene
and A. L. Hanson (BNL ES&T); and
P. Robertson (AWE)*

Introduction

Over 100 years ago Wilhelm Roentgen discovered x-rays and utilized their ability to penetrate matter to look within a living human body (his wife's hand). Since that time x-radiography has been used for a number of applications where the inside of an object must be viewed. A source of x-rays, usually produced by the interactions of an energetic electron beam with a metal anode, is directed at an object and the transmitted beam is measured on a detector located behind the object. The detector produces an image of the shadow cast by differential absorption of the material that composes the object.

Late time hydrotest radiography is the experimental cornerstone of the stockpile stewardship program, an important part of the Los Alamos National Laboratory (Laboratory) mission. In these experiments the fissionable material in a weapon primary is replaced by simulants and the material densities and flow, thus the name hydrotest, are studied in explosive driven systems. Although these experiments produce no nuclear yield, they can provide data on how material

properties influence the progression of a nuclear weapon up until the time when nuclear process began to dominate the dynamics. In these experiments data and models developed in science experiments can be integrated and tested, engineering changes can be tested, and aging effects measured in systems that are as close to those obtained in a nuclear explosion as can be obtained under a comprehensive test ban treaty. Until recently the only late time diagnostic of the compressed primary in a hydrotest has been flash x-radiography. Considerable resources have been expended to explore the limits of dose and spot size in order to provide the best possible data. It is becoming clear that these data are limited by the physics of electron and gamma ray interactions with matter, and do not meet the requirements of stockpile certification.

About six years ago, medium-energy proton beams were recognized to have a mean free path (the mean length that particles travel before interacting in material) much better matched to diagnose hydrotest systems than x-rays. Over the last six years, the techniques

needed to perform dynamic experiments using proton beams have been developed, and proton radiography has been demonstrated to provide data on dynamic systems that is far superior to that which can be obtained with flash x-rays, even for thin systems.

Dynamic experiments using the 800 MeV protons have become routine part of the Los Alamos Neutron Science Center (LANSCE) program at the Laboratory. In addition we have performed experiments at using 24 GeV protons from the Alternating-Gradient Synchrotron (AGS) accelerator at Brookhaven National Laboratory (Brookhaven) using static test objects to clearly show some of the advantages of proton radiography when compared with the Dual-Axis Radiographic Hydrotest (DARHT) facility, the state-of-the-art flash x-ray machine.

Transmission Radiography

In transmission radiography, the transmitted flux through an object is used to measure its areal density. The transmission, $t_\lambda = N/N_0$, is given in terms of the path length l through the object and the mean free path λ by:

$$t_\lambda = e^{-\frac{l}{\lambda}} \qquad (1)$$

Where N_0 and N are the incident and transmitted number of particles respectively. Transmission is measured as a function of position and inverted to calculate the thickness of the object as:

$$l = -\lambda \ln(t_\lambda) \qquad (2)$$

Here, λ, is given by:

$$\lambda = \frac{1.}{\rho\sigma}, \qquad (3)$$

Equations 1 and 2 assume that the material can be described with a constant λ. When this is not the case (e.g., for bremsstrahlung x-rays where the x-rays are produced into a continuous energy spectrum) Equation 1 needs to be convoluted with the energy spectrum. In this case the solution is more difficult to obtain.

The uncertainty in the path length can be calculated, assuming Poisson statistics for the transmitted beam, by taking the derivative of Equation 2 with respect to the transmitted flux and propagating the error in N to l. This gives

$$\Delta l = \frac{\lambda}{\sqrt{N}} = \frac{\lambda}{\sqrt{N_0}} e^{\frac{l}{2\lambda}}. \qquad (4)$$

Setting the derivative of Equation 4 to zero and solving for λ gives the optimum mean free path, $\lambda = l/2$, for minimizing the uncertainty, Δl, for a fixed incident particle budget, N_0.

Thick object radiography is driven by this result. The large machines that have been built for hydrotest radiography in the U.S. (DARHT, PHERMEX, and FXR) are optimized for producing 4 MeV x-rays, because this is the energy where the x-ray mean free path peaks in high-Z materials.

Comparing x-ray and proton doses requires taking into account a number of experimental effects shown in Table 1. These include effective vs actual dose for x-rays, geometry, practical detector efficiencies, and the effect of containment windows. The results of simulated radiographs, neglecting backgrounds bluing and other effects is shown in Figure 1. The comparison assumes doses of 10^{11} protons with a width of 2.5 cm and 500 rad at one meter for x-rays. These are the doses that have been obtained at the AGS proton accelerator and at DARHT respectively.

These simulations demonstrate the dramatic advantage obtained from protons for objects thicker than about 200 gm/cm^2. The large fluctuations observed near the thick end of the step wedge in the x-ray analysis result from pixels in which there are zero detected x-rays, and thus no information on the thickness. These simple predictions are supported by measurements on classified test objects.

500 gm/cm^2
x-ray
proton
50 gm/cm^2
1.05
x-ray
proton
0.95
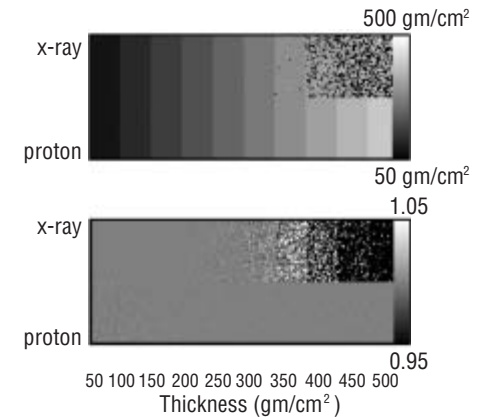50 100 150 200 250 300 350 400 450 500
Thickness (gm/cm^2)

Figure 1. Top panel: Image of inferred areal densities using equation 2 from simulated radiographs made with x-rays (top half of image) and protons (bottom half of the image) for a uranium step wedge. Bottom panel: The ratio if the inferred densities to the actual densities. The pixel size is 0.5 mm.

Table 1:
Correction Factors Applied to the Proton X-Ray Comparison

	Correction Factors	
	X-Ray	Protons
Useful Flux/Total Flux	0.3	1
DQE	0.3	0.4
Distance to Source	$(1./1.2)^2$	1
Absorption in Windows	$\exp^{-13.7/32.1}$	$\exp^{-54.86/106.4}$
Total	0.040787484	0.238856522

Charged-Particle Radiography

The invention that allows charged-particle radiography to be useful on thick objects is the idea that the transmitted beam can be focused in a magnetic lens creating an image with a long standoff from the dynamic object. The ability to focus both the beam and transmitted flux gives flexibility to charge particle radiography that doesn't exist for x-radiography.

A simple model for proton or other charged particle radiography can been obtained by assuming that nuclear scattering results in the removal of beam particles from the transmitted flux described by Equation 1 and that Coulomb scattering can approximated by assuming transmitted particles are scattered into a Gaussian shaped angular distribution. In this approximation integration of the angular distribution between limits imposed by angle collimators at the Fourier points in the lenses results in closed form expressions for the transmission. A beam transmitted though an object acquires an angular spread,

$$I(\theta) = \frac{1}{\pi \theta_0} e^{\frac{-\theta^2}{2\theta_0^2}} \qquad (5)$$

Where,

$$\theta_0 = \frac{14.1}{p\beta} \sum_i \frac{\rho_{Ai}}{X_i} \qquad (6)$$

Here p is the beam momentum, β = v/c where v is the beam velocity and c is the speed of light; X_i is the radiation length for the $i'th$ material. Throughout the rest of this work the sum will be implied. This can be integrated between angular limits, θ_1 and θ_2,

$$\int I(\theta)\sin(\theta)d\theta d\phi = (e^{-\frac{X_2}{\rho_x}} - e^{-\frac{X_1}{\rho_x}}) \qquad (7)$$

where $\rho_x = \sum_i \frac{\rho_{Ai}}{X_i}$ is the areal density of an object,

$$X_1 = \frac{p^2\theta_1^2}{2 \times 14.1^2},$$ is a characteristic areal density associated with the large polar angle limit, θ_1, and,

$$X_2 = \frac{p^2\theta_2^2}{2 \times 14.1^2},$$ is a characteristic areal density associated with the small polar angle limit, θ_2.

Multiple lenses on a single axis, with different angular collimators, allow Coulomb radiation lengths to be separated from nuclear attenuation lengths in proton radiography.

Transmission through a single lens, including both nuclear and Coulomb attenuation, is given by,

$$I = e^{-\rho_\lambda} (e^{-\frac{X_2}{\rho_x}} - e^{-\frac{X_1}{\rho_x}}) \qquad (8)$$

The most precision can be obtained with a set of two lenses where the first is optimized to measure only nuclear attenuation by having a large aperture. If the small angle cut is zero and the large angle limit is large enough so that second term can be ignored transmission through the first lens in a two-lens system is

$$I_1 = e^{-\rho_\lambda} \qquad (9)$$

If the second lens has a large, large angle limit, but does have a small angle cut (Ferm collimator) than transmission through the second lens is given by,

$$I_2 = e^{-\rho_\lambda - \frac{X_2}{\rho_x}} \qquad (10)$$

Equations 5 and 6 can be solved for the nuclear attenuation length weighted areal densities,

$$\rho_\lambda = \ln(I_1) \qquad (11)$$

and the radiation length weighted areal densities,

$$\rho_x = \frac{1}{\ln(I_1) - \ln(I_2)} \qquad (12)$$

Hydrotest radiography requires a high energy beam to penetrate thick objects while keeping the multiple scattering angle and energy loss small enough to allow good position resolution. Proton energy of 50 GeV has been chosen for the Advanced Hydrotest Facility (AHF) to meet the design goal of 1 mm for contained shots. The multiple scattering in an armored window, projected to the center of a containment vessel gives about a 500-micron contribution to the overall system resolution with this incident beam energy.

In spite of the intellectual arguments given above, proton radiography has meet with considerable skepticism from the weapons community. This has lead to a demonstration program whose goal has been to validate these ideas. This program has had two parts: one using low energy proton beams (800 MeV) from the LANSCE accelerator at the Laboratory to perform dynamic experiments on thin systems, and the other to use high energy beams (24 GeV) from the AGS accelerator at Brookhaven to obtain static data on thick systems.

Line C

The LANSCE linear accelerator at the Laboratory provides an 800-MeV proton beam. The beam is accelerated with a micro-structure of short 100-psec-long bursts of about 5×10^8 protons every 5 ns. The beam is provided at 120 Hz in 600-μsec-long pulses. The feasibility of radiographing small (1 lb of high explosives) dynamic experiments, with a lens system, was first demonstrated at line B. For the last three years, a program of dynamic experiments has been performed on a three-lens system constructed in line C. A photograph of the line C is shown in Figure 2 below.

Several new capabilities were added to line C in the past year. Both magnetic and optical magnification were demonstrated to improve the position resolution one can obtain for on the order of 400 μm using the standard set up to as good as 100 μm by reconfiguring the two magnetic lenses to provide a single lens with a magnification of × 3. We have discovered slit collimators can be used to trade off position resolution and statistical precision independently in the x- and y-planes. Beam blockers, as opposed to collimators, were shown to provide improved density precision and dynamic range. A capability was incorporated in two experiments to look at spall layers simultaneously in the radiographs and with visor. The results were found to be in good agreement.
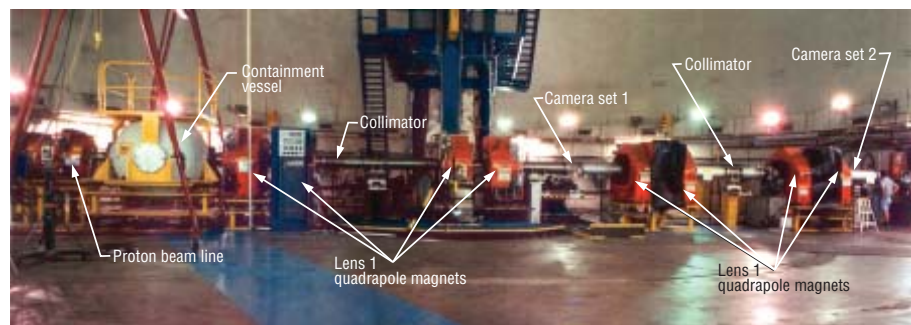
Camera Developments

Significant progress has been made in developing and applying thin (<3 mm) scintillators as radiation-to-light converters to replace the lower resolution scintillating fiber-optic converters utilized in initial proton radiography efforts. The ideal, final scintillator solution has not been completed but prototype, 42-mm-square tiles with blackened edges covering a 126-mm-square field of view have resulted in high quality images with better than 2.5 lp/mm resolution and interframe times of 358 ns. Materials for these scintillators are lutetium oxyorthosilicate (LSO), yttrium oxyorthosilicate (YSO), cesium-iodine (CsI), and mixtures of inorganics. Continued development is being carried out in this area.

Efforts are ongoing to implement "4-shooter" framing cameras in order to obtain fast shuttered (<200 ns interframe times) images with good resolution (<1.5 lp/mm). We are continuing to optimize this system with upgraded charge-coupled device (CCD) readout cameras, which will result in 20 images per image plane in the near future.

Figure 2. Photograph of the Line C proton radiography system.

The single snapshot camera system based on unique 12 KV diodes coupled to cooled CCD cameras with 1600 × 1600-pixel arrays has resulted in system resolutions better than 2.5 lp/mm. These cameras are very cost effective and have been implemented as our baseline imaging system. We continue to evaluate new, cooled CCD cameras to provide improved signal to noise, more reliable fiber optic coupling techniques, and better scene contrast. The latter is currently determined by the gated, high-voltage planar diodes.

A backthinned, 1600 × 1600 cooled CCD camera with mechanical shutter coupled to a tiled LSO scintillator was developed for experiments at the Brookhaven AGS facility to evaluate capabilities for proton radiography at 24 GeV. These results will permit extrapolation to higher energies envisioned for future proton radiography facilities.

Significant progress has been made in better defining directions for prototyping a detector system for future high energy proton radiography. Single imagers with a capability of more than 64 frames with interframe times as short as 200 ns and dynamic range in excess of 1000:1 are being targeted for a prototype utilizing photodiodes and backplane readout techniques only now reaching a maturity to permit implementation. A pixel-well capacity of >500 K is a goal to permit precision density measurements. Some work is continuing on in-proton-plane direct-conversion imagers.
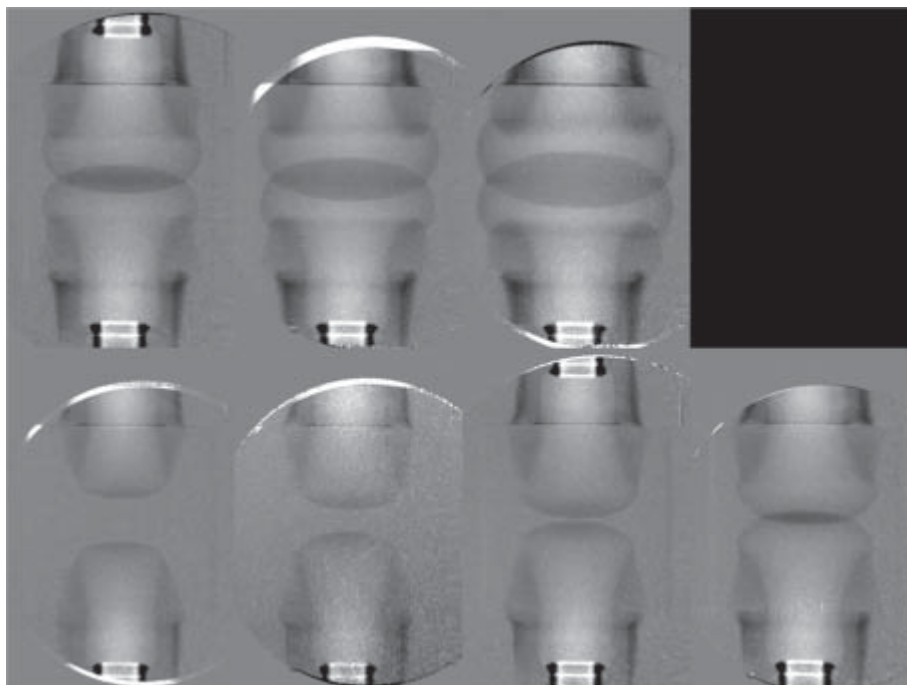

Figure 3. Radiographic sequence showing the collision of two burn fronts in PBX-9502 high explosives. The pictures are ratios of the dynamic to static radiographs. The time sequence runs from the lower left to the upper right.
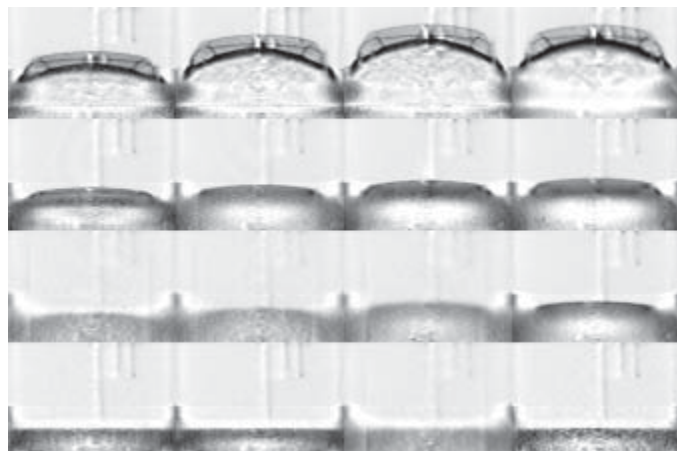
Experiments

We performed 40 dynamic experiments using line C during fiscal year 2000. An additional seven experiments were performed while LANSCE was on from October until December. Thirteen of these were classified. Typically between 7 and 16 radiographs were taken for each experiment.

A number of the experiments were aimed studying detonation of high explosives. A lot of effort has been focused on the insensitive high explosive (IHE) PBX9502. Unclassi-fied experiments were performed to measure the corner-turning properties and equation-of-state parameters for detonation products. A sequence of radiographs show the interaction of colliding detonation waves is shown in Figure 3.

Experiments aimed at studying dynamic material failure have formed an increasingly important part of the line C program. An example of an high-explosive-driven (Taylor wave) tin plate is shown in Figure 4. The failure of the tin is clearly observed in the later-time radiographs. Line out of the density distributions can be used to follow the development of the spall layers from shock break out at the tin surface. The spall of the surface was confirmed by visor data, but the radiographs provide much more data on the richness of the failure phenomena.

Figure 4. Reconstructed volume densities showing the Taylor driven (high explosive) spall of a tin plate.

Figure 5. A view of the Experiment 933 setup looking upstream from the first camera location. The active cameras can be seen in the middle of the photograph.

AGS Data

Two experiments have been completed at the AGS using single, 40-ns-long bursts of beam line U, Experiments 933 and 955. These have demonstrated many of the features of proton radiography. A matching section and two lenses were constructed using existing refurbished 8Q48 quadrapole magnets in line U at the AGS for Experiment 933. This system was installed and commissioned using single pulses of up to 10^{11} protons at 24 GeV/c provided by the AGS. The pulse intensity was administratively limited to this value by AGS safety requirements. A picture looking upstream from the end of the second lens is shown in Figure 5.

For Experiment 955, the magnets from the two-lens system were used to construct a single shorter lens with larger angular acceptance and smaller chromatic aberrations. Data from Experiment 955 are still under analysis, so results from Experiment 933 are presented below.

Beam Characterization

Diagnostic data were obtained on a pulse by pulse basis with transformers, which measured proton fluxes at three locations in the beam line; upstream of the diffuser location, and at each of the down image locations downstream. The beam position and angle at the diffuser location were monitored using two CCD cameras looking at two phosphors, one mounted on the diffuser and one located approximately 6 m upstream of the diffuser. Combining the data from these measurements allows accurate pixel-to-pixel normalization of transmitted flux through an object to be obtained by normalizing to the measured fluxes and correcting the beam profile for shifts in position measured using the upstream images. Although preliminary analysis of the upstream data shows a correlation with the down stream beam spot location, this information was not used in the Experiment 933 analysis. However analysis of the beam data in Experiment 955 showed that this method works, indicating a similar system would have a large impact on AHF costs by removing much of the need for an upstream lens in the matching region.
The matching lens was tuned by

removing the downstream collimator and installing a phosphor and CCD camera system at the collimator location. The beam was centered on the phosphor by steering it at the diffuser location and adjusting the matching quadrapoles to minimize the beam spot. The size of the beam at the collimator location corresponded to about 0.5 mrad of angle resolution at the object location. This size, which is related to the emittance of the accelerator, puts a scale on the thinnest objects that can be radiographed. The 0.5 mrad-measured resolution corresponds to about 0.85 radiation lengths or about 6 mm of

tungsten. This is radiographically equivalent to having a uniform, fixed amount of material in addition to any other object that is in the beam. There was also a diffuse halo amounting to about 4% of the total beam intensity. The beam halo was eliminated in Experiment 955 by changing the beam tune. The beam tune used for Experiment 933 resulted a significant fraction of the beam intercepting an upstream magnet, producing both a halo and background. The beam emittance can be accounted for radiographically by including it in the transmission.
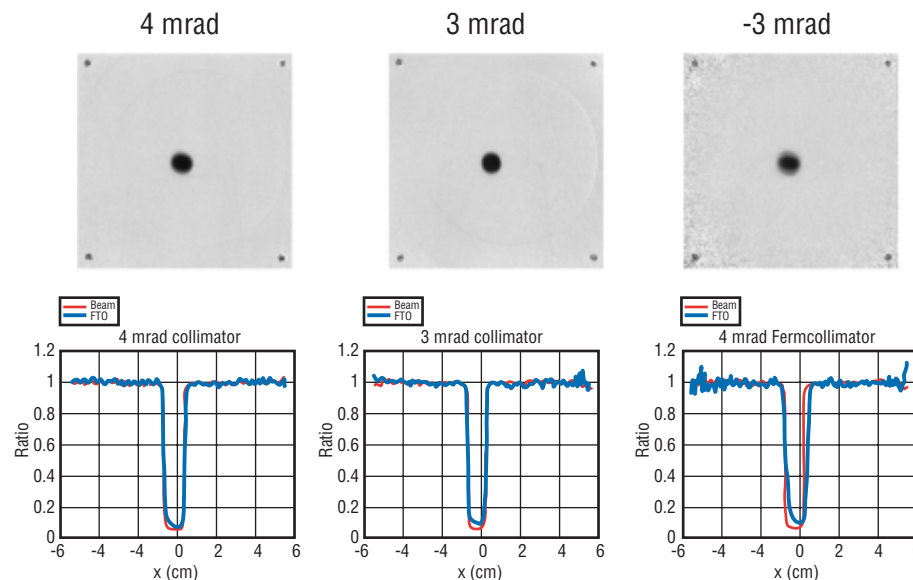
Background Measurements

After tuning the both the matching magnets and the lens focal length, a 1 mrad collimator was installed in the upstream lens, a 1-cm-diameter, 15-cm-long tungsten rod was mounted at the object location at the beginning of the first lens, and images were made with and without the French Test Object (FTO) mounted in the object location of the second lens. The tungsten rod produces in a hole in the beam downstream of the fist lens. The background produced by each of the collimators was measured by studying how much this is filled in when an object is put in the beam with the collimator mounted in the downstream lens. The backgrounds measured from the 4.4- and 3-mrad normal and 3-mrad Ferm collimators were 2.1%, 3.9%, and 4.6% at the limb of the FTO, respectively. Although these are somewhat higher than simulations predict, they are low enough to be easily dealt with. Some of these results are displayed in Figure 6.

Figure 6. Top: Ratios of radiographs of the FTO with the shadow bar in to the shadow bar out for each of the collimators. Bottom: Line outs of the beam ratioed images with the shadow bar in and the FTO in in blue and with the FTO out in red.

Position Resolution and Metrology

Position resolution and accurate metrology are important parameters for AHF applications of proton radiography. Quantitative measures of both of these parameters were obtained during Experiment 933.

The magnetic optics in the beam line and the photon optics in the detectors potentially introduce geometric distortions. These can be measured using a fiducial grid plate, shown in Figure 7.
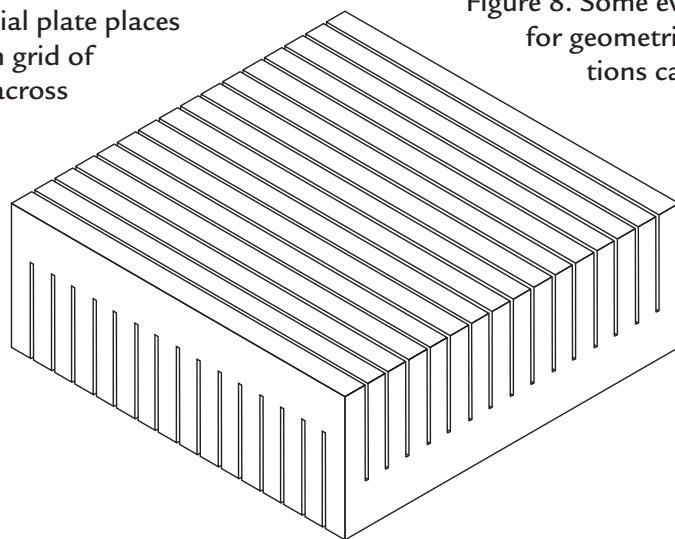
The fiducial plate places a uniform grid of features across the entire field of view. In the acquired data, the positions of these features can be used to measure geometric distortions.

A radiograph of this object is shown in Figure 8. The expected structure is clearly visible. The data have been divided by a beam image, the position scale was offset and adjusted with a rotation and linear scaling in both x and y. The residuals for all of the intersections are potted in the rest of Figure 8. Some evidence for geometric aberrations can be seen in the residual plots. The root mean square (RMS) position error average across the entire field of view is less than 100 μm, with the largest contribution coming from the corners, where geometric aberrations are the largest.

Position resolution was measured using a resolution pattern machined into a 2.5-mm-thick piece of platinum, in both image planes. These data are shown in Figure 9. The position resolution was measured to be 250 μm full width at half maximum (FWHM) in the first image plane. A similar value was obtained in thicker classified test objects.
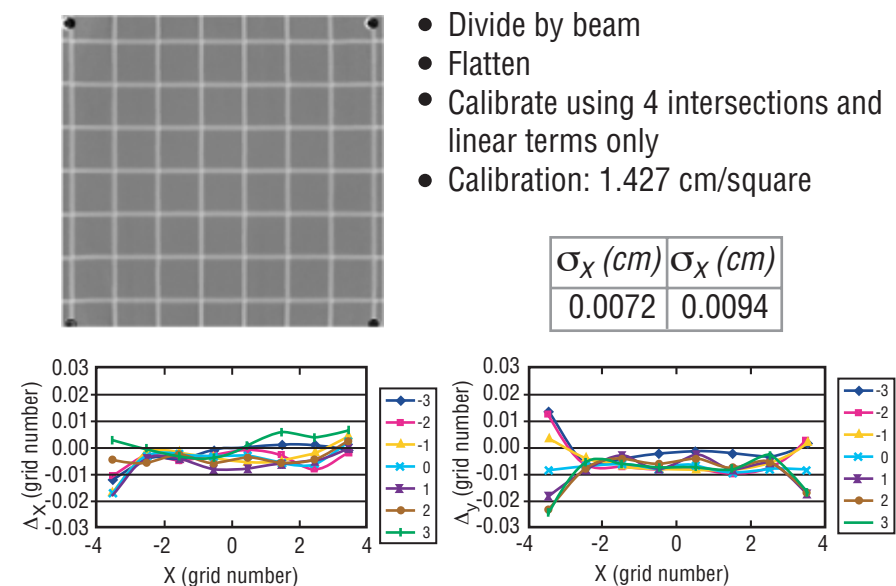

Figure 7. Fiducial grid plate. The plate is 3" thick, with perpendicular slots 2" deep cut into both faces. Each slot in the top face intersects each slot in the bottom face, forming a regular grid of square holes through the entire block.

- Divide by beam
- Flatten
- Calibrate using 4 intersections and linear terms only
- Calibration: 1.427 cm/square

σ_X (cm)	σ_X (cm)
0.0072	0.0094

Figure 8. Radiograph and position residuals from the fiducial plate test.

a

1 1p/mm   1 1p/mm
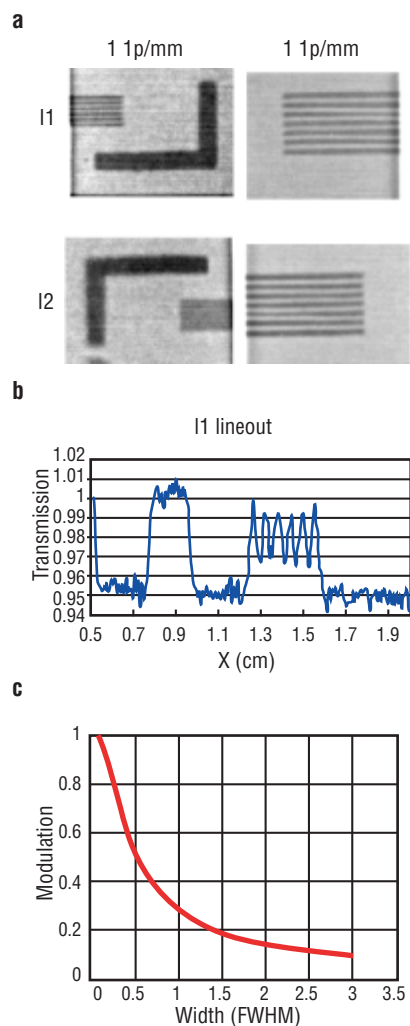
I1

I2

b

I1 lineout

c

Figure 9. (a) Radiographs of the resolution test pattern. (b) Lineout of the 2-line pair/ mm test pattern from image location 1,3. (c) Plot of the relationship between modulation and resolution.

Step-Wedge Measurements

After completing the lens characterization, a set of step-wedge measurements were completed on tungsten, copper, carbon and lucite, in order to provide cross sections to be used in quantitative analysis of other test objects. The finite acceptance of the beam line as a function of energy loss and scattering angle in an object can be expressed as an effective cross section, which must be known to reconstruct the density of an object from its radiograph. A simple way to measure the effective cross sections over the range of interest is

to use a set of step wedges constructed from the same materials as the object and that span the thickness range of the object.

Figure 10 illustrates the step wedges used in Experiment 933. This design using two wedges back to back allows us to make a new configuration, a pair of wedges with small steps separated by a spacer block of the same material. This allows us to make the measurement on steps that differ by a small amount across a large range of total thickness, using only one pair of wedges. The approximate mid-plane symmetry simplifies alignment along the beam direction, and arranging the thickest part of the wedge to be in the center of the beam provides a better match of attenuation to the flux, optimizing the statistical precision of the cross section measurement for a given proton flux.
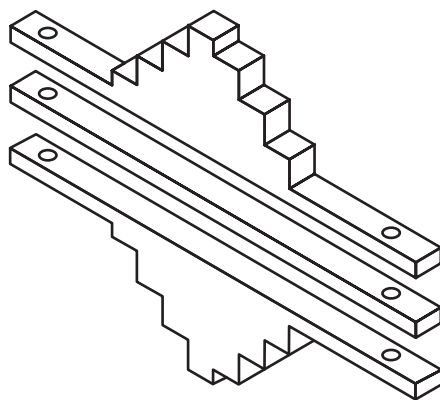

Figure 10. Doubly symmetrized step wedge. The thickness of the steps decreases on either side of center, more or less following the incident beam intensity. Using a pair of half-height wedges back to back keeps the center at a constant position and allows the insertion of spacer plates of the same material.

The steps in the analysis of the step-wedge data were to first align and average each of the four image plates exposed in each image plane for each picture. Four image plates were used to increase the detector quantum efficiency (DQE). Estimates made by comparing actual images with simulations suggested the resulting DQE was in the range of 20%–40%. The data from image location 1 (I1) where divided by a smoothed beam image. The results were "flattened" by fitting a two-dimensional polynomial to the regions of the picture were there was no material in the beam and then dividing the image by this polynomial. This helps to remove artifacts due to beam motion and nonuniform response of the image plates. The data from image

location 2 (I2) were taken with a Ferm collimator. These data were rotated to account for the inversion of the lens, aligned with the images from image location 1 (I1), and then divided by the I1 results. The procedure for IL1 is illustrated in Figure 11.

Cross sections were measured in steps of 1% of an attenuation length up to the full thickness of the FTO for each of the materials. Some of the results for the 10% step wedge are shown in Figure 12. The fit demonstrates the quality of quantitative agreement obtained between a semi-empirical model and the data. Step-wedge data

were also taken looking through an additional 345 g/cm² of tungsten. These data illustrate the capability of proton radiography to obtain quantitative data over an extremely wide dynamic range of object thickness. The full set of data for I1 for the tungsten step wedge is shown in Figure 12.

The data in Figure 12 demonstrate the potential for material identification. The step wedges have been designed to cover a similar thickness range in nuclear attenuation lengths, but have a much different thickness in Coulomb radiation lengths, with the tungsten being much thicker than the carbon in
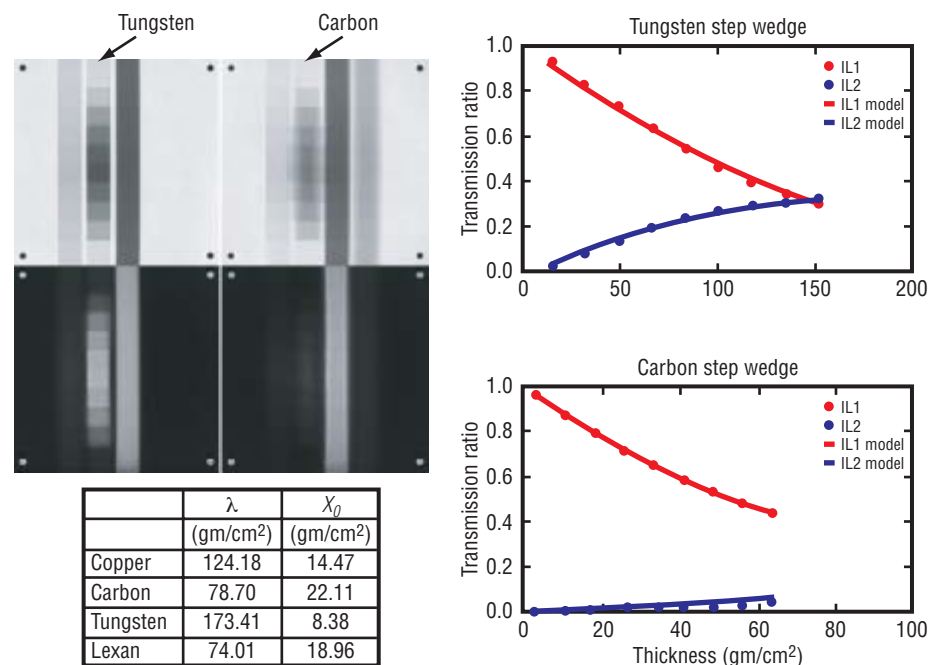

	λ (gm/cm²)	X_0 (gm/cm²)
Copper	124.18	14.47
Carbon	78.70	22.11
Tungsten	173.41	8.38
Lexan	74.01	18.96

Figure 12. The carbon and tungsten 10% step wedge radiographs and data.

$x'=a+bx+cy \; ; \; y'=d+ex+fy$　　Calibrate, align, average

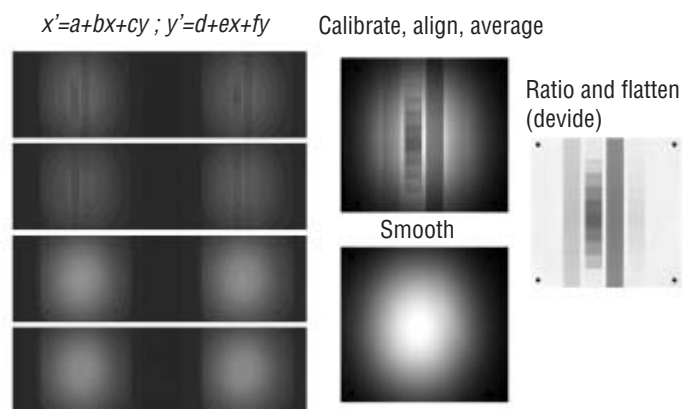Ratio and flatten (devide)

Smooth

Figure 11. Images from the various steps in the analysis procedure

radiation length units. This results in much more multiple scattering in the tungsten than in the carbon. Because of this there is a dramatic difference in the I2 images, where the tungsten step wedge is clearly visible and the carbon is difficult to discern.

For thin objects, Equations 10 and 11 apply. This can be seen below where the functions of the transmission given by Equations 10 and 11 are plotted for the various 10% step wedges are plotted. The slope of these curves, which should be a measure of material type, can be seen to display the expected material dependence.

The tungsten step-wedge data span a wide range of thickness. A fit to the entire data set, assuming a Gaussian multiple scattering angular distribution and a Guassian beam emittance is shown as the solid line in the figure. The function form fitted to the flattened transmission is:

$$I = e^{-\rho_\lambda} \frac{\left(1 - e^{-\frac{X_1}{\rho_x + \rho_{fixed}}}\right)}{\left(1 - e^{-\frac{X_1}{\rho_{fixed}}}\right)} \qquad (12)$$

The offset, ρ_{fixed}, has been added to account for the finite beam emittance. The denominator has been added to account for the flattening, which forces the transmission to be 1 for zero thickness, even though there is some attenuation due to the beam emittance. This function can be seen to give a good account of the data over a very wide range in step wedge thickness. The fixed offset is also the reason for the nonzero intercept of the curves in Figure 13.
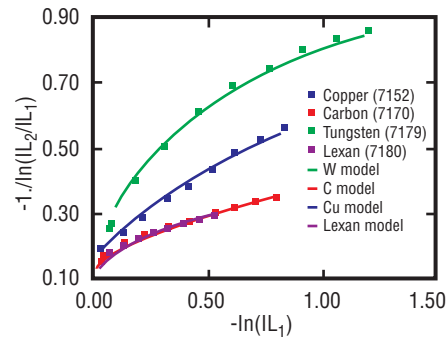

Figure 13. Plot of the functions of the transmission suggested by Equations 10 and 11 to demonstrate material identification. The materials in the step wedges are clearly distinguished by different slopes.

The approximations in Equation 12 do not work well for low-Z, thin objects because of the long tails on the beam that can be observed in Figure 6, and because of the single scattering tail on the multiple scattering angular distribution. This can also been seen by the departure from linearity for thin objects in Figure 13. The small amount of multiple scattering introduced by the low-Z step wedges results in exaggerated attenuation when it is convoluted with the tails on the beam distribution. Nevertheless the materials in the step wedges are clearly distinguished by different slopes. The effect of the angle cut in the first lens leads to the departure from linearity for the thicker steps of tungsten step wedge for which the multiple scattering cone doesn't fit within the lens acceptance.

Quantitative Density Analysis

The tungsten densities from the FTO have been reconstructed by using the data-analysis procedures similar to those outlined in the step-wedge analysis. After the four image plates were averaged, the results were divided by model radiographs of the outer foam and copper shells and then the flattening procedure was applied to the region of the radiograph outside of the tungsten region. The resulting transmission image was transformed from transmission to areal density using the same procedure as was used in the step-wedge analysis but being careful to take into account the overlying material, including the outer copper and foam shells of the FTO. The resultant areal density image was centered and volume densities were calculated using a conditioned Abel inversion method described previously.

The resultant volume densities can be compared with the measured tungsten density of 18.28 ±0.07 gm/cm^3. A histogram of the densities measured on (169 μm)^3 voxels in the region of the tungsten is shown in Figure 16. The agreement between radiographic density,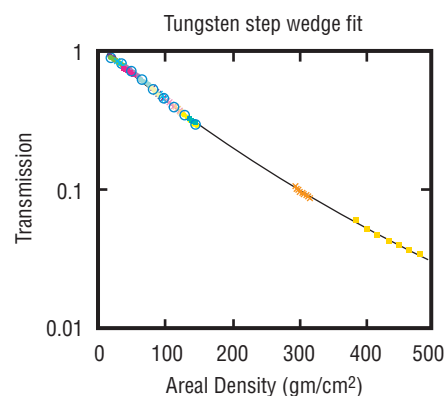 and that obtained from metrology is robust and precise at the level of a percent or so. The AHF goal, driven by the criticality requirement, is to measure densities to 1%–2% in absolute precision. This result meets that goal for the simple geometry of the FTO.

$\bar{\rho} = 18.2\ \gamma\mu/\chi\mu^3$
$\sigma = 4.8\%$

Figure 16. A histogram of radiographically measured densities in the tungsten region of the FTO. The mean value and the width are given in the figure.

Model of outer shells

Areal density
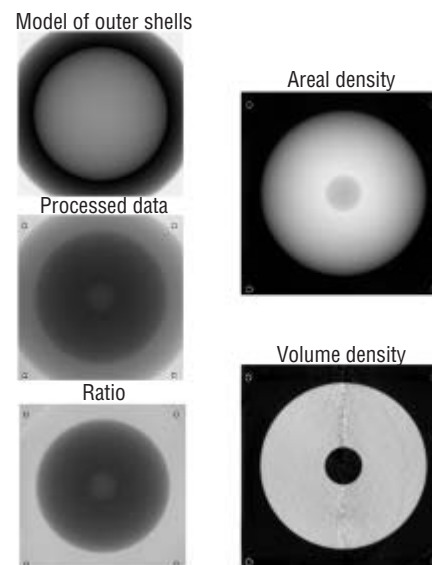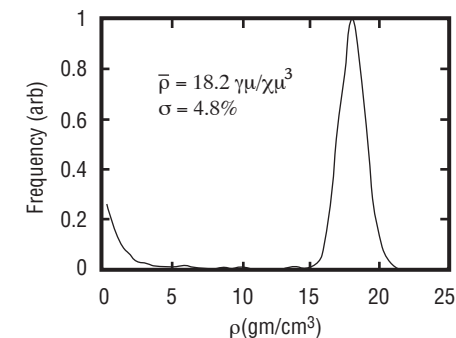
Processed data

Ratio

Volume density

Figure 15. (Left top) Model of outer shells
(Left middle) Measured transmission data
(Left bottom) Measured data divided by the model
(Right top) Tungsten areal density
(Right bottom) Volume density.

Tungsten step wedge fit

Figure 14. Image location 1 tungsten step-wedge data set. The line is a fit to the data that is used in the FTO analysis presented below.

Edge Resolution

The half density contour for both the inner edge and the outer edge of the FTO has been extracted and analyzed to determine the precision with which edges can be extracted from high-energy proton radiography. The AHF requirement for this quantity is 75 μm. The radius for each of the x-y pairs was extracted from the contours, and then the mean and standard deviation of these was calculated. There was no constraint on the radius of curvature and no additional smoothing beyond that from the conditioned-Abbel inversion. This analysis provides an unbiased estimate of the precision with which radii can be extracted. Limits to the precision are due to the statistical accuracy of the reconstruction (the exposure of 10^{10} protons) and by systematic sources of error such as magnetic aberrations. The contours are displayed as the red lines in Figure 17.
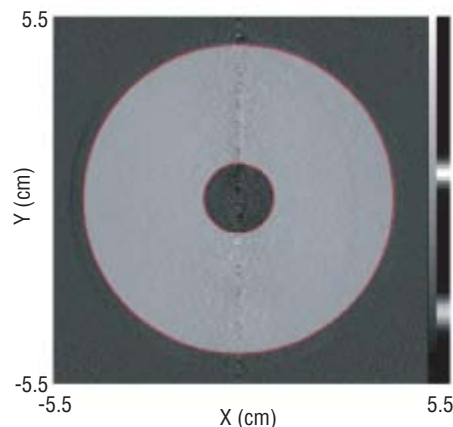

Figure 17. The red line shows the result of the contour finding routine on the volume density image from the FTO tungsten reconstruction.
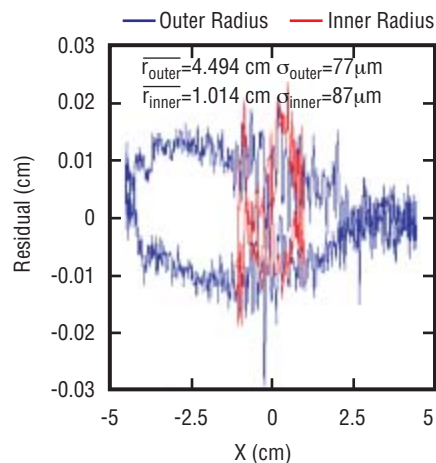

Figure 18. The residual (difference between the radius of the contour and the average radius) for the outer edge of the FTO in blue and the inner edge of the FTO in red.

The difference between the radii of the extracted contour and the average radius are plotted as a function of x in Figure 18 for both the inner radius and the outer radius. Also shown in the figure are the mean and the standard deviations averaged over the entire contour.

The average values for the measured outer and inner radii of 4.494 and 1.014 agree well with the known dimensions of the object of 4.500 and 1.000 cm respectively. However, systematic discrepancies clearly dominate the residuals. This can be seen in Figure 16 as the large correlation between the residual and x position. The random fluctuations, which are a measure of the statistical uncertainty and which impose the ultimate limit to the precision of edge determination, contribute about 30-μm to the total RMS.

Test-Object Measurements

Following this sequence of lens setup and radiographic calibration, experimental data were taken on a wide range of test objects. Some of these experiments allowed direct comparisons with DARHT, FXR and microtron x-radiography measurements. The dynamic range and sensitive of flash proton radiography were demonstrated to exceed both the current state of either flash or fixed target x-radiography in the qualitative results of all of these experiments.

Summary and Outlook

High-energy proton radiography has been shown to provide a new tool that is far superior to flash x-ray radiography. Results from the AGS at Brookhaven National Laboratory demonstrate a factor of 10–100 improvement over results obtained at DARHT on static test objects. The unique features of charged particle radiography, the ability to adjust the contrast using a collimator, to magnify the image using magnetic optics, and to provide composition dependence have all been demonstrated. The line C 800 MeV facility is continuing to be useful for making multiple-time radiographs of important dynamic experiments for Science Based Stockpile Certification.

Physics Applications
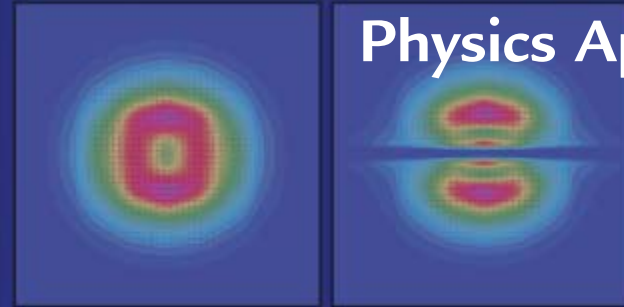
As mentioned before in this report, basic research and applied research exist in Physics Division in a synergistically symbiotic form; each nourishes and inspires the other. As researchers delve into the physics of plasmas or superconductors or optics, novel applications of those investigations present themselves and are developed. These applications benefit not only the scientific and national-security programs in which they are developed here at the Laboratory, but also spin off into technologies useful in other fields and industries. It is, in part, through the development of these applications that we also develop instruments and diagnostics with novel capabilities that can lead to the next great discoveries in our research programs. In this section of the Progress Report we highlight several just such applications.
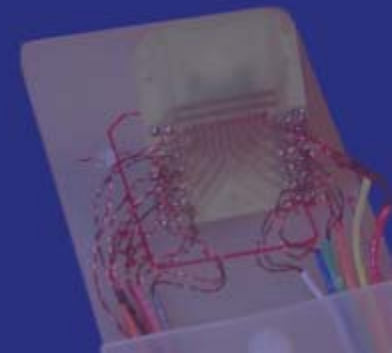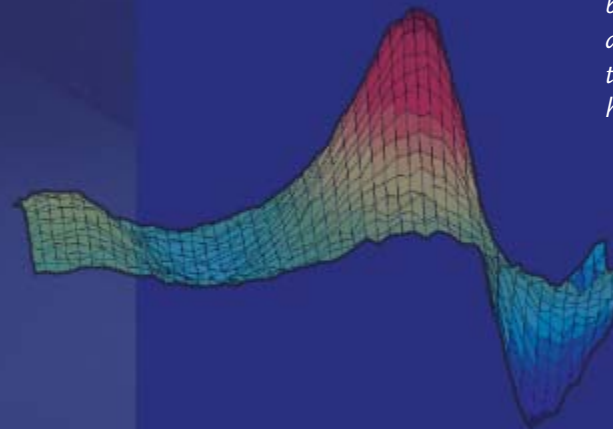
Virtual Pinhole Confocal Microscope

J. S. George and D. M. Rector (P-12), D. M. Ranken (CCN-12), B. Peterson (NIH), and J. B. Kesterson (VayTek, Inc.)

Introduction

For 400 years optical microscopy has been the principal method for the study of biological structure at the cellular level. Over the past century, the application of photography has allowed the capture and distribution of microscopic images to a wide audience. Optical microscopy, considered a mature technology for years, has undergone a renaissance in the past two decades. The advent of electronic imaging is producing a revolution in scientific microscopy that is redefining the frontiers of speed, temporal and spatial resolution, sensitivity, and perhaps most importantly, the capacity for quantitative photometric, spectral, and geometric measurements. New optical and imaging strategies are disclosing new structural and dynamic functional details of the microscopic domain. Confocal imaging techniques have provided striking improvements in the spatial resolution of optical microscopy, providing true three-dimensional (3-D) volume imaging.

Confocal Principle and Practical Instruments

The key insight that has driven the development of confocal imaging, is summarized by Marvin Minsky, a noted pioneer in the development of artificial intelligence, and in 1955 the inventor of a confocal microscope:
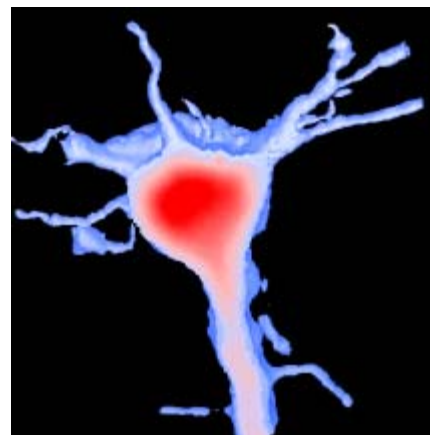

Figure 1. A three-dimensional (3-D) rendering of a nerve cell reconstructed from a series of virtual pinhole microscope (VPM) confocal images.

"An ideal microscope would examine each point of the specimen and measure the amount of light scattered or absorbed by that point. But if we try to make many such measurements at the same time, then every focal image point will be clouded by aberrant rays of scattered light that are deflected from points in the specimen that are not the points you are looking at…. It is easy to remove all rays not initially aimed at the focal point; just use a second microscope (instead of a condenser) to image a pinhole aperture on a single point of the specimen…. Still, some of the initially focussed light will be scattered by out-of-focus specimen points onto other points in the image plane. But we can reject those rays as well, by placing a second pinhole aperture in the image plane that lies behind the exit side of the objective lens. We end up with an elegant, symmetrical geometry: a pinhole and an objective lens on each side of a specimen."
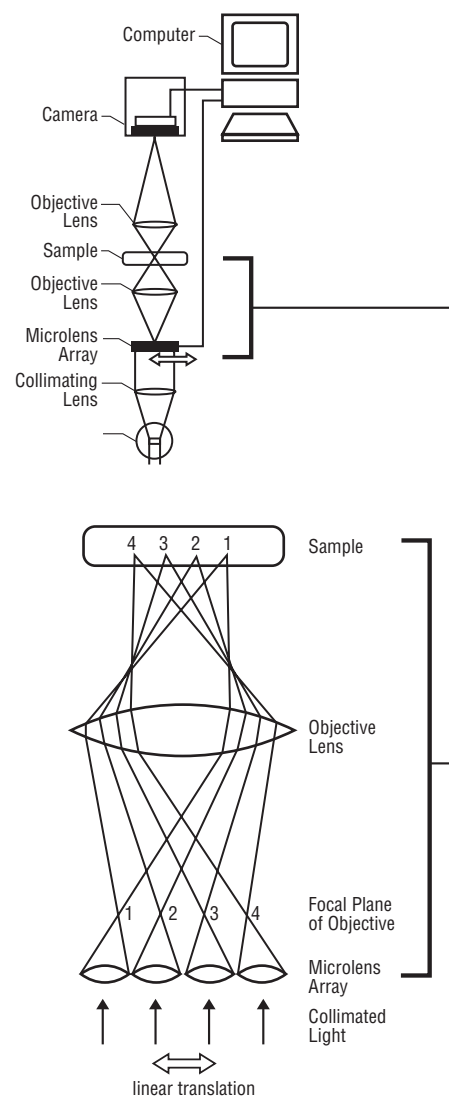
Figure 2. Conventional transmission confocal microscope. The most practical implementations scan the specimen stage to maintain optical alignment in the illumination and imaging path.

A conceptually simple embodiment of a confocal microscope of the sort described by Minsky is illustrated schematically in Figure 2. The system is configured for transmission imaging. Light from a source is transmitted through a pinhole. Light from the pinhole is brought to a point focus within the sample volume by imaging optics. Light emerging from the sample is brought to focus on a pinhole aperture by a second set of imaging optics. This aperture acts as a spatial filter for imaging, rejecting most of the light that did not pass through the confocal point in the sample volume, thereby reducing image contributions from light scattered or refracted from other locations within the medium. The detector for such a system typically consists of a single-channel device such as a photodiode or photomultiplier.

In order to collect an image, it is necessary to scan the illumination and detection subsystems relative to the sample. However, the technical requirements for coupled electromechanical scanning to preserve the required optical alignment between illumination and imaging pathways are

formidable. Most practical embodiments of a transmission confocal system utilize mechanical scanning of the sample so that the imaging elements do not move, however scanning in such systems is very slow.

Confocal microscopy systems offer a number of advantages for quantitative imaging including improved image contrast, resolution, and limited depth-of-field. The limited depth-of-field of scanned confocal microscopes has supported applications not previously feasible, such as the optical sectioning and volumetric reconstruction of complex subcellular structures, or mapping the spatial and temporal distributions of intracellular ions. Conventional confocal systems incorporate several key functional subsystems:

· a system for scanned illumination;

· a spatial filter or aperture in the focal plane of the detector to reject out-of-focus light; and

· a single channel or imaging detector.

Imaging optics bring the illumination and imaging paths into focus at the same location within a sample—hence the term "confocal".

Most existing commercial systems are designed for epifluorescence imaging (*i.e.*, using reflected light), allowing scanning and aperture functions for illumination and imaging to be performed by a single piece of hardware. Initial commercial confocal microscopes appearing in the mid-1980s utilized laser illumination and single-channel photomultiplier detectors. Although a number of important technical advances have emerged over the intervening years, most confocal systems remain complex, inflexible, slow, and expensive.

At Los Alamos National Laboratory, we have developed a novel approach for confocal microscopy that uses available illumination, detection, and data-processing technologies to produce an imager with a number of advantages: reduced cost, faster imaging, improved efficiency and sensitivity, improved reliability, and much greater flexibility. This system has three key components:

1. an electronically or electromechanically scanned illumination subsystem,

2. an area sensor such as a charge-coupled device (CCD) imager, and

3. a "virtual pinhole"—synthetic aperture constituted during image processing after sensor readout.

Our approach provides the core technologies for a family of microscopic-imaging methods that will significantly advance the utility of optical microscopy for clinical applications and basic research. The initial focus of our work has been the development of a low-cost system for confocal imaging suitable for retrofit integration with conventional research microscopes. However, our approach also offers simple and effective solutions for transmission confocal imaging, a practical approach for confocal imaging through an endoscope, and for high-performance confocal spectral imaging.
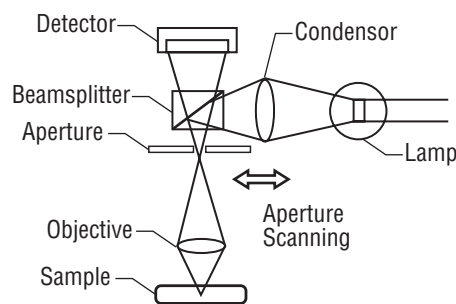

Figure 3. A conventional confocal microscope configured for epifluorescence or reflected-light imaging. The aperture configuration and scanning strategies vary widely.

Confocal Imaging Approaches

The conventional configuration for confocal imaging in reflected light or epifluorescence modes is illustrated in Figure 3. This configuration employs the same imaging optics and often the same pinhole aperture for both the illumination and imaging paths. This arrangement simplifies optical alignment and facilitates optical scanning by mechanical movement of the aperture, or by shifting the image of the aperture by mirrors in the optical path. In many designs the scanning of the illumination path and the "descanning" of the imaging path are accomplished with the same set of mirrors. Image acquisition in most existing systems is relatively slow, which complicates both the preliminary inspection of a sample and focusing.

Spinning-disk confocal systems are a useful implementation of the principles illustrated in Figure 3. In such systems the scanning and aperture functions are embodied in an opaque disk containing a pattern of optically transmissive pinholes. These systems can significantly enhance the speed, flexibility, and ease of use of confocal microscopy. However, they typically suffer from low sensitivity (illumination is inefficient because most light is absorbed by the opaque regions of the disk) and from reflection from the disk surface. Another strategy for high-performance imaging is to use an illumination source configured as a line instead of as a point, with a slit aperture instead of a pinhole. In a line-scan configuration, out-of-focus light that happens to fall onto the slit aperture contributes to the image, however in practice the degradation of confocal image quality is not unacceptably severe.

An alternative approach, developed by Greenberg and colleagues at NIH, in principle offers higher performance because the need for mechanical scanning is eliminated. The system scans a laser in two dimensions using a pair of optoacoustic beam-steering devices. The detector is based on an image dissector videcon—a television detector tube that allows random access readout of the tube photocathode at user-defined coordinates (defined by a pair of voltages). However, like most other tube-based video detectors, the image dissector has been rendered obsolete by solid-state video devices, and a commercial version of this confocal imager has not been produced.

Virtual Pinhole Microscope—A New Approach

Our virtual pinhole microscope (VPM) can use a method analogous to slit scanning for fast, full-field scanning. Because the system integrates image-processing techniques, it can correct image degradation associated with slit scanning. The video-scan configuration of the VPM allows fast, continuous confocal point measurements at arbitrary locations within a sample. Even using standard video technologies, the VPM provides full-frame imaging rates comparable to those of most laser-scan confocal instruments. The VPM can reconstruct and display clear point-scan confocal images in real time using high-performance video cameras and a data-acquisition system that we developed. The low-cost, high-speed CCDs that are now available can achieve full-field imaging rates approaching 1,000 frames per second (or more, with slightly more complex devices). Though typically lower resolution than standard video cameras, these CCDs are particularly well-suited for "hyperacuity" imaging: a reconstructed VPM image can have higher resolution than the camera used to collect the component images.

Our approach to confocal imaging operates on the same principles as existing confocal imagers, but realizes the necessary functional subsystems in a novel way. The first key subsystem is a system for electro-optically scanned illumination. Several classes of technology satisfy our basic requirements for speed and precision. Scanned illumination is achieved by the use of spatial light modulators (SLMs)—devices that can be electronically driven to produce time-varying spatial patterns of illumination.

We have explored the use of display devices used in video projectors. Most computer-compatible video projectors now employ liquid crystal devices (LCDs). Texas Instruments recently introduced digital light processor (DLP) technology, based on an electronically addressable micromirror array. In our usual scanning method, only a small fraction of the total number of pixels is illuminated at any given time, typically on the order of 1 in 25. Separation between illuminated spots is maintained to avoid cross-talk between scanned points. However, most (*e.g.*, 96%) of the available light is wasted. For some applications this poses little concern and the flexibility of programmable illumination and solid-state devices justifies the tradeoff. However, for light-limited applications such as fluorescence microscopy, this is a significant problem.

In order to address this problem, we have built a scanning system based on a microlens array. This is a small replicated optical element consisting of an array of microscopic lenslets, typically formed in a regular (square or hexagonal) grid. Lenslet diameters (and thus the pitch between elements) are on the order of tens to hundreds of microns. As in macroscopic convex lenses, if collimated light is passed through the lenslet, the light will be focused to a point at the focal length of the lens. With an array, most of the light is focused in a grid of illuminated points. Each of these points is a much better approximation to a Gaussian profile than is achieved with the LCD or DLP projection arrays. The illumination pattern can be scanned by mechanical translation of the microlens array, over

relatively short distances, comparable to the pitch of the lenslet array. Because exposures are made in parallel, shifts in the grid occur at low frequencies—typically 10–1000 Hz. The comparatively low speeds and small distances of translation allow a range of low-cost technologies to be used.

Figure 4 illustrates two methods for scanned illumination using such a lens array. The lenslets are illustrated by the larger circles in Figure 4; focused points of illumination are illustrated by the smaller circles. Figure 4a illustrates partial sampling of the image plane produced by translation of the microlens array in two dimensions. The illustrated grid is produced by three positions of the microlens array. By additional translations in two dimensions, the entire image plane can be sampled. Figure 4b illustrates a novel alternative scanning geometry achieved by tilting the microlens array. This configuration achieves high density sampling by translation along a single dimension. The most obvious

strategies for scanning the array include rotary or linear stepping motor drives, galvanometer drives; or piezoelectric or ceramic devices. Mechanical scanning reintroduces concerns about system reliability, vibration, and the resolution and reproducibility of positioning. However, the performance requirements are comparable to modern mass-storage devices and thus we can use well-developed technical solutions. We have built a prototype scanner based on precision stepping motors, however galvanometer systems, or piezoceramic actuators may have advantages.
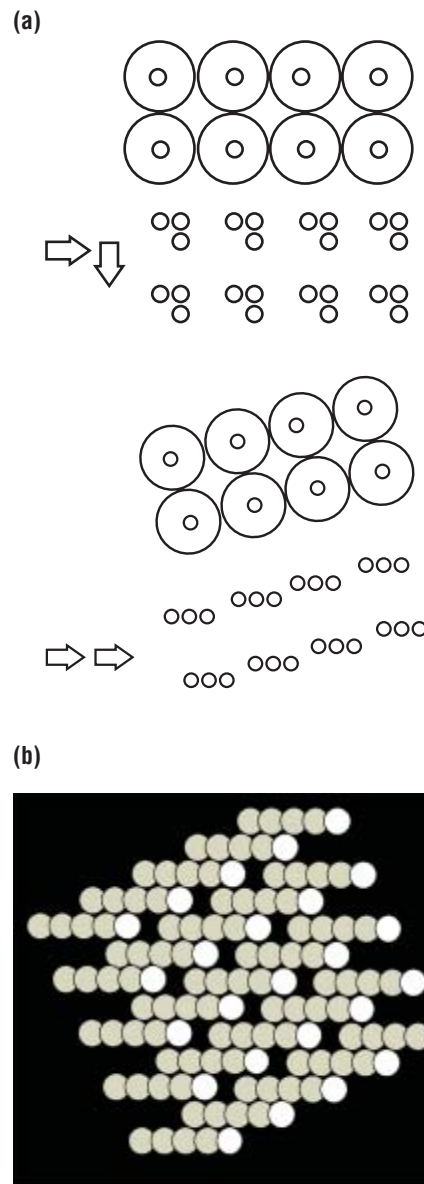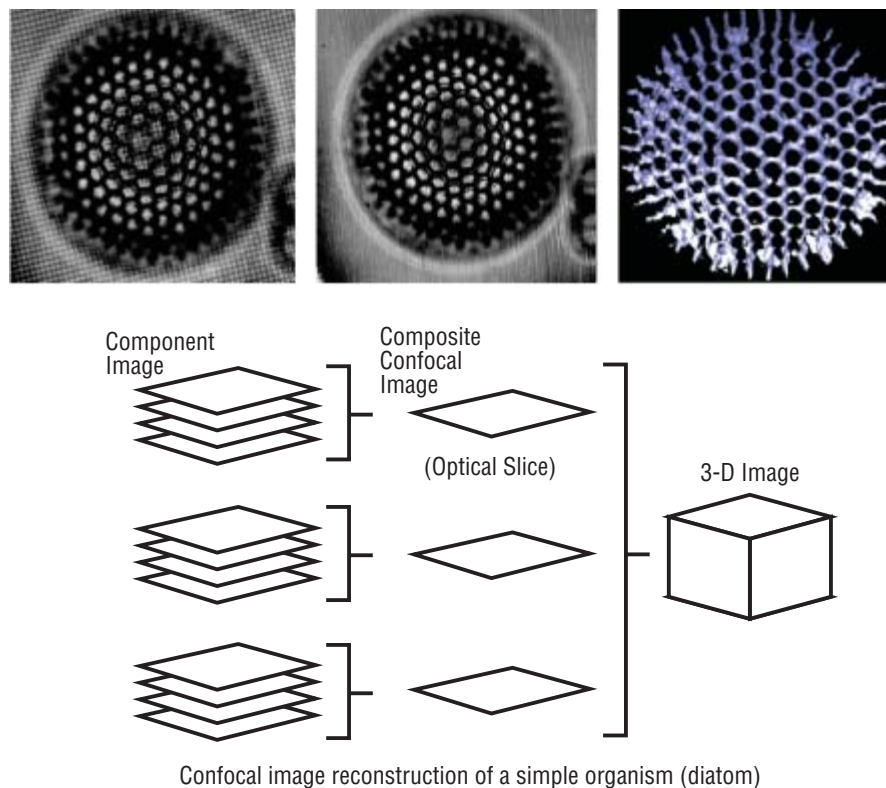
(a)

(b)

Figure 4. Scanned illumination using a microlens array. (a) A 2-D raster scan using two actuators. (b) A 2-D raster scan using a single actuator.

The second key technical strategy is the use of a "virtual pinhole"—a synthetic aperture constituted after readout of a solid-state video imaging array—typically a CCD, charge-injection device (CID), photodiode-array camera, or similar device. In general, the synthetic aperture is implemented in software on the host computer or in a specialized digital signal-processing engine after digital image acquisition. These computations predict how much light would have passed through a physical aperture located in the focal plane of the microscope. We have demonstrated several workable algorithms, including some that are very efficient to compute. Because functional parameters are implemented in software, it is possible to adjust key parameters (such as effective aperture size) to optimize image tradeoffs, even after the basic data are acquired.

The system has a great deal of flexibility not available in other confocal systems. The detector can be operated as a conventional video camera, allowing easy focusing and survey of the microscope image field. The imager

Figure 5. Data Flow in the VPM: A series of component images are collected. Each is spatially subsampled using patterned illumination, produced by a MLA in this example. A composite confocal image (an optical slice) is reconstructed as a linear combination (a weighted sum) across the stack of component images. This operation implements the synthetic aperture. A 3-D image is reconstructed from a stack of confocal slices.

Component Image

Composite Confocal Image

(Optical Slice)

3-D Image

Confocal image reconstruction of a simple organism (diatom)

can be readily configured to operate in transmitted light modes as well as the reflected light or epifluorescence modes offered by most confocal microscopes. A number of image contrast mechanisms can be digitally synthesized; *e.g.*, transmitted light or dark field (scattered light) images can be produced by changing the calculation used to create the synthetic aperture. Multiple images can be computed from a single data set to optimize image data for a given application.

Our system provides confocal imaging capabilities to existing research microscopes, for little more than the cost of a conventional microscope with digital video capability. The system

initially has been developed for confocal transmission imaging, because this is a commercially under-served application. Component systems are designed for flexibility; reflected light and fluorescence imaging capabilities use the same components. The imaging system provides a family of instruments, optimized for different applications: a spectrally-resolved microscopic imaging system that produces a complete spectrum for each image pixel; a high-performance system with extended sensitivity, speed, and dynamic range; and a confocal and spectroscopic endoscope system—rugged and light weight because no moving parts are required. We anticipate that other advanced systems based on these ideas will be developed in future work.

The principal application of existing confocal microscopes is in biological research studies of cell structure and function. Studying intact, functioning cells *in vivo*—for example, looking at how nerve cells process information in real time—could help researchers understand how the brain works or explore the root cause of crippling neuro-degenerative diseases. Our VPM technology promises to extend the technical advantages of confocal imaging to many applications in science and technology that depend on the flexibility and functionality of conventional video microscopy: biological research, histology and pathology studies, geological sample characterization, material science, and electronics manufacturing. Because the VPM system is compact, flexible, and free of alignment problems, it will facilitate the development of confocal endoscopes. The marriage of confocal and spectral imaging capabilities with endoscopy will provide new diagnostic methods that are minimally invasive in accessible areas.

Summary

By integrating state-of-the-art technologies in optics, electronics, and digital computing, we have developed a confocal imaging system for standard optical microscopes at much lower cost and with improved efficiency, reliability, and ease of use. Ours is a very flexible, high-performance imager, adaptable to a number of imaging configurations and applications not feasible or practical with other confocal imaging systems.

Our complete hardware system consists of imaging optics, typically supplied by a standard research microscope; a system for scanned illumination; a standard or high-performance solid-state video camera; and a computer system for image acquisition, scan control, and image reconstruction.

We have demonstrated several workable systems for electronically or electromechanically scanned illumination of many points in parallel. These methods have different strengths: LCD technology is flexible and compact; DLP technology is flexible and has high performance; MLA technology is compact and optically efficient. All methods provide adequate performance for at least some applications, at low cost. We have developed data-acquisition systems that control illumination scanning and perform image acquisition and processing. We have developed two classes of reconstruction method: an efficient calculation for real-time implementation, and advanced high-resolution algorithms that require substantial processing off-line. The combination of flexibility, high performance, and low cost in confocal imaging offered by our system should find a wide range of applications in science and technology.

References and Further Reading

R. Juskaitis, T. Wilson, M. A. Neil, M. Kozubek, "Efficient Real-Time Confocal Microscopy with White Light Sources," *Nature* 383, 804–806 (1996).

J. B. Pawley, *Handbook of Biological Confocal Microscopy*. 2nd Edition. (Plenum Press, New York, 1995).

D. M. Rector, R. F. Rogers, J. S. George, "A Focusing Image Probe for Assessing Neural Activity *in-vivo*," *J. Neurosci. Meth.* 91, 135–145 (1999).

D. Shotton, Ed, *Techniques in Modern Biomedical Microscopy: Electronic Light Microscopy*, (Wiley-Liss, New York, 1993).

T. Wilson, "Scanning Optical Microscopy" in *Advances in Microscopy* (Alan R. Liss, Inc., New York, 1985).

About the Authors

John George, Ph.D. is a Technical Staff Member in the Biophysics group (P-21) at Los Alamos National Laboratory. He came to Los Alamos as a Postdoctoral Fellow in the Life Sciences Division after completing his Ph.D. in Physiology from Vanderbilt University. His dissertation research, on the biochemical and ionic mechanisms of visual transduction in photoreceptor cells was conducted in the Laboratory of Chemical Physics at the National Institutes of Health. He has an educational background in biophysics, physiology, and computer science, and extensive experience in the development of biophysical instrumentation and electronic imaging. He is the inventor of the Virtual Pinhole Confocal Microscope and leads the continuing development of hardware and software systems and applications of the technology.

David Rector, Ph.D. is a Technical Staff Member in the Biophysics group (P-21) at Los Alamos National Laboratory. After completing his Ph.D. in Neuroscience at UCLA, he came to Los Alamos as a Director's Postdoctoral Fellow. He is an experimental neuroscientist with a background in digital computing as well as the design and development of high-performance electronic systems, in particular for physiological and image data acquisition. His work has demonstrated the feasibility of optical imaging of fast dynamic processes associated with the functional activation of neural tissue. Rector works on the illumination subsystem, and image-reconstruction algorithms and has primary responsibility for the development of the data acquisition and processing subsystem.

SQUID Array Microscope—An Ultrasensitive Tool for Nondestructive Evaluation

M. A. Espy, R. H. Kraus, Jr.,
A. Matlachov, P. Ruminer, and T. Lobb
(P-21) and J. Mosher (NIS-9)

Introduction

Nondestructive evaluation, or NDE, is a field devoted to finding out if objects are developing fractures, flaws, or other mechanical problems without actually having to rip the object apart to find out. This can be very valuable if your object is something like an aircraft wheel, subject to enormous stress every day and prone to getting cracks in places where you can't see them without removing the wheel and disassembling it. The NDE of an aging nuclear weapon can save large amounts of time and expense by showing what is happening to it on the inside without actually having to open it up. Conventional NDE techniques include ultrasound, x-rays, and conventional eddy-current testing. Eddy-current inspection works by injecting or inducing currents into a conducting sample and then looking at how these currents flow. If the sample has no flaws, the current will flow unimpeded. If the sample contains a flaw, such as an inclusion or rust spot, the current will flow differently through that material. If the flaw is a crack, the current will flow around it (see Figure 1).

The trick is in the measuring of how the currents are flowing. Conventional eddy-current techniques use a receiver coil and measure the impedance changes as it scans across the sample. In the Biophysics group at Los Alamos, we have developed a system that replaces the receiver coil with a linear array of superconducting quantum interference devices (SQUIDs). The array of SQUIDs measures the magnetic fields produced by the eddy currents in the sample directly. The result is an NDE system that has unsurpassed sensitivity to features that are very small or buried deeply.
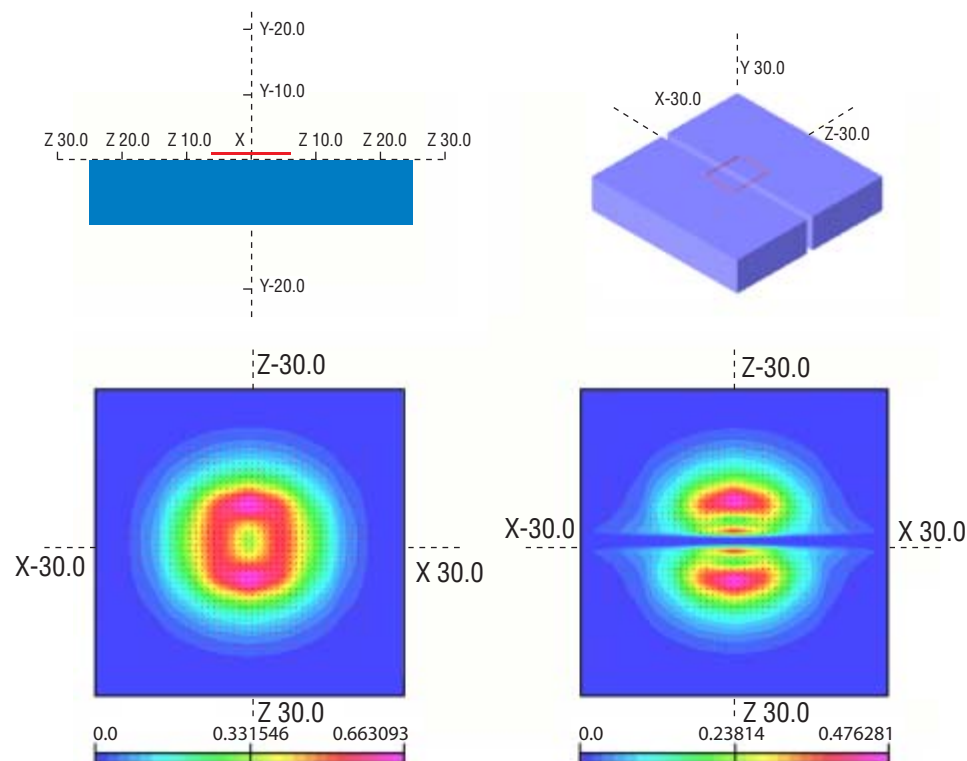

Figure 1. Left: As illustrated in a simple eddy current simulation, in a sample with no flaws the current flows unimpeded. **Right:** The simulation shows that in a sample with a flaw, the current has to deviate. This produces the magnetic-field anomaly measured by the SQUID.

What Is a SQUID?

The top panel of Figure 2 shows an example of the species of SQUID we are discussing. The SQUID is a loop of superconducting material (made of either low- [liquid helium: 4 K] or high-temperature [liquid nitrogen: 77 K] superconducting material) that is interrupted by two weakly superconducting regions known as Josephson Junctions. During operation of a SQUID, a bias current is applied to the device. Up to some critical biasing current, there is no voltage across the SQUID. It acts as a superconductor and current flows without resistance. However, above the critical bias-current level, the junction becomes resistive and a voltage does appear across the device. This is roughly analogous to water flowing in a hose with a kink in it. Once the device shows this voltage, it behaves very interestingly —the quantum-mechanical wave functions which describe the electrons in the SQUID on either side of the Josephson Junctions interfere with each other. As a result, the voltage across the SQUID, for a fixed bias current, oscillates. The oscillation is a function of the amount of flux that is threading through the SQUID loop, as shown in Figure 3. The period of this oscil-

lation is called the flux quantum, (Φ_0). One Φ_0 is equivalent to the amount of magnetic flux from the Earth's magnetic field passing through an area the size of one human red blood cell. A SQUID is sensitive to changes in magnetic flux as small as one millionth of one Φ_0!
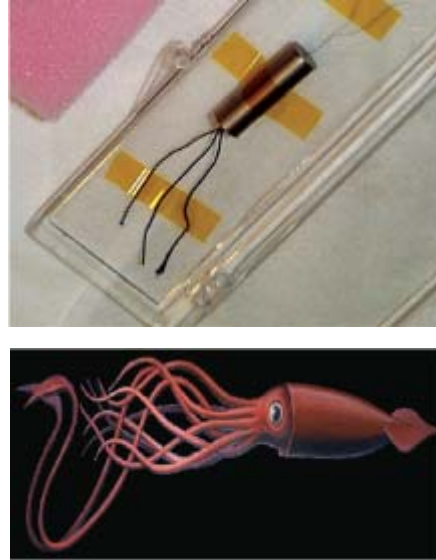

Figure 2. Bottom: A squid, not the type we are talking about. Top: a superconducting quantum interference device, SQUID.

Figure 3. A bias current is applied so that the SQUID has a voltage across it. This voltage will oscillate depending on the amount of magnetic field passing through the SQUID loop.

Why Use a SQUID?

SQUIDs can be appropriate for some NDE problems because they are the most sensitive detector of magnetic flux known. In particular, SQUIDs can be well suited to the problem of buried features. A technique such as conventional eddy-current NDE has to go to lower eddy-current frequencies (ω) to get the required skin depth (δ). This dependence is shown in Equation 1,

$$\delta = \sqrt{\frac{2\rho}{\omega\mu_0}} \ , \qquad (1)$$

where ρ is the resistivity of the material. However, the voltage measured is proportional to the frequency, $V \propto \omega$. To see a flaw 1 cm deep in an aluminum plate, conventional eddy-current NDE

DC SQUID
Superconduction (Red)   DC SQUID Concepts
Φ Josephson Junction
Magnetic   (resistive barrier)
Flux

SQUID Output vs Magentic Flux (Applied current above Critical current)

Voltage

$(n+1/2)\Phi_0$ $(n+1)\Phi_0$ $(n+3/2)\Phi_0$ $(n+2)\Phi_0$
Magnetic Flux

requires ω less than 100 Hz. This is a difficult regime for conventional eddy-current testing, whereas SQUIDs are uniformly sensitive at frequencies from near DC to megahertz.

Other NDE techniques also have limitations. Ultrasound has difficulties with signal reflection at the boundaries of material layers that are sonic absorbers (most plastics and electrical insulators), which reduces the technique's sensitivity to features below such layers. Radiographic techniques can be expensive, nonportable, and insensitive to small one-dimensional features.

SQUIDs can be appropriate for some NDE problems because they are the most sensitive detector of magnetic flux known. In particular, SQUIDs can be well suited to the problem of buried features. SQUID sensitivity does not depend on frequency, enabling these sensors to be used for detecting features and defects over a broad range of material depths. Furthermore, the induction signal at a given frequency depends only on ρ, not on gaps or intervening layers. Also, a SQUID system can be portable and relatively inexpensive.
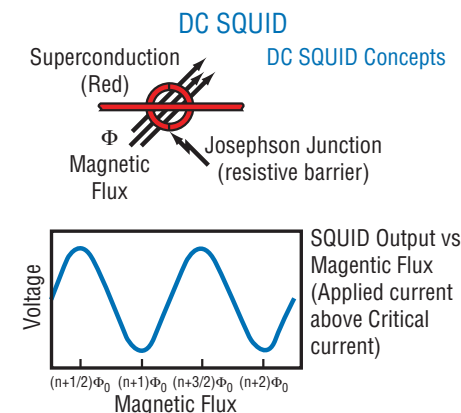
SAMi

The SQUID array microscope (SAMi) was developed for the stockpile-stewardship program at Los Alamos National Laboratory. SAMi is capable of finding features that are small and buried at depths of 1 cm or much more. SAMi is the first instrument of its kind to use a linear array of 11 high-temperature SQUIDs spaced 0.75 mm apart. A picture of the SQUID array is shown in Figure 4. All the SQUIDs were manufactured on a single chip. This means that their geometry is well understood and their performance characteristics are very uniform. Using an array such as this affords two distinct advantages: decreased scanning time and increased resolution.

Another advantage to the SAMi system is that it can induce an eddy current at a single frequency like a conventional NDE system or use a unique white-noise induction scheme (patent pending) to induce at multiple frequencies at the same time. As we showed in Equation 1, the skin depth to which these eddy currents penetrate the sample depends on the frequency. Using white-noise induction, the SQUID's response at multiple skin depths (frequencies) can be simultaneously acquired and analyzed. The operator then uses the response to extract information about the feature depth and character.

The fiberglass SAMi dewar was custom built with a ~4 mm hot-cold distance. The SQUIDs as well as the induction coil are in the liquid nitrogen bath. Samples are scanned beneath the dewar by a dual-axis translation stage. A schematic diagram of the SAMi dewar and a picture of the system operating in our laboratory are shown in Figures 5 and 6.
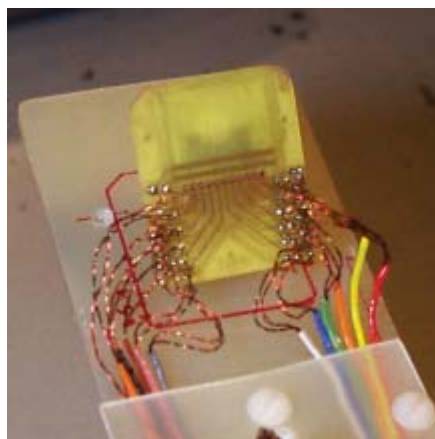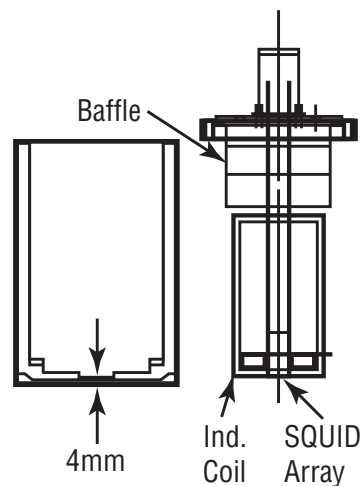

Figure 5. A schematic drawing of the SAMi dewar and insert.

Figure 6. The SAMi system. A sample is positioned below the white dewar. The motion-control stage scans the samples below the SQUIDs.

Figure 4. The SAMi uses a linear array of 11 SQUIDs.

SAMi Results

Laser Welds

A quality-control issue important to stockpile stewardship and industrial applications is the inspection of the quality of laser welds. We inspected welds in samples of incoloy 825. The samples consisted of two 20 mm × 76 mm plates of ~3 mm thickness. The plates were laser welded in three places along their length. Energy and focus of the welding laser were varied for each of the welds. The results are shown in Figure 7. The different curves are SAMi scans for welds of different laser energies. Notice that for the weld at a laser energy of 2.5 J (solid blue line, upper panel) there is a fairly deep "dip" in the data. If there were no weld, there would be no change in conductivity. The eddy currents would flow unimpeded and there would be no such feature in the data. For the weld at 7.5 J (dotted green line, upper panel) the dip in the data is less pronounced, implying better conductivity, less current deviation, and thus possibly a better weld. In the lower panel of Figure 7, one can compare the 10-J weld (red dashed line) with a weld at the same energy but where the laser was defocused (green dotted line). Defocusing the laser could mean that less energy was available for the weld, and the mechanical strength might not be as good. The trend in the data implies that the defocused weld is at a lower energy than the same weld with the laser focused. The samples still need to be destructively tested to provide final validation, but our initial results are encouraging.
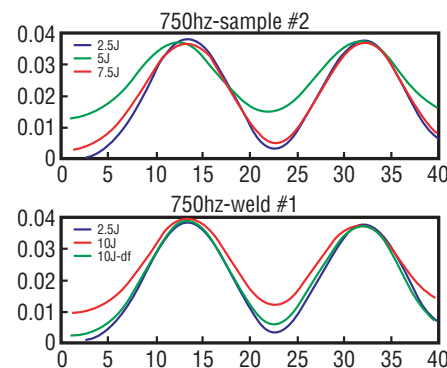

Figure 7. Upper panel: scans of three welds on the same sample. Lower panel: scans of welds in the same position for different samples.

Upset-Forge Welds

The Allied Signal Kansas City Plant invested significant amounts of money developing a reliable new weld technique for reservoirs. They believe this technique will allow them to improve their process—to make their welds stronger and less likely to fail while being less costly. However, they cannot certify a reservoir safe for use without being able to inspect the quality of the weld and quantitatively determine its strength. While destructive tests have shown that the weld technique works, currently no other method tested besides the SAMi (ultra-sound, x-ray, or conventional eddy-current techniques) appears able to tell them the mechanical strength of their welds without destroying

Figure 8. Photograph of two samples, one welded and one solid. The two are visually identical.

them in the process. The other techniques have thus far lacked the sensitivity required to characterize a strong bond from a weak one.

Figure 8 shows a photograph comparing a solid and a welded part. The two parts are virtually indistinguishable visually. NDE techniques such as ultra-sound and x-ray also would also have great difficulty distinguishing between the two. Figure 9 shows a SAMi scan of the two parts. The welded and unwelded parts have very different responses.
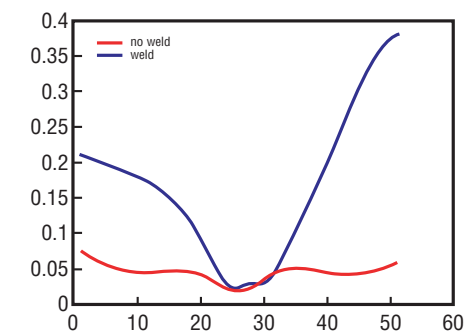

Figure 9. SAMi scans of the solid (red) and welded (blue) upset forge weld samples.

White-Noise Technique

The ability of the white-noise induction scheme to provide depth information was tested with plates of aluminum that were 15 cm × 15 cm and 1.5 mm thick. The distance between the top plate and the dewar bottom was ~2 mm. Holes appear as a two-lobed feature in the data. In Figure 10, the data plots show amplitude vs position for a stack of three plates. The top plate had a 5-mm-diameter hole at x = 40, the middle plate was blank, and the lower plate had a 5 mm diameter hole at x = 10. The bottom hole (4.5 mm deep) is visible at frequencies < 700 Hz where the skin-depth is > 3 mm. As the frequency increases, the skin depth decreases and the sensitivity to the buried feature also decreases. The hole on the top becomes more visible as frequency is increased. The images were acquired simultaneously.
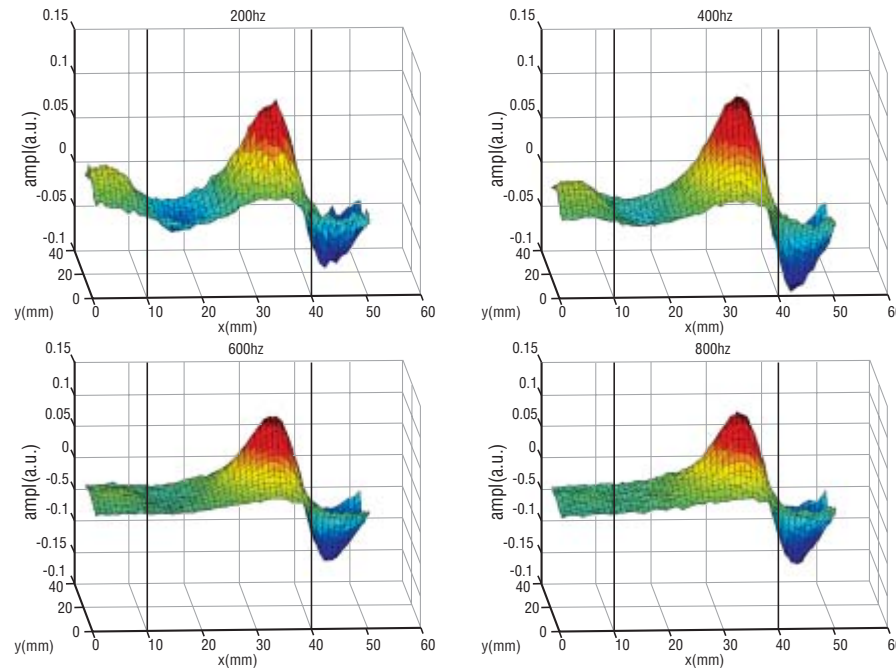

Figure 10. Plots of amplitude vs x-y for 4 different frequencies (indicated at the top of each plot). The sample was a stack of three 1.5-mm-thick aluminum plates. The top plate had a 5-mm-diameter hole at x = 40 mm. The middle plate was blank. The lower plate had a 5-mm-diameter hole at x = 10 mm.

Summary and Outlook

SAMi is a tool for NDE of unsurpassed sensitivity. SAMi is the first of its kind to use an array of SQUIDs all fabricated on a single chip. The SQUID is the most sensitive detector of magnetic field in the world. SAMi uses eddy current induction methods to induce eddy currents in the sample of interest and then map the magnetic fields produced by the eddy currents. Small features in the sample will cause the eddy currents to deviate and produce anomalies in the magnetic field. These anomalies can be seen even if the feature is very small or buried under intervening layers of conductive or nonconductive material. In cases where the feature of interest is very small, deeply buried, or buried under an insulating layer, the SAMi has strong advantages over conventional NDE techniques. SAMi uses a novel white-noise induction method (patent pending) that induces at multiple frequencies simultaneously, providing information about the depth at which a feature is located.

We have used SAMi to look at a host of NDE problems from small,

deeply buried cracks to the inspection of welds. SAMi has proven to be as robust as it is sensitive, and is able to operate without magnetic shielding even in a noisy laboratory environment on room-temperature samples.

It is our hope that other SAMis will be deployed to various laboratory and industrial sites to help solve NDE problems ranging from the stockpile applications to aircraft worthiness.

About the SAMi team

Michelle Espy first came to Los Alamos as a graduate student from the University of Minnesota in 1991. She did her thesis work at the Los Alamos Meson Physics Facility (now LANSCE) and earned her Ph.D. in experimental nuclear physics in 1996. Michelle has worked for the Biophysics Group (P-21) since her graduation, first as a post-doc and more recently as a staff member. She has no plans to live anywhere as flat as Minnesota ever again.

Bob Kraus came to Los Alamos as a postdoctoral fellow with Clark University in 1984 as part of the TOFI collaboration that discovered more than a dozen new light neutron-rich isotopes. In 1986 he joined the Laboratory as the Section Leader of the Ion Optical Design and Magnetic Measurement section of the Accelerator Optics group (AT-3 at the time). In 1994 Bob joined the SQUID sensor effort of the Biophysics group (P-21) where he changed the focus of his work from Tesla accelerator magnets to measuring "femto" Tesla of human brains.

Andrei Matlachov got his Ph.D. in Experimental Physics from the Russian Academy of Sciences,

Moscow in 1988. He spent two years as the Deputy Director of Research at the Biophysics Center at the Institute of Radio-Engineering & Electronics in Moscow, Russia and came to America in 1994 to join the staff at Conductus, Inc. Andrei has been a staff member at Los Alamos since 1997.

Pat Ruminer has been at LANL for over fifteen years. He came to the P-21 to work in the SQUID group in 1992. Among Pat's responsibilities has been the design and construction of a large SQUID-based system for measuring the magnetic fields from the human brain.

The SQUID team (including LeRoy Atencio, now retired) won a distinguished performance award for SAMi's single SQUID predecessor in 1997.

Ted Lobb was with the SQUID group from Dec. 1999- Dec. 2000 and has since moved on to ITT Industries in Albuquerque.

John Mosher is currently with NIS-9. John has worked with P-21 for years on the analysis of SQUID-based magnetic field data from human brain function and other projects.

Further Reading

To learn more about SQUIDs:

J. Clarke, "SQUIDs, Brains, and Gravity Waves," *Physics Today* March (1986).
J. Clarke, "SQUIDs." *Scientific American* August (1994).

To learn more about the physics of SQUIDs:

R. P. Feynman, R. B. Leighton, M. L. Sands, *The Feynman Lectures on Physics*, Vol. 3, (Addison-Wesley, Boston, Massachusetts, 1989) 1552 pp.

To learn more about SAMi:

M. Espy *et al*., "A Linear Array of 11 HTS SQUIDS for Non-Destructive Evaluation," *IEEE Transactions on Applied Superconductivity* 11, 1303–1306 (2001).

Quantum Information Science

R. J. Hughes, D. J. Berkeland,
G. L. Morgan, J. E. Nordholt, and
C. G. Peterson (P-23)

Introduction

The representation of information by classical physical quantities such as the voltage levels in a microprocessor is familiar to everyone. But over the past decade, quantum information science has been developed to describe binary information in the form of two-state quantum systems, such as photon polarization states. (A single bit of information in this form has come to be known as a "qubit.") Remarkable new capabilities in the world of information security have been predicted that make use of quantum-mechanical superpositions of information, a concept that has no counterpart in conventional information science. For example, quantum cryptography allows two parties to communicate securely even in the presence of hostile monitoring by a third party. A quantum computer would make use of logical operations between many qubits and would be able to perform many operations in parallel. Certain classically intractable problems, such as factoring large integers, could be solved efficiently on a quantum computer. We have experimental projects underway in quantum cryptography, quantum computation, and in quantum optics with trapped strontium ions.

Quantum Cryptography

One of the main goals of cryptography is for two parties ("Alice" and "Bob") to render their (binary) communications unintelligible to a third party ("Eve"). This can be accomplished if Alice and Bob both possess a secret random-bit sequence, known as a cryptographic key. For example, in "one-time pad" encryption Alice adds the key to the original message, known as plaintext, and communicates the sum (ciphertext) to Bob. He is able to recover the plaintext by subtracting his key from the ciphertext, but Eve, who is assumed to have monitored the transmitted ciphertext, is unable to discern the underlying plaintext through the randomization introduced with Alice's key. So, although key material conveys no useful information itself, it is a very valuable commodity, and methods for Alice and Bob to generate key material securely are correspondingly important.

Using quantum cryptography, or, more accurately, quantum key distribution (QKD), Alice and Bob can create shared cryptographic key material whose security is assured by the laws of quantum mechanics. They first independently generate secret random-number sequences, which then undergo a bit-wise comparison that requires the preparation, transmission, and measurement of a single photon for each bit. Alice's photon-state preparations and Bob's measurements are determined by their bit values and are chosen from sets of nonorthogonal possibilities, such as linear and circular polarization. This comparison algorithm, which may be publicly known, ensures that Bob detects a photon (with some quantum-mechanically determined probability) only if he has the same bit value as Alice. They retain only the detected bits from their initial sequences. These subsets are the raw key material from which a pure key is distilled using classical error-detection techniques. Eve can neither "tap" the key transmissions (owing to the indivisibility of a photon) nor copy them (owing to the quantum "no-cloning" theorem). Furthermore, the nonorthogonal nature of the quantum states ensures that if Eve makes her own measurements, she will be detected through the elevated error rate arising from the irreversible "collapse of the wave function" that she introduces.

QKD offers many security and ease-of-use advantages over existing key-distribution methods. Traditional

key distribution using trusted couriers requires cumbersome security procedures for preparing, transporting, and handling the key before any communications can take place and may even be impractical (*e.g.*, rekeying a satellite). In contrast, quantum keys do not even exist before the QKD transmissions are made, and a key can be generated at message transmission time. Public-key cryptography also avoids many of the difficulties of key distribution by courier but provides only the conditional security of intractable mathematical problems, such as integer factorization. Accurate assessment of an adversary's computing power over the useful lifetime of encrypted information, which may be measured in years or even decades, is notoriously difficult: unanticipated advances in fields such as quantum computation could render public-key methods not just insecure in the future but also retroactively vulnerable. QKD could be used for real-time key generation in cryptographic applications where this long-term risk is unacceptable.

The physical systems that can support QKD transmissions determine the potential uses of quantum cryptography. We have demonstrated that QKD is possible over multikilometer optical-fiber paths: the necessary quantum coherence of the QKD transmissions persists even outside the controlled environment of a physics laboratory. At the infrared wavelengths required, germanium or indium-gallium arsenide avalanche photodiodes can be persuaded to detect single photons but at the penalty of a high noise and, hence, a high error rate. Removing these errors reduces the amount of key material and limits transmission distances to 100 km or so. (Optical amplifiers cannot be used to extend this range because they cannot replicate the nonorthogonal quantum states used in QKD.)

Quantum Cryptography: Recent Achievements

In our experiment we have demonstrated quantum cryptography over 48 km of optical fiber that had been installed for network applications between two LANL technical areas. Our system incorporates an encryption/decryption feature that allows us to use the quantum-key material to encrypt short text messages at the sending computer and decrypt them at the receiving computer. (See Figure 1.) This experiment shows that QKD could be used to generate cryptographic keys over "open" optical-fiber links between secure "islands," such as between different government agencies in the Washington, D.C., area.

In a separate experiment we are developing QKD for "free-space," line-of-sight communications, such as surface-to-aircraft, surface-to-satellite or satellite-to-satellite in low-earth orbits. We have designed, constructed, and tested a quantum cryptography system that
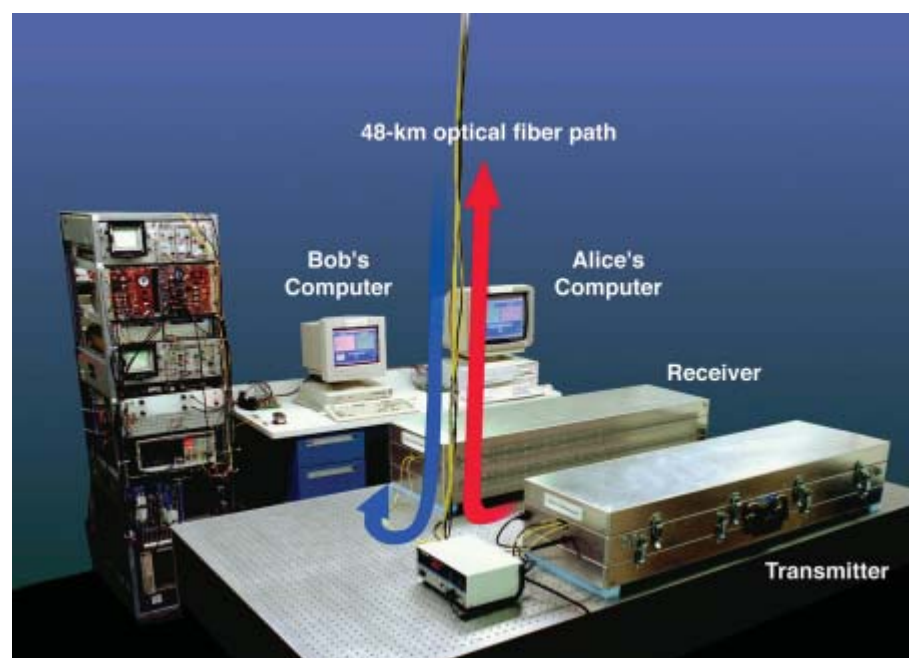

Figure 1. The optical fiber quantum cryptography experiment

Quantum Computation

creates and transmits—using single-photon transmissions—cryptographic random numbers between sending-and-receiving instruments that were separated by a 1.6-km outdoors optical path in daylight. The system is based on the propagation and detection of nonorthogonal polarization states of single photons in free space at a wavelength (772 nm) for which the atmosphere has a very low attenuation. We are now planning to extend the transmission range to more than 2 km and we are developing plans for a surface-to-satellite test experiment. Quantum cryptography is likely to be the first practical application of the foundations of quantum mechanics, which illustrates the often unexpected value of basic research.

With two or more qubits it becomes possible to consider quantum logical-"gate" operations in which a controlled interaction between qubits produces a (coherent) change in the state of one qubit that is contingent upon the state of another. These gate operations are the building blocks of a quantum computer, which in principle is a very much more powerful device than any classical computer because the superposition principle allows an extraordinarily large number of computations to be performed simultaneously. In 1994 it was shown that this "quantum parallelism" could be used to efficiently find the prime factors of composite integers. Integer factorization and related problems that are computationally intractable with conventional computers are the basis for the security of modern public-key cryptosystems. However, a quantum computer running at desktop-PC speeds could break the keys of these cryptosystems in only seconds (as opposed to the months or years required with conventional computers). This single result has turned quantum computation from a strictly academic exercise into a subject whose practical feasibility

must be urgently determined.

The architecture of a quantum computer is conceptually very similar to a conventional computer: multiqubit, or "multibit," registers are used to input data; the contents of the registers undergo logical-gate operations to effect the desired computation under the control of an algorithm; and, finally, a result must be read out as the contents of a register. The principal obstacles to constructing a practical quantum computer are (1) the difficulty of engineering the quantum states required; (2) the phenomenon of "decoherence," which is the propensity for these quantum states to lose their coherence properties through interactions with the environment; and (3) the quantum measurements required to read out the result of a quantum computation. The first proposals for practical quantum-computation hardware, based on various exotic technologies, suffered from one or more of these problems. However, in 1994 it was proposed that the basic logical-gate operations of quantum computation could be experimentally implemented with laser manipulations of cold, trapped
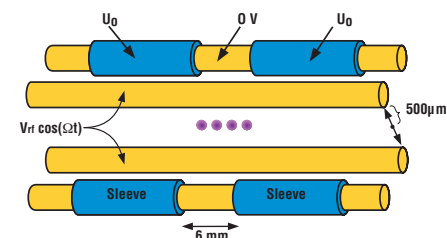

Figure 2. A schematic diagram of the segmented linear Paul trap confining four ions along its axis.

ions: a qubit would comprise the ground (S) state (representing binary 0) and a suitably chosen metastable excited (D) state (to represent binary 1) of an ion isolated from the environment by the electromagnetic fields of a linear radio-frequency quadrupole ion trap.

The principles of this proposed quantum computer can be illustrated with our trapped strontium ion project. We have recently confined strontium ions in a novel yet simple linear Paul trap with segmented electrodes, as depicted in Figure 2. A radio frequency (rf) potential $V_0 \cos(\Omega t)$, where $V_0 < 100$ V and $\Omega/2\pi = 7$ MHz, is applied to two diagonally opposite rods of the trap to confine the ions radially. To confine the ions axially, the outer segments of the remain

ing two rods are connected to a potential U_0, typically between 5 and 50 V. Additional potentials can be applied to any of the electrodes and their segments to move the ions to the nodal line of the rf field, where perturbations to the ion motion from the rf field are minimized. Figure 3 shows an image of two ions confined in this trap.

Figure 4 shows a partial-energy-level diagram of $^{88}Sr^+$ and the optical transitions that are relevant to these experiments. The 422-nm $S_{1/2} \leftrightarrow P_{1/2}$ transition is used to Doppler-cool the ions. Approximately 7.5% of the decays from the $P_{1/2}$ state are to the metastable $D_{3/2}$ state. To optically pump the atomic population out of the $D_{3/2}$ state, resonant 1092-nm light from a multimode fiber laser drives the $D_{3/2} \leftrightarrow P_{1/2}$ transition. Finally, a
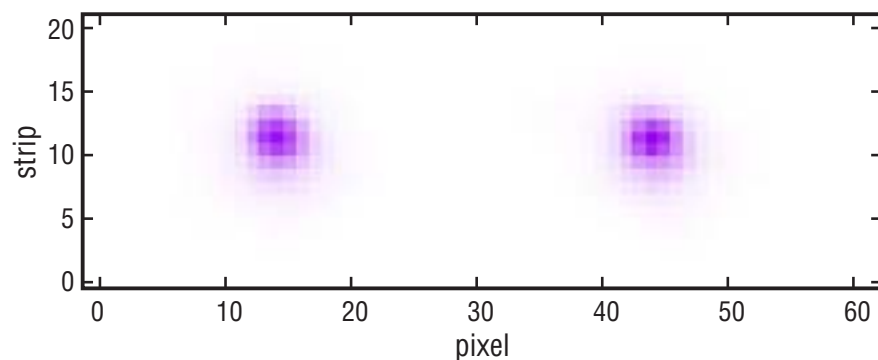
diode laser emitting 674-nm light drives the narrow $S_{1/2} \leftrightarrow D_{5/2}$ transition. The metastable $D_{5/2}$ state and the $S_{1/2}$ ground state would be the qubits in the quantum-computation experiment.
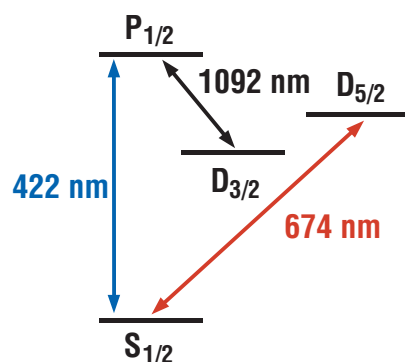

Figure 4. Relative energy levels and transitions of Sr+.

Figure 3. An image of two strontium ions approximately 20 μm apart.

By driving both the strong $S_{1/2} \leftrightarrow P_{1/2}$ and weak $S_{1/2} \leftrightarrow D_{5/2}$ transition in these ions, as depicted in Figure 5, we have observed quantum jumps[1] as shown in Figure 6. Here, the fluorescence from the broad $S_{1/2} \leftrightarrow P_{1/2}$ transition vanishes when the ion has been excited to the long-lived $D_{5/2}$ state and returns when the ion either decays out of the $D_{5/2}$ state or is laser-driven out of the $D_{5/2}$ state. According to quantum theory, the times at which the atom makes a transition to or from the $D_{5/2}$ state are random. As with other quantum-mechanical processes (such as scattering photons from a beam splitter into one of two ports), this can form the basis of a random number generator, which is of crucial importance to cryptological applications. Unlike in other quantum mechanical systems, however, a single ion undergoing quantum jumps can very cleanly test whether these quantum processes are truly random[2]. Previously, such tests have been made with relatively short and nonsequential strings of quantum jump data with single mercury ions[3]. We are in the progress of making such tests in one and several strontium ions, using data

sequences long enough ($\approx 10^4$ jumps) to yield cryptographically significant results.

We can also perform spectroscopy on the $S_{1/2} \leftrightarrow D_{5/2}$ transition. For example, when the 674-nm diode laser's frequency is scanned over the resonance, we see a resonance curve as shown in Figure 7. Being able to control the ion as it makes the transition between these two states is a critical component in the development of an ion quantum logic gate, and we are further developing our apparatus to do this.
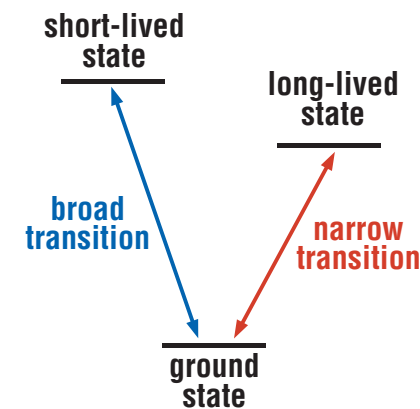

Figure 5. V-configuration for observing quantum jumps.
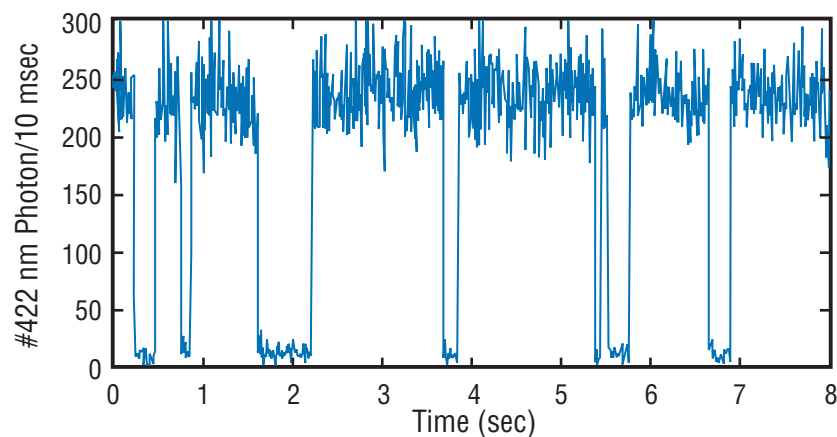
Figure 6. Quantum jumps in ^{88}Sr$^+$.

References/Further Reading

[1] R. J. Cook, "Quantum Jumps," in *Progress in Optics XXVIII*, E. Wolf, ed. (Elsevier B.V., 1990) pp. 362-416.

[2] T. Erber and S. Putterman, *Nature* 318, 41 (1985).

[3] T. Erber et al., *Ann. Phys.* (NY) 190, 254 (1989).
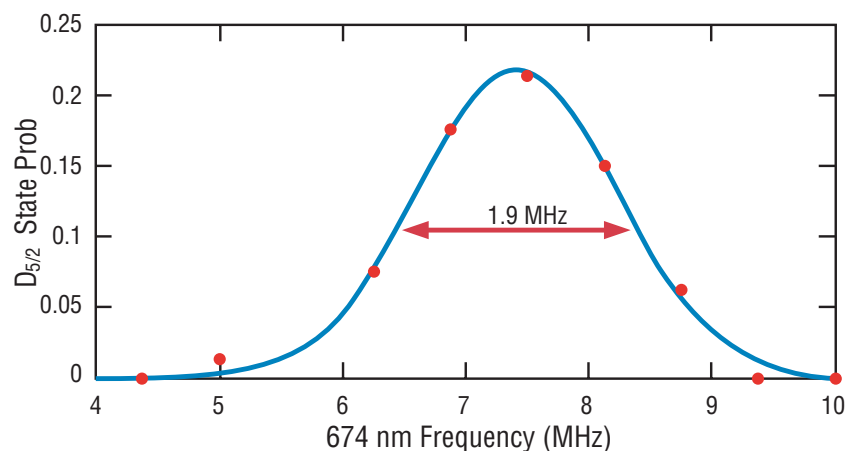
Figure 7. A low-resolution spectrum of the $S_{1/2} \leftrightarrow D_{5/2}$ transition.

Materials Processing using an Atmospheric-Pressure Plasma Jet

G. S. Selwyn, H. W. Herrmann, J. Park, and I. Henins (P-24)

Abstract

Processing materials at atmospheric pressure provides clear advantages over traditional, vacuum-based plasma processing. In addition to reducing the capital cost of equipment and eliminating constraints imposed by vacuum-compatibility, high-pressure and low-temperature plasma processes offer unprecedented improvements for the generation of active chemical species, high chemical selectivity, minimal ion densities that result in low surface damage, and surface-treatment methods unattainable by other means. We describe several variations of this unique plasma source and some of its potential applications.

Introduction

Plasmas have been extensively used for materials-processing applications for the past 30 years.[1] Yet, these applications have generally been limited to select, high "value-added" uses, such as steps required for manufacture of semiconductor devices, magnetic media, or deposition of energy-efficient films for architectural glass. In these applications, plasmas are used because they provide a rich source of chemically active species that react with a surface, or which react with each other to produce secondary, short-lived chemical precursors needed for thin-film deposition. The success of plasma processing technology stems from its low-temperature operation and the fact that no other method can provide the same nondestructive, materials-treatment capability. As such, plasmas are typically used for selective film etching, surface treatment to enhance wetability or to improve adhesion, and in the manufacture of thin films, including diamond-like carbon (DLC), and films having desired metallic, dielectric, or other composite properties.

But, what happens when traditional plasma treatment methods overlap conventional means of surface treatment, such as cleaning applications, or when vacuum-based processing presents obstacles, such as in sterilization or food treatment? In these cases, plasma processing often fails, either because the operation cost for the plasma-based method exceeds the cost for an alternative method or because the demands imposed by vacuum processing are excessive. This case is more the rule than the exception, as demonstrated in Figure 1.

Figure 1 shows two major constraints that arise for traditional, vacuum-based plasma processing: (1) the physical pressure limit required for operation of the plasma, and (2) the economic constraint imposed by this plasma treatment process. The first constraint arises from the need for vacuum operation in order to achieve plasma generation that is nondestructive to materials; the second constraint comes from the fact that the combined processing cost (*i.e.*, the cost of consumables plus the amortized capital cost)

Figure 1. Comparison of the process limits that result from vapor pressure and economic constraints for both vacuum and atmospheric-pressure plasma processing. The rectangular box in the lower right corner represents the domain for vacuum processing. The larger box represents the domain constraints for atmospheric-pressure plasma processing. The larger box also contains much of the process domain represented for vacuum-based plasma processing.
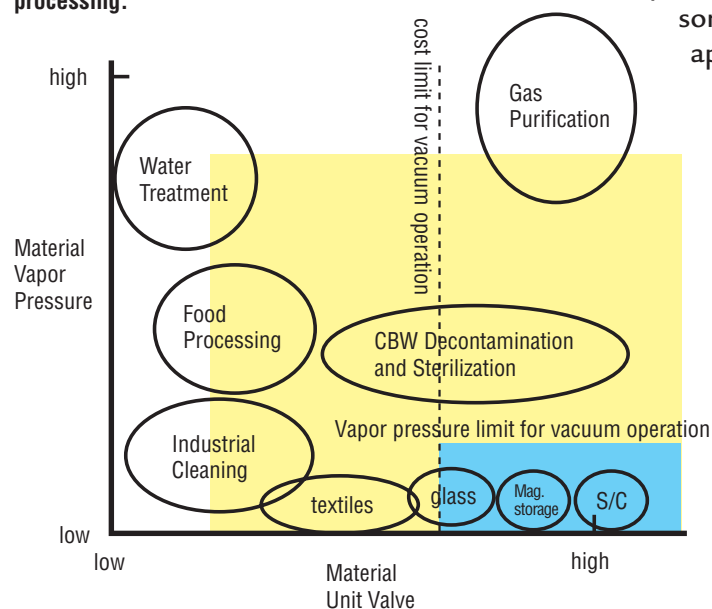
must remain within a level acceptable to the customer. If both constraints cannot be simultaneously met, then the process is infeasible.

The capital equipment cost and the high operation and maintenance costs required for vacuum-processing results in the relatively limited domain illustrated by the small crosshatched (blue) region in the lower right hand corner of Figure 1.

This figure shows that vacuum-compatible, high-value items, such as semiconductors, magnetic media, and specialty films used in architectural glass, are suitable opportunities for vacuum-based plasma processing. In contrast, the larger crosshatched (yellow) region in Figure 1 illustrates the domain available for atmospheric-pressure plasma processing. The greater domain available to this technology

results from a higher vapor-pressure limit and the lower materials-processing cost associated from operation outside of vacuum at normal pressure. Even opportunities such as water and wastewater treatment pose potential opportunities for plasma processing—provided that the materials-processing cost is acceptably low. Of course, developments that reduce the materials-

processing costs will change these results. Figure 1 is intended for qualitative comparison.

Table 1 illustrates some of the applications associated with the materials processes shown in Figure 1. Clearly, a broad range of treatment opportunities exists. For simplicity, only several examples are shown below. Several of these processes are illustrated diagrammatically in Figure 2.

a) Plasma generation of active species

$$e^- + CF_4 \diamondsuit CF_3 + F$$

b) Plasma etching/ ashing/cleaning

$$4F + Si \diamondsuit SiF_{4(g)}$$

c) Plasma deposition of thin films

$$e^- + SiH_4 \diamondsuit Si_{(s)} + 4H$$

d) Plasma decon. of CBW agents

$$O + organic \diamondsuit H_2O + CO_2$$

e) Plasma surface treatment

(ion induced surface change)

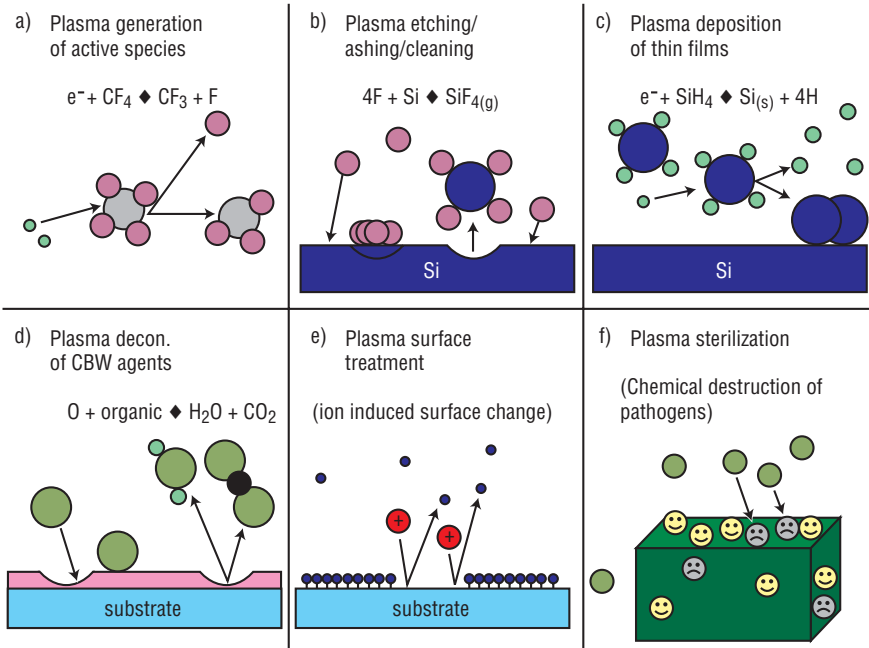f) Plasma sterilization

(Chemical destruction of pathogens)

Figure 2. An illustration of several of the fundamental processes used in plasma processing of materials. Some are purely chemical in nature; some involve physical contributions, such the impact of ions with the surface. Combinations of both chemical and physical processes are common.

Table 1. A Brief Compilation of Various Plasma/Surface Interactions and the Active Component of the Plasma that Contributes to the Desired Product or Change Material/ Substrate Plasma Component Desired Product

Material/Substrate	Plasma Component	Desired Product
Semiconductor substrates	Active neutral and ionic species generated by electron impact	Etching, thin film deposition, stripping, cleaning
Magnetic Storage Media	Sputtered atoms generated by ion bombardment of the target	Magnetic thin films, anti-corrosive coatings
Glass	Thin film chemical precursors, neutrals	Energy efficient coatings
Textiles	Ion bombardment, active neutrals	Increased wettability, wear properties,
Industrial Cleaning	Oxygen atoms, ions	Oxidation and removal of organic films
Food Processing/ Decontamination of CBW Agents/Medical Equipment Sterilization	O, O_2^+, H, OH: chemical reactions initiated by plasma chemistry	Destruction or denature of pathogens, prions; chemical destruction of toxins
Water/Wastewater Treatment	O, O_2^+, O_3, OH: chemical reactions initiated by plasma chemistry	Removal or destruction of water contaminants, pathogens, and reduction of biological oxygen demand (BOD)

Plasma Characteristics

In the most general cases, the plasma is used as a chemical reactor, to produce short-lived, active species that are formed by interaction of plasma electrons with the feed gas present in the plasma. This generality applies whether the plasma is produced in a vacuum or at atmospheric pressure.

Ions are always present in any plasma. Ions may enhance the surface reactivity contributed by active neutrals, such as in etching processes[2], or they may cause unwanted side effects, such as surface damage[3]. As such, design of materials-processing methods requires a means to either increase or reduce the amount of ion interaction with the surface. In many cases, ions impart significant energy to a surface. This helps to drive a chemical reaction, or may even bring about a purely physical reaction process, such as sputtering of target material for metallic coatings. The use of combined, chemical plus physical, reactions are common in many plasma process steps. Note that a significant benefit of atmospheric-pressure plasma processing results from the greater control available

for selecting chemical or physical processes that result from ion interaction with the surface. This is because ion recombination and loss rates at high pressure are much faster than in vacuum.

Plasmas are generally classified as either thermal or nonthermal. Thermal plasmas are characterized by an equilibrium, or a near equality, between the three components of the plasma: electrons, ions, and neutrals: (i.e., $T_e \approx T_i \approx T_n$). Thermal plasmas are always "hot"; temperatures of several thousand degrees are not unusual. Flames, arc discharges, and nuclear explosions are examples of thermal plasmas. While these plasmas have uses in waste treatment and sintering, they are not well suited for most materials-processing applications because of their destructive nature.

Nonthermal plasmas, in contrast, are characterized by a large difference in the temperature of the electrons relative to the ions and neutrals. Because the electrons are extremely light, they move quickly and have almost no heat capacity. In these plasmas, $T_e \gg T_i \approx T_n$. Ionization is maintained by the impact of electrons (which may have temperatures ranging from

0.1 to more than 20 eV) with neutral species, which produces additional electrons and ions. These plasmas are typically maintained by the passage of electrical current through a gas. The low temperatures of nonthermal plasmas makes them well suited for materials-processing applications. However, unlike thermal plasmas, nonthermal plasmas generally have required vacuum or low-pressure operation. Table 2 summarizes the characteristics of thermal and nonthermal plasmas.[4]

Table 2. Comparison of Properties of Thermal and Nonthermal Plasmas

	Thermal Plasma	Nonthermal Plasma
Pressure (atm)	low pressure to many atm.	typically low pressure
Electron/ion Density (cm⁻³)	10^{12}–10^{19}	10^{8}–10^{13}
Electron Temperature (K)	5,000–500,000 (0.5–50 eV)	1,000–50,000 (0.1–5 eV)
Ion/Neutral Temperature (K)	5,000–30,000	100–1,000
Energy Source	electrical, nuclear, combustion	electrical, ionizing radiation

Atmospheric-Pressure Plasma Sources

Besides the aforementioned use of nonthermal plasmas in vacuum environments, several kinds of atmospheric-pressure plasmas also are known.[5] Figure 3 illustrates some of the varieties of atmospheric-pressure plasmas. The so-called "dielectric barrier" discharge, Figure 3a, utilizes a dielectric covering over one or both of the electrodes of which one is typically low-frequency, radio-frequency (rf), or alternating-current (ac) driven while the other is grounded. The purpose of the dielectric film is to rapidly terminate the arcs that form in the potential field between the two electrodes. The discharge consists of a multitude of rapidly forming and equally rapidly terminated arcs that fill the volume between the electrodes. Materials processing may be done using the ozone generated (in the case of an air or oxygen feed gas) or even by passing the substrate material—assuming it is a dielectric—within the discharge region between the electrodes.

The corona discharge, shown in Figure 3b, is a nonarcing, nonuniform plasma that ignites adjacent to the high electric field generated by the sharp points of the electrodes. To prevent arcing, no grounded surface can be near these field emission points, so the discharge is, by nature, nonuniform: plasma density drops off rapidly with increasing distance from the electrode.

The plasma torch, shown in Figure 3c, is often confused with the atmospheric-pressure plasma jet to be described next. Unlike the other plasma sources shown in this figure, the plasma torch is a thermal plasma characterized by a high ion temperature ≈ electron temperature. This source makes use of its very high gas temperatures for materials-processing applications, primarily for chemical-waste destruction, deposition of ceramic coatings, and sintering applications.

The fourth source, shown as Figure 3d, is the atmospheric-pressure plasma jet (APPJ). It is similar to the plasma torch in some respects but is a true nonthermal plasma, as demonstrated by the vast difference in ion and electron temperatures. The APPJ source produces a stable, homogeneous and uniform discharge at atmospheric pressure using 13.56 MHz rf power and a predominate fraction of helium feed gas. Unlike the silent discharge, the APPJ operates without any dielectric electrode cover, yet is free of filaments, streamers, and arcing. The gas temperature of the discharge is typically between 50 and 300°C, so thermal damage to materials is easily avoided.

Figure 4 shows a photograph of the APPJ in operation. As described in the next section, this so-called cylindrical version of the plasma jet is only one kind of APPJ source. Several different variations exist. These different versions provide added benefit for certain applications. We have previously published several technical articles on the plasma physics and chemistry of this unique source.[6,7,8,9,10,11,12]

In the design shown in Figures 3 and 4, helium feed gas (^{a}99%) mixed with a small amount of reactive gas (typically 1%–3% oxygen) enters the annular volume formed between the rf-powered electrode (along the longitudinal axis of the source) and the outer, grounded metal tube. One novel aspect of this APPJ source is that the discharge is formed in this small volume—which typically has insufficient room for immersion of the workpiece or substrate, but the
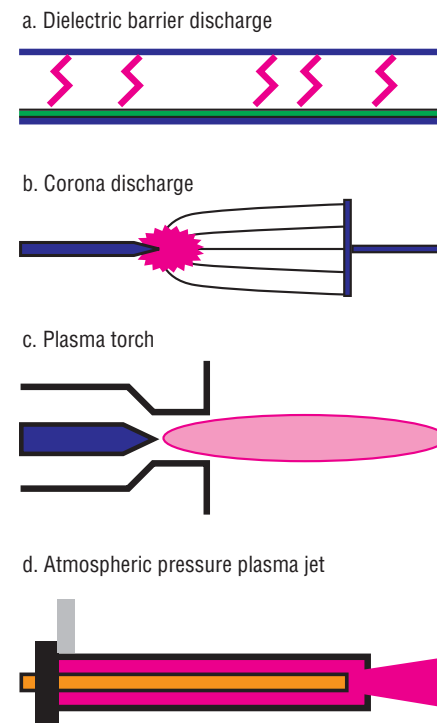

a. Dielectric barrier discharge

b. Corona discharge

c. Plasma torch

d. Atmospheric pressure plasma jet

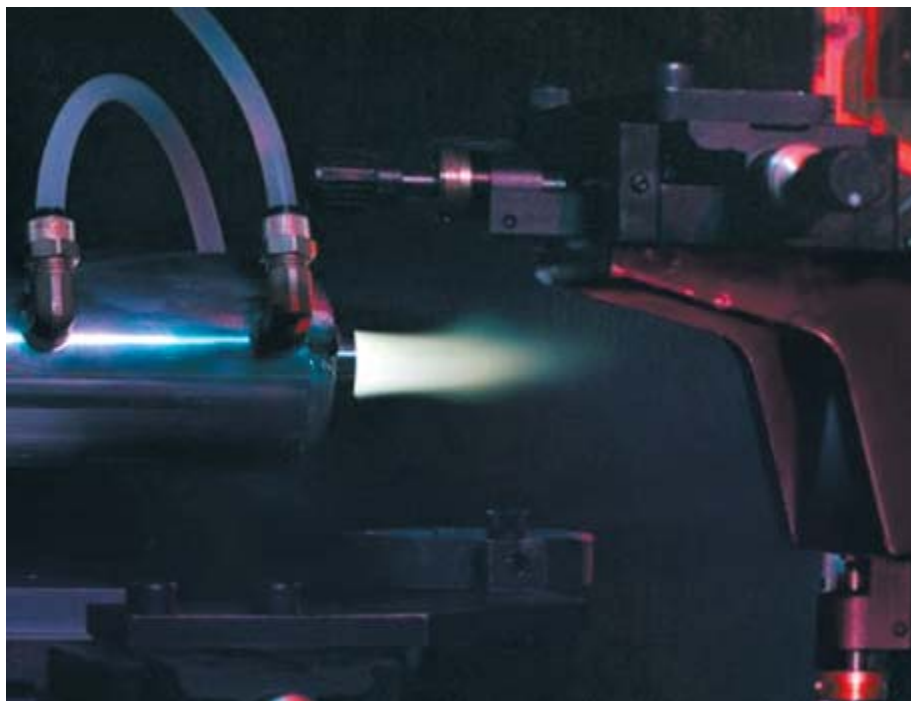**Figure 3. Four different kinds of atmospheric-pressure plasma sources.**

Figure 4. Operation of a cylindrical version of the APPJ. Note the effluent stream of reactive chemical species that exits from the end of the APPJ source.

Table 3. Typical Process Parameters for the Cylindrical APPJ Source

RF frequency	13.56 MHz
RF power	250 W
Plasma power density	35 W/cm^3
Discharge voltage	320 V$_{rms}$
Electron density	~10^{11} cm^{-3}
Electron temperature	~2-3 eV
He flow	92 slpm
O$_2$ flow	0.72 slpm
Gas velocity[a, b]	43 m/s
Effluent temperature[b]	150ºC
Ozone density[b]	~1x10^{15} cm^{-3}
Atomic oxygen density[b]	~5x10^{15} cm^{-3}
Metastable oxygen (O$_2$ $^1\Delta_g$) density[b]	~5x10^{15} cm^{-3}
[a] using 8 mm diameter nozzle	
[b] measured or estimated at nozzle exit	

active chemical species formed by the plasma rapidly exit the source and can impinge downstream on the workpiece.[13] In this way, the substrate is mostly exposed to active neutrals and radicals, rather than ions. The absence of ion chemistry in the downstream flow increases chemical selectivity and reduces surface damage. Of course, this design also uses large quantities of helium feed gas, because slow flow rates result in longer transit times, which favors the recombination or loss of the active, chemical species. Table 3 shows typical process parameters for this source used under normal conditions.

Atmospheric-Pressure Plasma Jet Sources and Applications

The cylindrical design shown in Figures 3d and 4 represents only one variation of the APPJ-source technology. In some applications, especially where large area surface treatment is needed, it may be more desirable to use a similar design, but one in which flat, parallel, planar electrodes are used. A clear advantage of this approach is that the electrode size may be readily scaled up. Because the electrodes are securely held in place on either side, large areas (*i.e.*, 1 m^2 or more) may be achieved, while still keeping the gap between the electrodes precise. Figure 5 shows the design of a "flat jet" and a photograph of this source in operation. By placing the rf electrode between the two (outer) grounded electrodes, we can achieve dual-source operation, as well as provide a safer approach to handling the flat jet.

The flat jet also presents an interesting process opportunity for high-pressure plasma processing. It may be used in either of two modes: 1) downstream operation, as shown in Figure 5a, or 2) for in-situ treatment of materials, accomplished by immersing the material on, or between, the rf-driven and grounded electrodes. Silicon wafers are ideally suited for the latter application because of their thin dimensions, as well as other materials, such as textiles. Even water or wastewater may be channeled to flow along the surface of an electrode in order to expose it to the plasma. With the exception of wafer treatment, these opportunities would clearly be infeasible for vacuum-based plasma processing—not only because of the difficulty of feeding these materials into a vacuum chamber, but also because of the vapor pressure of the workpiece.

Figure 6 shows various means by which the APPJ source has been employed. All have similar properties and characteristics: *i.e.*, use of helium to maintain a nonthermal plasma, low temperature processing, and high flux of reactive species impinging upon the substrate.
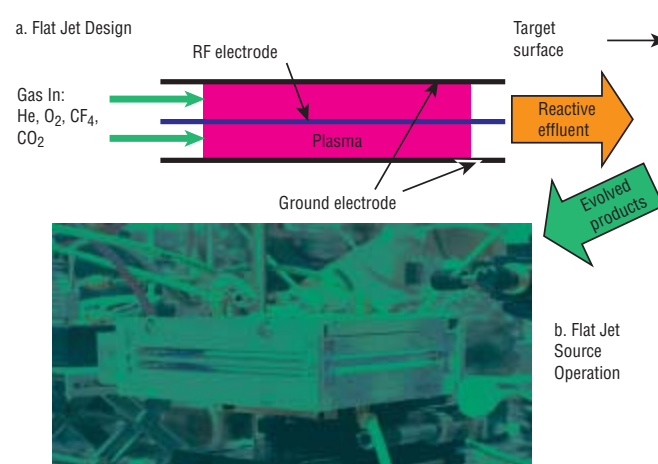

Figure 5. A schematic drawing (a) of the flat jet and a photograph (b) of the same in operation.

Comparison of the APPJ Technology to Other Plasma Sources

All plasma processes have their relative advantages and disadvantages. For example, the highly collisional nature of the APPJ discharge makes it unlikely that this plasma would be used for directional etching of silicon, whereas a vacuum-based plasma serves this purpose well. Collisions are also responsible for the rapid removal of ions in the effluent stream as it exits the source of the APPJ, so this same phenomenon acts to reduce damage in photoresist ashing processes.

Still, a problem that APPJ applications must face is the high use rate of helium feed gas. Helium is used to stabilize the discharge, and for electrode cooling, by virtue of its high thermal conductivity. For this reason, most commercial applications that employ APPJ technology will have to use equipment to recirculate and repurify the feed gas. While this slightly increases the capital cost of the equipment, the operating costs are greatly reduced. Complete systems for filtering helium are commercially available. A helium reprocessing system is indicated in Figure 6d. Not only do these systems reduce COO by reusing the helium carrier gas, but

they also increase the domain of potential applications by moving the left axis of the large box in Figure 1 further to the left—enabling applications that have lower material unit value. We have demonstrated this helium recovery system in a system designed for decontamination of materials having chemical or biological warfare agents, another potential use for the plasma jet.[14]
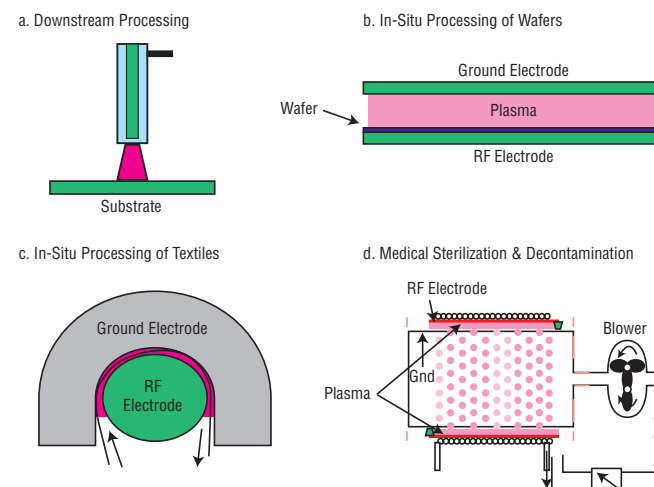

Figure 6. Variations in use of the APPJ technology and different source designs.

Summary and Outlook

Cold, atmospheric-pressure plasmas have the potential to displace many traditional, vacuum-based, plasma-processing practices as well as open up entirely new plasma applications. This results from its ability to inexpensively treat low-value items as well as materials incompatible with vacuum processing owing to their high vapor pressure or cumbersome shape or size. Commercial possibilities abound and the University of California (UC) is currently in the process of licensing this technology out to the private sector. In terms of applications of Department of Energy (DOE) interest, we have primarily been developing these plasmas for chemical, biological, and nuclear decontamination.

DOE NN-20, now part of the newly formed National Nuclear Security Administration (NNSA), has been supporting research to strengthen our nation's defense against chemical and biological terrorism through its Chemical/Biological National Security Program (CBNP). Our effort is aimed at providing domestic emergency responders with a means to quickly neutralize these horrific weapons of mass destruction through oxidation by plasma-activated gases. The

primary advantages of this technology for chemical/biological decontamination is that it is dry and relatively nondestructive to most materials, hence it can be used on "sensitive" equipment such as electronics and optics for which there is currently no suitable decontamination option. A plasma decontamination chamber, similar to the one depicted in Figure 6d, is currently undergoing "live agent" testing on chemical nerve agents, such as VX and Sarin, and blister agents, such as Mustard, at the Army's Dugway Proving Ground. Ultimately, this device may be commercialized as a low-temperature medical sterilizer to help displace the health care industry's current standard of ethylene oxide, a flammable, toxic, and environmentally unsound gas. We are also developing methods to be used in a plasma decontamination jet, a hand-held wand that can decontaminate sensitive equipment in-situ while installed at facilities such as control centers for commercial communications, power, and transportation facilities as well as conventional office space. Naturally, these technologies have military defense applications as well.

Under DOE's Environmental Management Science Program (EMSP), we have also been developing actinide decontamination in collaboration with UCLA's Chemical Engineering Department. By adding fluorine containing gases, such as CF_4 or NF_3, to the APPJ's helium stream we can also produce atomic fluorine capable of etching the actinides plutonium and uranium. Reaction with the fluorine produces volatile byproducts which can then be trapped in filters. This allows one to take a large item considered transuranic (TRU) waste, such as a glove box, and convert it to low-level radioactive waste. Only a small filter then needs to be disposed of as TRU waste, allowing the DOE to save large sums of money through volume reduction. We are currently optimizing the process on actinide surrogates, such as tantalum, and designing a system to be used in a plutonium decontamination demonstration in the CMR facility next fiscal year.

The atmospheric-pressure plasma jet, invented at the Laboratory in 1995 and winner of an R&D 100 Award in 1999, represents a new direction for the plasma processing of materials. The ability to dispense

with the vacuum chamber will make plasmas much more attractive in numerous applications that range from surface treatments such as cleaning, etching, decontamination, thin-film deposition, and surface modification to volume processing of gases and liquids. Recent improvements, such as replacement of the helium carrier gas with cheaper and more readily available gases such as argon, steam, and even air, continue to make this technology even more practical. Of course, developments such as these necessitate basic research that leads to a fundamental understanding of this relatively new realm of plasma physics. By spinning-off this technology to the private sector, the UC stands to generate a substantial income stream which can be reinvested in research and development, further strengthening our intellectual-property portfolio in atmospheric-pressure plasmas.

References/Further Reading

[1] C. J. Mogab in, *VLSI Technology*, S. M. Sze Ed., (McGraw Hill, New York, 1983), pp 303–346.

[2] J. W. Coburn, *Plasma Chemistry and Plasma Processing* 2, 1 (1982).

[3] K. F. You, M. C. Chang, C. Y. Wu, *IEEE Trans. Elect. Dev.* 45, 239 (1998).

[4] M. A. Lieberman and A. J. Lichtenberg, *Principles of Plasma Discharges and Materials Processing*, (Wiley-Interscience, New York, 1994), pp 6–10.

[5] A. Schuetze, J. Y. Jeong, S. E. Babayan, *et al.*, *IEEE Trans. Plasma Sci.* 26, 1685 (1998).

[6] S. E. Babayan, J. Y. Jeong, V. J. Tu, *et al.*, "Deposition of Silicon Dioxide Films with an Atmospheric-Pressure Plasma Jet," *Plasma Sources Science and Technology* 7, 286–288 (1998).

[7] J. Y. Jeong, S. E. Babayan, V. J. Tu, *et al.*, "Etching Materials with an Atmospheric-Pressure Plasma Jet," *Plasma Sources Science and Technology* 7, 282–285 (1998).

[8] J. Y. Jeong, J. Park, I. Henins, *et al.*, "Reaction Chemistry in the Afterglow of an Oxygen-Helium, Atmospheric-Pressure Plasma," *Journal of Physical Chemistry A* 2000, 104 (34) 8027–8032 (2000).

[9] J. Park, I. Henins, H. W. Herrmann, *et al.*, Discharge Phenomena of an Atmospheric Pressure Radio-Frequency Capacitive Plasma Source," *Journal of Applied Physics* 89, 20–28 (2001).

[10] V. J. Tu, J. Y. Jeong, A. Schutze, *et al.*, "Tantalum Etching with a Nonthermal Atmospheric-Pressure Plasma," *Journal of Vacuum Science and Technology A* 18, 2799–2805 (2000).

[11] J. Park, I. Henins, H. W. Herrmann, *et al.*, "Gas Breakdown in an Atmospheric Pressure Radio-Frequency Capacitive Plasma Source," *Journal of Applied Physics* 89, 15–19 (2001).

[12] J. Park, I. Henins, H. W. Herrmann, *et al.*, "An Atmospheric Pressure Plasma Source," *Applied Physics Letters* 76, 288–290 (2000).

[13] US Patent No. 5,961,772 issued Oct. 5, 1999.

[14] H. W. Herrmann, I. Henins, J. Park *et al.*, "Decontamination of Chemical and Biological Warfare (CBW) Agents Using an Atmospheric Pressure Plasma Jet," *Physics of Plasmas* 6, 2284–2289 (1999).